SEGMENTATION AND QUANTITATIVE CHARACTERIZATION OF BREAST MASSES IMAGED USING DIGITAL MAMMOGRAPHY

BY

SUSSAN ACHO NKWENTI

Thesis submitted to comply with the requirements for the Ph.D. (Medical Physics) degree in the Faculty of Health Sciences at the University of the Free State

Promoter: Prof. William Ian Duncombe Rae

Department of Medical Physics

September 2018

DECLARATION

AUTHOR:	SUSSAN ACHO NKWENTI
DEGREE:	PhD
TITLE:	Segmentation and Quantitative Characterization of Breast Masses Imaged Using Digital Mammography
DATE OF DEPOSIT	15 September 2018

I, Sussan Acho Nkwenti, certify that the thesis hereby submitted by me for the PhD (Medical Physics) degree at the university of the Free State is my independent effort and had not previously been submitted for a degree at another University/Faculty. I furthermore waive copyright of the thesis in favour of the University of the Free State.

Signature: Sussan Acho Nkwenti

Table of Contents

LIST OF FIGURES

LIST OF TABLES

ABSTRACT

Breast cancer is the leading cause of cancer death among women. Screening Mammography is the most effective method currently available for early detection of breast cancer. When breast cancer is detected at an early stage the prognosis is good because the tumour is smaller and more often well-differentiated, and less likely to have spread to regional lymph nodes.

Computed radiography and direct digital detector mammography imaging systems provide a wide dynamic range for proper display of different densities of breast tissue areas. Their response over a wide range of X-ray intensities is linear; consequently, small differences between the attenuation coefficients of breast structures over a wide range of densities are clearly displayed. This includes the low signal areas associated with high densities found within tumours. Some masses infiltrate the surrounding breast tissue hence they exhibit ill-defined and intensity inhomogeneous boundaries with rough contour, while other masses exhibit well-defined edges and in most cases they possess smooth, round or oval shapes with macro-lobulations. The morphologic features of a mass such as its shape, margin and density give a clue to its benign or malignant nature.

This study investigates and quantifies the changes in shape-based descriptors due to changes in the location of the initial level set contour in region based active contour models in delineating mammographic masses and proposes new methods to eliminate contour leakage and contour traps in active contour segmentation models which are due to intensity inhomogeneity within tumours and boundary regions of tumours. Furthermore, the study proposes a contextual region of interest model to assess the variation of texture features from the core to its periphery of biopsy proven malignant masses as a concept of tumour modelling in mammography and also the variation of texture features between grade 2 and grade 3 masses as a concept of tumour grading in mammography with texture analysis.

GLOSSARY

BIRADS	-Breast Imaging Report and Data System
BSE	-Breast self-exam
CAD	-Computer Aided Detection
CC	-Cranio-caudal
CR	-Computed Radiography
CV	-Chan-Vese
DF	- Fourier descriptors
EDFD	-Euclidean distance between Fourier descriptors
GLN	-Grey level non-uniformity
GS	-Global segmentation model
HGRE	-High grey level run emphasis
H0	-Null Hypothesis
H1	Alternative Hypothesis
JI	-Jaccard index
JSC	-Jaccard similarity coefficient
L	-Left
LGRE	-Low grey level run emphasis
LRE	-Long run emphasis
MRI	-Magnetic resonance imaging
MLO	-Mediolateral-Oblique
PACS	-Picture archiving and communication system
R	-Right
RLN	-Run length non-uniformity

ROI	-Region of interest
RP	-Run percentage
SC	-shape convexity
SR	-Shape rectangularity
SRE	-Short run emphasis
TFT	-Thin film transistor
TV	-Total Variation
Winsize	-Window size

CHAPTER1: INTRODUCTION

1.1 Mammography

Mammography is one of the most effective imaging modalities for early detection of breast cancer [1], [2], [3] because it has a high sensitivity and a specificity for early detection of breast cancer in screening mammography It uses low energy X-rays photons to produce an image of the human breast called a mammogram. Mammographic units (Fig. 1.1) are designed to produce mammograms with high contrast, high resolution and minimal radiation dose to the breast to ensure maximum visualization of breast anatomy and the signs of disease without subjecting the breast to unnecessary amounts of radiation. The low energy X-rays improve the differential absorption of X-rays between different components of the breast tissue, such as fatty tissue, fibrous connective tissue, mass lesions, micro-calcifications and thus improving image information (visibility of signs of disease) captured on mammograms.

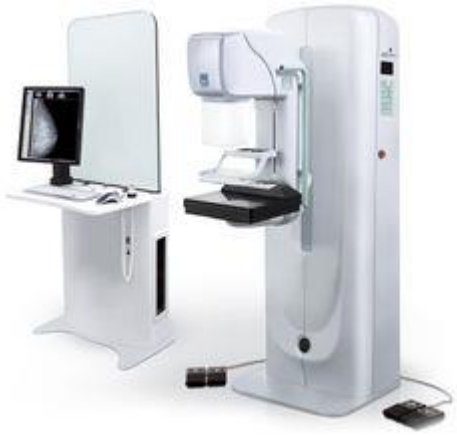

Fig 1.1 A mammographic X-ray unit with an acquisition station and monitor for softcopy display [Adapted from http://www.medicalexpo.com/prod/villa-sistemi-medicali/product-70463-534527.html [26].]

Screening mammography is a system of generalised breast cancer screening used to obtain mammograms from patients who have no symptoms of breast cancer [4], [5]. The mammograms are investigated for the presence of early stages of breast cancer, which might

be too small to be felt by the patient, or the physician. A standard screening examination requires two mammographic views of each breast. Nowadays it is a common practice in many countries for women above a locally defined age, and/or having a history of breast cancer in the family, to regularly undergo mammographic screening. The age at which this commences varies from country to country, due to differing availability of resources. The main purpose is to identity and remove any detected malignant tumour at an early stage when the presence of metastatic disease is less probable, and the possibility of local control is highest [6].

Diagnostic mammography is requested after a suspicious finding on a screening mammogram, or the finding of abnormalities that may have been detected through breast self-exam (BSE) and/or clinical examination [7]. This examination is more time consuming and additional mammographic views such as a changed angle, magnification or spot compression views of the breast may be requested. These mammograms identify the location and size of the breast abnormality. They provide information about the surrounding tissue and the lymph nodes associated with the abnormality which are markers or indicators for malignancy. Studies have shown that dense breasts can limit the sensitivity of mammography both for detection of breast cancers and for delineating disease extent; thus, for dense breast imaging, another imaging modality such as ultrasound, or contrast-enhanced breast magnetic resonance imaging (MRI) may be requested to complement mammographic findings [5].

1.2 Standard mammographic views in screening mammography

The cranio-caudal (CC) and the mediolateral-oblique (MLO) views are routinely acquired for screening mammography [8]. These projections maximize the amount of breast tissue that can be visualized on a detector. The CC projection is taken from a horizontally compressed breast and this view illustrates all the medial tissue, the nipple and in some cases part of the pectoral muscle. The MLO projection is taken at an angle such that the X-ray beam is directed from the superior-medial to the inferolateral aspect of the breast while the imaging detector is parallel to the long axis of the pectoral muscle. This view captures an image of part of the pectoral muscle. It ensures that the inframammary fold is open, while deep and superficial breast tissues

are well separated for optimal visualization. Fig. 1.2 illustrates the CC and the MLO projections with their respective mammograms.

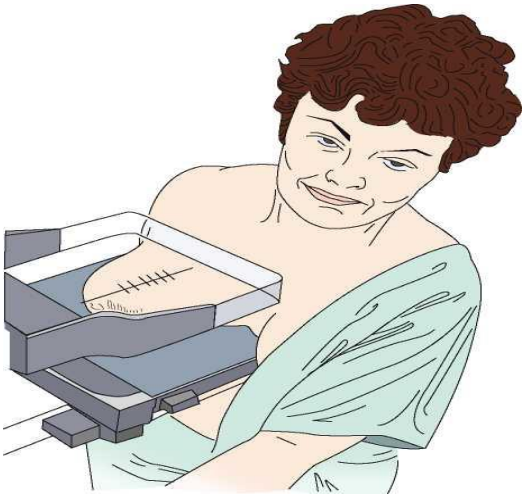

Cranio-caudal (CC) projection

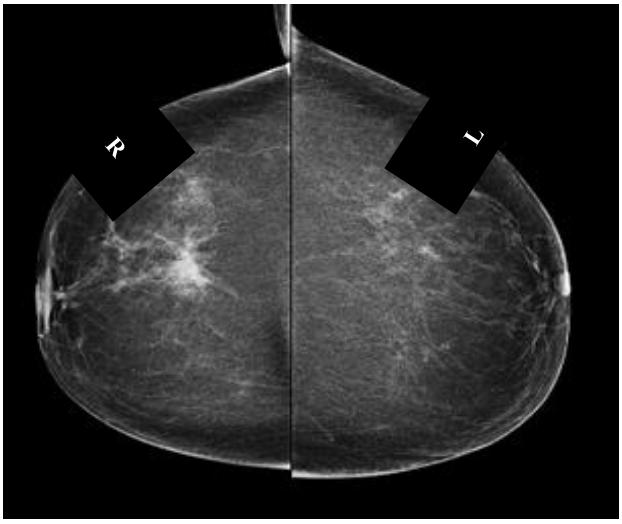

Right CC view and the Left CC view

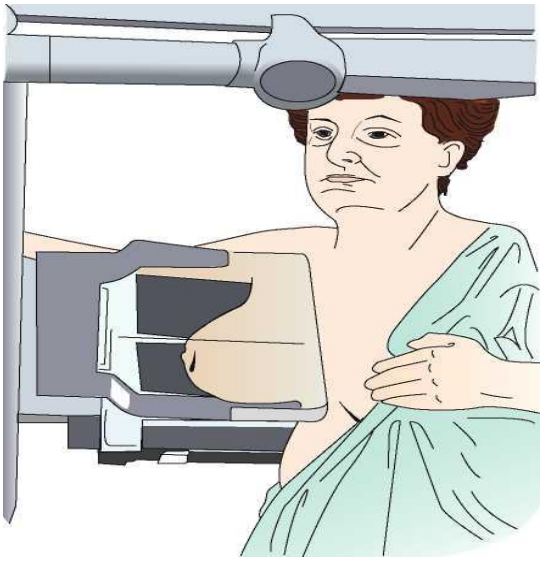

Mediolateral-oblique (MLO) projection

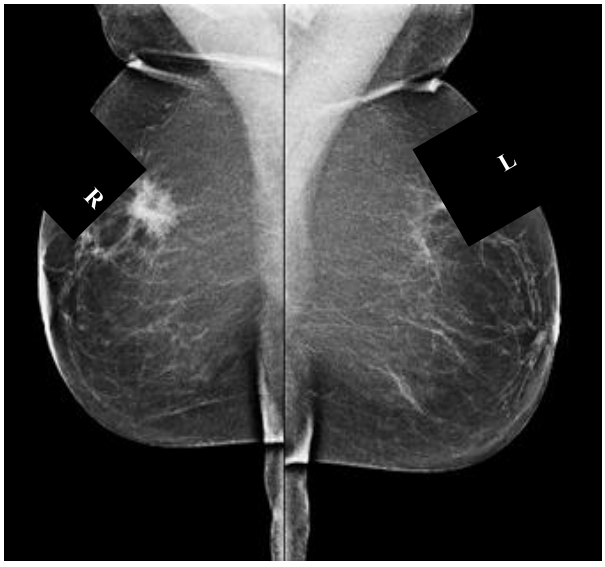

Right MLO view and the Left MLO view

(a) (b)

Fig. 1.2: Standard mammographic projections and their corresponding mammograms (a) The CC projection and the MLO projection [Adapted from http://aibolita.com/womens-diseases/39943-performing-the-examination.html [27]]. (b) The CC and MLO views of the right and left breast, displayed as mirrored pairs for image interpretation.

1.3 Mammography X-ray detectors

The X-ray detector of a mammographic imaging system is designed to produce analogue or digital signals which are representative of the spatial pattern of X-rays transmitted through the breast tissue. These signals are transformed into grey scale values for visualization of the breast tissue (mammogram).

1.3.1 Film-screen detector system

Conventional film-screen mammography uses an intensifying screen in close proximity to the film to capture transmitted X-rays from the breast. The intensifying screen converts the transmitted X-ray to light photons, which spread out depending on the characteristics of the screen and illuminate the film to form a latent image of the breast. The conversion of X-rays to light photons is necessary in film screen imaging systems because film is more sensitive to light photons than X-ray photons. The use of screens thus significantly reduces the radiation dose required to create a satisfactory image of the breast. Although the film has a high spatial resolution, its response to X-ray intensities is not linear, having an S-shaped response curve. It has a limited dynamic range over which it can distinguish structures with small differences in contrast meanwhile tissue areas of high and low densities are sub-optimally imaged with poor contrast resolution. Generally, with this type of imaging system, the film is the sole medium for acquisition, display and storage of images, therefore any suboptimal conditions in any of these steps will have an adverse effect on the overall image quality of the mammographic imaging process [9].

1.3.2 Digital detector system

Digital detector systems in mammography have replaced analogue film screen systems in mammography over the last decade. This detector system decouples the image acquisition, image display, and the image archiving (storage) processes, thus allowing each stage of the

imaging chain to be optimised separately. Its response over a wide range of X-ray intensities is linear and it has a wide dynamic range for proper display of different densities of breast tissue areas and consequently improves the visibility of all mammographic features within the breast [10], [11]. Post processing of the images allows for the application of optimised histogram equalisation algorithms which ensure maximal display contrast over all areas of the image so that display window adjustment during the reporting process can be minimised.
A digital detector system in mammography captures images in two ways: indirect conversion and direct conversion.

1.3.2.1 Indirect Conversion digital detector system.

This system uses a two-step process to capture the spatial distribution of X-rays photons transmitted through the breast in mammography. The X-ray detection device consists of a scintillator and an array of photodetectors. The scintillator absorbs the transmitted X-ray photons to produce light photons which are collected and detected with a photodetector. The most common scintillators are caesium iodide and gadolinium oxysulfide.
The cassette-based computed radiography (CR) detector system in mammography is included in this category. Its detector system consists of a storage-phosphor plate with a layer of photostimulable crystals. The plate is placed in a cassette to fit the Bucky slot of a mammographic unit in the same manner as a screen-film cassette. The imaging plate absorbs and stores the transmitted X-ray photons from the breast in proportion to the intensity it receives to create a latent image. After exposure, the cassette is placed in a CR reader device which automatically opens the cassette and retrieves the image plate to extract the latent image. The image plate is scanned with a laser beam and the stored energy is released as light photons in an amount proportional to the stored energy. These light photons are collected and detected by a light guide and a photomultiplier tube respectively. The analogue signal is amplified and digitized for soft copy display, or processed and printed on a film. In the final stage, white light is incident on the plate to erase all residual signals and the plate is ready for reuse.

1.3.2.2 Direct Conversion digital detector system.

In the direct detection approach, a high atomic number photoconductor is coated on a flat panel thin film transistor (TFT) array with a charge storage capacitor device. During exposure, the transmitted X-ray photons are absorbed by the photoconductor and charge carriers (electron-hole pairs) are released. These charges drift towards the electrode of the charge-storage-capacitor under the influence of an applied electric field, where they are collected, amplified and quantized for each pixel by the readout electronics.

This detection system excludes the problems associated with lateral spread of light which is inherent to the indirect conversion detector system: lateral spread of light photons causing loss of high frequency image information and general degradation in spatial resolution and signal to noise ratio.

In mammography, breast compression determines the quality of the mammogram. Breast compression is necessary because it spreads out the breast tissue and thus reduces the overlapping tissue and the effective thickness of the breast. This reduces the radiation dose required to produce diagnostic mammograms with adequate image quality and furthermore improves visualization of the breast tissue on mammograms. It also immobilizes the breast to avoid image blurring. Breast compression is painful for some women. Direct conversion mammographic detector system offers the possibility of a decrease in the breast compression force, because of its high detective quantum efficiency at higher x-ray energies. Post processing of the image also allows compensation for the differences in thickness from the chest wall edge of the breast to the nipple side of the breast which may occur when the applied compression force is reduced.

1.4 Interpretation process of digital mammograms

1.4.1 Hanging protocol

After image acquisition and processing, the digital mammograms are displayed on the monitor of the picture archiving and communication system (PACS) workstation for image interpretation. The hanging protocol layout for image display on the monitor is a series of

actions performed to arrange mammograms for optimal viewing. It provides a consistent manner in which the different mammographic views of prior and current studies of a patient can be automatically displayed and hence reduces the amount of manual image arrangement and display adjustment required from the radiologist [12], [13]. Standard viewing practice is to compare the images of the right and the left breast using the same projection, and to also compare the current and prior views of the same breast and same projection. Fig. 1.3 illustrates the softcopy display of a prior and current study of a patient in a standard viewing format.

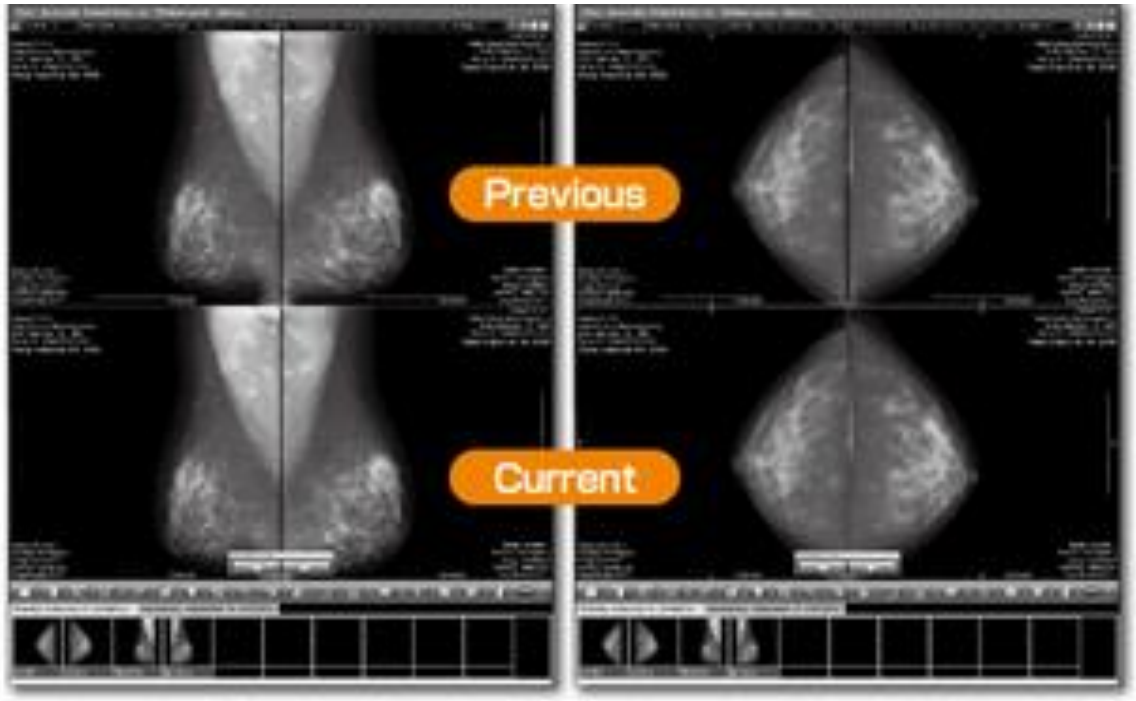

Figure 1.3: Softcopy display of a prior and current study of a patient in a standard viewing format. Adapted from https://www.konicaminolta.com/healthcare/products/mammo/acies_mammo_viewer_license/feature.html [28]

1.4.2 Interpretation of mammograms

The hanging protocol automatically displays the bilateral CC views and bilateral MLO views as a mirrored pair on the high-resolution monitor of a workstation as shown in Fig. 1.2. The

mammograms of left and right breasts of the same view are inspected carefully and compared to evaluate breast symmetry, size, general density and glandular distribution. Next, corresponding regions on each mammogram of the same views are evaluated and compared to search for masses, densities, calcifications, architectural distortions, and associated findings, such as, skin or nipple retraction, skin thickening (which may be focal or diffuse), trabecular thickening and skin lesions. Usually when a suspicious region of interest has been identified on a mammogram, the radiologist will estimate, or measure, the distance of the lesion seen on one view from the nipple and look for a possible lesion at about the same distance from the nipple on the other view. The two most common abnormal mammographic findings that are associated with breast cancer are microcalcifications and mammographic masses.

1.4.2.1 Microcalcifications

These are tiny irregular granule like deposits of calcium with sizes less than 0.5mm, with density greater than the dense mammary tissue, which can be easily identified on mammograms of dense breasts. The radiologist assesses the size, distribution, form, and density of microcalcifications to determine the possibility of malignancy since the risk of malignancy varies with their morphology [14].

1.4.2.2 Mammographic masses

Mass lesions usually stand out against the grey-white mammary tissue or dark fat tissue, but in some cases, they have almost the same appearance as surrounding tissue and are therefore difficult to detect. This is especially so for dense breasts. They must be seen on more than one view, if not they are labelled as a density. The nature of malignancy is assessed with the characteristic of the morphologic features of the mass, which are shape, margin and density. Generally mammographic findings are described and classified with the Breast Imaging Report and Data System (BI-RADS ®) [15], [16]. Digital mammography allows maximal enhancement of the display contrast between the mass and the surrounding tissues. This should

allow easier detection and visualisation of masses acquired using digital mammographic systems.

1.5 Breast Imaging Report and Data System

BIRADS® is the earliest standard protocol for the classification of mammographic studies. It was developed by the American College of Radiology to harmonize the assessment of mammograms in the USA so that doubtful regions of interest on a mammogram could be assigned to a category reflecting the level of suspicion of the radiologist. This system of classification provides a standard set of guidelines for the interpretation of mammograms thus ensuring that clinical reports are reproducible and expressed in a common language to facilitate communication between referring clinicians and the reporting radiologists.

Double reading is defined as the interpretation of a mammogram by two independent radiologists. Swedish and the European guidelines recommend double reading and this practice has been shown to increase cancer detection rates by 5-17% [17]. However recent study from Posso et al [18] has shown that double reading of digital mammograms is more expensive that single reading. They reported that, the cancer detection rate was similar for both reading strategies, however double reading yielded a higher proportion of false- positive results than single reading. The process of independent double reading of a mammogram can exert a lot of time pressure in institutions where there is a shortage of trained mammogram readers; therefore, commercially available, automated image analysis and prompting systems, such as computer aided detection (CAD) systems, whose performance has been evaluated and shown to match those of experienced readers, can be used as a second reader [19]. These systems mark suspicious areas for second look or areas that the radiologist might have overlooked. The algorithms of these computerised assessment techniques interpret breast density, or image signal intensities, as the spatial distribution of pixel values, or grey levels. These grey levels are grey tones whose spatial distribution patterns are known as texture. Therefore, texture analysis, which represents a set of mathematical models and procedures, can be used for characterisation of the variations in these distributions. Abnormal regions of interest in a mammogram such as tumour masses, architectural distortions and microcalcifications usually

manifest as a change in texture and/or anatomical structures from surrounding tissue. Algorithms utilising texture analysis models should therefore possibly be able to identify and quantify these textural and structural changes in a mammogram [20], [21].

1.6 Problem statement

CR and direct digital detector imaging systems provide a wide dynamic range for proper display of different densities of breast tissue areas. Their response over a wide range of X-ray intensities is linear; consequently, small differences between the attenuation coefficients of structures over a wide range of densities are clearly displayed. This includes the low signal areas associated with high densities found within tumours, even though the signal to noise ratio within these areas is relatively low. In film screen mammography used previously, these areas had low exposure and thus low signal. Poor detail and contrast were thus achieved in image areas representing mammographic masses. These differences, now detectable and visible because of the use of digital acquisition systems, may translate to textural changes within a mass. The local distribution of these textural changes is concatenated to form feature vectors for classification of mammographic masses [22]. We are however not aware of any publication or literature in which these local textural changes have been used for modelling of texture changes in mass, to give an insight into the growth rate or clinical properties of a mass. This might be because most of the masses investigated by most researchers are relatively small, and in most cases compact with little or no textural information, since small masses are the most common type of breast mass seen in a population where screening programs are offered. Or it may be that these local micro-changes within a mass are small as one moves from the centre of the mass to the periphery and thus are difficult to quantify. A mammographic database with large masses (with diameter greater than 3 cm) representing malignant masses could potentially provide additional information for mathematical models that can describe the textural evolution of masses with time, hence predicting the future behaviour of non-malignant masses, which are relatively uniform and well defined. On the other hand, the ‘progressive changes’ in texture (both macro and micro-texture) (that is if they do exist) with different diameters of large masses, can also provide additional information. Current literature on

mathematical models of tumour progression in breast cancer screening have been developed based on the tumour size and the event of detection (age) for the European population [23], [24], [25] , but no literature could be found where these models take into consideration the classification of different types of breast tumours or textural changes from the core to the periphery of mammographic masses.

1.7 Research objective

The aim of this project is to extract quantifiable projection image features from mammograms, including texture features, which will be used for the assessment of mammographic masses and tumour modelling. These features and analysis could then potentially be incorporated into mammographic CAD systems, which could then be used to generate quantitative descriptors of tumours being investigated.

The research objective consists of two main contributions:

(1) Investigation of changes in one dimensional shape-based descriptors and the segmented areas of masses in direct digital mammograms due to changes in the location of the initial level set contours
(2) Segmentation of the mass region with an appropriate segmentation algorithm.
(3) Evaluation of texture analysis in mammographic tumour modelling and tumour grading.

1.8 Thesis summary and organization

In this Section we summarize the content of each chapter of the thesis.

Chapter 2: Segmentation methods in mammographic masses

This chapter presents an extensive literature survey covering segmentation methods of mammographic masses in mammography. It highlights the strengths and weaknesses of some

of these methods. In particular, the region based active segmentation methods are highlighted where the placement of the initial level set contour may influence the final segmentation outcome of objects with intensity inhomogeneity and weak boundaries.

Chapter 3: Changes in shape-based descriptors and mass segmentation areas due to changes in the placement of the initial level set contour in region based active contour models.

In this chapter the origin of intensity inhomogeneity is discussed, ill-defined and weak boundaries in mammographic masses. It investigates and quantifies the changes in shape-based descriptors due to changes in the location of the initial level set contour in region based active contour models in segmentation of digital mammographic masses.

Chapter 4**:** Mass- specific threshold values of global minima for convex energy functionals with an interactive segmentation model.

This chapter proposes a semi-automatic method to derive a user-independent location for the initial level set contour to ensure that final segmentation outcomes are precise and reproducible in region based active contour segmentation methods.

Chapter 5: Mammographic mass characterization for tumour modelling and tumour grading.

This chapter reviews the morphologically structure of mammographic masses and mathematical methods for texture analysis in mammography. It proposes a contextual region of interest model to assess the variation of texture features from the core to its periphery of biopsy proven grade 2 and grade 3 masses and hence, provides data to evaluate the existence or non-existence of changes in texture features from the core to the periphery of these masses as a concept of tumour modelling in mammography. It investigates the concept of texture feature analysis as a tool for tumour grading in mammography.

Chapter 6: This chapter summarises the findings of the study, concludes the work and also discuss the limitation of the study.

1.9 References

[1] K. Kerlikowske, D. Grady, S. Rubin, C. Sandrock and V. L. Ernster, "Efficacy of screening mammography: a meta-analysis," *JAMA*, vol. 273, pp. 149-154, 1995.

[2] P. C. Gøtzsche, "Beyond randomized controlled trials," *Cancer,* vol. 94, no. 2, pp. 578-578, 2002.

[3] L. Tabár , B. Vitak, . H. H. Chen, M. F. Yen, S. Duffy and . R. A. Smi, "Beyond randomized controlled trials : organized mammographic screening substantially reduces breast carcinoma mortality ," *Cancer:Interdisciplinary International Journal of the American Cancer Society* , vol. 91, no. 9, pp. 1724-1731, 2001.

[4] Y. C. Teh, G.H. Tan, N. A. Taib and K. Rahmat, C J Westerhout, F Fadzli, M H See, S Jamaris. and C H Yip, "Opportunistic mammography screening provides effective detection rates in a limited resource healthcare system," *BMC cancer* , vol. 15, no. 1, p. 405, 2015.

[5] D. G. Dodge and J. L. Kegel, "Advances in Breast Cancer Screening and Diagnosis.," *The Journal of Lancaster General Hospital,* vol. 1, no. 2, 2006.

[6] L. Nyström, I. Andersson, N. Bjurstam, B. Nordenskjöld and E. L. Rutqvist, "Long-term effects of mammography screening: updated overview of the Swedish randomised trials," *The Lancet,* vol. 359, no. 9310, pp. 909-919, 2002.

[7] E. A. Sickles, D. L. Miglioretti, R. Ballard-Barbash, B. M. Geller, J. W. Leung, R. Smith-Bindman and B. C. Yankaskas, "Performance benchmarks for doagnostic mammography," *Radiology*, vol. 235, pp. 775-790, 2005.

[8] L. W. Bassette, I. A. Hirbawi, N. DeBruhl and M. K. Hayes, "Mammographic positioning: evaluation from the view box," *Radiology,* vol. 188, pp. 803-806, 1993.

[9] M. Mahesh, "AAPM/RSNA physics tutorial for residents : Digital Mammography: An Overview," *RadioGraphics,* vol. 24, pp. 1747-1760, 2004.

[10] M. J. Yaffe and J. G. Mainprize, "Detectors for digital mammography," *Technology in cancer research & treatment* , vol. 3, no. 4, pp. 309-24, 2004.

[11] A. P. Smith, "Fundamentals of digital mammography: physics, technology and practical considerations," hologic, 2015. [Online]. Available: http://www. hologic. com/oem/pdf . [Accessed 25 08 2017].

[12] B. M. Hemminger, "Soft Copy Display Requirement for Digital Mammography," *Journal of Digital Imaging,* vol. 16, no. 3, pp. 292-305, 2003.

[13] S. V. Destounis, "Acquisition and workflow issues in Digital Mammography," *Applied Radiology,* vol. 37, no. 10, pp. 10-16, 2008.

[14] C. K. Bent, L. W. Bassett and C. J. D'Ors, "The positive predictive value of BI-RADS microcalcification descriptors and final assessment categories.," *American Journal of Roentgenology,* vol. 194, no. 5, pp. 1378-1383, 2010.

[15] L. Liberman and J. H. Menell, "Breast imaging reporting and data system (BI-RADS).," *Radiologic Clinics,* vol. 40, no. 3, pp. 409-430, 2002.

[16] C. J. e. D'Orsi, ACR BI-RADS Atlas: Breast Imaging Reporting and Data System, 2013.

[17] M. Helvie, "Improving mammographic interpretation: double reading and computer-aided diagnosis," *Radiologic Clinics of North America,* vol. 45, no. 5, pp. 801-811, 2007.

[18] M. C. Posso, T. Puig, M. J. Quintana, J. Solà-Roca and X. Bonfill, "Double versus single reading of mammograms in a breast cancer screening programme: a cost-consequence analysis.," *European radiology,* vol. 26, no. 9, pp. 3262-3271, 2016.

[19] X. Bargalló, G. Santamaría, M. del Amo, P. Arguis, J. Ríos, J. Grau, M. Burrel, E. Cores and M. Velasco, "Single reading with computer-aided detection performed by selected radiologists in a breast cancer screening program," *European journal of radiology,* vol. 83, no. 11, pp. 2019-2023, 2014.

[20] J. Y. Choi,, D. H. Kim, K. N. Plataniotis and Y. M. Ro, ""Classifier ensemble generation and selection with multiple feature representations for classification applications in computer-aided detection and diagnosis on mammography," *Expert Systems with Applications,* vol. 46, pp. 106-121, 2016.

[21] F. S. S de Oliveira, F. A. O. de Carvalho, A. C. Silva, A. C. de Paiva and M. Gattass, "Classification of breast regions as mass and non-mass based on digital mammograms using taxonomic indexes and SVM.," *Computers in biology and medicine,* vol. 57, pp. 42-53, 2015.

[22] Y. Li, H. Chen, X. Wei, Y. Peng and L. Cheng, "Mass classification in mammograms based on two-concentric masks and discriminating texton," *Pattern Recognition,* vol. 60, pp. 648-656, 2016.

[23] J. Michaelson , A. B. Satija, R. Moore and R. e. a. Weber, "Estimate of the sizes at which breast cancers become detectable on mammographic and clinical grounds," *Journal of women`s imaging* , vol. 5, pp. 3-10, 2003.

[24] H. Weedon-Fekjaer, B. H. Lindqvist, L. J. Vatten, O. O. Aalen and S. Tretli, "Breast cancer tumour growth estimated through mammography screening data," *Breast Cancer Res,* vol. 10, no. 3, p. R41, 2008.

[25] H. Weedon-Fekjaer, O. O. Aalen and S. Tretli, "Estimating screening test sensitivity and tumour progression using tumour size and time since previous screening.," *Statistical Methods in Medical Research,* vol. 00, pp. 1-21, 2010.

[26] "Full Field digital mamography unit Villa Sistemi Medicali - MedicalExpo," Medical Expo, [Online]. Available: http://www.medicalexpo.com/prod/villa-sistemi-medicali/product-70463-534527.html. [Accessed 25 08 2017].

[27] "Performing the examination," Aibolita, [Online]. Available: http://aibolita.com/womens-diseases/39943-performing-the-examination.html. [Accessed 25 08 2017].

[28] "Acies Mammo Viewer License," Konica Minolta, [Online]. Available: https://www.konicaminolta.com/healthcare/products/mammo/acies_mammo_viewer_license/feature.html. [Accessed 25 08 2017].

CHAPTER 2: SEGMENTATION METHODS IN MAMMOGRAPHIC MASSES

2.1 Introduction

A mammogram contains a large amount of image information (grey level values) which can be described as a complex combination of several different structures such as patterns, lines, edges and shapes. This visual information provides the relevant data for clinical interpretation and decision making in mammography [1]. Segmentation occurs naturally in the human visual system and this is certainly also the case during mammographic interpretation. Usually the radiologist will ignore some regions on the mammogram, but will place more emphasis on areas or regions deemed suspicious for further analysis [2]. Therefore, digital mammographic segmentation can be described as the problem of partitioning a mammogram in a semantically meaningful way, predominantly into the suspicious region of interest (object of interest) and the background (surrounding tissues). The delineated region of interest can be used for object recognition and classification [3]. The contour delineating the object of interest, such as a mammographic mass, represents its shape and this can provide relevant information as to the nature of its origin (that is malignant, infective, benign etc.) [1]. Useful information such as texture features can be derived from the delineated mass region for further assessment. Regions of interest (ROIs) indicating the mass-regions can be drawn manually, or with an algorithm supervised by the radiologist, or automatically. When contours (outlines of the masses) are drawn with a supervised algorithm or automatically, it is a good practice to quantify the precision of the algorithm, so that they provide regions of interest which closely match those of the radiologist, since an ill-defined region of interest (ROI) can cause ambiguity, or wrongful classification, and thus wrongful diagnosis of the mass. Segmentation accuracy can be expressed using a range of statistical measures such as: the Jaccard similarity, over-segmentation or under-segmentation measures [4]. Mammograms can also be pre-processed to enhance texture and structural features before the application of segmentation algorithms. These pre-processing techniques can be implemented either in the frequency or spatial domain and they include global histogram modification [5], local processing [6] and multi scale processing techniques [7].

2.2 Segmentation methods for mammographic masses

2.2.1 Threshold algorithms

In mammograms, some abnormalities have grey level intensities different from those of the surrounding tissues. Thresholding then becomes a simple and efficient technique to separate these abnormalities from surrounding tissues. Generally, it involves the determination of an optimal grey level threshold value according to some objective criteria and then assigns each pixel to the foreground or the background if its grey level value is more than or less than the prescribed threshold value respectively [8]. Global thresholding methods are based on global information of the mammogram whilst local thresholding makes use of regional information [9]. These algorithms exploit histogram shape-based information, entropy-based information, local characteristics and spatial information, while utilizing a predefined threshold value. However, mammograms with masses present a very challenging problem because an optimal threshold value is not always feasible for a specific mammogram. This is because the edge strength between the foreground (mass region) and the background (non-mass region) is not a constant value around the ROI. This is due to the unavoidable overlap between the mass and surrounding structures, such as the breast parenchyma tissue, which is inevitably present in projection mammography. This algorithm can serve as a pre-processing step for other algorithms.

2.2.2 Iterative pixel classification

Criteria for pixels in an image to be classified into different groups are determined by probability distribution functions such as:

- Markov random field and its similarity with its neighbours based on prior information [10]
- Region growing, with or without prior information [11]
- Region clustering

- Dynamic programming based on the minimization of a cost function can also be included in this category [4].

These algorithms are all limited because they require that grey level intensities in the ROIs are roughly homogenous, which not the case in mammography is imaging. Intensity inhomogeneity is not only introduced by the anatomical structure of the breast, but it is also inherent to the imaging process (heel effect). Therefore, in most cases the grown region or the final cluster will depend on the initial seed position and the process of combining pixels with similar characteristics may converge to a local minimum within the ROI**.**

2.2.3 Template matching

A template is generated with prior information from a given data set of mammograms. These may be useful in identifying objects such as micro-calcifications. Templates separate the objects of interest from the background and usually they represent prototypes of the objects of interest generated from global or local features of the images which may or may not be part of the data set to be classified. The similarity between the template and the search image, or sub-region in an image, can be measured by least square techniques, distance measures, mutual information etc [12] [13]. Mammographic masses have a variety of densities, sizes and shapes, therefore designing a deformable template model to extract each mass can be computationally expensive. In most cases, masses are grouped into different sizes and a template constructed for each range of sizes, as a result sub-pixel accuracy of mass boundaries, is rarely attained.

2.2.4 Fuzzy technique

Fuzzy set theory is the foundation of fuzzy techniques in image processing. It employs a fuzzy membership function which indicates the degree of certainty to which a feature vector belongs to a set. Unlike a crisp set, whereby a feature vector can or cannot be allocated as a member of a set, the membership function allows every feature to belong to a defined set with a certain degree of uncertainty. In segmentation algorithms, this technique incorporates other methods like thresholding and region growing or clustering [14]. Generally, a fuzzy membership function assigns a fuzzy membership to each pixel in the image, then an iterative process

begins, and the parameters of the fuzzy membership function are fine-tuned to achieve the desired level of performance which is characterized by a set of criteria (Fuzzy rules) [15]. Finally, pixels with the same membership value are grouped together. The main disadvantage of this method is the requirement of prior expert information to set up the membership function parameters and the fuzzy rules.

2.2.5 Edge detection algorithms

These algorithms detect the outlines of objects such as micro calcifications and masses in a mammogram. Boundaries are discontinuities in a ROI which can be assessed by gradient-based methods. These methods employ gradient-based algorithms in conjunction with other methods to refine the edge detection process. In some cases, an edge map is constructed where the value for each pixel is equivalent to the magnitude of the gradient image at that point and pixels along strong edges are selected and linked to each other thus defining the boundary of the object of interest. Edge based algorithms include density-weighted contrast enhancement [16], active contours [17] and filters [18] such as Gaussian and Laplacian of Gaussians. Sometimes strong edges may be detected within the ROI due to the non-homogeneity of the grey values within the ROI and at some places along the boundary, a gentle, or even no transition, of grey levels between the ROI and the surrounding tissue may occur. Hence obtaining a threshold value for the edge strength which can be defined as the magnitude of the local changes in intensity of the ROI may not be as easy as it seems.

2.2.6 Active contour segmentation model

An active contour segmentation model [19] [20] is commonly applied in digital images because it provides sub-pixel accuracy in boundary detection. This model can be designed within the framework of minimizing an energy functional, thus allowing prior knowledge such as shape or intensity distribution to be incorporated into the function for a robust segmentation model. An active contour is a deformable spline consisting of a set of *control points* connected by straight lines. Each control point has a position in the image domain given by the x and y coordinates. Each point along the curve is under the influence of both internal and external forces, and the snake continuously tries to position itself so that the combined energy of these forces is minimized. The entire spline moves as adjustments are made by moving the control

points. Generally, the deformable spline is a closed loop, guided by external constraint forces and influenced by image forces towards the boundary of an object. The essential property of an active contour is its energy functional which causes it to evolve to reduce its energy as it approaches the boundary of the region of interest. Active contours can be classified broadly as parametric models [21] [22] and geometric models [23]. In the geometric models, the initial contour is embedded in an implicit level set function of a two-dimensional distance function during curve evolution while in parametric models the curves are explicitly represented as parametrized curves during evolution.

2.3 Parametric active contours (snakes)

Each point on the initial contour is parametrized such that a given point(x, y) on the contour is expressed as

$$\vartheta(s) = [x(s), y(s)] \tag{2.1}$$

where, s, is a local parameter. Then a contour(C), parametrized by the arc length(s), is written as:

$$C(s) = \left[\left(x(s), y(s)\right): 0 \leq s \leq L\right], R \rightarrow \Omega \tag{2.2}$$

where: L is the arc length of the contour, R represents a set of real numbers and Ω is the image domain.

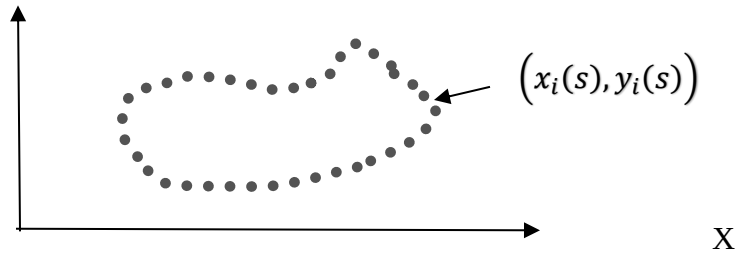

Figure 2.1. Parametric curve in the (x, y) plane

Kass et al [24] proposed an energy minimization scheme for the movement of a parametric curve, with total energy $\left(E(c)\right)$ expressed as:

$$E(c) = E_{internal} + E_{external} \tag{2.3}$$

where the internal energy $(E_{internal})$ of the curve aims to smooth the edge of the deforming curve and is expressed as:

$$E_{internal} = \int_0^L \alpha|C'(s)|^2 + \beta|C''(s)|^2 \tag{2.4}$$

and the external energy $(E_{external})$ attracts the deforming curve to the boundaries of the object.

$$E_{external} = \int_0^L E_{img}\left(C(s)\right)ds \tag{2.5}$$

The image forces $\left(E_{img}\right)$ is commonly expressed as an edge indication function which is a function of the image gradient$(-\|\nabla I(x,y)\|^2)$.

This deformable curve model cannot deal with changes in topology during deformation, that is, it cannot split to multiple boundaries or merge from multiple initial contours, hence it cannot detect all the objects in an image and secondly it is sensitivity to initialization conditions.

2.4 The geometric active contour models

Geometric active contours [25] combine the theory of curve evolution and the level sets method to determine the boundaries of objects within digital images such that the evolution of the contour is independent of curve parameterization and thus easily adapts to changes in the topology of the image domain. In the general formulation, it is set as the variation of an energy functional which is expressed as a partial differential equation in the Eulerian framework and takes a minimum value as the contour approaches the boundary of the object. Geometric active contours can be classified into two categories, namely edge–based active contour segmentation models and region-based active contour models. The foundations of both models are built on

the theory of level set function which can be modelled as a moving boundary or interface. Some of the terminologies in level set functions will be explained as the concept is gradually introduced into curve evolution.

2.4.1 Some definitions in modelling the level set function as a moving interface

Boundary interface

A two-dimensional interface boundary, $C(\mathrm{t})$, can be defined as a closed curve in the image domain, (Ω), that partitions of the image domain into the foreground, (Ω_1), and the background, (Ω_2), such that $\Omega = \Omega_1 + \Omega_2$ as shown below:

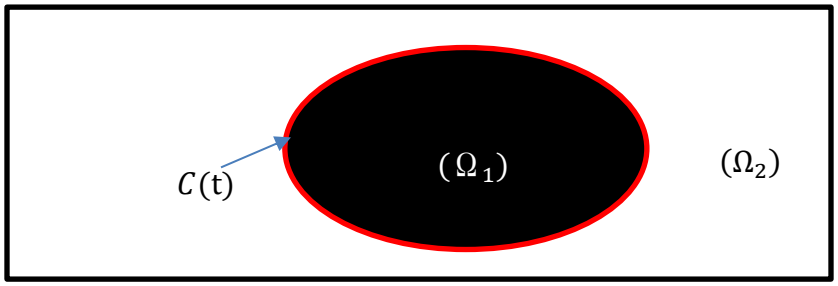

Figure 2.2. Shows the partition of an image domain with an interface boundary into the foreground and background.

Level set of a function

A level set of a function, $\varphi(x, y)$, is the curve connecting the set of points, (x, y), where $\varphi(x, y)$ is some constant value, c. It can be visualized as the cross section of the graph of $\varphi(x, y) = c$, where c is a constant value. For example, suppose $\varphi(x, y) = -x^2 - y^2$. The level sets of the function $\varphi(x, y)$ are defined by:

$$\{(x, y) : -x^2 - y^2 = c\} \qquad (2.6)$$

Assuming that c = -300, then the graph below illustrates the relationship between the level set curve $\varphi(x, y) = c$ and the function $\varphi(x, y)$. Hence $\varphi(x, y)$ is a two-dimensional function that can be embedded in a three-dimensional space (x, y and z)

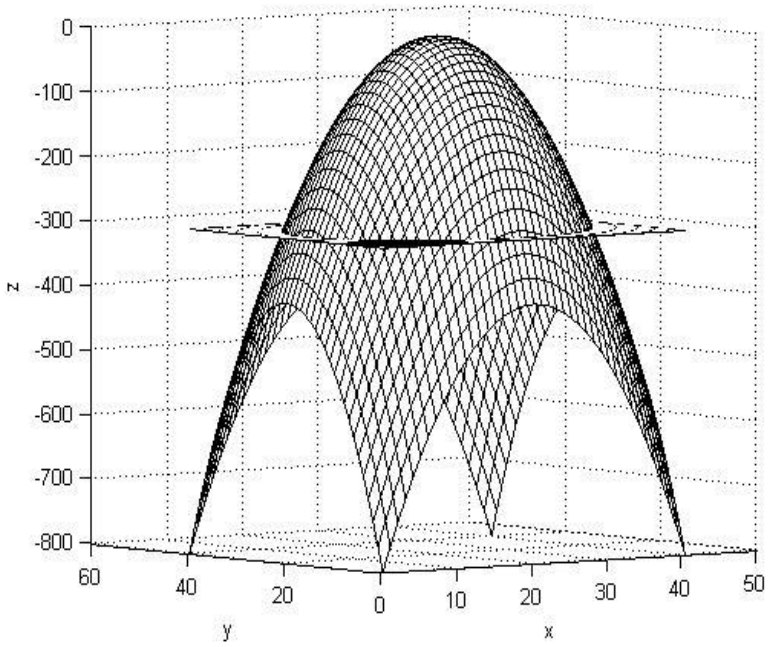

Figure 2.3. Illustration of the function $\varphi(x, y) = -x^2 - y^2$ and the level set curve $\varphi(x, y)$ = -300, which a slice of the graph $z = \varphi(x, y)$ through the plane z = c =-300.

Zero Level set of an implicit function.

Suppose the function, $\varphi(x, y)$, is an implicit function, expressed as $\varphi(x, y) = -x^2 - y^2 - c$. The values of $\varphi(x, y)$ can be represented as points in the Z axis in a three-dimensional Cartesian coordinate system. Suppose c= -300, then $\varphi(x, y) = -x^2 - y^2 + 300$, then the zero level set of the function is given by $300 = x^2 + y^2$, which is a circle of radius $\sqrt{300}$. The plot of the function is shown in Figure 2.3. Data points (x, y) within the radius have positive signs while points outside of the radius have negative signs. Hence to test if a data point is inside or outside the circle is simply a sign test. Generally, the zero level set of the function, $\varphi(x, y)$, is defined by:

$$\{(x, y) : \varphi(x, y) = 0\} \tag{2.7}$$

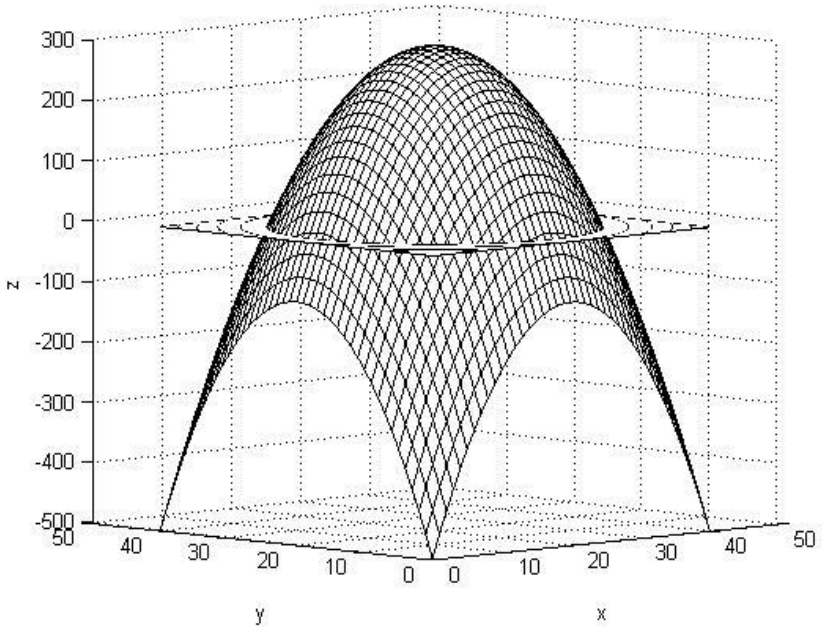

Figure 2.4. The zero level set of the function $\varphi(x, y) = -x^2 - y^2 + 300$ is denoted as the circle. $x^2 + y^2 = 300$ at the plane Z=0;

2.5 Level set functions and curve evolution in segmentation

Osher-Sethain [26] [27] proposed a level set method as an efficient and stable algorithm in curve evolution to overcome the limitations of the parametric model of curve evolution. They transformed the evolution of a curve (usually set in two dimensions: x, y) into the evolution of a three-dimensional level set function. In this method, the equation governing the propagation of the curve is expressed as a function that describes the speed of the curve flow in the direction normal to the curve. It uses a function, $\varphi(x, y, t)$, whose isocontour, $\varphi(x, y, t) = 0$, represents an interface (boundary enclosing the region of interest) $C(t)$, and t is an artificial time to track the motion of the interface as it evolves. The interface $C(\mathrm{t})$ (two-dimensional surface) is embedded in a three-dimensional space which defines the level set function. The level set function, $\varphi(x, y, t) = 0$, is numerically kept close to the signed distance function, where every point in the image domain is expressed as its closest distance to the boundary, $C(\mathrm{t})$, and the sign of each point determines whether the point is inside or outside the boundary (Figure 2.5). The signed distance function provides data for the geometric features such as the curvature or the normal to the contour during curve evolution.

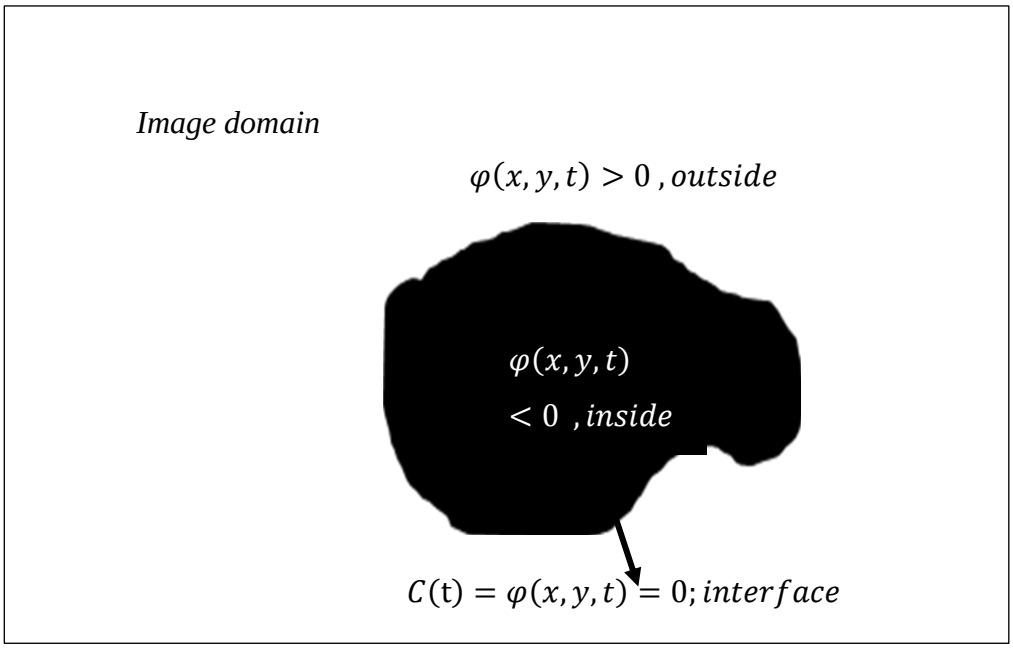

Figure 2.5. Partition of the image domain by the signed distance function.

Consider a signed distance function $\varphi(x, y, t = 0) = \pm\epsilon$, where ϵ is a narrow band of pixels around $C(\mathrm{t})$ such that the values of $\varphi(x, y, t)$ for points (x ,y) with distance, ϵ, outside the contour, $C(\mathrm{t})$, are positive and the values of $\varphi(x, y, t)$ for points, (x ,y), with distance, ϵ, inside the contour, $C(\mathrm{t})$, are negative. Then any boundary, $C(\mathrm{t})$, can be represented by an arbitrary function, $\varphi(x, y, t)$, as long as the zero level set matches $C(\mathrm{t})$.

2.5.1 Derivation of the mathematical formula for moving-front curve evolution of the zero level set function

Let each data point of a moving interface (boundary$\big(C(t)\big)$) at time $= t$, be represented as, $\mathrm{X}(t) = \big(x(t), y(t)\big)$. The evolution of the zero-level set ($\varphi(\mathrm{X}(t), t) = 0$) of the implicit function, $\varphi(\mathrm{X}(t), t)$, can be described as:

$$\frac{\partial \varphi(\mathrm{X}(t), t)}{\partial t} = 0 \tag{2.8}$$

$$\frac{\partial \varphi}{\partial \mathrm{X}(t)} * \frac{\partial \mathrm{X}(t)}{\partial t} + \frac{\partial \varphi}{\partial t} = 0 \tag{2.9}$$

$$\frac{\partial \varphi}{\partial \mathrm{X}(t)} * \mathrm{X}_t + \varphi_t = 0 \tag{2.10}$$

$$\bar{v}.\nabla\varphi + \varphi_t = 0 \tag{2.11}$$

Let the velocity of the moving interface, $\bar{v} = v_n\bar{N} + v_T\bar{T}$, with v_n and v_T as the normal and the tangential components of the velocity respectively. Suppose $\bar{N}$ and $\bar{T}$ are the unit normal vector and unit tangent vector respectively, then the above equation can be written as:

$$\nabla\varphi \,.\, (v_n\bar{N} + \, v_T\,\bar{T}\,) + \, \varphi_t = 0 \tag{2.12}$$

The unit normal vector is in the same direction as $\nabla\varphi$, but it is perpendicular to $\bar{T}$, hence $\nabla\varphi.T = 0$, therefore the above equation becomes:

$$\nabla\varphi \,.\, (v_n\bar{N}) + \, \varphi_t = 0 \tag{2.13}$$

$$\nabla\varphi \,.\, (\bar{N}) = \, \frac{\nabla\varphi}{|\nabla\varphi|} \,.\nabla\varphi = \, |\nabla\varphi| \tag{2.14}$$

The evolution of the level set function is

$$v_n.\,|\nabla\varphi| + \, \frac{\partial\varphi}{\partial t} = 0 \tag{2.15}$$

$$v_n = \, v.\frac{\nabla\varphi}{|\nabla\varphi|} \tag{2.16}$$

Where $\frac{\partial\varphi}{\partial t} = \frac{\partial\varphi}{\partial x} \,.\frac{\partial x}{\partial t} = v.\ \nabla\varphi\ and\ |\nabla\varphi| = \, \sqrt{\sum_{i=1}^{n} \varphi_{x,y,i}^2}$

The curve represented by the function, $\varphi(x, y, t)$, evolves, with its level set function expressed as $\varphi(x, y, t) = 0$. The level set function is the hypersurface, $C(t)$, and it can split, merge and change topology unlike the parametric active contours discussed in section 2.3. The above equation (equation 2.16) can easily be solved on a discrete grid in the x,y domain and the derivatives of $\varphi(x, y, t)$ approximated with the finite difference method. v_n is also called the speed function (F). Generally, the partial differential equation for the image segmentation process is expressed as:

$$\frac{\delta\varphi}{\delta t} = F|\nabla\varphi| \tag{2.17}$$

where (F) is expressed as a function of image data, that is the local curvature (κ), at the zero-level set which controls the evolution of the zero level set contour of $\varphi(x, y, t)$ while the

implicit function, $\varphi(x, y)$ is the signed distance function. If $F > 0$ then the level set contour will expand outwards normal to the boundary and vice versa, however as $\rightarrow 0$, the contour approaches a steady state and finally becomes stationary, thus depicting the boundary of the region of interest.

2.5.2 Classical edge–based active contour segmentation model

The basic equation of the classical edge based active contour model [28] [29] [30], uses local edge information to attract the active contour towards the boundary of the object during curve evolution. The speed term, which regulates the convergence of the contour to the boundary of the object, is modelled on the mean curvature of data points on the level set curve of φ. The speed function is generally expressed as:

$$F = g(|\nabla I|)\left(div\left(\frac{\nabla\varphi}{|\nabla\varphi|}\right) + \alpha\right), \text{ in } (0, \infty)\ x\ \Re^2 \tag{2.18}$$

The function, $g(|\nabla I|)$ is an edge detector function which forces the evolving curve to attain a zero speed as it gets closer to the boundaries of the object and α is a balloon force which then increases the speed of convergence and I is the image.

This algorithm will have some difficulties in segmenting objects with weak or ill-defined boundaries because the edge detector function is the stopping term to detect the desired boundary and this situation is common with medical image segmentation in which regions of interest are obscured in surrounding tissues, creating objects with blurry boundaries.

2.5.3 Classical region–based active contour segmentation model

Region-based variational level set method [31] [32] does not use an edge detector function to propagate the curve towards the desired boundary. Rather, its energy functional propagates the curve with statistical information from regions inside and outside the evolving curve. For a bimodal image, this model seeks to partition the image domain, (Ω), into 2 non-overlapping regions (Ω_1, Ω_2) with an evolving curve, C, as shown in Figure 2.5, by minimizing the following energy functional:

$$E = \sum_{i}^{2} E(\Omega_i) \; + \; \lambda E_r(C) \tag{2.19}$$

where $E(\Omega_i)$ is the statistical information in region, Ω_i, and, $E_r(C)$, is a regularizing term and, λ, a tuning parameter. The regional statistical competition between Ω_1 and Ω_2 has been modelled with known distributions, intensity histograms, texture maps or structure tensors by different authors, but the Chan-Vese algorithm [33] is the most popular model.

2.6 Chan-Vese region-based segmentation model

The energy functional for minimization is defined as a competition of the first moments of the local intensity distribution of the foreground (Ω_1) and the background(Ω_2). Suppose C is an evolving curve that partitions the image domain into the foreground, Ω_1 , and the background, Ω_2. The Chan-Vese model [33] seeks an optimal contour, representing the boundary of an object, by minimizing the following energy functional:

$$F(C, c_1, c_2) = \mu.length(C) + \upsilon.Area\big(inside(C)\big) + F_{data} \tag{2.20}$$

μ and υ are positive constants while F_{data} represents the regional term guiding the contour in the image domain and is given by:

$$F_{data} = \; \lambda_1 F_1(C) + \lambda_2 F_2(C) \tag{2.21}$$

in which,

$$F_1(C) = \int_{inside(C)} |I(x,y) - \; c_1|^2 \; dxdy \tag{2.22}$$

$$F_2(C) = \int_{outside(C)} |I(x,y) - \; c_2|^2 \; dxdy$$

λ_1 and λ_2 are positive constants while the average image intensities of regions inside and outside the contour are c_1 and c_2 respectively. Hence the Chan-Vese segmentation method is summarised as:

$$\begin{aligned}\arg\min_{c_1,c_2 C} &= \mu.\, length(C) + v.\, Area\big(inside(C)\big) \\ &+ \lambda_1 \int_{inside(C)} |I(x,y) - c_1|^2 \, dxdy \\ &+ \lambda_2 \int_{outside(C)} |I(x,y) - c_2|^2 \, dxdy\end{aligned} \tag{2.23}$$

2.6.1 Level set method to solve the Chan-Vese active contour models

Suppose the function, $\varphi(x,y,t)$, has an iso-contour, $(x,y,t) = 0$, which represents an interface (boundary) C and t is an artificial time to track the motion of the interface as it evolves. Then the relationship between the function $\varphi(x,y,t)$ and the boundary of the region of interest C can be written as

$$C = \{(x,y) \in \Omega : \varphi(x,y) = 0\} \tag{2.24}$$

In other words, the zero crossing of the function $\varphi(x,y,t)$ is the curve representing the boundary of the ROI (curve C) and $\varphi(x,y,t)$ is commonly known as a level set function for Ω and generally expressed as the sign distance function ($ie\ |\varphi| = 1$). If H_ε is a regularized Heaviside function, then the interior of C ($inside(C)$) can be approximated as:

$$H_\varepsilon\big(\varphi(x,y)\big) = \begin{cases} 1, & \varphi(x,y) < -\epsilon \\ 0, & \varphi(x,y) < -\epsilon \\ \frac{1}{2}\left(1 + \frac{2}{\pi}\arctan\left(\frac{t}{\epsilon}\right)\right), & otherwise \end{cases} \tag{2.25}$$

and the exterior of C ($outside\ (C)$) is given as $\Big(1 - H_\varepsilon\big(\varphi(x,y)\big)\Big)$. Then the Chan-Vese energy functional is:

$$F(C, c_1, c_2) = \mu \int_{\Omega} |\nabla H_{\varepsilon}(\phi)|\, dxdy + \lambda_1 \int_{\Omega} (I(x,y) - c_1)^2\, H_{\varepsilon}(\phi)\, dxdy + \lambda_2 \int_{\Omega} (I(x,y) - c_2)^2\, (1 - H_{\varepsilon}(\phi))\, dxdy \quad (2.26)$$

and the minimization equation expressed as:

$$\arg\min_{c_1, c_2 C} = \mu \int_{\Omega} |\nabla H_{\varepsilon}(\varphi)|\, dxdy + \upsilon \int_{\Omega} H_{\epsilon}\big(\varphi(x,y)\big)\, dxdy + \lambda_1 \int_{\Omega} (I(x,y) - c_1)^2\, H_{\varepsilon}(\varphi)\, dxdy + \lambda_2 \int_{\Omega} (I(x,y) - c_2)^2\, (1 - H_{\varepsilon}(\varphi))\, dxdy \quad (2.27)$$

and

$$|\nabla H_{\varepsilon}(\varphi)| = \delta_{\epsilon}(\varphi) |\nabla \varphi| \quad (2.28)$$

with the derivative of $H_{\varepsilon}(t)$ given as

$$\frac{d}{dt} H_{\epsilon}(t) := \delta_{\epsilon}(t) = \frac{\epsilon}{(\epsilon^2 + t^2)} \quad (2.29)$$

Minimizing $F(C, c_1, c_2)$ with respect to ϕ yields the follow gradient descent flow:

$$\frac{\partial \varphi}{\partial t} = \delta_{\varepsilon}(\varphi)\left[\mu\nabla\left(\frac{\nabla\varphi}{|\nabla\varphi|}\right) - \upsilon - \lambda_1(I(x,y) - c_1)^2 + \lambda_2(I(x,y) - c_2)^2\right] \quad (2.30)$$

where the averaging of the grey values, c_1 and c_2, are assessed as

$$c_1 = \frac{\int_{\Omega} I(x,y)H_{\epsilon}(\varphi(x,y))dxdy}{\int_{\Omega} H_{\epsilon}(\varphi(x,y))dxdy} \quad (2.31)$$

$$c_2 = \frac{\int_{\Omega} I(x,y)\left(1 - H_{\epsilon}(\varphi(x,y))\right)dxdy}{\int_{\Omega}\left(1 - H_{\epsilon}(\varphi(x,y))\right)dxdy} \quad (2.32)$$

and $\delta_{\varepsilon}(\varphi)$ is the Dirac function. The level set function is periodically re-initialized to a signed distance function during evolution so that geometric features such as the curvature or the normal to the contour are estimated accurately for curve stability.

2.6.2 Narrow band concept of curve evolution in the level set method

In the level set method computation is restricted to a narrow band of pixels surrounding the (interface) zero level set contour between the bounded regions ϵ and $-\epsilon$ to reduce the computational time. Numerical implementation is carried out on a discrete grid (Figure2.6).

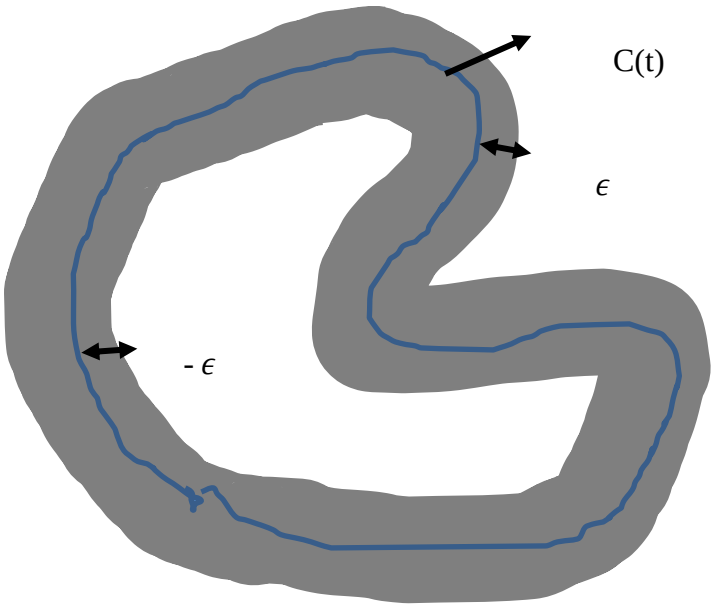

Figure 2.6. Illustration of the narrow band concept in curve evolution

2.7 Active contours with selective local or global segmentation model [34]

The signed pressure force function [35] is derived from the means of regions inside and outside the contour to control the direction in which the curve evolves, the contour shrinks when it is outside the object and expands when it is inside an object. It has values in the range $[-1,1]$ and is defined as:

$$spf\big(I(x,y)\big) = \frac{I(x,y) - \frac{c_1 + c_2}{2}}{\max\left(\left|I(x,y) - \frac{c_1 + c_2}{2}\right|\right)}, \quad x, y \in \Omega_p \tag{2.33}$$

where c_1 and c_2 are defined in Eq. 2.31 and Eq. 2.32 respectively. The active contour with selective local or global segmentation model utilizes the geodesic active contour to formulate the level set equation as:

$$\frac{\partial \phi}{\partial t} = spf\big(I(x,y)\big).\left(div\left(\frac{\nabla \phi}{|\nabla \phi|}\right) + \alpha\right)|\nabla \phi| + \nabla spf(I(x,y)).\nabla \phi, \qquad x, y \in \Omega_p \tag{2.34}$$

Using the Gaussian filtering process to regularize the level set function, the above equation can be written as follows:

$$\frac{\partial \phi}{\partial t} = spf\big(I(x,y)\big).\alpha|\nabla \phi| \quad x, y \in \Omega_p \tag{2.35}$$

where α is a tuneable parameter.

Generally, the level set contour is periodically, regularize with a Gaussian function G_σ. The Gaussian filtering process smooths the level set function and regularises the moving interface so that it more stable and does not shift into undesirable positions.

2.8 Problems encountered during segmentation of mammographic masses with active contour segmentation methods`

Most mammographic masses are presented with intensity inhomogeneity, therefore for a given mass of interest and there are regions within and at the margins of the mass, with low grey scale values (local minima). Regions of low grey scale values within a mass can entrap a moving curve while weak and ill-defined boundaries can cause contour leakage and thus provide variations in shape-based descriptors which are vital for classification of regions of

interest in medical images especially in mammograms. where the shape of a breast mass is indicative of its clinical pathology. These changes in shape-based descriptors have not been investigated nor quantified in segmentation of mammographic masses. Hence the next chapter deals with the investigation and quantification of changes in shape-based descriptors due to changes in the location of the initial level set contour in region based active contour models in segmentation of digital mammographic masses.

2.9 References

[1] American College of Radiology, Breast Imaging Reporting and Data System (BI-RADS), 2nd ed., Reston, VA: American College of Radiology, 2003.

[2] J. N. Wolfe, "Risk for breast cancer development determined by mammographic parenchymal pattern," *Cancer,* vol. 37, no 5, pp. 2486-2492, 1976.

[3] I. T. Gram, E. Funkhouser and L. Tabar, "The Tabar Classification of mammographic parenchymal patterns," *Eur. J. Radiol.,* vol. 24, pp. 131-136, 1997.

[4] A. Rojas and A. K. Nand, "Improved DP-based algorithms for segmentation of breast masses,," *Medical Physics,* vol. 34, pp. 4256-4269, 2007.

[5] S. H. Nam and J. Y. Choi, " A method of image enhancement and fractal dimension for detection of microcalcifications in mammogram, "In *Engineering in Medicine and Biology Society* , 1998. *Proceedings of the 20th Annual International Conference of the IEEE* (Vol. 2, pp. 1009-1012). IEEE.

[6] J. K. Kim , J. M. Park, K. S. Song and H. W. Park, "Adaptive mammographic image enchancement using frist derivative and local statistics," *IEEE Trans. Med. Imaging,* vol. 16, no. 5, pp. 495-502, 1997.

[7] A. Laine, J. Fan and W. Wang, "Wavelet for contrast enchancement of digital mammography," *IEEE Eng. Med. Biol.,* vol. 5, no. 14, pp. 536-550, 1995.

[8] S. Segzin and B. Sankur, "Survey over image thresholding techniques and quantitative performance evaluation," *Journl of Electronic Imaging,* vol. 13, no. 1, pp. 146-165, 2004.

[9] M. Kallergi, K. Woods, L. P. Clarke, W. Qian and R. A. Clark, "Image Segmentation in digital mammography: comparison of local thresholding and region growing algorithms," *Computerized medical imaging and grapics,* vol. 16, no. 5, pp. 323-331, 1992.

[10] M. Suliga , R. Deklerck and E. Njssen, "Markov random field-based clustering applied to the segmentation of masses in digital mammograms.," *Computerized Medical Imaging and Graphics,* vol. 32, no. 6, pp. 502-512., 2008.

[11] A. Mencattini, M. Salmeri, G. Rabottino, R. Lojacono and E. Colini, "Breast mass segmentation in mammographic images by an effective region growing algorithm," *International Conference on Advanced Concepts for Intelligent Vision Systems,* pp. 948-957, 2008.

[12] M. A. Mazurowski, J. Y. Lo, B. P. Harrawood and G. D. Tourassi,, "Mutual information-based template matching scheme for detection of breast masses: From mammography to digital breast tomosynthesis," *Journal of biomedical informatics,,* vol. 44, no. 5, pp. 815-823, 2011.

[13] F. Shirazi and E. Rashedi, "Detection of cancer tumors in mammography images using support vector machine and mixed gravitational search algorithm," *2016 1st Conference on Swarm Intelligence and Evolutionary Computation (CSIEC). IEEE,* pp. 98-101, 2015.

[14] F. R. Cordeiro, W. P. Santos and A. G. Silva-Filho, "A semi-supervised fuzzy GrowCut algorithm to segment and classify regions of interest of mammographic images," *Expert Systems with Applications,* vol. 65, pp. 116-126, 2016.

[15] H. Mahersia, H. Boulehmi and K. Hamrouni, "Development of intelligent systems based on Bayesian regularization network and neuro-fuzzy models for mass detection in mammograms: A comparative analysis," *Computer methods and programs in biomedicine,* vol. 126, pp. 46-62, 2016.

[16] Y. Li, H. Chen, L. Cao and J. Ma, "A Survey of Computer-aided Detection of Breast Cancer with Mammography," *Journal of Health & Medical Informatics,* 2016.

[17] W. Xie, Y. Li, and Y. Ma, " PCNN-based level set method of automatic mammographic image segmentation, " *Optik-International Journal for Light and Electron Optics, ,* vol. 127, no. 4, pp. 1644-1650., 2016.

[18] A. Verma and G. Khanna, "A survey on image processing techniques for tumor detection in mammograms," *Computing for Sustainable Global Development (INDIACom), 2016 3rd International Conference on. IEEE,* pp. 988-993, 2016.

[19] B. Chen and J. H. Lai, "Active contour models on image segmentation: a survey," *Journal of Image and Graphics ,* vol. 1, p. 002, 2007.

[20] T. McInerney and D. Terzopoulos, "Deformable models in medical image analysis: a survey," *Medical image analysis,* vol. 1, no. 2, pp. 91-108, 1995.

[21] H Delingette and J Montagnat, "Shape and topology constraints on parametric active contours.," *Computer Vision and Image Understanding ,* vol. 83, no. 2, pp. 140-171, 2001.

[22] Z. Hou and C. Han, "Force field analysis snake: an improved parametric active contour model.," *Pattern recognition letters,* vol. 26, no. 5, pp. 513-526, 2005.

[23] V. Caselles, F. Catté, T. Coll and F. Dibos, "A geometric model for active contours in image processing," *Numerische mathematik ,* vol. 66, no. 1, pp. 1-33, 1993.

[24] M. Kass, A. Witkin and D. Terzopoulos, "Snakes: Active contour models," *International journal of computer vision,* vol. 1, no. 4, pp. 321-331., 1988.

[25] S. Osher, and N. Paragios. eds " *Geometric level set methods in imaging, vision, and graphics*, Springer Science & Business Media, 2003.

[26] S. Osher and J. A. Sethian, " Fronts propagating with curvature-dependent speed: algorithms based on Hamilton-Jacobi formulations.," *Journal of computational physics,* vol. 79, no. 1, 1988.

[27] J. A. Sethian, "Level set methods and fast marching methods: evolving interfaces in computational geometry, fluid mechanics, computer vision, and materials science", vol. 3, Cambridge university press, 1999.

[28] N. Paragios and R. Deriche, "Geodesic active regions and level set methods for motion estimation and tracking," *Computer Vision and Image Understanding*, vol. 97, no. 3, p. 259–283, 2005.

[29] S. Shah and A. Ross, "Iris segmentation using geodesic active contours," *IEEE Transactions on Information Forensics and Security*, vol. 4, no. 4, p. 824–836, 2009.

[30] C. Li, C. Xu, C. Gui and M. D. Fox, "Level set evolution without reinitialization: a new variational formulation,"," in *Computer Vision and Pattern Recognition*, 2005. June

[31] R. Ronfard, "Region-based strategies for active contour models," *International Journal of Computer Vision,*, vol. 13, no. 2, p. 229–251, 1994.

[32] N. Paragios and R. Deriche, "Geodesic active regions and level set methods for supervised texture segmentation," *International Journal of Computer Vision,* vol. 46, no. 3, p. 223–247, 2002.

[33] T. F. Chan and L. A. Vese, "Active contours without edges,," *IEEE Transactions on Image Processing,* vol. 10, no. 2, p. 266–277, 2001.

[34] K. Zhang , L. Zhang , H. Song and W. Zhou , "Active contours with selective local or global segmentation: a new formulation and level set method," *Image and Vision Computing* , vol. 28, no. 4, p. 668–676, 2010.

[35] C. Y. Xu, A. Yezzi and J. L. Prince, "On the relationship between parametric and geometric active contours," in *Processing of 34th Asilomar Conference on Signals Systems and Computers,*, 2002.

CHAPTER 3. VARIATIONS IN SHAPE BASED DESCRIPTORS AND MASS SEGMENTATION AREAS DUE TO INITIAL LEVEL SET CONTOUR PLACEMENT

An extract from the work published by the author – Appendix I (S. N. Acho and W. I. D. Rae)

3.1 Introduction

The image acquisition system in direct digital mammography consists of a flat panel detector with a wide dynamic range which is separated from the image processing and display system [1]. Usually raw image data can be processed with a varietry of image processing algorithms for soft copy display on high-resolution monitors and in most cases the source codes of these algorithms are not available to the operator. Operators are also allowed to adjust image contrast and magnification. The wide dynamic range of the flat panel detector system records small differences between the attenuation coefficients of structures or regions present in any present mass lesion and these are clearly displayed over a wide range of densities, whereas in film screen mammography, the exposure latitude of the film limits the dynamic range of information captured on the film. Hence masses which may have appeared as dense structures without significant topographical relief features on film- screen mammograms will emerge as regions with varying densities on soft copy display. Enhancement of these variations by the processing algorithms of the manufacturers cannot be ruled out. Differences in density may sometimes appear as low signal areas which can act as local minima for contour entrapment each time an evolving curve determines its path within the lesion and in most cases, these areas also render deformable contours susceptible to inital contour placement in mass segmentation. The margins of some of these masses are often occluded or hidden in the lobular and duct structures of the breast parenchyma tissue and these present pathways for contour leakage as an evolving contour approaches the boundary of the mass and thus produces an unsuitable segmentation outcome or an outcome which depends on the location of the initial level set contour.

3.2 Aim

We investigate changes in one dimensional shape-based descriptors and the segmented areas of masses in direct digital mammograms due to changes in the location of the initial level set contours with the implementation of two region-based active contour models: Chan-Vese and active contours with selective local or global segmentation models.

3.3 Methods

3.3.1 Digital mass database

A mammogram database designed to store the images of the masses, patient history, category of mass and the biopsy report if performed, was utilized in this study. The design of the database is described elsewhere [2] and furthermore, Meyer et al [3] assessed the diagnostic accuracy of mammograms (that is, the accuracy in breast cancer detection on these mammograms by the radiologists)in this database with different soft-copy display algorithms. The database has ninety mammograms of which forty of these mammograms have masses with low signal areas within the mass and margins described as obscured, or ill-defined, while the others have masses with well-defined or distinct margins. In this study, the region of interest containing the mass lesion was cropped and then resized to a 208 x 208 matrix to create a sub-image of the mammogram.

3.3.2 Locations of the initial level set contours

3.3.2.1 Traditional method to establish the initial level set contour

Enclosing the mass lesion with a manually drawn contour representing the initial level set contour and the initial contour deforms to towards the boundary of the mass

3.3.2.2 A semi – automatic method which derives the initial level set contour from the iso-level contour map of the mass

A semi-automatic method derives a user-independent initial contour as a curve connecting points with maximum gradient in the radial direction. This curve represents an optimum curve characterizing the intrinsic shape of the mass lesion. The image is smoothed with the weighted total variation (TV) algorithm [4] and thresholded to locate pixel positions with maximum gradients in radial directions.

3.3.3 Weighted total variation scale-space smoothing technique

This section describes the weighted-total variation scale-space algorithm. Suppose $I: \Omega \rightarrow \mathbb{R}$ denotes an image and $\Omega \subset \mathbb{R}^2$ the image domain. The variational approach for image de-noising for this model involves the minimization of the following energy functional:

$$E_{TV}(I, \lambda) = \int_{\Omega} (|\nabla I| + \lambda (I - I_0)^2) dxdy \tag{3.1}$$

Where I_0 is the noisy input image and I its regularized approximation. λ is the Lagrange multiplier indicating the scale of detail desired in the smoothed image. Using the approach of Bresson et al. [4], the L^2 –norm square in equation (3.1) is replaced with an L^1-norm to preserve image contrast and in addition, the TV norm of I is multiplied with a function, g, which is an edge indicator function. This represents the weighted TV model with an L^1- norm as a data fidelity measure. The energy functional for minimization is given as:

$$E_{gTV}(I, \lambda) = \int_{\Omega} (g|\nabla I| + \lambda |I - I_0|)\, dxdy \tag{3.2}$$

with

$$g = \frac{1}{1 + \Upsilon |\nabla G_\theta * I_0|^2} \tag{3.3}$$

Υ is a constant > 0 and G_θ is a Gaussian kernel with standard deviation, θ. The minimization of $E_{gTV}(I, \lambda)$ results in the following weighted TV flow equation:

$$I_t = div\left(g\frac{\nabla I}{|\nabla I|}\right) + \lambda\left(\frac{I - I_0}{|I - I_0|}\right) \quad (3.4)$$

Weighted TV flow filtering technique preserves edges. The smoothed image provides the global boundary information which is modelled as the initial contour for the gradient descent flow equation of the level set function. This contour depends on the boundary properties of a given mass lesion and it is independent of the input of the operator. Figure 3.1 shows a mammographic mass and its weighted TV flow smoothed image

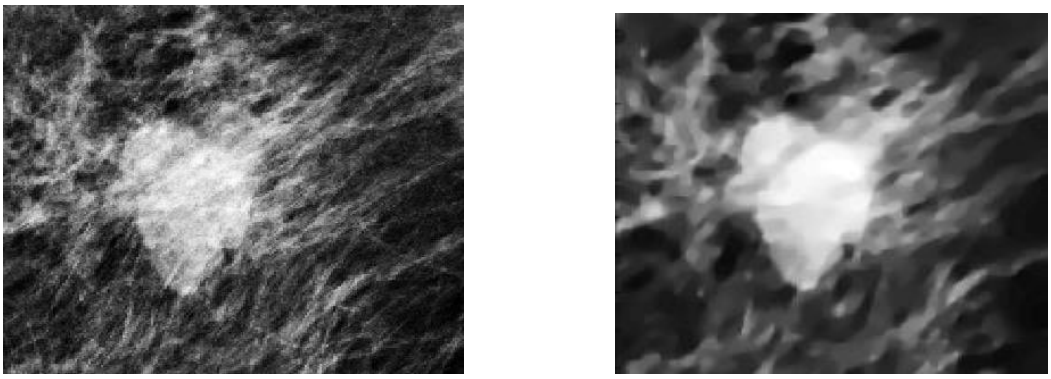

(a) (b)

Figure 3.1 (a) Original mass-lesion (b) The weighted TV flow de-noised image

3.3.4 A thresholding method to locate search space on mass margin for a user-independent initial level set contour

Let I: $\Omega \rightarrow \mathbb{R}$ denote the smoothed image and $\Omega \subset \mathbb{R}^2$ the image domain. The image domain Ω is thresholded into multiple regions with an ordered set of equally spaced gray level threshold values within the intensity range of the image domain [5] [6]. Suppose $I_{max} =$ the maximum gray level intensity in the image domain, $I_{min} =$ minimum gray level intensity, $W = \{w_1, w_2, w_3, \ldots\ldots, w_N\}$ a finite sequence of equally spaced partition weights in ascending order,

$N =$ number of threshold values and $T = \{t_1, t_2, t_3, \ldots \ldots, t_N\}$ the ordered set of equally spaced gray level threshold values, then:

$$T = I_{max} * W \qquad \text{with} \qquad t_N \leq I_{max} \; and \; t_1 \geq I_{min} \qquad (3.5)$$

The sub-regions in the image domain with gray level intensities greater than or equal to the threshold value, t_i, are given as:

$$R(t_i) = \{(x, y) | I(x, y) \geq t_i\}, \qquad \forall (x, y) \in \Omega \qquad (3.6)$$

and the iso- level contours $C(t_i)$ of these regions are boundaries of $R(t_i)$. The iso level contour map of the image domain represents the set of all $C(t_i)$ for $i = 1{:}N$. In our implementation, the boundary region of the breast mass is the region around the base contour with the dense nested pattern of iso-level contours, indicating the search space for the actual boundary of the mass and the placement of the initial level set contour. The dense nested pattern of iso-level contours is extracted and superimposed on the gradient map of the smoothed image as shown in Figure 3.2c

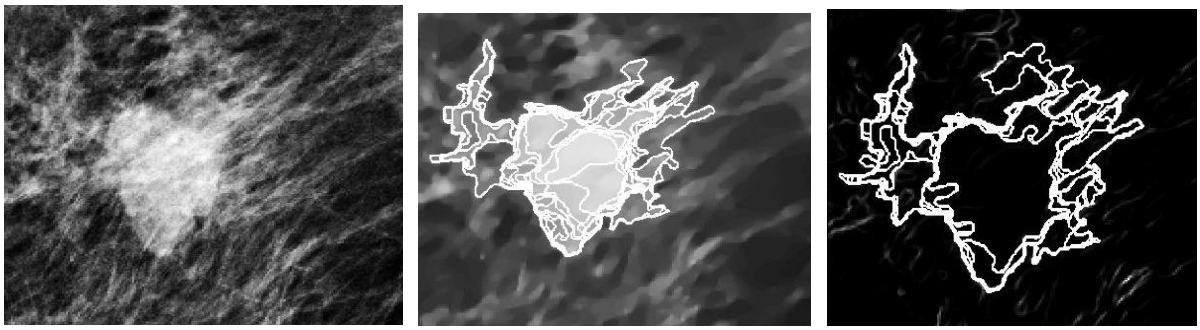

(a) (b) (c)

Figure 3.2. (a) mass lesion (b) 1so-level contour map of the smoothed mass lesion (c) nested pattern iso-level contours superimposed on the gradient map of the smoothed mass

3.3.5 Initial level set contour as a curve connecting pixel positions with maximum gradient along each radial line

A set of uniformly spaced radial lines, $L = \{l_1, l_2, \ldots\ldots\ldots l_m\}$ are generated at a point close to the centre of the edge map of the mass in the image, as shown in figure 3.3a. Let this point be noted as the point of reference. The gradient strength is noted at every point of intersection of the nested iso-level contours and radial lines. Along each radial line, l_i, $i = 1,2, \ldots\ldots, m$, the coordinates of the point of intersection with the greatest gradient strength is noted and the radial distance from this point to the point of reference is calculated and noted as r_i.

Let $r_{ave} = \frac{1}{m}\sum_{i=1}^{m} r_i$, then the radial description of the initial level set contour is given by:

$$r_i = \begin{cases} r_i\,, & r_i < r_{ave} \\ r_{ave}, & r_i \geq r_{ave} \end{cases} \qquad i = 1,2, \ldots\ldots\ldots m \qquad (3.7)$$

The spatial coordinates of the points of intersection of $r_i's$ and the iso-level contours are the coordinates of the initial level set contour (Figure 3.3b).

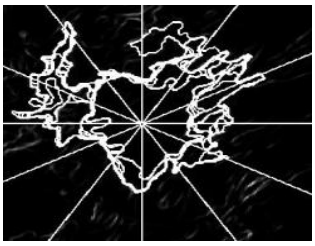

(a)

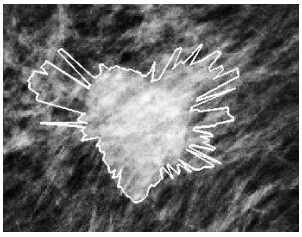

(b)

Figure 3.3. Search space for localizing the initial contour. (a) radial distances from a reference point to the iso-level contours, (b) initial level set contour, representing points with maximum gradient in the radial direction within a predefined radius.

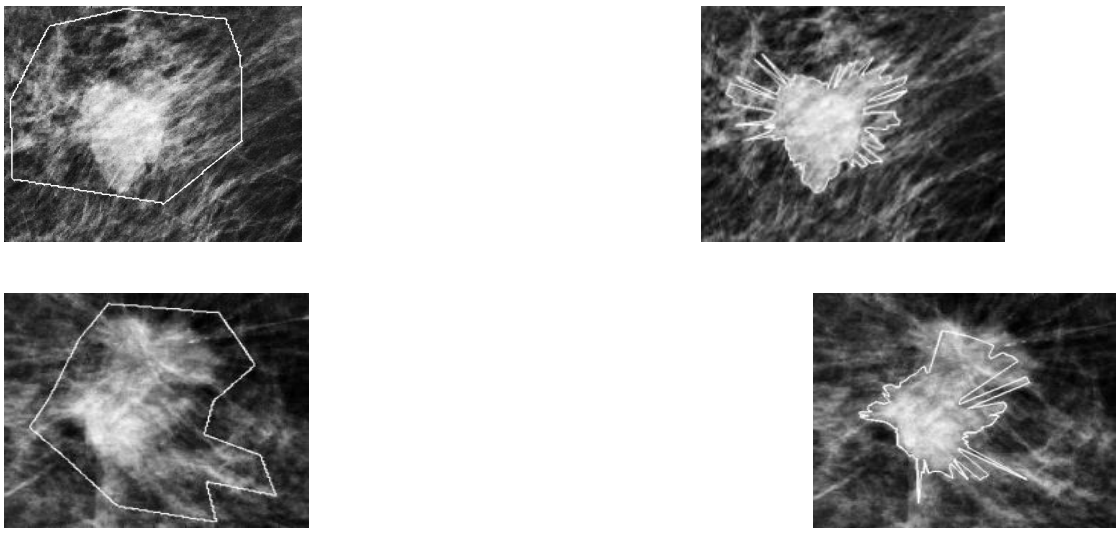

(a) (b)

Figure 3.4. Examples of the dual locations of the initial level set contours of some masses (a) Manually drawn contour surrounding the mass (b) initial level set contour from the proposed semi-automatic method

Each mass is segmented, or delineated, with the Chan-Vese and the active contour with selective local or global (SLG) segmentation methods. In the first instance the initial level set contour is drawn manually (as in figure 3.4a) and propagated with the above mentioned methods to obtain the final level set contour for each segmentation method and in the second instance, the initial level set contour for curve evolution is derived from the proposed method (as in figure 3.4b),

3.3.6 Implementation of the Chan-Vese equation on a grid

Suppose an image is sampled on a grid, $\Omega = \{0,1,2,3\ , \dots i \dots \dots \dots \dots M\} \times \{0,1,2,3\ , \dots \dots j \dots \dots \dots M\}$ and h is the space step, Δt, the time step and $\left(x_i y_j\right) = (ih, jh)$ are points on the M x M grid, then the Chan-Vese equation can be implemented on a grid.

The gradient descend flow of the Chan Vese equation is

$$\frac{\partial \varphi}{\partial t} = \delta_{\varepsilon}(\varphi)\left[\mu \nabla\left(\frac{\nabla \varphi}{|\nabla \varphi|}\right) - \upsilon - \lambda_1(I(x,y) - c_1)^2 + \lambda_2(I(x,y) - c_2)^2\right] \tag{3.8}$$

where $$div\left(\frac{\nabla \varphi}{|\nabla \varphi|}\right) = \nabla\left(\frac{\nabla \varphi}{|\nabla \varphi|}\right) \tag{3.9}$$

let $$\varphi(x,y,t) = \varphi_{i,j}^{n} \cong \varphi(n\Delta t, x_i, y_j) \tag{3.10}$$

$$\Delta_{\pm}^{x}\varphi_{i,j} = \pm\left(\varphi_{i\pm1,j} - \varphi_{i,j}\right) \tag{3.11}$$

$$\Delta_{\pm}^{y}\varphi_{i,j} = \pm\left(\varphi_{i,j\pm1} - \varphi_{i,j}\right) \tag{3.12}$$

$$L = \frac{\mu}{h}\Delta_{-}^{x}\left(\frac{\Delta_{+}^{x}\varphi_{i,j}^{n}}{\sqrt{\left(\Delta_{+}^{x}\varphi_{i,j}^{n}\right)^2 + \left(\Delta_{+}^{y}\varphi_{i,j}^{n}\right)^2}}\right) + \frac{\mu}{h}\Delta_{-}^{y}\left(\frac{\Delta_{+}^{y}\varphi_{i,j}^{n}}{\sqrt{\left(\Delta_{+}^{x}\varphi_{i,j}^{n}\right)^2 + \left(\Delta_{+}^{y}\,\varphi_{i,j}^{n}\right)^2}}\right) \tag{3.13}$$

$$R = -\upsilon - \lambda_1\left(I_{i,j} - c_1\left(\varphi_{i,j}^{n}\right)\right)^2 + \lambda_2\left(I_{i,j} - c_2\left(\varphi_{i,j}^{n}\right)\right)^2 \tag{3.14}$$

Then the Chan-Vese iterative equation is carried out as:

$$\frac{\varphi_{i,j}^{n+1} - \varphi_{i,j}^{n}}{\Delta t} = \delta_{\varepsilon}\left(\varphi_{i,j}^{n}\right)[L + R] \tag{3.15}$$

The iterative process is implemented as follows:

1. Keep φ fixed,
2. Calculate the average gray values of regions c_1 and c_2 using equation 2.31 and equation 2.32 respectively
3. Evolve the level set contour according to equation 3.15.

4. Check whether a numerical stopping criterion (the maximum number of iterations defined by the user) on φ is reached, if it is reached then stop iterations, if not continue.

In our implementation of this method, we set $\mu = 0.2, \lambda_1 = 2.5$ and $\lambda_2 = 1$. We chose $\lambda_1 > \lambda_2$ to give a greater weight to the variance of pixels in the foreground so as to achieve measurable segmentation differences between the proposed locations for the initial level set contours. Furthermore, we assigned $\lambda_1 = \lambda_2 = 1$, to investigate changes in the final segmentation results due to differences in tunable parameters. The average time for curve evolution for these images was 15 ± 10 s . Algorithms were performed with Matlab R2013a (The MathWorks, Inc., Natick, MA, USA),

3. 3.7 Implementation of the active contours with selective local or global segmentation model on a grid

The gradient descent flow of the active contours with selective local or global segmentation equation (see equation 2.33) is

$$\frac{\partial \phi}{\partial t} = \left[\frac{I(x,y) - \frac{c_1 + c_2}{2}}{\max\left(\left|I(x,y) - \frac{c_1 + c_2}{2}\right|\right)}\right].\alpha|\nabla\phi| \quad x, y \in \Omega_p \tag{3.16}$$

Let $$\varphi(x,y,t) = \varphi_{i,j}^n \cong \varphi\left(n\Delta t, x_i, y_j\right) \tag{3.17}$$

$$\Delta_{\pm}^{x}\varphi_{i,j} = \pm\left(\varphi_{i\pm1,j} - \varphi_{i,j}\right) \tag{3.18}$$

$$\Delta_{\pm}^{y}\varphi_{i,j} = \pm\left(\varphi_{i,j\pm1} - \varphi_{i,j}\right) \tag{3.19}$$

$$L1 = \frac{\alpha}{h}\left\{\frac{I_{i,j} - \frac{c_1\left(\varphi_{i,j}^n\right) + c_2\left(\varphi_{i,j}^n\right)}{2}}{max\left(\left|I_{i,j} - \frac{c_1\left(\varphi_{i,j}^n\right) + c_2\left(\varphi_{i,j}^n\right)}{2}\right|\right)}\right\} \tag{3.20}$$

$$R1 = \sqrt{\left(\Delta_{+}^{x}\varphi_{i,j}^n\right)^2 + \left(\Delta_{+}^{y}\varphi_{i,j}^n\right)^2} \tag{3.21}$$

Then the iterative equation of this segmentation model is carried out as

$$\frac{\varphi_{i,j}^{n+1} - \varphi_{i,j}^{n}}{\Delta t} = [L1 + R1] \tag{3.22}$$

Equations 3.13 and 3.14 are not the same as 3.20 and 3.21 because the speed functions are formulated differently.

The iterative process is implemented as follows:

1. Keep φ fixed,
2. Calculate the average gray values of regions c_1 and c_2 using equation 2.31 and equation 2.32 respectively
3. Evolve the level set contour according to equation 3.22
4. Let $\varphi = 1$ if $\varphi > 0$; otherwise, $\varphi = -1$
5. Set $= \varphi * G_\sigma$, where G_σ is a Gaussian function with standard deviation σ
6. Check whether a numerical stopping criterial on φ is reached, if it is reached then stop iterations, if not continue.

Experimentally, we set α = 5 for our database of masses, so that masses with ill-defined boundaries could be accurately segmented. The segmentation performances of this algorithm were poor with values of α > 5 for masses with ill-defined boundaries. The average time for curve evolution for these images was 15 ± 10 s for the segmentation methods

3. 3.8 Morphological shape description and comparison of the final level set contours which describe the periphery of mass-lesions

The shape representation and description techniques of mammographic masses can be categorized into 2 groups: Contour–based methods which exploit only the global boundary

information of the region occupied by the mass and region-based methods which considers all the pixels within the area occupied by the mass to obtain a shape representation metric.

3. 3.8.1 Contour–based shape representation and comparison metrics

Boundary moments

A boundary-based shape signature of the segmented mass lesion from a given initial contour model is represented as the centroid distance function (figure 3.5), which is a one dimensional function representing the Euclidean distance, $r(n)$, between an ordered set of boundary coordinates $\Big(\big(x(n), y(n)\big), \text{for } n = 0,2,3, \ldots\ldots, N-1\Big)$ and the centroid (xc, yc) signifying the centre of mass of the binary image generated from the contour:

$$r(n) = \sqrt{((x(n) - xc)^2 + (y(n) - yc)^2)} \tag{3.23}$$

where N is the total number of points on the contour.

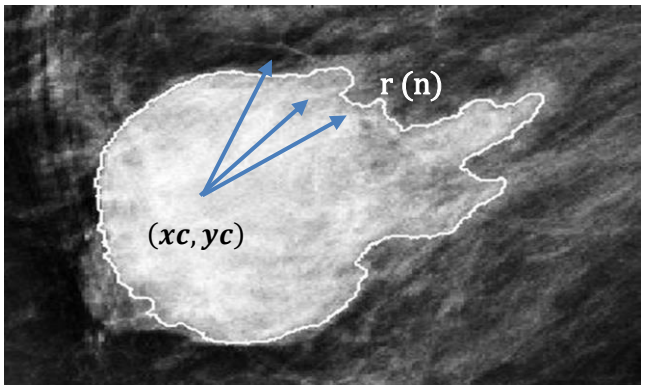

Figure 3.5. Centroid distance function

The centroid distance function captures the local and global characteristics of the final shape of the segmented mass lesion. Its statistical characteristics are assessed as shape features derived from the contour sequence moments m_p and μ_p where the pth contour sequence moment is estimated as,

$$m_p = \frac{1}{N}\sum_{n=0}^{N-1}[r(n)]^p \tag{3.24}$$

and the p[th] central moment:

$$\mu_p = \frac{1}{N}\sum_{n=0}^{N-1}[r(n) - m_1]^p \tag{3.25}$$

These shape features are normalized low–order boundary moments [7] [8] described as:

$$F_1 = \frac{(\mu_2)^{\frac{1}{2}}}{m_1}dxdy \quad , \quad F_2 = \frac{(\mu_4)^{\frac{1}{4}}}{m_1} \text{ and } F_3 = F_1 - F_2 \tag{3.26}$$

where F_1 is the normalized amplitude variation, F_2 and F_3 are indicators of shape roughness.

Highly spiculated masses will exhibit large variations in the radial distances and this will be expressed in the boundary moments F_1, F_2 and F_3. The evaluation metric, $FS_i(imX, imY)$, for the change in the degree of spiculation between the imX and imY is the percentage change in the boundary moments, F_i s;

$$\%\ FS_i(imX, imY) = \left|\frac{F_i(imY) - F_i(imX)}{F_i(imY)}\right| \times 100 \tag{3.27}$$

Fourier descriptors

The centroid distance function can be analysed in the frequency domain to obtain spectral descriptors of its characteristics. Its spectral representation is expressed as the coefficients of its discrete Fourier transform, yielding:

$$a_i = \frac{1}{N}\sum_{n=0}^{N-1} r(n)\, exp\left(\frac{-j2\pi in}{N}\right), i = 0,1,2, \ldots\ldots\ldots, N-1 \tag{3.28}$$

Feature vectors which are invariant to translation, scale and rotation are extracted from these coefficients and are known as the Fourier descriptors (FD_i) for shape representation:

$$FD_i = \left[\frac{|a_i|}{|a_0|}\right], i = 1,2, \ldots \ldots . N/2 \tag{3.29}$$

Sixty $FD_i s$ were used for shape indexing. We define the evaluation metric of the initial level set contours yielding, imX and imY based on the boundary signatures of the final contours delineating imX and imY in the frequency domain as the Euclidean distance between the Fourier descriptors:

$$DF(imY, imX) = \sqrt{\sum_{i=1}^{60} |FD_i\,(imY) - FD_i(imX)|^2} \tag{3.30}$$

where $FD_i\,(imX)$ and $FD_i\,(imY)$ are the i^{th} Fourier descriptors of the final contours delineating imX and imY.

3. 3.8.2 Region–based shape representation and comparison metrics

Area metric of relative size of the segmented mass lesion

Let imY represent the binary image obtained by evolving the initial contour from our proposed method and imX from the manually drawn initial level set contour, then; the measure of the area of overlap, which is the Jaccard similarity coefficient between the binary images, imX and imY is given as:

$$JSC(imX, imY) = \frac{imY \cap imX}{imY \cup imX} \tag{3.31}$$

$JSC(imX, imY)$ lies between 0 and 1. A perfect matched between imX and imY is achieved as $JSC(imX, imY) \rightarrow 1$, consequently, the same segmentation outcome for both initial level set contours.

Shape convexity

The shape convexity of a binary image is defined as the ratio of the area of the binary image to the area of its convex hull [9]. Let $CimX$ and $CimY$ be the convexity of binary images imX and imY respectively, the evaluation metric of the differences between the shape convexities of images imX and imY is defined as:

$$\%SC(imX, imY) = \left|\frac{CimY - CimX}{CimY}\right| \times 100 \tag{3.32}$$

Shape rectangularity

Shape rectangularity [10] is defined as the ratio of the area of the binary image to the area of its minimal bounding rectangle. Let $RimX$ and $RimY$ be the rectangularity of binary images imX and imY respectively, the evaluation metric of the difference between the shape rectangularities of images imX and imY is defined as:

$$\%\Delta SR(imX, imY) = \left|\frac{RimY - RimX}{average(RimY, RimX)}\right| \times 100 \tag{3.33}$$

3.4 Experimental Results and Discussion

Boundary information represents sharp changes in image properties. Figure.3.6 shows that as the degree of smoothing (λ) increases the radial distance functions of the initial level set contours form a dense nested pattern of curves. Programming was implemented in Matlab 7.0 on an Intel Core 2 Duo 3.0 GHz

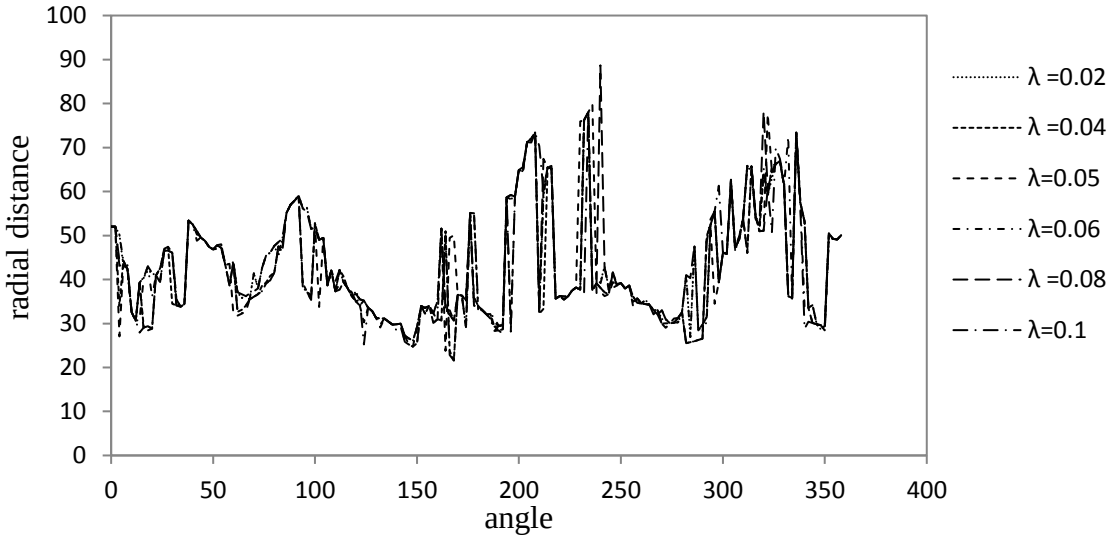

Figure 3.6. Variation of the radial distance function of the initial level set contours sampled at an angle of 1° with different λs for the mass lesion in Figure 3.4a.

The differences between these curves are very small because edge is preserved through different values of λs in weighted TV scale-space smoothing technique (equation 3.4), consequently segmentation results with the initial level set contours generated from these curves are expected to be similar. Segmentation results for some masses with low signal areas and having obscured, or ill-defined, margins are shown in figure 3.7. The proposed method defines the initial level set contour as the curve connecting points with maximum gradients in the radial direction as shown in column 3. Each curve characterizes the intrinsic shape of its mass lesion and its evolution is guided by the statistics of pixels surrounding the region. For this group of masses, the mean area overlap measure between segmented areas generated from

the final contours of our proposed method and that of the manually drawn initial level set contours was 0.81 ± 0.07. This is almost comparable to the mean area overlap measures between expert radiologists [11] and expert radiologists against segmentation methods [12], [13], [14], [15] as shown in Table 3.1. Therefore, changes in shape-based descriptors as expressed in our setup will be suggestive of changes in shape-based descriptors encountered by the abovementioned publications.

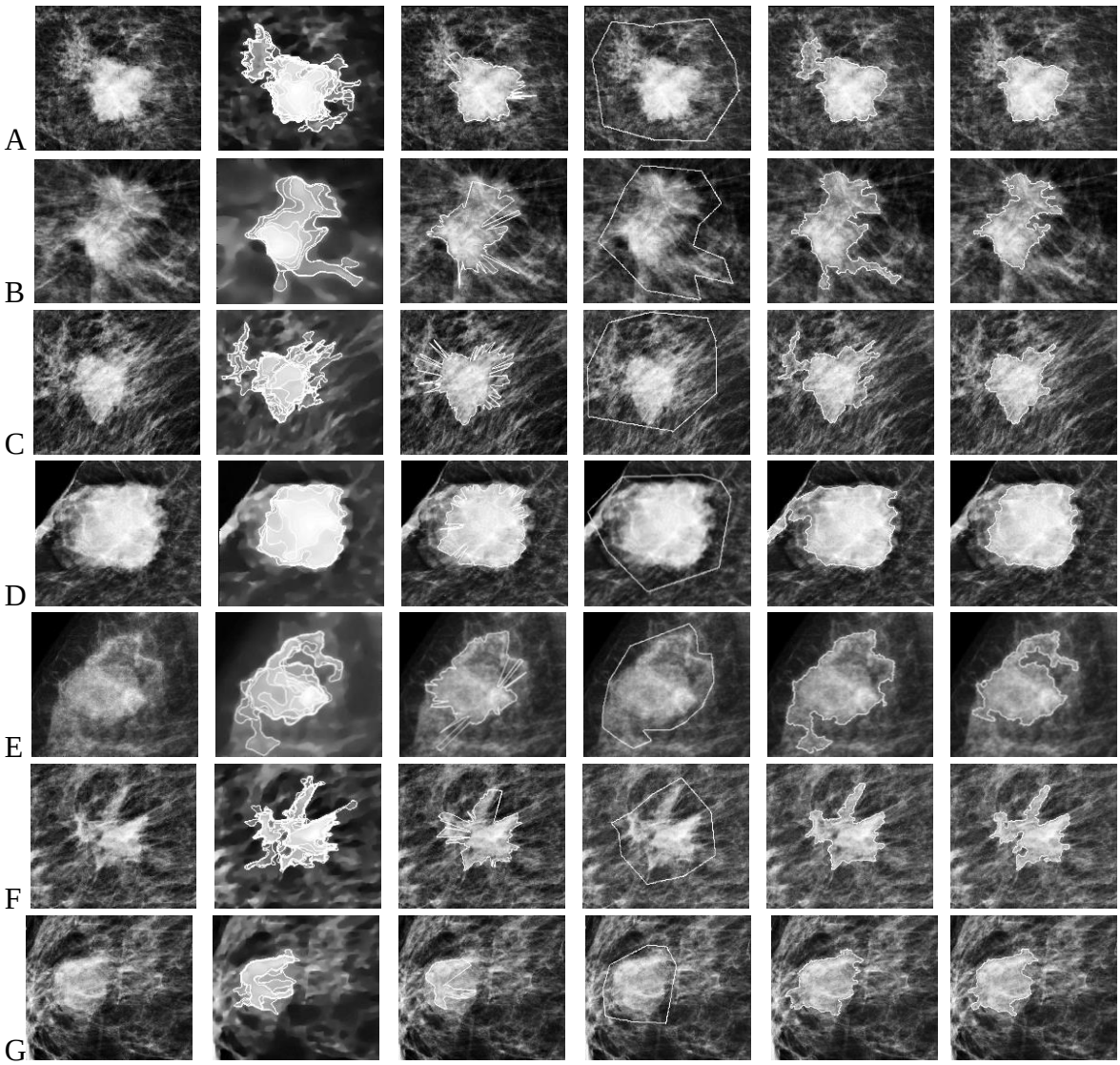

Figure 3.7. Comparisons of segmentation results with different locations for the initial level set contours for masses with low signal areas having obscured, or ill-defined, margins. The first column presents the original mass lesions; the second column shows the corresponding weighted TV flow images and the search space for locating the initial contour. The third column shows the initial contours as curves connecting points with maximum gradients in the radial direction. The fourth column shows the manually drawn initial level set contours. The fifth column presents the segmentation outcomes with manually drawn initial level set and the last column presents the final segmentation results of the proposed method evolved with the same tuning parameters.

Table 3.1. Comparison of mean area overlap measures of masses with characterized margins due to changes in the location of the initial level set contour with cited inter-observer variability amongst radiologists and with mean area overlap measures between radiologists and other segmentation methods in boundary delineation.

	Characteristics of mass-lesion margins	**Mean area overlap measures due to inter-observer variability amongst radiologists**	**Mean area overlap measures between radiologists and segmentation methods**	**Mean area overlap measures due to placement of the initial level set contours**
Sahiner et al [11]	-	**0.76 ± 0.13**	**0.74 ± 0.13**	
Tao et al. [12]	**Ill-defined and spiculated**		**0.69 ± 0.16**	
Xu et al. [13]	-		**0.72 ± 0.13**	
Rahmati et al. [14]	-		**0.87 ± 0.05**	
Pereira et al [15]			**0.79±0.08**	
This study ($\lambda_1 = 2.5, \lambda_2 = 1$)	**Obscured/ill-defined with Low signal areas within**			**0.81 ± 0.07**
This study ($\lambda_1 = 2.5, \lambda_2 = 1$)	**Distinct/well-defined**			**0.97 ± 0.02**
This study ($\lambda_1 = 1, \lambda_2 = 1$)	**Obscured/ill-defined with low signal areas within**			**0.93± 0.07**
This study ($\lambda_1 = 1, \lambda_2 = 1$)	**Distinct/well defined**			**0.96± 0.04**

Table 3.2 illustrates an example of seven masses out of a database of ninety masses. It shows the variation in the area overlap measures with percentage differences in boundary moments F_1, F_2 and F_3 when masses in Figure 3.7 were evolved with tuneable parameters $\lambda_1 = 2.5, \lambda_2 = 1$ The area overlap measure of mass D is greater than 0.8, however the percentage difference in boundary moments were above 50%, with $\%\Delta F_1$ being 87.0%. The mean values of $\%\Delta F_1, \%\Delta F_2$ and $\%\Delta F_3$ for this group were 20.2% (range 1.7-87.0%), 18.9% (range 2.7-86.8%) and 29.6% (range 3.4-86.0%) respectively, as shown in Table 3.6. The mean values are large with wide range. For $\lambda_1 = 1, \lambda_2 = 1$ the mean values of the percentage change of each boundary moment was less than 20.7%. These large ranges and mean values show that, boundary moments are sensitive to the location of the initial level set contour for masses with obscured or ill-defined margins and the degree of sensitivity depends on the choice of tuneable parameters. $\%\Delta F_1, \%\Delta F_2$ and $\%\Delta F_3$ are .estimated from the final level set contour and not from the initial level set contour such as in Figure 3.2

Table 3.2. Evaluation metrics for differences in segmented areas ($\boldsymbol{JSC}$) and boundary moments($\%\Delta\mathbf{F_1}, \%\Delta\mathbf{F_2}, \%\Delta\mathbf{F_3}$) , due to changes in the location of the initial level set contours evolved with tuneable parameters $\boldsymbol{\lambda_1 = 2.5, \lambda_2 = 1}$ for masses in Figure 3.7

Masses	**JSC (eqn 3.31)**	**F_1 (Eqn3.26)**	**F_2 (Eqn3.26)**	**F_3 (Eqn3.26)**	**Method**	$\%\Delta F_1$	$\%\Delta F_2$
A	**0.83**	**0.32**	**0.37**	**0.05**	**Manual**	**68.4**	**67.1**
		0.16	**0.18**	**0.03**	**Proposed**		
B	**0.77**	**0.34**	**0.43**	**0.08**	**Manual**	**8.1**	**7.2**
		0.32	**0.39**	**0.08**	**Proposed**		
C	**0.78**	**0.27**	**0.33**	**0.06**	**Manual**	**9.7**	**3.1**
		0.24	**0.32**	**0.07**	**Proposed**		
D	**0.84**	**0.25**	**0.31**	**0.06**	**Manual**	**87.0**	**86.8**
		0.09	**0.12**	**0.02**	**Proposed**		
E	**0.71**	**0.27**	**0.33**	**0.06**	**Manual**	**6.0**	**8.1**
		0.29	**0.36**	**0.07**	**Proposed**		
F	**0.89**	**0.29**	**0.38**	**0.09**	**Manual**	**8.2**	**7.4**
		0.32	**0.41**	**0.09**	**Proposed**		
G	**0.87**	**0.18**	**0.22**	**0.03**	**Manual**	**1.7**	**9.9**
		0.1866	**0.2394**	**0.0528**	**Proposed**		

In Table 3.3, the variation in Euclidean distances of the Fourier descriptors and the percentage differences in shape convexity and rectangularity for the masses in Fig.3.7 are illustrated. In Table 3.6, for $\lambda_1 = 2.5, \lambda_2 = 1$ the mean Euclidean distance between the Fourier descriptors of the segmented areas was 0.1 ± 0.05 while the mean values of percentage changes in shape convexity and rectangularity were 10.8% (range 0.3-28.1%) and 14.1% (range 0.5- 42.0%) respectively, and more than 50% reduction in the mean values with tuneable parameters $\lambda_1 = 1, \lambda_2 = 1$. The values for the mean percentage difference in shape convexity and rectangularity, and their range was less than those from boundary moments.

Figure 3.8 illustrates the segmentation results with different locations for the initial level set contours for some masses with distinct, or well-defined, margins. The initial level set contour from the proposed method is shown in column 3. Fewer points defining the maximum gradients in the radial direction are found within the mass lesion, as compared with the previous group. Most points defining the maximum gradients in the radial direction are found on the mass boundary; consequently, the statistics of the pixels surrounding the initial level set contour will be similar to those of the manually drawn contour when it arrives at the edge of the mass lesion.

Table 3.3. Variation in Euclidean distances between Fourier descriptors (DF), percentage differences in shape convexity (%$\Delta \boldsymbol{SC}$) and shape rectangularity (%$\Delta \mathbf{SR}$) due to changes in the location of the initial level set contours evolved with tuneable parameters $\boldsymbol{\lambda_1 = 2.5\ \lambda_2 = 1}$ for masses in Figure 3.8.

Masses	DF eqn(3.3)	SC (eqn3.32)	SR (eqn3.33)	Method	%Δ SC	%Δ SR
A	0.16	0.72	0.49	Manual	16.50	31.50
		0.84	0.67	Proposed		
B	0.10	0.54	0.38	Manual	22.40	9.60
		0.67	0.41	Proposed		
C	0.08	0.56	0.38	Manual	28.20	21.60
		0.75	0.48	Proposed		
D	0.13	0.81	0.63	Manual	12.50	16.60
		0.91	0.74	Proposed		
E	0.06	0.77	0.50	Manual	16.70	3.80
		0.91	0.48	Proposed		
F	0.05	0.59	0.42	Manual	10.10	10.90
		0.54	0.37	Proposed		
G	0.03	0.7899	0.53	Manual	1.70	8.80
		0.8036	0.58	Proposed		

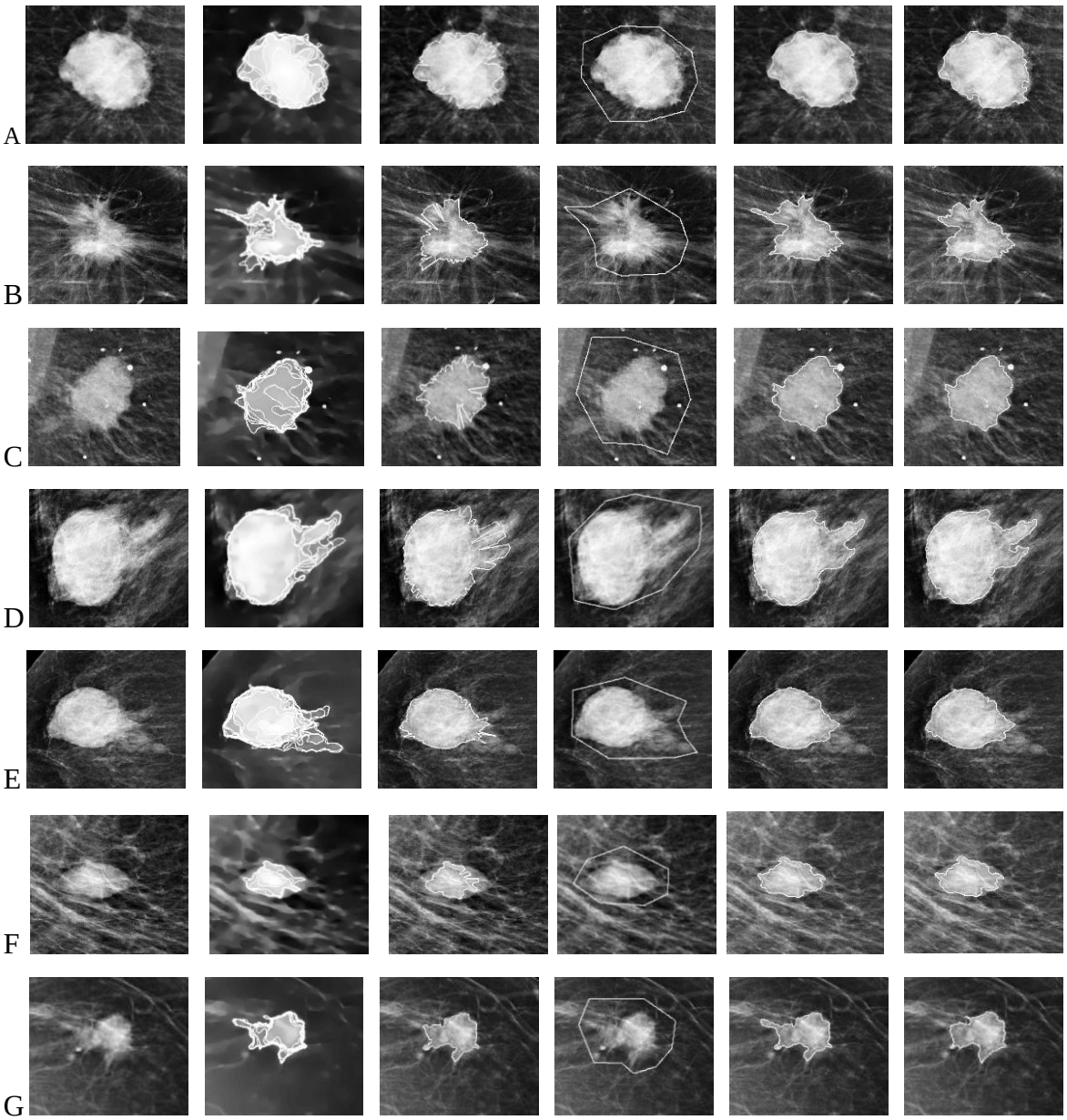

Figure 3.8. Comparisons of segmentation results with different locations for the initial level set contours for masses with distinct, or well-defined, margins. The first column presents the original mass lesions; the second column shows the corresponding weighted TV flow images and the search space for locating the initial contour. The third column shows the initial contours as curves connecting points with maximum gradients in the radial direction. The fourth column shows the manually drawn initial level set contours. The fifth column presents the segmentation outcomes with manually drawn initial level set contours and the last column presents the final segmentation results of the proposed method evolved with the same tuning parameters.

Table 3.4, shows the variation in the area overlap measures and the percentage differences in boundary moments F_1, F_2 and F_3 while Table 3.5 illustrates the variation in Euclidean distances between the Fourier descriptors *(DF)*, percentage differences in shape convexity $(\%\Delta SC)$ and shape rectangularity $(\%\Delta SR)$ when the masses in Fig. 3.8 were evolved with tuneable parameters $\lambda_1 = 2.5, \lambda_2 = 1$. The area overlap measure of mass B was greater than 0.95, however the percentage differences in boundary moments were above 18%. For masses with distinct or well-defined margins, similar segmentation results are expected, and this is confirmed with a mean area overlap measure of 0.97 ± 0.02 as shown in Table 3.6. For this category of masses, the mean value of $\%\Delta F_1$ was 10.2% (range 0.3-22.0%), $\%\Delta F_2$, 9.6% (range 2.1-31.2%) and $\%\Delta F_3$ 14.9% (range 0.9-53.0%). The mean Euclidean distance between the Fourier descriptors of the segmented areas was 0.04 ± 0.02 and the mean values of percentage changes of shape convexity and rectangularity were 5.0% (range 0.5-17.2%) and 5.1% (range 0.1-14.9%) respectively. The values for the mean percentage differences in shape convexity and rectangularity were almost 50% less than those from boundary moments. This group presented a small percentage change in shape convexity, shape rectangularity, and also a smaller mean Euclidean distance of the Fourier descriptors as compared to the previous group due to segmentation results having relatively similar shapes. For these groups of masses, shape-based descriptors derived from final contours of tuneable parameters $\lambda_1 = 1, \lambda_2 = 1$ were less sensitive to changes in the location of the initial level set contours.

Table 3.4. Evaluation metrics for differences in segmented areas (JSC) and boundary moments ($\%\Delta F_1, \%\Delta F_2, \%\Delta F_3$), due to changes in the location of the initial level set contours evolved with tuneable parameters $\lambda_1 = 2.5, \lambda_2 = 1$ for masses in Figure 3.8.

Masses	JSC	F_1	F_2	F_3	Method	$\%\Delta F_1$	$\%\Delta F_2$	$\%\Delta F_3$
A	0.98	0.08	0.11	0.02	Manual	29.00	31.20	39.4
		0.11	0.14	0.03	Proposed			
B	0.97	0.21	0.28	0.07	Manual	21.90	21.10	18.7
		0.26	0.34	0.08	Proposed			
C	0.99	0.15	0.18	0.03	Manual	6.10	2.60	13.6
		0.14	0.17	0.03	Proposed			
D	0.98	0.21	0.26	0.04	Manual	12.00	9.00	6.6
		0.24	0.28	0.04	Proposed			
E	0.98	0.11	0.14	0.03	Manual	2.20	2.90	5.9
		0.11	0.13	0.03	Proposed			
F	0.94	0.19	0.22	0.03	Manual	2.00	1.30	19.3
		0.19	0.22	0.04	Proposed			
G	0.94	0.29	0.37	0.07	Manual	18.70	12.40	10.9
		0.25	0.32	0.08	Proposed			

Table 3.5. Variation in Euclidean distances between the Fourier descriptors *(DF)*, percentage differences in shape convexity ($\%\Delta SC$) and shape rectangularity ($\%\Delta SR$) due to changes in the location of the initial level set contours evolved with tuneable parameters $\lambda_1 = 2.5, \lambda_2 = 1$ for masses in figure 3.8

Masses	*DF (eqn3.30)*	*SC (eqn 3.32)*	*SR (eqn3.33)*	*Method*	*%Δ SC*	*%Δ SR*
A	**0.04**	**0.66**	**0.46**	**Manual**	**17.1**	**14.5**
		0.78	**0.53**	**Proposed**		
B	**0.062**	**0.66**	**0.46**	**Manual**	**7.0**	**14.4**
		0.71	**0.53**	**Proposed**		
C	**0.04**	**0.89**	**0.61**	**Manual**	**1.1**	**1.2**
		0.89	**0.62**	**Proposed**		
D	**0.08**	**0.85**	**0.61**	**Manual**	**0.0**	**0.0**
		0.85	**0.61**	**Proposed**		
E	**0.02**	**0.93**	**0.65**	**Manual**	**0.3**	**1.1**
		0.93	**0.65**	**Proposed**		
F	**0.03**	**0.86**	**0.60**	**Manual**	**2.9**	**5.2**
		0.84	**0.57**	**Proposed**		
G	**0.07**	**0.66**	**0.46**	**Manual**	**17.1**	**14.5**
		0.79	**0.53**	**Proposed**		

Table 3.6. Mean values for the Jaccard similarity coefficient (*JSC*) and the Euclidean distances of the masses. The mean values and ranges of percentage differences in boundary moments (*%*Δ F_1, *%*Δ F_2 , *%*Δ F_3*)*, percentage differences in shape convexity (*%*Δ *SC)* and percentage differences in shape rectangularity (*%*Δ *SC)* for the masses , labelled as groups with pre-defined margin characteristics and also a group with arbitrary margin characteristics, due to changes in the location of the initial level set contours evolved with tuneable parameters $\boldsymbol{\lambda_1 = 2.5, \lambda_2 = 1}$ and $\boldsymbol{\lambda_1 = 1, \lambda_2 = 1}$.

Margin Characteristics	**Obscured/ill-defined Margins**		**Distinct/well-defined Margins**		**Unlabelled Margins**	
Tuneable parameters	**λ_1=2.5,λ_2 =1**	**λ_1 =1,λ_2 =1**	**λ_1 =2.5,λ_2 =1**	**λ_1 =1, λ_2 =1**	**λ_1=2.5,λ_2 =1**	**λ_1 =1, λ_2 =1**
Average *JSC*	**0.81 ± 0.07**	**0.93 ± 0.07**	**0.97 ± 0.02**	**0.96± 0.04**	**0.89 ± 0.09**	**0.95 ± 0.06**
Average *DF*	**0.10 ± 0.05**	**0.04 ± 0.04**	**0.04 ± 0.02**	**0.03 ± 0.02**	**0.06 ± 0.05**	**0.03 ± 0.03**
Mean of *%*Δ F_1	**20.2 %**	**15.6 %**	**10.2 %**	**8.6 %**	**15.1 %**	**11.6%**
Range of *%*Δ F_1	**1.7-87.0%**	**0-57.8%**	**0.3-22.0%**	**0-20.8%**	**0.3-87.0%**	**0-57%**
Mean of *%*Δ F_2	**18.6 %**	**15.8 %**	**9.6%**	**14.7 %**	**13.4 %**	**15.1 %**
Range of *%*Δ F_2	**2.7-86.8%**	**0-59.1%**	**2.1-31.2%**	**0-46.0%**	**2.1-86.8%**	**0-59.1%**
Mean of *%*Δ F_3	**29.6%**	**20.7%**	**14.9 %**	**14.6 %**	**21.2 %**	**17.2 %**
Range of *%*Δ F_3	**3.4 -86.0%**	**0-80.9%**	**0.9-53.0%**	**0-54.0%**	**0-86.0%**	**0-54.0%**
Mean of *%*Δ *SC*	**10.8 %**	**3.4 %**	**5.0%**	**2.9 %**	**7.5 %**	**3.1 %**
Range of *%*Δ *SC*	**0.3-28.1%**	**0-21.0%**	**0.5-17.2%**	**0.2-13.9%**	**0.3-28.1%**	**0-21.0%**
Mean of *%*Δ *SR*	**14.1 %**	**6.4 %**	**5.1 %**	**3.8 %**	**8.9%**	**4.9%**
Range of *%*Δ *SR*	**0.5-42.0%**	**0-38.9%**	**0.1-14.9%**	**0-21.9%**	**0.1-42.0%**	**0-38.9%**

The evaluation metrics of shape-based descriptors of both groups of masses were combined and assessed with Bland-Altman [16] plots to investigate the inter-method agreement between placements of the initial level set contours. These plots represent a graphical method to compare two segmentation algorithms and each Bland-Altman plot was evaluated within a 95% confidence interval as the limits of agreement.

Figures 3.9 and 3.10 illustrate the linear regression plots of boundary moments, shape rectangularity and shape convexity with their associated Bland-Altman plots. The Pearson correlation analysis indicated good correlations between the shaped-based descriptors: shape rectangularity (r = 0.81) and shape convexity (r=0.82) resulting from the final contours of the proposed and manual methods as compared to boundary moments F_1 $(\mathrm{r} = 0.70)$, F_2 $(\mathrm{r} = 0.70)$and F_3 $(\mathrm{r} = 0.68)$. Table 3.7 shows the summary results of the linear regression analysis of shape-based descriptors for these masses and their variation with tuneable parameters. The p-values indicated that the correlations of shape-based descriptors derived from these methods were statistically significant ($p < 0.0001$). The strength of the linear relationship (r) between the descriptors derived from these methods depends on the values of tuneable parameters, λ_1 and λ_2. For this set of masses the correlation coefficients of descriptors obtained with tuneable parameters $\lambda_1 = 1$ and $\lambda_2 = 1$ were higher than those with parameters $\lambda_1 = 2.5$ and $\lambda_2 = 1$, however, this does not imply that, tuneable parameters $\lambda_1 = 1$ and $\lambda_2 = 1$ will provide higher values of similarity measures when segmentation results are compared with segmentation outcomes of expert radiologists.

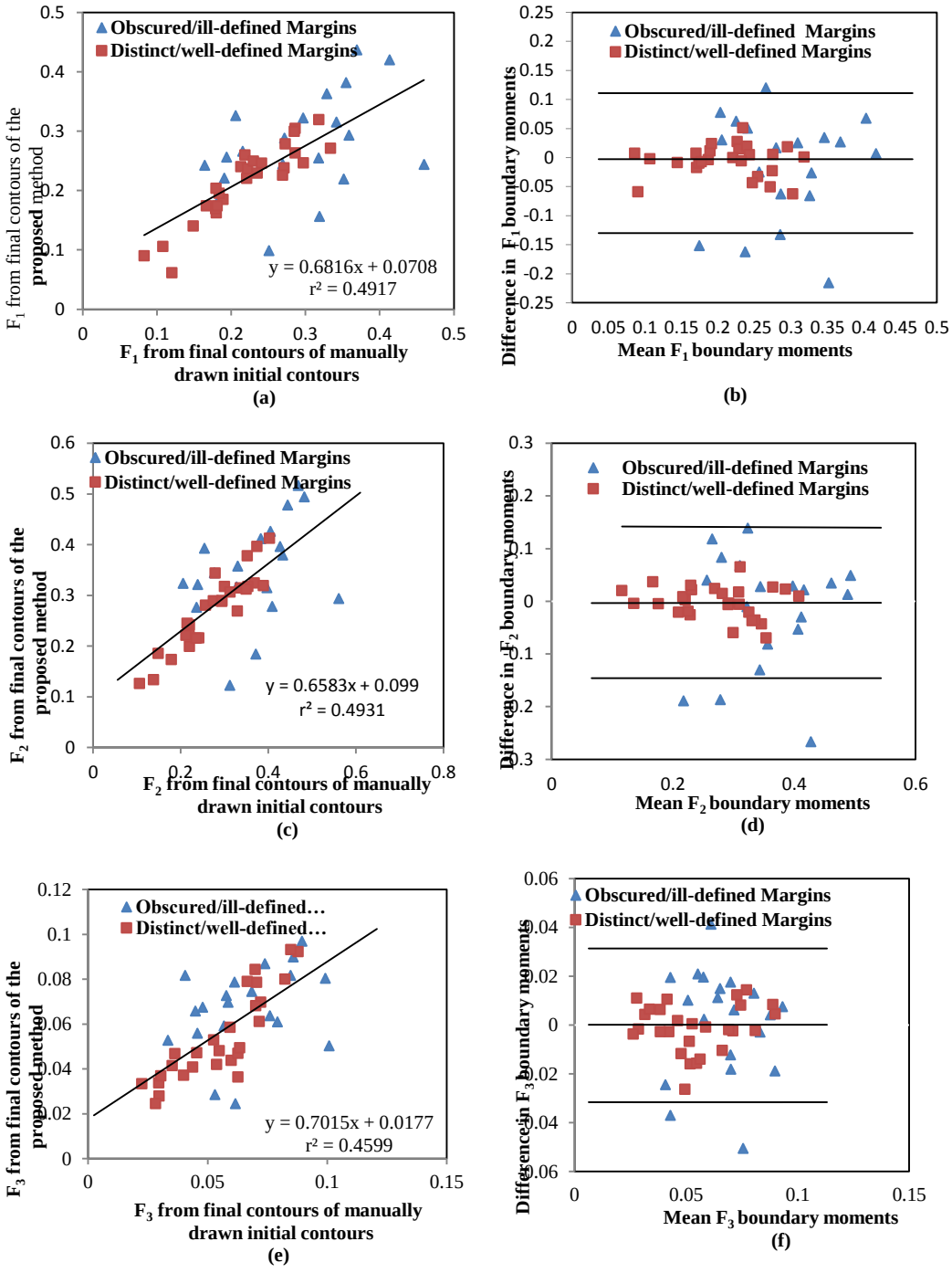

Figure 3.9. Linear regression plots, a, c and e along with Bland-Altman plots, b, d and f of boundary moments F_1, F_2 F_3 respectively for tuneable parameters $\lambda_1 = 2.5, \lambda_2 = 1$

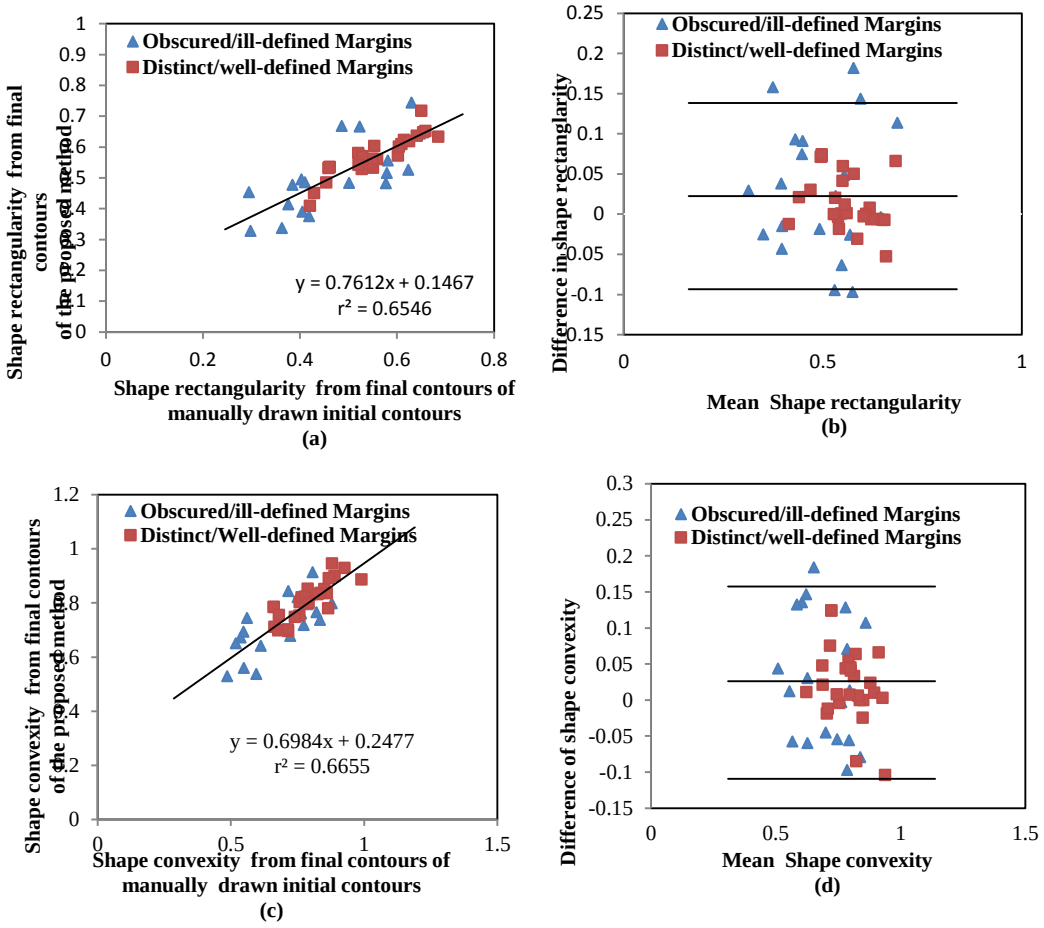

Figure 3.10. Linear regression plots, a and c with associated Bland-Altman plots, b and d of shape rectangularity (SR) and shape convexity (SC) respectively, for tuneable parameters $\lambda_1 = 2.5, \lambda_2 = 1$

Table 3.7. Summary results of linear regression analysis for tuneable parameters λ_1 =2.5, λ_2 =1 and λ_1 =1, λ_2 =1.

Tuneable parameters	**λ_1 =2.5, λ_2 =1**			**λ_1 =1, λ_2 =1**		
	slope	**r**	**p-value**	**slope**	**r**	**p-value**
F_1	**0.68**	**0.70**	**<0.0001**	**0.78**	**0.82**	**<0.0001**
F_2	**0.66**	**0.70**	**<0.0001**	**0.72**	**0.75**	**<0.0001**
F_3	**0.70**	**0.68**	**<0.0001**	**0.75**	**0.79**	**<0.0001**
SC	**0.69**	**0.82**	**<0.0001**	**0.93**	**0.93**	**<0.0001**
SR	**0.76**	**0.81**	**<0.0001**	**0.82**	**0.88**	**<0.0001**

The difference plots in Figures 3.9 and 3.10, show that differences in shape-based features for masses with distinct or well-defined masses are scattered very close to the central bias line as compared to masses with obscured, or ill-defined, margins thus indicating that, the magnitude of differences in shape-based descriptors due to changes in the placement of the initial level set contours depends on the mass margin characteristics. The correlations between differences in shape-based descriptors due to changes in the placement of the initial level set contours and the average magnitude of descriptors from both algorithms were very poor and they were not significantly different from zero. The intercept doesn't play any role in the analysis between the two methods because the goal is to find out if the shape characteristics of the masses delineated with the two methods correlates

In general, the mean area overlap measure of the combined categories (manual and proposed methods) was 0.89 ± 0.09, the mean Euclidean distance between the Fourier descriptors was 0.06 ± 0.05 and moreover in the Bland-Altman plots, the differences in shape-based descriptors of 90% of these masses are within the limits of agreement, therefore the inter-placement agreement of the initial level set contours based on these descriptors is acceptable. Nevertheless, boundary moments should be utilized with caution because they exhibit large percentage differences.

3.5 Conclusion

The results show that the magnitude of the changes in shape –based descriptors expressed as area overlap measures and percentage differences in shape-based features depend on the characteristics of the mass margins and the choice of tuneable parameters. For masses with distinct or well-defined margins, percentage differences are reduced as compared to those with ill-defined, or obscured, margins. The mean percentage differences in boundary moments and their ranges were large as compared to those of shape convexity and shape rectangularity, even though the area overlap measures were within acceptable values. Finally, we concluded that boundary moments are sensitive to the placement of initial level set contours while Fourier descriptors, shape convexity and shape rectangularity exhibit a certain degree of robustness to changes in the location of the initial level set contours. The ultimate goal in active contour segmentation of mass lesion is deriving a segmentation algorithm whose final level set contour is independent of the position of the initial level set contour. In chapter 4 we propose a segmentation method which combines an artificial intelligence algorithm with a region based active contour model (chapter 3) to derive the desired segmentation method.

3.6 References

[1] E. D. Pisano and M. G. Yaffe, "Digital mammography," *Radiology,* vol. 234, no. 2, pp. 353-362, 2005.

[2] V. Balanica, W. D. Rae , M. Caramihai, S. Acho and C. P. Herbst, "Integration of Image and Patient Data, Software and International Coding Systems for Use in a Mammography Research Project," in *World Academy of Science, Engineering and Technology*, 2009.

[3] C. Meyer , C. Herbst, G. Joubert and W. I. Rae, "Assessment of basic soft-copy reporting training on diagnostic accuracy of mammography reporting," in *16th ISRRT World Congress*, Gold Coast, Australia, 2010.

[4] X. Bresson, S. Esedoglu, P. Vandergheynst, J. Thiran and S. Osher, "Global minimizers of the active contour/snake model," *UCLA CAM Report 05-04,* 2005.

[5] B. W. Hong and M. Brady, "A topographic representation for mammogram segmentation," *International Conference on Medical Image Computing and Computer-Assisted Intervention,* pp. 730-737, 2003.

[6] F. Ma, M. Bajger and M. J. Bottema, "Automatic mass segmentation based on adaptive pyramid and sublevel set analysis," in *Proceedings of the Digital Image Computing: Techniques and Applications(DICTA'09) IEEE,* Melbourne, Australia, 2009.

[7] L. Shen, M. R. Rangaraj and J. L. Desautels, "Detection and classification of mammographic calcifications," *International Journal of Pattern Recognition and Artificial Intelligence,* vol. 7, no. 06, pp. 1403-1416, 1993.

[8] L. Shen, R. M. Rangayyan and J. L. Desautels, "Application of shape analysis to mammographic calcifications," *IEEE transactions on medical imaging,* vol. 13, no. 2, pp. 263-274., 1994.

[9] B. Sahiner, H. P. Chan, N. Petrick, M. A. Helvie and I. M. hadjiiski, "Improvement of mammographic mass characterization using spiculation measures and morphological features," *Medical Physics,* vol. 28, no. 7, p. 1455–1465, 2001.

[10] M. Yang, K. Kpalma and J. Ronsin, "A survey of shape feature extraction techniques," *Pattern recognition,* pp. 43-90., 2008.

[11] B. Sahiner, N. Petrick, H. Chan, L. Hadjiiski, C. Paramagui, M. Helvie and M. Gurcan, "Computer-aided characterization of mammographic masses:accuracy of mass segmentation and its effects on characterization," *IEEE Transactions on Medical Imaging,* vol. 20, no. 12, pp. 1275-1284, 2001.

[12] Y. Tao, S.-C. Lo, M. Freedman, E. Makariou and J. Xuan, "Multilevel learning-based segmentation of ill defined and spiculated masses in mammograms," *Medical Physics,* vol. 37, no. 11, pp. 5993-6002, 2010.

[13] S. Xu, H. Liu and E. Song, "Marker- Controlled Watershed for Lesion Segmentation in Mammograms," *Journal of Digital Imaging,* vol. 24, no. 5, pp. 754-763, 2011.

[14] P. Rahmati, A. Adler and G. Hamarneh, "Mammography segmentation with maximum likelihood active contours," *Medical Image Analysis,* vol. 16, no. 6, pp. 1167-1186, 2012.

[15] D. C. Pereira, R. P. Ramos and M. Z. Do Nascimento, "Segmentation and detection of breast cancer in mammograms combining wavelet analysis and genetic algorithm," *Computer methods and programs in biomedicine,* vol. 114, no. 1, pp. 88-101, 2014.

[16] D. G. Altman and J. M. Bland, “Measurement in medicine: the analysis of method comparison studies,” *The statistician*, pp.307-317, 1983.

CHAPTER 4: MASS-SPECIFIC THRESHOLD VALUES OF GLOBAL MINIMA FOR CONVEX ENERGY FUNCTIONALS WITH AN INTERACTIVE SEGMENTATION MODEL

An extract from the work published by the author – Appendix II (S. N. Acho and W. I. D. Rae)

4.1 Introduction

The results of the previous chapter show that the position of the final level set contour delineating the boundary of a mammographic mass is dependent on the placement of the initial level set contour in region based active contour models such as the Chan-Vese (CV) [1] segmentation method and the active contour with selective local or global (GS) iterative method [2]. Consequently, the task of delineating the boundary of a mammographic mass with an active contour segmentation model is challenging and in some cases, can produce unsuitable solutions.

Bresson et al [3] have proposed a fast global minimization model which unifies the geodesics model, Mumford-Shan segmentation model [4] and the Rudin-Osher-Fatemi denoising model [5] and they have extended this approach to link the snake model to the Chan-Vese`s active contour model via the weighted total variation (TV) norm. Bresson et al [3] is relevant because it gives a grief explanation of the origin of the fast global minimization model which is one of the core methods in this chapter. The energy functional of the fast-global minimization model is convex; hence segmentation results are independent of the placements of the initial contours and the curve evolution process does not require the implementation of the contour re-initialization procedures because deformable contours are not expressed as zero level sets of higher dimensional functions. In this chapter the energy functional will be modified in the propose method.

Nguyen et al [6] have combined the probabilistic matrix from the random walker segmentation method with a convex energy functional to derive a robust interactive segmentation model. They modelled the convex energy functional as a linear mixture of Gaussian distributions and expressed the probability matrix as a binary classifier to propagate the contour whenever the statistical models of the foreground and the background are similar. However, in their implementation, the

user fixes the threshold value of the global minimum for the convex energy functional. In mass lesion segmentation, a fixed threshold value for the global minima of a database of mass lesions is not feasible because the grey level intensity distributions of the background tissues surrounding most masses are heterogeneous. A fixed threshold value may underestimate or overestimated the optimum threshold values of these masses and consequently lead to unsuitable segmentation outcomes. Furthermore, hand tuning each threshold value for an optimum mass boundary delineation is time consuming. As a result, we propose an automatic parameter tuning process that embraces the morphological characteristics of each mass lesion, and provides a reliable threshold value. This ensures that, final segmentation outcomes are not only independent of the placement of the initial level set contour, but also are highly reproducible because the optimum threshold value of each mass lesion is independent of the user's input. Our algorithm models the convex energy functional with empirical intensity means and variances of the foreground and the background.

The main contribution of this section lies in extracting reliable information from the probability matrix to provide a reliable mass-dependent estimate of the threshold value for each global minimizer symbolising the intrinsic nature of the mass lesion. It utilises the particle swarm optimization algorithm to provide a mass-specific threshold value of the global minimum for the convex energy functional of each mass in the database of section 3.3.1.

.

4.2 Methods

4.2.1 Active contour model with prior probabilities for binary segmentation

The binary partitioning of the image domain Ω, into Ω_1 and Ω_2 by an evolving curve, C, can be achieved by maximizing the posterior partitioning probability. Assuming that all pixel intensities are independently distributed, and all prior probabilities are equally likely, then the binary partition can be formulated as the minimization of the following energy functional:

$$E(\Omega_1, \Omega_2, p_1, p_2) = -\sum_{i=1}^{2} \int_{\Omega_i} log\left(p_i\big((I(x,y)|\Omega_i)\big)\right) dxdy + \mu length(C) \tag{4.1}$$

where, $I(x\,, y)$ is the value of the grey intensity value at pixel position $(x\,, y)$ in region Ω_i, $p_i\big((I(x,y)|\Omega_i)\big)$ is the likelihood of a pixel $(x\,, y)$ in Ω_i having the value $I(x,y)$ and $\mu > 0$.

Supposed the grey level pixel values, $I(x,y)$, are drawn from a Gaussian distribution and the curve, *C*, is embedded in the level set function, $\phi(x,y)$, such that the regularized Heaviside function, H_ϵ, is the characteristic function separating the foreground and background. Then the optimum partition [7] [8] is obtained by solving the following gradient descent flow

$$\frac{\partial \phi}{\partial t} = H'_\epsilon(\phi)\left[div\left(\frac{\nabla \phi}{|\nabla \phi|}\right) + log(\sigma_2) - log(\sigma_1) + \left(\frac{(I(x,y)-\mu_2)^2}{2\sigma_2^2}\right) - \left(\frac{(I(x,y)-\mu_1)^2}{2\sigma_1^2}\right)\right] \tag{4.2}$$

With $\sigma_i^2$and μ_i the variance and mean of Ω_i respectively.

4.2.2 Convex active contour model with prior probabilities for binary segmentation

With the same approach as in [9], the steady state solution of (2) is given as:

$$\frac{\partial \phi}{\partial t} = div\left(\frac{\nabla \phi}{|\nabla \phi|}\right) + \lambda\left(log(\sigma_2) - log(\sigma_1) + \left(\frac{\big(I(x,y)-\mu_2\big)^2}{2\sigma_2^2}\right) - \left(\frac{\big(I(x,y)-\mu_1\big)^2}{2\sigma_1^2}\right)\right) \tag{4.3}$$

which is the gradient descent flow of the energy functional

$$E(\phi, \sigma_1, \sigma_2, \mu_1, \mu_2) = \int_{\Omega} |\nabla\phi| dxdy + \lambda \int_{\Omega} r(x, y, \sigma_1, \sigma_2, \mu_1, \mu_2)\, \phi dxdy, \tag{4.4}$$

with $(x, y, \sigma_1, \sigma_2, \mu_1, \mu_2) = log(\sigma_2) - log(\sigma_1) + \left(\frac{(I(x,y)-\mu_2)^2}{2\sigma_2^2}\right) - \left(\frac{(I(x,y)-\mu_1)^2}{2\sigma_1^2}\right)$.

$E(\phi, \sigma_1, \sigma_2, \mu_1, \mu_2)$ has a global minimizer [10] when the minimization of Φ is restricted to the interval [0, 1]. Suppose u is a characteristic function of a set, Ω_c, with boundary denoted by C. As in Bression et al [3] , we propose an expression for the energy functional in (4) as

$$E\left(u, \sigma_1, \sigma_2, \mu_1, \mu_2\right) = TV_g(u) + \lambda \int_{\Omega} r\left(x, y, \sigma_1, \sigma_2, \mu_1, \mu_2\right) u\, dxdy, \tag{4.5}$$

where $TV_g(u)$ is the weighted total variation energy and expressed as follows:

$$TV_g(u) = \int_{\Omega} g(x, y)|\nabla u| dxdy \tag{4.6}$$

with $g(x, y)$ as an edge indication function

The relaxed minimization problem for the binary segmentation with the energy functional $E(u, \sigma_1, \sigma_2, \mu_1, \mu_2)$ is expressed as:

$$\min_{0 \le u \le 1} \left\{ \mathrm{TV_g(u)} + \int_{\Omega} \lambda\, \mathrm{r(x, y, \sigma_1, \sigma_2 \mu_1, \mu_2)\, u} + \alpha\, \upsilon\, \mathrm{(u) dxdy,} \right\} \tag{4.7}$$

Where $\alpha > \frac{\lambda}{2}\|r\|_{L\infty(\Omega)}, \upsilon(\xi) = max\{0{,}2|\xi - 0.5| - 1\}$ and λ is a constant. A fast algorithm to solve the relaxed minimization problem with the Chambolle`s dual formulation of the total

variation regularization function [3], [11], is implemented by redefining the unconstrained minimization problem as

$$\min_{u,v}\left\{TV_g(u)+\frac{1}{2\theta}\|u-v\|_{L^2}^2+\int_\Omega \lambda r(x,y,\sigma_1,\sigma_2,\mu_1,\mu_2)\,v+\alpha v(v)\,dxdy\right\} \tag{4.8}$$

with $\theta > 0$ and v a new variable. $TV_g(u)$ is the boundary term and $r(x,y,\sigma_1,\sigma_2\mu_1,\mu_2)$ the global term representing the statistical competition between the regions inside and outside the contour.

The dual formulation of the unconstrained minimization problem is solved by iterating u and v separately. This approach splits the relaxed minimization problem into two problems:

1. Fix v and solve for u in the following minimization equation:

$$\min_u\left\{\int TV_g(u)dxdy+\frac{1}{2\theta}\|u-v\|_{L^2}^2\right\} \tag{4.9}$$

The gradient descent flow is given by:

$$u_t = div\left(\frac{\nabla u}{|\nabla u|}\right)-\frac{u-v}{\theta} \tag{4.10}$$

and it is solved as:

$$u = v-\ \theta.div(\vec{p}) \tag{4.11}$$

with a fixed point method, the update scheme for $\vec{p}$ is:

$$\vec{p}^{\,n+1} = \frac{\vec{p}^{\,n}+\ \Delta t\left(\nabla\left(div(\vec{p}^{\,n})\right)-v/\theta\right)}{1+\ \Delta t\left|\nabla\left(div(\vec{p}^{\,n})\right)-v/\theta\right|} \tag{4.12}$$

while setting $\vec{p}^{\,0} = (0,0)$ and $\Delta t \leq 1/8$ for convergence (Chambolle).

2. Fix u and solve for v in the following minimization equation:

$$\min_{v}\left\{\int_{\Omega} \frac{1}{2\theta}\|u-v\|_{L^2}^2 + \lambda r(x,y,\sigma_1,\sigma_2,\mu_1,\mu_2)\, v + \alpha\upsilon(v)\, dxdy\right\} \tag{4.13}$$

The minimization solution is expressed as:

$$v_t = min\{max(u - \theta\lambda(r(x,y,\sigma_1,\sigma_2,\mu_1,\mu_2),0),1)\} \tag{4.14}$$

Generally, $r(x,y,\sigma_1,\sigma_2,\mu_1,\mu_2)$ is updated after a few iterations and when the algorithm converges the final segmentation solution is obtained by thresholding u. The threshold value is an arbitrary constant restricted to the interval [0, 1] and typically 0.5 as cited by some researchers [12] [3] [6]

4.2.3 Random walk probability matrices

An image is considered as a weighted graph consisting of nodes and edges. Image pixels are denoted as nodes and the similarity between neighbouring nodes associated with an edge is expressed as a Gaussian weighting function representing changes in the grey levels of the pixels which symbolizes the likelihood of a random walker crossing the edge.

Supposed sets of nodes are labelled as belonging to the mass region and non-mass region; then the probability that a random walker starting from an unlabelled node first reaches a labelled node is equivalent to the solution of a Dirichlet problem formulated on a combinatorial graph with boundary constraints provided by the labelled image pixels. Generally, this solution is the random walk probability matrix generated by the random walker as he starts moving from each unlabelled node and first reaches a labelled node of the mass region. This probability matrix is taken as the mass- specific probabilistic map for segmentation tasks. In our implementation, the mass-specific probabilistic map was derived from a smoothed model of the original mass. The weighted TV

scale-space smoothing method [3] [13] was utilized because it removes fine details and preserves important dominant mass boundary characteristics through different degrees of smoothing.

4.2.4 Proposed model of convex active contour driven by global probability distributions and mass- specific probabilistic maps

We define the global term representing the statistical competition between the regions inside and outside the contour as:

$$r(x, y, \sigma_1, \sigma_2, \mu_1, \mu_2, P, \beta) = \beta * r(x, y, \sigma_1, \sigma_2, \mu_1, \mu_2) + (1 - \beta) * \big(1 - 2 * P(x, y)\big) \quad (4.15)$$

Where *P(x, y)* is the mass-specific probabilistic map of the mass, with values within the interval [0 1]. The term $\big(1 - 2 * P(x, y)\big)$ acts as a classifier which influences the direction of propagation of (x, y). In regions where *P(x, y)* equal to 0.5, $u(x, y)$ is propagated with the global probability distribution and the contribution of the classifier to the global term is zero. While for regions with P*(x, y)* > 0.5, $u(x, y)$ expands and favours classification of these regions as mass regions and vice versa. The classifier propagates $u(x, y)$ whenever $r(x, y, \sigma_1, \sigma_2\mu_1, \mu_2) = 0$ whereas β is a positive constant $(0 \leq \beta \leq 1)$ which controls the influence of the classifier on the global term. The proposed unconstrained minimization problem for binary segmentation with the Chambolle`s dual formulation of the total variation regularization function is expressed as:

$$\min_{u,v} \left\{ TV_g(u) + \frac{1}{2\theta} \|u - v\|_{L^2}^2 + \int_\Omega \lambda r(x, y, \sigma_1, \sigma_2, \mu_1, \mu_2, P, \beta)\, v + \alpha v(v)\, dxdy \right\} \quad (4.16)$$

4.2.5 Mass-specific threshold value for the global minimizer of the proposed relaxed minimization problem

We define an optimal threshold level (T_1), as the value of *P(x, y)* that divides the mass-specific probabilistic map, *P(x, y)* into mass region and non-mass region. The optimal threshold value for the global minimizer (T_2) of each mass is expressed as the mean grey level of pixels whose probability of belonging to the mass region is greater than T_1.

Suppose the confidence map, P(x,y) is rescaled to an interval of [0 255] and its histogram is partitioned into two categories with a fitness function $(f(t))$ such as the sum of the variances of the grey level distributions of the foreground and background. The Otsu's nonparametric method [14] of the between-class variance function for a bi-level thresholding is given by:

$$f(t) = \sum_{i=1}^{2} \partial_i \tag{4.17}$$

Where ∂_i is the variance of level i, t is a threshold value and $0 \leq t \leq 255$. The optimal threshold value (T_1) is obtained by maximizing $f(t)$, that is:

$$T_1 = argmax(f(t)) \tag{4.18}$$

We implemented the particle swarm optimization method to solve for T_1. It is a nature inspired global optimization algorithm which uses equations representing the velocities and positions of a group of birds flocking and mimics this social behaviour as a means to search for a global minimum of an objective function [15]. Each particle is a potential solution for the fitness function in the problem space. The particle keeps track of its coordinates in the problem space and updates its solution after iteration with its historical personal best solution and the best solution of the group until particles in the group surround the coordinates with the most optimal solution. This solution represents the best value for the fitness function hence the global minimum. The flow chart proposed method is illustrated in figure 4.1.

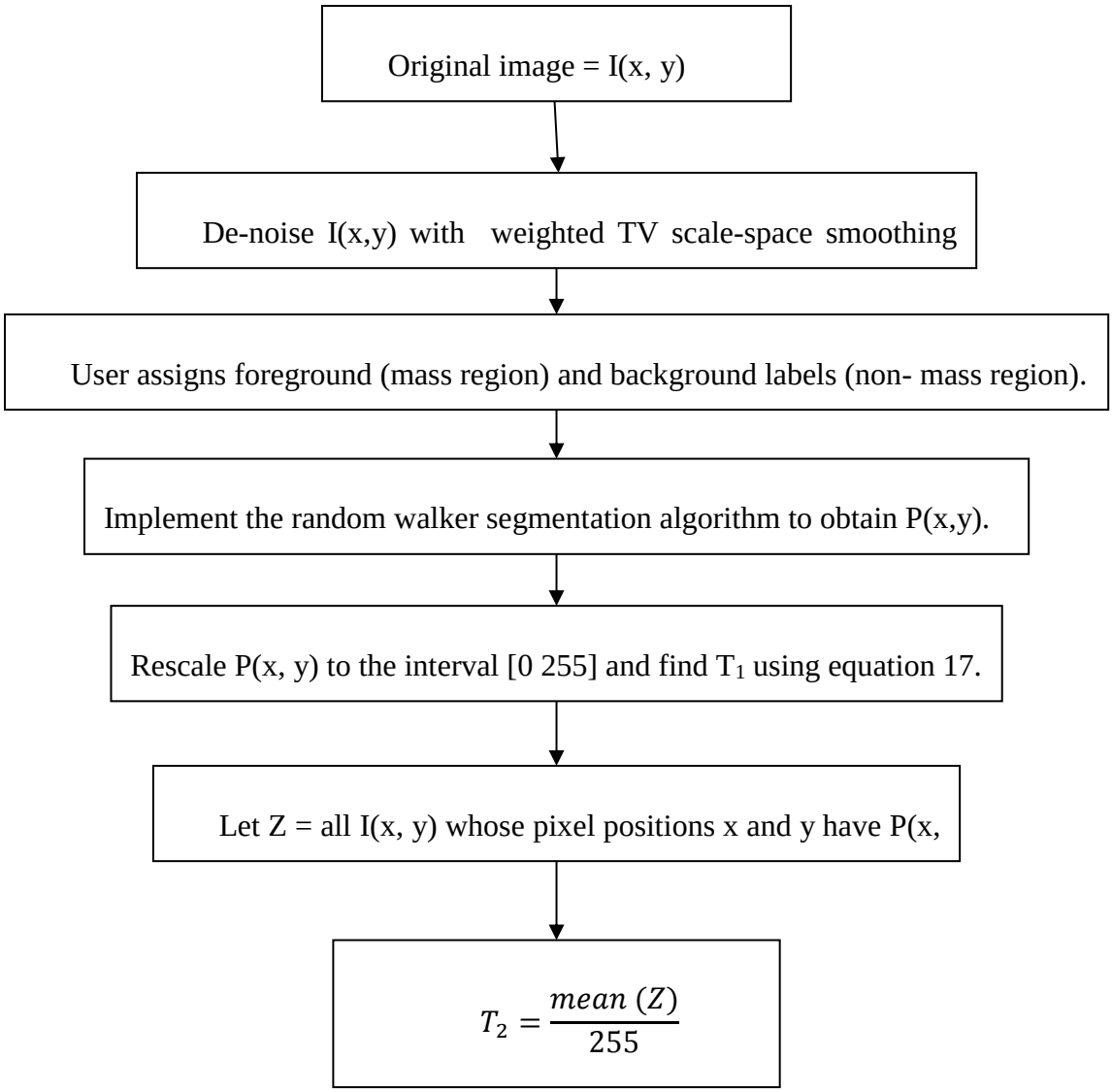

Figure 4.1. The proposed framework for a mass-specific threshold value of a global minimum for a convex energy functional in digital mammography.

4.2.6 Iterative step to implement the proposed segmentation method

The proposed iterative procedure can be summarized as follows:

Step 1: Compute P(x, y) and T_2.

Step 2: Minimize equation 15 using the dual formulation as shown in equation 4.12 and 4.14.

Step 3: Update $r(x, y, \sigma_1, \sigma_2, \mu_1, \mu_2, P, \beta)$ after a few iterations until convergence.

Step 4: Segmentation outcome = $u > T_2$

4.3 Results and Discussion

The performance of the proposed iterative procedure was evaluated on fifty mammograms with mass lesions with default parameters set to $\theta = 1/1.5$, $\lambda = 1$, $\beta = 0.5$ and the time step parameter for the fixed point iteration method was 1/8. The proposed method is compared to segmentation methods of breast mass currently found in literature. These methods have been compared with ground truths hence comparing the proposed method with these cited methods is sufficient

Figure 4.2 shows the differences in global minima with a typical threshold value of 0.5 and the mass-specific threshold values from the proposed iterative method. The highlighted focal region of the mass lesion is represented with higher probability values of being classified as a mass region than other regions in the image domain. Therefore, the threshold value for binary segmentation of the probability matrix of a mass lesion can be considered as a realistic estimate of the mass-specific threshold value for the global minimizer of its convex energy functional.

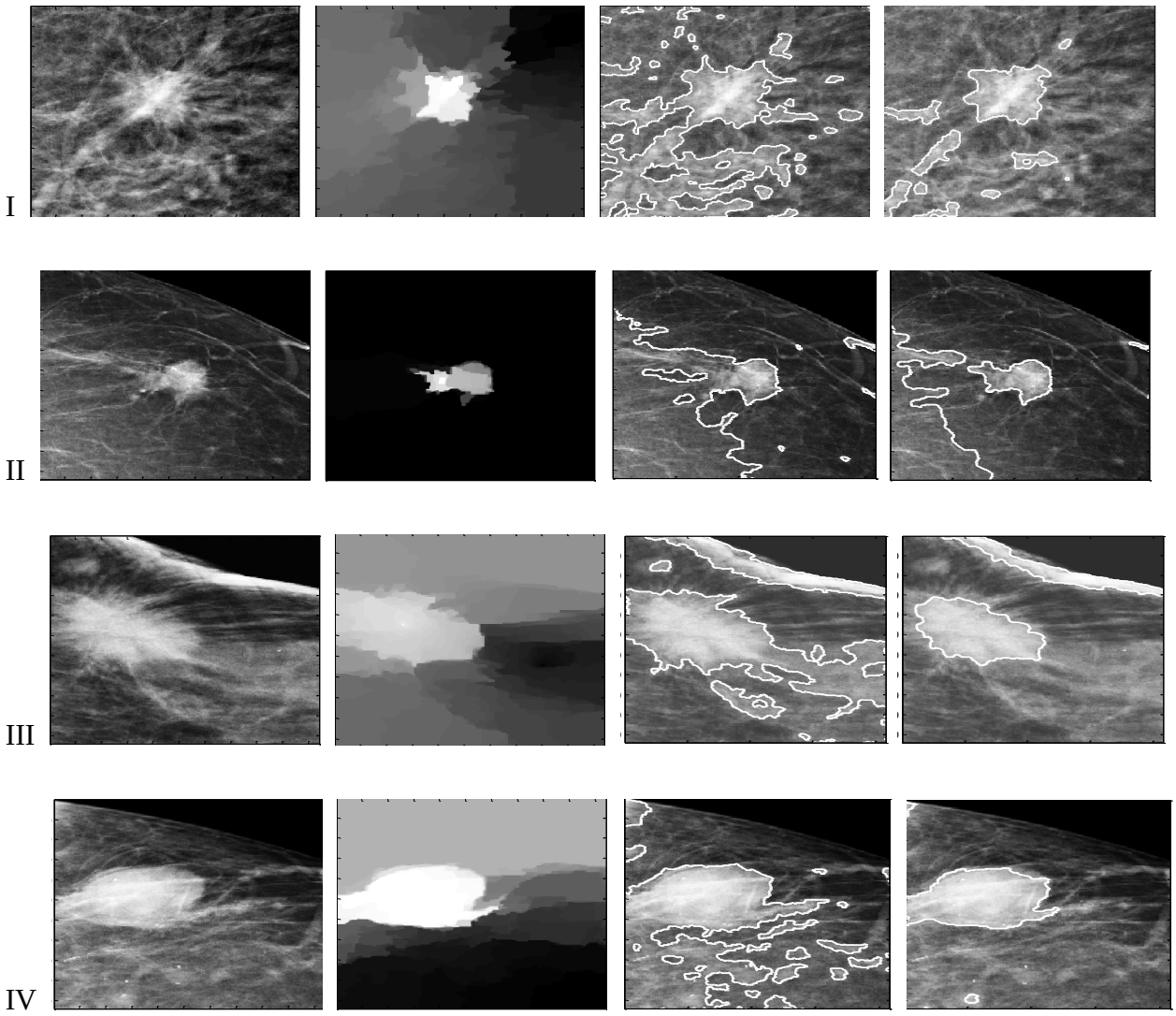

Figure 4.2. Differences in global minimizers with the typical threshold value of 0.5 and mass-specific threshold values from the proposed iterative method. (a) Original mass lesions (b) confidence maps from the random walk method (c) the global minimizer with threshold values 0.5 and (d) global minimizers from the proposed iterative method.

I.

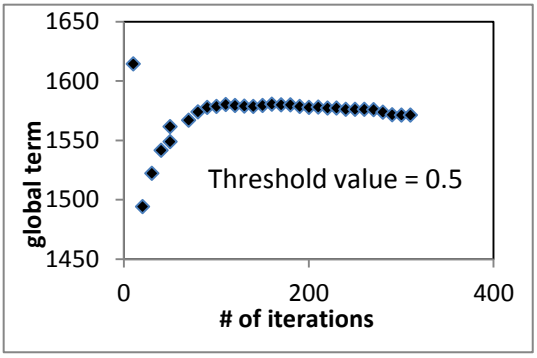

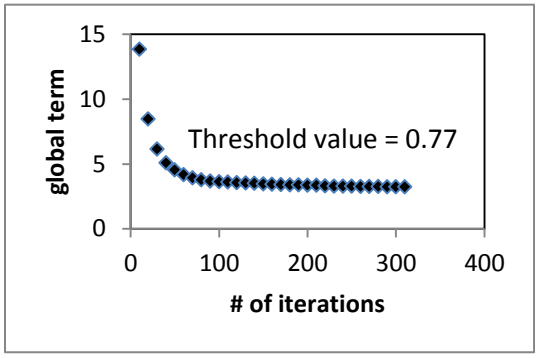

II.

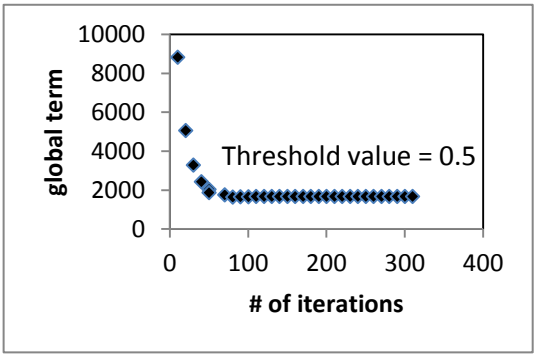

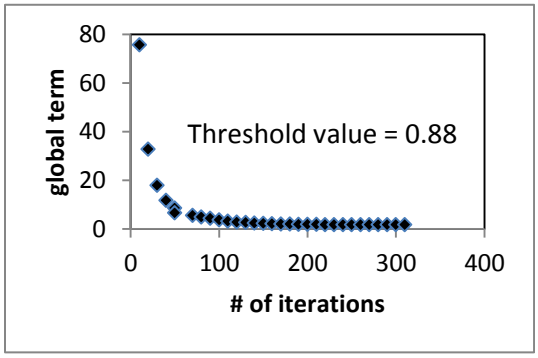

III.

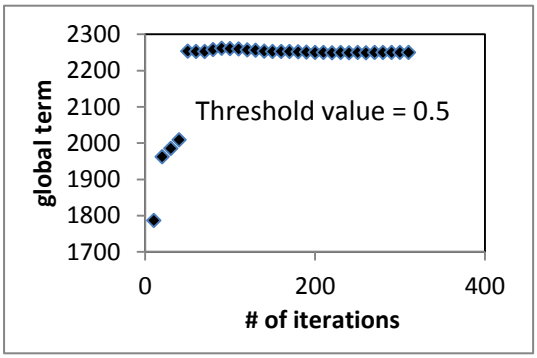

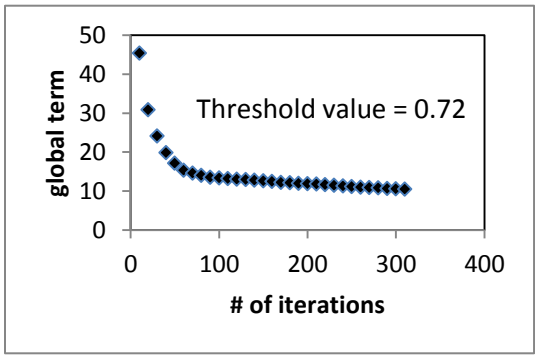

IV

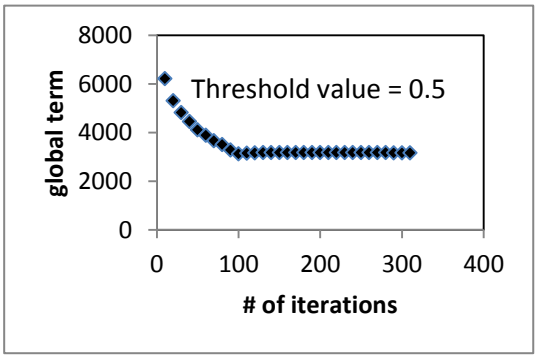

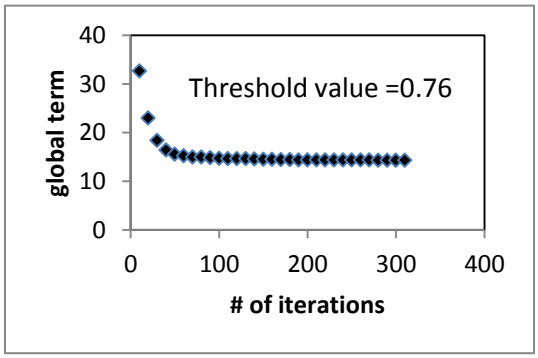

Figure 4.3. Variation of the global term $(r(x, y, \sigma_1, \sigma_2, \mu_1, \mu_2, P, \beta)$ with the number of iterations for mass lesions in Fig2 for a typical threshold value of 0.5 and for threshold values derived from the proposed method.

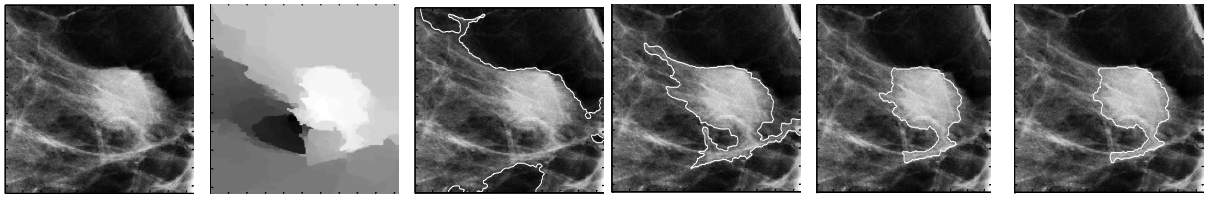

(a) (b) (c) (d) (e) (f)

Figure.4.4. Sensitivity of segmentation results to the threshold value, T_2 (a) Original mass (b) Probability map of the mass (c) segmentation result with $T_2 = 0.5$ (d) segmentation result with $T_2 = 0.6$ (e) segmentation result with our proposed method ($T_2 = 0.67$) (f) segmentation result with $T_2 = 0.8$

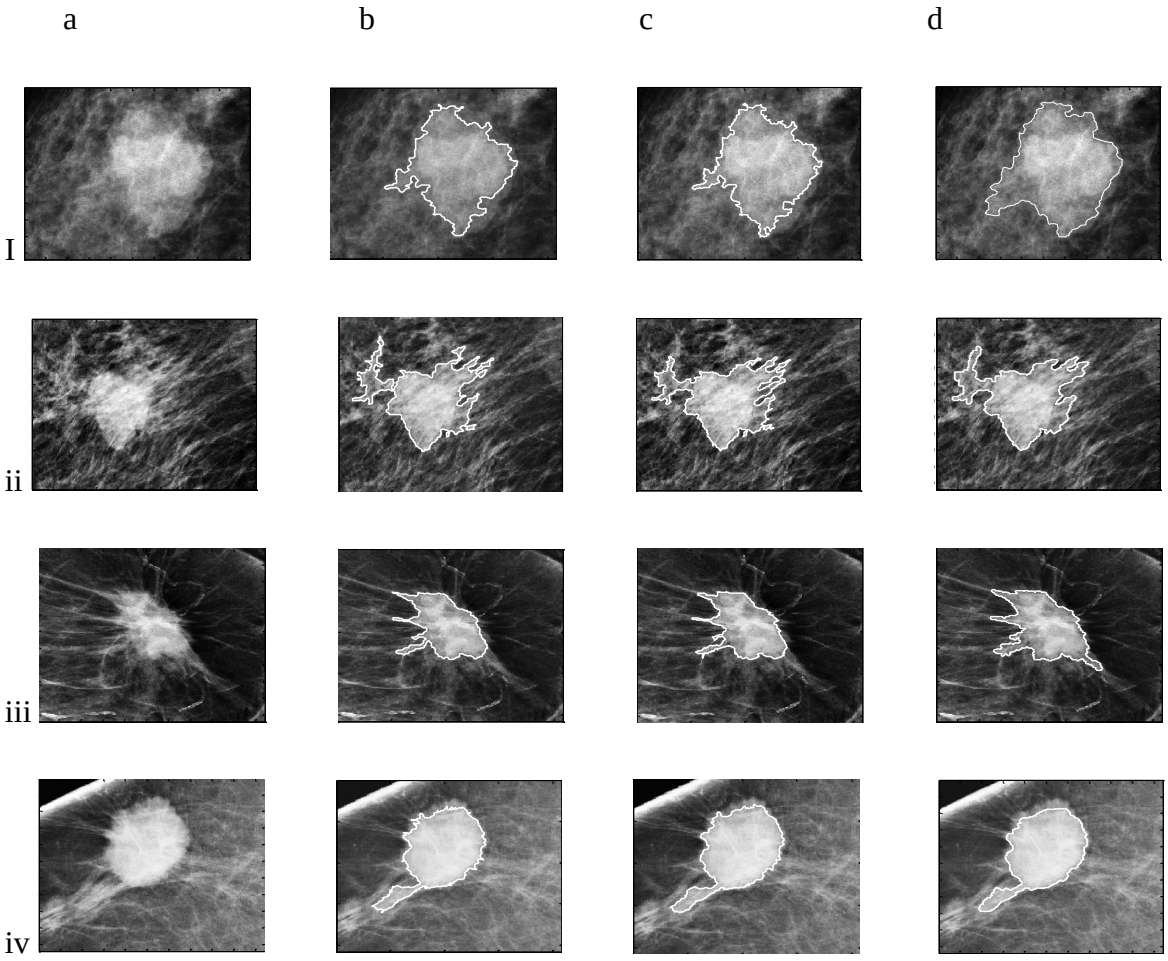

Figure 4.5. Comparison of the proposed method with other segmentation schemes. (a) original images (b)segmentation results with the GS model (c) segmentation results with the CV model (d)segmentation result with the proposed method

The global term, $r(x, y, \sigma_1, \sigma_2, \mu_1, \mu_2, P, \beta)$ converges with near zero values as illustrated in Figure 4.3. When T_2 is a good estimate for the global minimum, $r(x, y, \sigma_1, \sigma_2, \mu_1, \mu_2, P, \beta)$ decreases rapidly as the number of iterations increases and finally remains stable on a near zero value. As shown in Figure 4.4, T_2 may not be the only threshold value for a reliable segmentation outcome for a given mass, but in most instances our proposed method provides the required minimum threshold value for the global minimizer. For this database, the mean value for T_2 was 0.67 ± 0.09 with a minimum value of 0.4 and a maximum value of 0.8.

Figure 4.5 compares the segmentation performance of the proposed method (PM), the classical Chan-Vese model (CV) and the active contour with selective local or global segmentation model (GS) on direct digital mammograms. Figures 4.5 (i) and (iii) show that the proposed method achieved similar segmentation performance as the CV and GS models except in regions with slowly varying pixel intensity values, whereas the proposed method slightly under - segments. We quantified the differences between segmented areas with the Jaccard index (JI) and estimate, the agreement between the shape-based descriptors of segmented areas with the Euclidean distance (EDFD) between their Fourier descriptors, given that, they have been cited as the best performing shape-based descriptor for binary classification of mammographic masses. The shape of each segmented area was indexed with sixty Fourier descriptors.

Table 4.1. Quantitative evaluation of the performance of proposed method with different segmentation models

	Mean values of the JIs	Mean values of the EDFDs
PM/CV	0.89 ± 0.07	0.05 ±0.03
PM/GS	0.88 ± 0.06	0.06 ±0.04
CV/GS	0.95 ± 0.04	0.04 ± 0.03

The mean value of JIs and EDFDs for the database of masses in this study are listed in Table 4.1. The proposed method achieved similar segmentation results as the CV and GS model on the size and shape of the segmented areas. Rahmati et al [16] reported a mean value for Jaccard indices of 0.87 between their segmentation algorithm and expert radiologists, while Hao et al [17] reported mean values less than 0.85 for their proposed method and other segmentation methods. The mean values for the proposed method are higher than the values reported by these researchers, but it should be noted that their database of masses was larger than the database for this study. The distributions of the JIs and EDFDs for each pair of segmentation models were investigated with boxplots, as shown in Figures 4.6 and 4.7 respectively. Less than 7% of the Jaccard indices and EDFDs were classified as outliers for each pair of segmentation schemes. The EDFDs show that shapes of the segmented areas from the proposed method are similar to those of the CV and GS model, although the GS model presented more outliers than the others. These segmentation algorithms were implemented in Matlab R2013a on an Intel Core 2 Duo 3.0 GHz processor. The average processing time for the proposed method was 14 ± 2.5s as compared to the CV and GS models, which were 10± 1.5 s and 8± 2.1s respectively

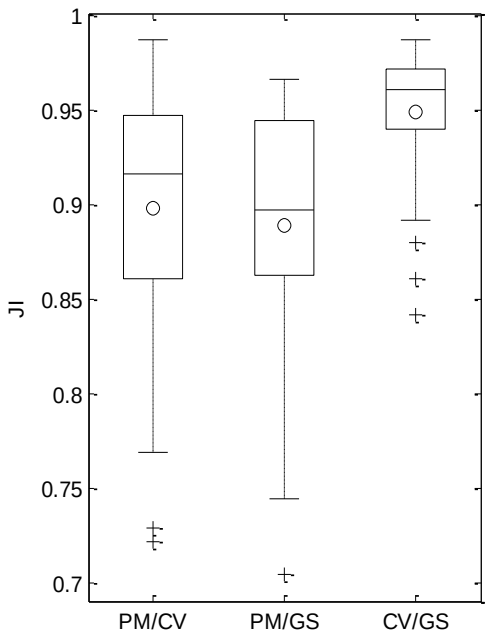

Figure 4.6..Boxplots illustrating the distribution of JIs with paired segmentation schemes. The central lines and the circles are the median and mean values of the JIs respectively. The edges of the box represent the 25th and 75th percentile, the end of the whiskers extreme values and the crosses are the outliers.

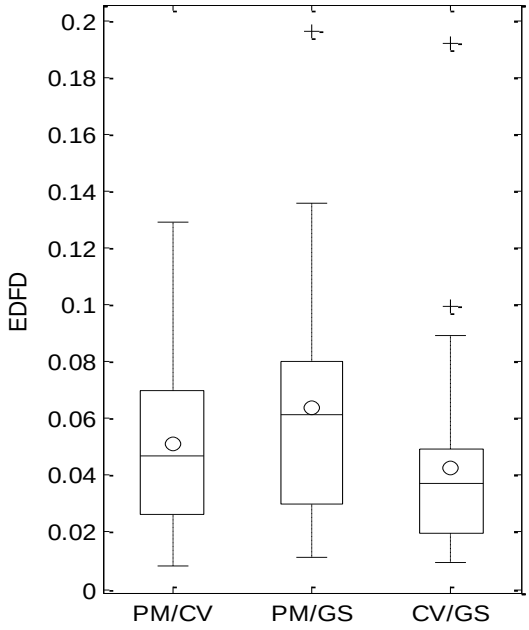

Figure 4.7. Boxplots illustrating the distribution of EDFDs with paired segmentation schemes. The central lines and the circles are the median and mean values of the EDFDs respectively. The

edges of the box represent the 25th and 75th percentile, the end of the whiskers extreme values and the crosses are the outliers.

The proposed method combines the random walker algorithm and particle swarm optimization to search for a reliable estimate of a mass-specific threshold value for the global minimum, therefore factors influencing any of the above-mentioned algorithms may compromise the segmentation accuracy of the proposed method. The particle swarm optimization method is prone to premature

convergence to a local minimum. Consequently, this step can be avoided if T_1, is set to a value representing the mean pixels in the focal region of the probability map. We set $T_1 = 0.7$ for our database and more than 80% of the masses produced reasonable segmentation results with the derived T_2 values.

4.4 Conclusion

The proposed approach searches a mass-specific threshold value for the global minimization of the convex energy functional that is representative of the mean pixel values of the highlighted focal region of the mass. This method is efficient in producing segmentation results that are similar to other segmentation methods and more importantly; it avoids the problems encountered by most active contour segmentation models (Figure 4.5) which are the placement of the initial contours, contour re-initialization and contour leakage due to a weak boundary. A minimum level of intervention by the user is required; therefore, this method can improve the statistical significance of the variability associated with delineation of the mass boundary. The placement of the initial level set contour is not influence by the user.

4.5 References

[1] T. F. Chan and L. A. Vese, "Active contour without edges," *IEEE Transaction on ImageProcessing*, vol. 10, no. 2, pp. 266-277, 2001.

[2] K. Zhang, L. Zhang, H. Song and W. Zhou, "Active contours with selective local or global segmentation: a new formulation and level set method," *Image and Vision computing*, vol. 28, no. 4, pp. 668-676, 2010.

[3] X. Bresson, S. Esedoglu, P. Vandergheynst, J. P. Thiran and S. Osher, "Global minimizers of the active contour/snake model," *UCLA CAM Report 05-04*, 2005.

[4] D. Mumford and J. Shah, "Optimal approximations by piecewise smooth functions and associated variational problems," *Communications on Pure and Applied Mathematics*, vol. 42, no. 5, pp. 577-685, 1989.

[5] L. Rudin, S. Osher and E. Fatemi, "Nonlinear Total Variational Based noise removel algorithms," *Physica D*, vol. 60, pp. 259-268, 1992.

[6] A. N. Nguyen , J. Cai, J. Zhang and J. Zheng, "Robust Interactive Image Segmentation Using Convex Active Contours," *IEEE Transactions on Image Processing* , vol. 21, no. 8, pp. 3734-3743, 2012.

[7] T. Brox, M. Rousson, R. Deriche and J. Weickert, "Colour,textur and motion in level set based segmentation and tracking," *Image and Vision Computing*, vol. 28, pp. 376-390, 2010.

[8] D. Cremers, M. Rousson and R. Deriche, "A review of statistical approaches to level set segmentation: integrating color, texture, motion and shape," *Int.J. Comput.Vis.*, vol. 72, no. 2, pp. 195-215, 2007.

[9] T. F. Chan, S. Esedoglu and M. Nikolova, "Algorithms for finding global minimizers of image segmentation and denoising models.,"*SIAM journal on applied mathematics* vol. 66, no. 5, pp. 1632-1648, 2006.

[10] G. Strang, "Maximal Flow Through a Domain," *Math. Programming,* vol. 26, no. 2, pp.123-143, 1983.

[11] A. Chambolle, "An algorithm for variation minimization and applications," *Journal ofMathematical Imaging and Vision* , vol. 20,no. 1-2, pp. 89-97, 2004.

[12] J. C. Moreno, S. V. Prasath, H. Proenca and K. Palaniappan, "Fast and globally convex multiphase active contours for brain MRI srgmentation," *Computer Vision and Image Understanding,* vol. 125, pp. 237-250, 2014.

[13] D. Strong and T. Chan, "Spatially and adaptive total variational based regularization and anisotropic diffusion in image processing," *UCLA CAM Report,* pp. 96-46, 2004.

[14] N. Otsu, "A threshold selection method from gray-level histograms," *IEEE Transactions on Systems, Man, and Cybernetics,* vol. 9, no. 1, pp. 919-926, 1979.

[15] J. Kennedy and R. Eberhart, "Particle swarm optimization," *Proceedings of the IEEE International Conference on Neural Networks,* vol. 4, pp. 1942-1948, 1995.

[16] P. Rahmati, A. Adler and G. Hamarneh, "Mammography segmentation with maximum likelihood active contours," *Medical Image Analysis,* vol. 16, no. 6, pp. 1167-1186, 2012.

[17] X. Hao, Y. Shen and S. R Xia, "Automatic mass segmentation on mammograms combining random walks and active contour," *Journal of Zhejiang University Science C,* vol. 13, no. 9,pp. 635-648, 2012.

CHAPTER 5: MAMMOGRAPHIC MASS CHARACTERIZATION FOR TUMOUR MODELLING AND TUMOUR GRADING

5.1. Introduction

Texture has been defined as 'the pattern of spatial distribution of grey tone' [1] and major texture regions in an image can be delineated with segmentation algorithms. In mammography, the texture composition of a mammographic mass differs from that of the surrounding breast tissue. For this reason, the segmentation procedure of a mammographic mass involves the process of extracting the boundary between two major texture regions of the mammogram; the mammographic mass region and the surrounding breast tissue. Texture analysis represents a set of mathematical models and procedures developed to characterise the variation of spatial distribution of grey levels (signal strength related to object density) for feature extraction. Feature extraction methods therefore consist of a set of mathematical algorithms to compute the characteristics (features) of an image which numerically describes its texture properties. These features are usually grouped as feature vectors for segmentation and classification purposes in image analysis, depending on the similarity criterion which specifies the quantitative measure of a certain texture feature.

Radiologists can detect abnormal regions in mammograms because these regions exhibit obvious or subtle changes in appearance (grey tone) from surrounding tissues, which consequently translate to changes in texture. The BIRADS (Breast Imaging Reporting and Data System) [2] lexicon describing the appearance of a mammographic mass uses density, shape and margin. These features provide 80-85% of the diagnostic information relating to the degree of malignancy of a mammographic mass. Therefore, mathematical models utilising texture and shape analysis techniques can be implemented effectively in mammographic mass analysis. Numerous methods have been proposed in the literature for quantification and classification of texture in mammographic masses [3], [4], [5], [6]. However, since these methods are many and varied, but are still effective, one can conclude that a particular choice of method or combination of methods

will greatly depend on the following: understanding the mathematical basis of the method, ease of implementation and use, reported performance and possibly popularity in the literature (which would indicate widespread acceptance of the method). Texture analysis is the core of any Computer Aided Diagnosis (CAD) system in mammography [7], [8]. These systems utilize mathematically based texture features characterizing mammographic masses as input feature vectors to distinguish between benign and malignant lesions in a machine learning classifier algorithm. In contrast to all previous works in CAD systems in mammography, our approach characterizes and investigates the differences in statistical patterns of the intensity distribution of the pixels (texture features) from the surrounding tissue to the core of the mass as the clinical traits of the mass develop. In clinical projection mammography the mass overlaps surrounding normal tissues, so it is anticipated that there is a gradual transition from the centre of the mass in the mammographic image where the mass predominates, to the periphery of the mass in the mammographic image, where the normal tissue will dominate.

A mammographic mass or tumour can be benign or malignant. If a tumour is suspected to be malignant [9] all or part of it is removed. The cells and tissues are examined under a microscope by a pathologist to determine the tumour's grade and other characteristics. The tumour is graded as (a) Grade 1: tumour cells are well-differentiated, that is, the tumour cells look like normal tissue and are slow growing. (b) Grade 2: moderately –differentiated that is they fall between grade 1 and grade 3. (c) Grade 3; poorly –differentiated, that is, the tumour cells look very abnormal and are fast growing. The organization of these tumour cells within the mass maybe reflected in the computed texture features and may also depend on the grade of the tumour. To the best of our knowledge, tumour grading [9] has not been incorporated in the mammography CAD systems.

Hence, the aim of this section of the thesis is to assess the texture features of mammographic masses in relationship to tumour modelling which is a new concept in texture analysis and tumour grading. Wherein, tumour modelling characterises the variation of texture features from the cores of biopsy-proven malignant mammographic masses to their peripheries while tumour grading verifies the existence of texture features that can differentiate biopsy-proven grade 2 from grade 3 masses.

5.2. Statistical methods for texture analysis

Statistical methods for quantification and classification of texture in mammography are based on the random spatial distribution of the grey values in mammograms with or without taking into consideration spatial information of the pixels in relation to other pixels. In some cases, each pixel is assigned a value corresponding to a specific local feature which is often derived from the spatial distribution of grey values within a local window, centred on the pixel of interest. Some of these methods are described in the following sections.

5.2.1. First order statistical features from the histogram of image intensities [10], [11].

Suppose a random variable, i, represents the grey level intensity of a region of interest (ROI) of an image, I, such that $I(x,y) = i$, where (x,y) represents the pixel position. Then, the probability density of occurrence of grey level intensity, i, within the ROI is given as:

$$h(i) = \frac{number\ of\ pixels\ with\ gray\ level,\ i,\ within\ a\ ROI}{total\ number\ of\ pixels\ in\ the\ \ ROI(N)} \qquad (5.1)$$

Let G be the total number of intensity levels in the image, then, the descriptive metrics of the spatial distribution of the grey values in the ROI are defined as:

$$mean = \mu = \sum_{i=0}^{G-1} ih(i) \qquad (5.2)$$

$$variance = \sigma^2 = \sum_{i=0}^{G-1} (i-\mu)^2 h(i) \qquad (5.3)$$

$$skewness = \mu_3 = \sigma^{-3} \sum_{i=0}^{G-1} (i-\mu)^3\, h(i) \qquad (5.4)$$

$$kurtosis = \mu_4 = \sigma^{-4} \sum_{i=0}^{G-1} [(i-\mu)^4 h(i)] - 3 \qquad (5.5)$$

$$uniformity = E = \sum_{i=0}^{G-1} [h(i)]^2 \tag{5.6}$$

$$entropy = H = -\sum_{i=0}^{G-1} h(i) \log_2 [h(i)] \tag{5.7}$$

The sliding window algorithm is implemented for the assessment of these features. These statistical features are independent of the relative positions of the various grey level intensities within the region. The variance is a measure of deviation of the grey level intensity from the mean value, the skewness is a measure of the degree of the histogram asymmetry about the mean, the kurtosis is a measure of how peaked the histogram of the distribution is (or the flatness of the histogram of ROI) and the entropy measures the uniformity of the histogram.

5.2.2. Second order statistical features

Second order statistical features [12], [13], [14] are derived from the probability of observing a specific pair of pixel values, or grey level intensities (i, j), in an image, separated by a distance, d, along a given direction, θ. The co-occurrence matrix is a measure of the probability of co-occurrence of pairs of pixel values. It becomes the probability distribution function for the derivation of second order statistical features with parameters, d and θ. Generally, the orientation, θ, is quantized into four directions of angular degree, $0^0, 45^0, 90^0$ and 135^0, however when $d = 0$, the second order statistics become first order statistics. For a given image, I, where $I(x_1, y_1)$ is the grey value of pixel position (x_1, y_1); $I(x_2, y_2)$ is the grey value of another pixel at a distance d from pixel position(x_1, y_1) with direction θ, such that $x_2 - x_1 = d|cos\theta|$ and $y_2 - y_1 = d|sin\theta|$, then the co-occurrence matrix, $P(i, j) = \{|(x_1, y_1), (x_2, y_2)|\, I(x_1, y_1) = i\, , I(x_2, y_2) = j\}$.

From the co-occurrence matrix, $P(i, j)$, the following second order statistical features [15] are computed:

$$Energy = \sum_{i=0}^{G-1}\sum_{j=0}^{G-1} P(i,j)^2 \quad 5.8$$

$$Entropy = \sum_{i=0}^{G-1}\sum_{j=0}^{G-1} P(i,j)\log_2 P(i,j) \quad 5.9$$

$$Contrast = \frac{1}{(G-1)^2}\sum_{i=0}^{G-1}\sum_{j=0}^{G-1}(i-j)^2 P(i,j) \quad 5.10$$

$$Correlation = \frac{1}{\sigma_x \sigma_y}\sum_{i=0}^{G-1}\sum_{j=0}^{G-1} ijP(i,j) - \mu_x \mu_y \quad 5.11$$

where,

$$\mu_x = \sum_{i=0}^{G-1} i \sum_{j=0}^{G-1} P(i,j) \quad 5.12$$

$$\mu_y = \sum_{j=0}^{G-1} j \sum_{i=0}^{G-1} P(i,j) \quad 5.13$$

$$\sigma_x = \sum_{i=0}^{G-1}(i-\mu_x)^2 \sum_{j=0}^{G-1} P(i,j) \quad 5.14$$

$$\sigma_y = \sum_{j=0}^{G-1}(j-\mu_x)^2 \sum_{i=0}^{G-1} P(i,j) \quad 5.15$$

$$Dissimilarity = \sum_{i=0}^{G-1}\sum_{j=0}^{G-1} |i-j|P(i,j) \quad 5.16$$

$$Homogeneity = \sum_{i=0}^{G-1}\sum_{j=0}^{G-1} \frac{P(i,j)}{1+|i-j|} \quad 5.17$$

$$sum\ of\ squares\ variance = \frac{1}{2}\sum_{i=0}^{G-1}\sum_{j=0}^{G-1}(i-\mu_x)^2 P(i,j) + \left(i-\mu_y\right)^2 P(i,j) \quad 5.18$$

$$sum\ of\ average = \frac{1}{2}\sum_{i=0}^{G-1}\sum_{j=0}^{G-1} iP(i,j) + j\ P(i,j) \quad 5.19$$

Suppose

$$P_x(i) = \sum_{j=0}^{G-1} P(i,j) \quad 5.20$$

$$P_y\,(j) = \sum_{i=0}^{G-1} P(i,j) \quad 5.21$$

$$P_{x+y}(k) = \sum_{i=0}^{G-1}\sum_{j=0}^{G-1} P(i,j) \qquad , \qquad i+j=k \quad 5.22$$

for k $= 0, 1, 2 \ldots\ldots\ldots 2(\mathrm{G}-1),$ 5.23

$$P_{x-y}(k) = \sum_{i=0}^{G-1}\sum_{j=0}^{G-1} P(i,j) \qquad , \qquad |i-j|=k \quad 5.24$$

for k $= 0,1, \ldots\ldots\ldots\ldots\ldots\ldots \mathrm{G}-1,$

then

$$sum\ entropy = -\sum_{i=0}^{2G-2} P_{x+y}(i) \log P_{x+y}(i) \quad 5.25$$

$$Difference\ entropy = -\sum_{i=0}^{G-1} P_{x-y}(i) \log P_{x-y}(i) \quad 5.26$$

$$Difference\ \ variance = \sum_{i=0}^{G-1} \left[\left(i - \sum_{i=0}^{G-1} \left[i P_{x-y}(i) \right] \right)^2 P_{x-y}(i) \right] \quad 5.27$$

Table 5.1 gives a brief description of some of these local texture features.

Table 5.1: A selection of some second order statistical texture features and their meaning

Texture features	**Meaning**
Energy	Measures the smoothness of the image.
Entropy	Measures the amount of randomness of the entries in the co-occurrence matrix, generally homogenous images have low entropy
Correlation	Measures the linear dependency of grey levels on those of neighbouring pixels
Contrast	Measures the similarity of pixel pairs
Variance	Measures the spread in pixel intensities
Sum average	Average of pixel intensities
Homogeneity	Measures the uniformity of the image
Dissimilarity	Dissimilarity feature is highly correlated to the variance of the entries in the co-occurrence matrix.

5.2.3. Run length grey–level statistics [16]

Texture features representing continuous patterns of image intensity in specific directions can be extracted from the run-length matrix of an image. The run length defined as the number of pixels of a given grey value in a sequence in a given direction, hence, the $(i,j)^{th}$ entry of the run-length matrix $p(i,j)$ for a specific direction is defined as the number of runs with pixels grey level, i, and run length, j. Suppose N_r is the number of different run lengths and P is the total number of pixels in the image, then the following texture features can be derived from the run-length statistics:

$$short\ run\ emphasis(SRE) = \frac{\sum_{i=0}^{G-1}\sum_{j=1}^{N_r} p(i,j)/j^2}{\sum_{i=0}^{G-1}\sum_{j=1}^{N_r} p(i,j)} \quad 5.28$$

$$long\ runs\ emphasis(LRE) = \frac{\sum_{i=0}^{G-1}\sum_{j=1}^{N_r} j^2 p(i,j)}{\sum_{i=0}^{G-1}\sum_{j=1}^{N_r} p(i,j)} \quad 5.29$$

$$grey\ level\ non-uniformity\ (GLN) = \frac{\sum_{i=0}^{G-1}\left[\sum_{j=1}^{N_r} p(i,j)\right]^2}{\sum_{i=0}^{G-1}\sum_{j=1}^{N_r} p(i,j)} \quad 5.30$$

$$Run\ length\ non-uniformity(RLN) = \frac{\sum_{j=1}^{N_r}\left[\sum_{i=0}^{G-1} p(i,j)\right]^2}{\sum_{i=0}^{G-1}\sum_{i=1}^{N_r} p(i,j)} \quad 5.31$$

$$Run\ percentage(RP) = \frac{\sum_{i=0}^{G-1}\sum_{j=1}^{N_r} p(i,j)}{P} \quad 5.32$$

$$low\ Grey-level\ Run\ Emphasis(LGRE) = \frac{\sum_{i=0}^{G-1}\sum_{j=1}^{N_r} p(i,j)/i^2}{\sum_{i=0}^{G-1}\sum_{j=1}^{N_r} p(i,j)} \quad 5.33$$

$$high\ Grey-Level\ Run\ Empasis(HGRE) = \frac{\sum_{i=0}^{G-1}\sum_{j=1}^{N_r} i^2 p(i,j)}{\sum_{i=0}^{G-1}\sum_{j=1}^{N_r} p(i,j)} \quad 5.34$$

Standard mammography is plagued by overlapping tissues whereby breast structures will project on each other on a mammogram, creating the appearance of random variation in pixel values or

texture primitive within the mass region and surrounding breast tissue. As a result, texture features are non- directional, hence each run length feature is expressed as the average value evaluated in the directions; 0^0, 45^0, 90^0 and 135^0. These features capture the coarseness, homogeneity and uniformity of a region of interest. For example, homogeneous images exhibit high long-run emphasis, low grey-level non-uniformity and low run percentage. The run length histogram will be considered as a texture feature for tumour modelling. Table 5.2 gives a brief description of the features captured by the different run length variables.

Table 5.2: Run length texture features and description.

Texture feature	**Description**
Short Run emphasis	Measures the occurrence of short runs
Long Run Emphasis	Measures the occurrence of long runs
Low Grey Level Run Emphasis	Measures the distribution of pixels weighted towards low intensity
High Grey level Run emphasis	Measures the distribution of pixels weighted towards high intensity
Short Run Low Grey level emphasis	Measures the occurrence of short runs weighted towards low intensity
Long Run Low Grey level emphasis	Measures the occurrence of long runs weighted towards low intensity
Short run high Grey level emphasis	Measures the occurrence of short runs weighted towards high intensity
Long run high Grey level emphasis	Measures the occurrence of long runs weighted towards high intensity
Run Grey level non-uniformity	Measures the similarity of pixel intensities
Run length non- uniformity	Measures the similarity of lengths of pixel
Run percentage	Measures the overall homogeneity of the histogram. This value is maximal, when all runs are of unity length irrespective of the gray level

5.3. Structure and characteristics of mammographic masses in standard mammography

Mammographic masses have highlighted focal regions [17] also known as cores, with dimmer concentric layers radiating outwards with diversified clinical indicators. These masses present varying statistical patterns from the core to the periphery as the clinical traits of the mass develops. Malignant masses normally infiltrate the surrounding breast tissue [2] hence they exhibit ill-defined boundaries with rough contour, spiculations, concavities and micro-lobulations while benign masses are homogenous with well-defined edges and in most cases they possess smooth, round or oval shapes with macro-lobulations as shown in Figure 5.1 and Table 5.3 respectively. In two dimensional standard mammography some of these features are intertwined with features from normal tissues which surround the masses because projection imaging gives rise to partial overlap of different tissues and structures of the breast anatomy.

Summary of typical mass characteristics

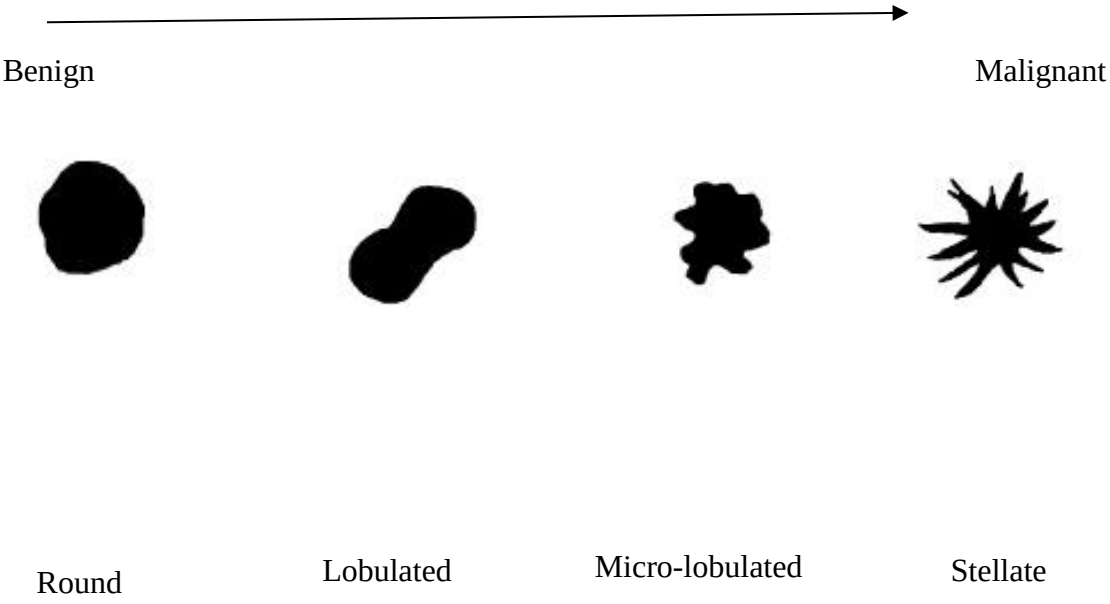

Figure 5.1: Morphological Shape type description of mammographic masses [20]

Table 5.3: Margin descriptive features [20]

Margin	Likely Benign	Suspicious	Highly Suspicious of Malignancy
Well-defined	X		
Obscured/75% hidden or more		X	
Micro-lobulated		X	
Indistinct and ill-defined		X	X
Spiculated			X

Local features are encoded in the statistical patterns of sub-regions of a mass and the spatial pattern distribution of these local features reveal clues on the clinical diagnosis of a mass. For this reason, the problem of classifying or determining the characteristics of a mass can be expressed as a problem of natural scene classification in which cues from different contextual regions of interest, are integrated to build a holistic global representation of the mass region to improve classification performance [18]. Many approaches have been considered, such as a pair of contextual regions of interest, namely: the core region and the margin. Peripheral diagnostic information of the mass is extracted from the margin [19] and it is generally represented as a narrow band or a ribbon of pixels surrounding the edge of the mass. The ribbon of pixels is obtained by morphological dilation of the contour depicting the edge of the mass with a circular structuring element of a specified number of pixels.

5.3.1. Mathematical expression of the binary contextual regions of interest model[18]

Consider a mass of mean radius, R. Suppose L_0 is a binary mask of the mass and D is a disk structuring element with radius αR, where $\alpha < 1$. Let the dilation of L_0 be given as $L_1 = L_0 \oplus D$ and the erosion as $L_2 = L_0 \ominus D$, then the margin is expressed as, $M = (L_1 - L_2)\text{x}\, Mass$. The rest of the mass $= L_2 * mass$. Figure 5.2 gives an example of a binary contextual region of mass.

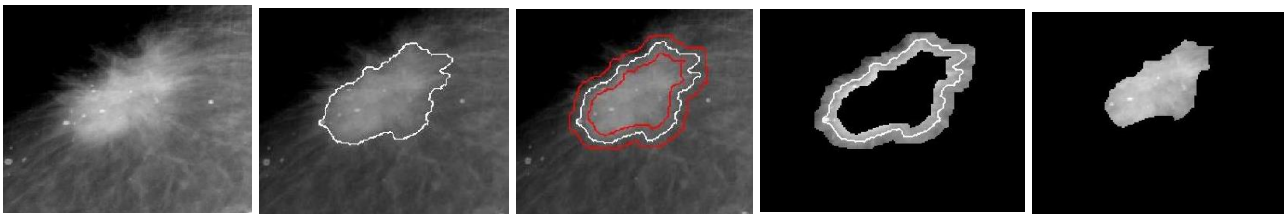

(a) (b) (c) (d) (e)

Figure: 5.2. Example of a binary contextual ROI. (a) Original mass (b) Delineated mass with boundary (c) boundary with the dilation and erosion shown in red, (d) Mass margin (M), (e) The rest of the mass

`

5.4 Aim

The aim of this chapter is to assess the variation of texture features from the cores of biopsy-proven malignant mammographic masses to their peripheries and to verify the existence of texture features that can differentiate biopsy-proven grade 2 from grade 3 masses.

5.5. Methods

The database is described and the set procedures required for tumour modelling and tumour grading is outlined.

5.5.1 DATABASE

Digital mammograms were acquired from a dedicated digital mammography unit, Selenia DIMENSIONS (Hologic, Bedford, MA), in two standard projections (MLO and CC). The digital image receptor is a 24x29 cm amorphous selenium detector with a pixel size of 70 µm. Each digital mammogram is displayed on a high luminance, high spatial resolution monitor at 14 bit gray scale. The data set for tumour modelling consisted of 15 biopsy-proven malignant masses from 15 mammograms of which six are grade 3 masses and nine grade 2 masses. The region of interest containing each mass lesion was cropped and the matrix size ranges from 1500x1500 to 900x800 pixels for the malignant masses. Each mass was delineated with the three layer concentric ring model as shown below in Fig 5.3. An ethics approval number of 72/02c (2015) which was an extension of study 72/07A (2010) was given for the study

5.5.2. Three layers concentric ring model: outer region boundary, margin and the core

Outer region boundary	$(Region\ 1) = (L_1 - L_2)\mathrm{X}Mass$	5.45
Margins region	$(Region2) = (L_2 - L_3)\mathrm{X}Mass$	5.46
Core of the mass	$(Region\ 3) = L_3\mathrm{X}Mass$	5.47

where L_3 is the erosion of L_2, that is $L_3 = L_2 \ominus D$.

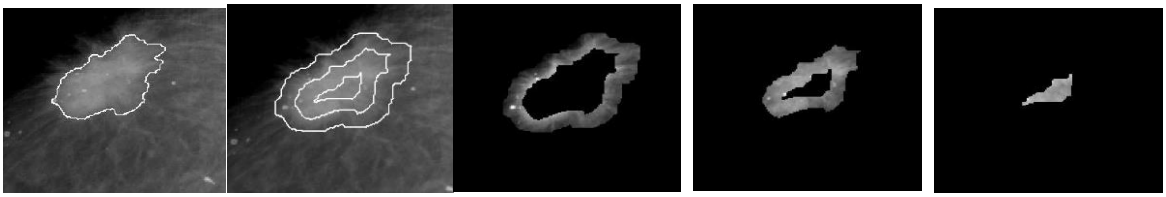

(a) (b) (c) (d) (e)

Fig. 5.3. Example of three layers concentric ring model (a) Original mass, (b) Delineated regions of interest, (c) Region 1, (d) Region 2, (e) Region 3.

5.6 Data collection and texture feature vector computation

Region 1, Region 2 and Region 3 denote the outer region boundary, margin and the core of the mass respectively and they constitute the three layers concentric ring model. For each mass in the database, the first order statistics [10, 11], second order statistics [12, 13] and the run length grey statistics [16] where computed for each region (region 1, region 2 and region 3) with different sizes of the sampling window. The mean and standard deviation of each texture feature was calculated for Region 1, Region 2 and Region 3 for each window size to represent the texture feature vector for the corresponding region and window size. Graphs and bar charts were plotted to provide a visual representation of the differences in texture feature vectors between regions and mass grade. On a mammogram there are different groups of pixels which are mutually related by a specific texture pattern. These groups have random sizes (areas), hence a varying sampling widow size is needed to capture the content of these texture primitives effectively. In this thesis, the sampling window sizes were 7X7, 9X9, 11X11 and 13X13 pixels representing square patches of 490 X 490 µm, 630 X 630 µm, 770 X 770 µm and 910 X 910 µm respectively.

5.7 Results

The bit-depth of an image is the number of different tones that can be assigned to each pixel in the image, hence each pixel in the mammograms is assigned a grey value between 0-255 representing a bit-depth of 8 bits. Generally, the more grey tones an image has the more detail can be represented in the image. The sampling window defines the sub -region within the mammogram within which the textural characteristics is assessed and a single value is assigned to the central pixel of the sampling window to represent the content or the texture feature vector of the window. As the size of the sampling window increases more data points are added to the data set for texture feature assessment. Hence the magnitude of the calculated texture feature will vary with the bit-depth of the image and the sampling window size. In this thesis, the bit-depth for all images was set at 8 bits to avoid loss of micro-texture features since a bit-depth less than 255 will effectively smooth the image.

5.7.1 Variation in first order statistical texture features

Variation in first order statistical texture features in regions 1, 2 and 3. The sampling window size (winsize) were 7, 9, 11 and 13 while the bit-depth of each image was 8 bits.

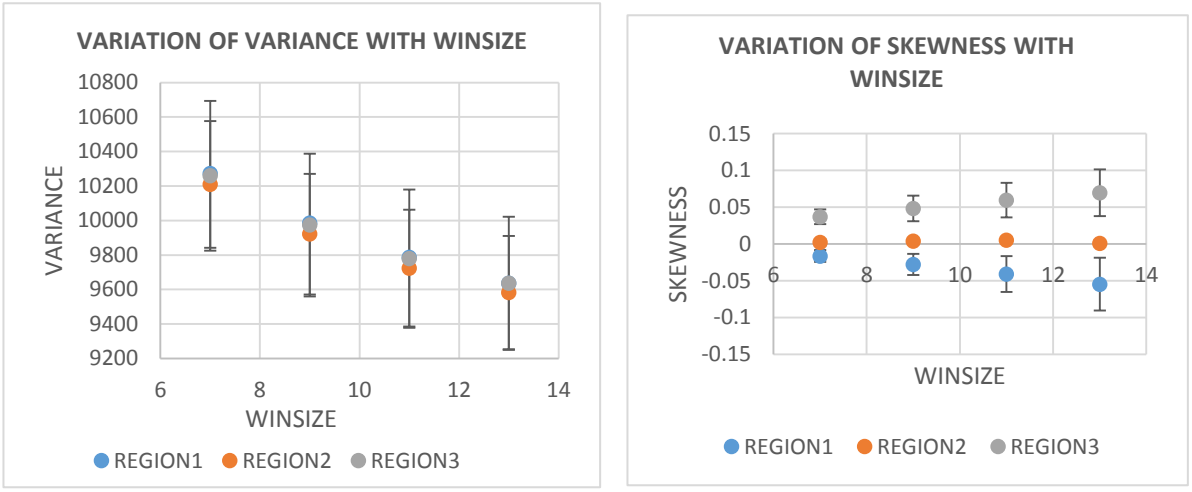

(a) (b)

Figure 5.4. Variation of first order texture features with winsize in regions 1, 2 and 3. (a) Variation of variance with winsize (b) variation of skewness with winsize

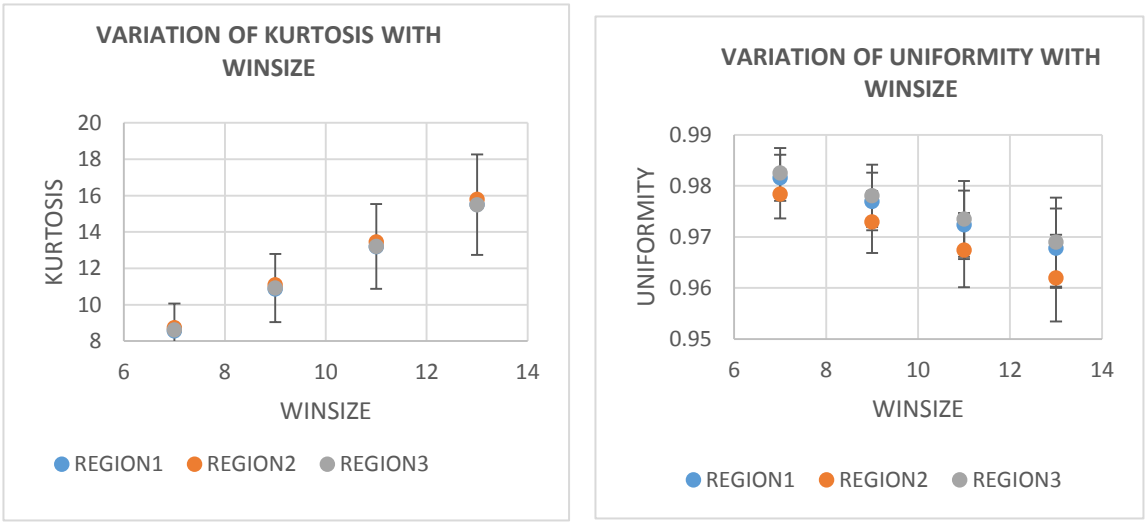

(a) (b)

Fig. 5.5. Variation of first order texture features with winsize in regions 1, 2 and 3. (a) Variation of kurtosis with winsize (b) Variation of uniformity with winsize

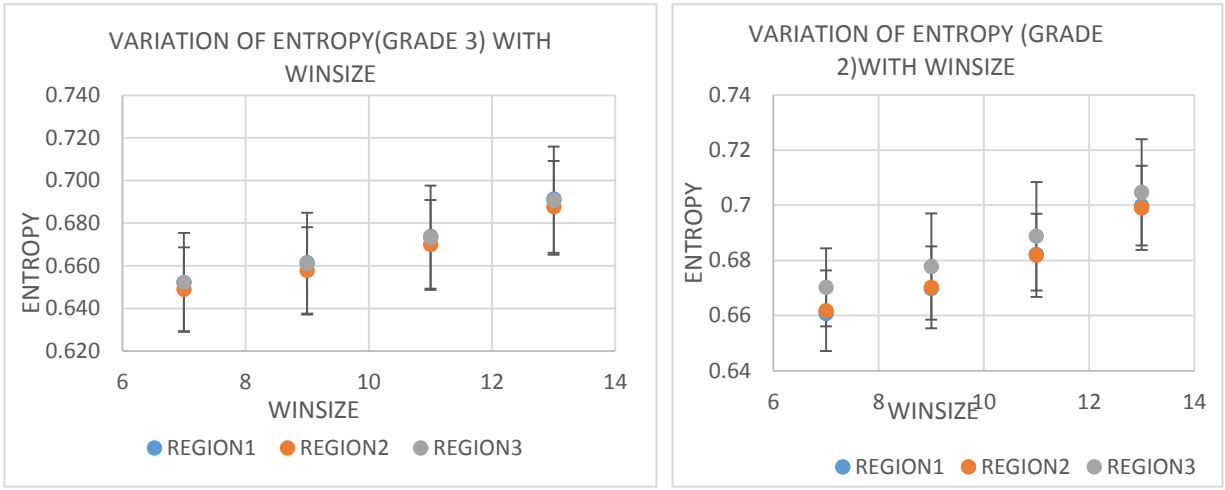

(a) (b)

Fig. 5.6 Variation of entropy with winsize in regions 1,2and 3 for grade 3 and grade 2 masses

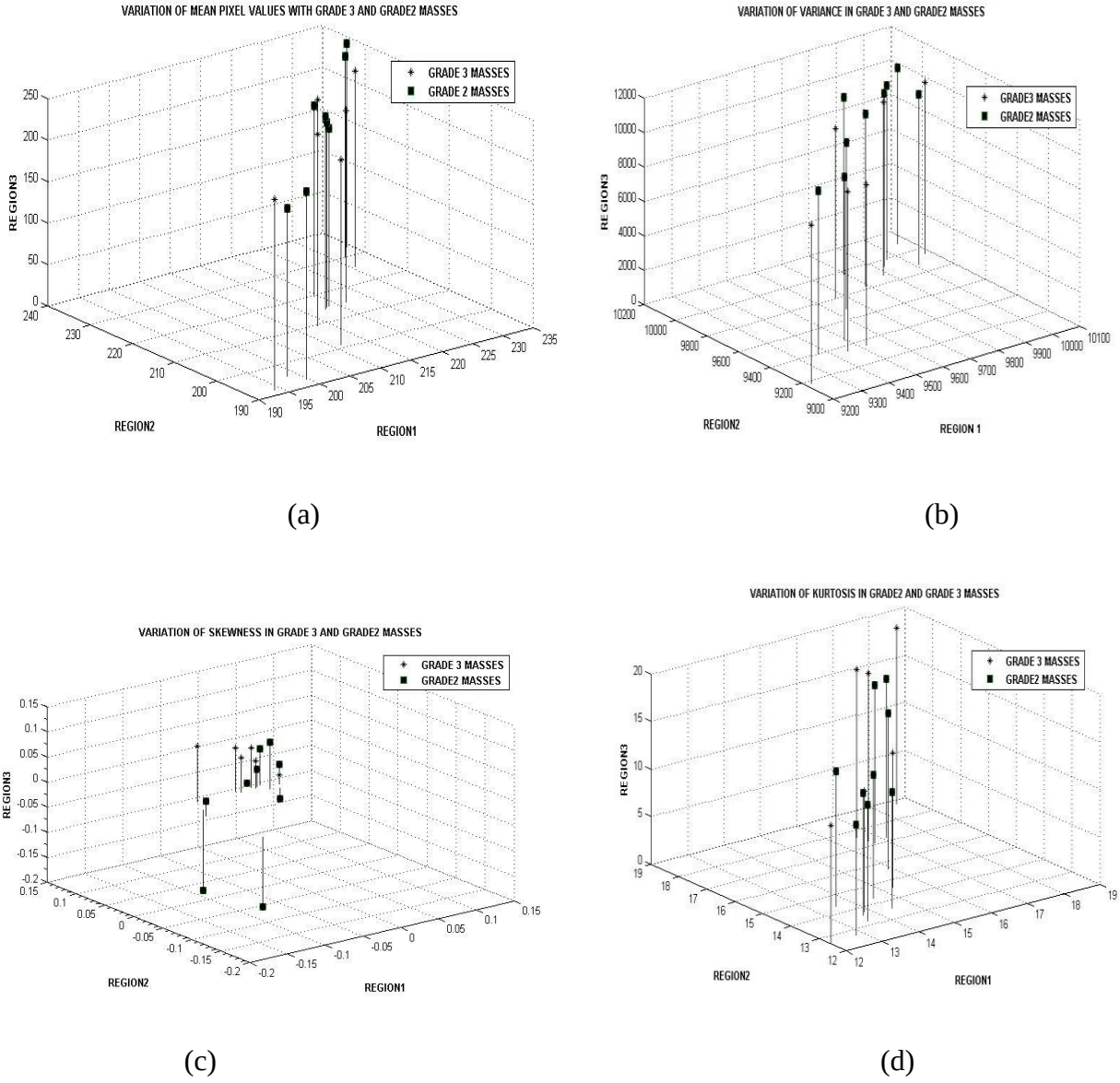

Fig. 5.7. Variation of mean pixel values, variance, skewness and kurtosis in grade 3 and grade 2 masses

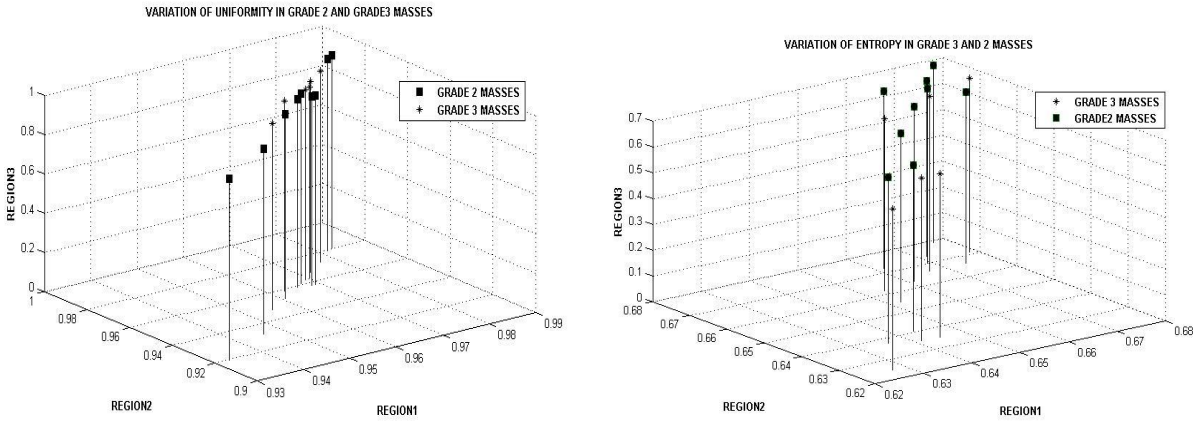

(b)

Fig.5.8. Variation of uniformity (a) and entropy (b) in grade 2 and grade 3 masses

Both the anova test and the t-test can be used to determine if the difference between the means of two population groups is significant. Hence it was appropriate to use the t-test to compare paired regions.

Table 5.4**:** Statistical analysis of first order texture features in tumour modelling with the two sample t-test for difference of means.

H0 (Null hypothesis): The mean of region i ($Mean_{Ri}$) is equal to the mean of region j ($Mean_{Rj}$)

H1 (Alternative): The mean of region i ($Mean_{Ri}$) is greater than the mean of region j ($Mean_{Rj}$) Or that the mean of region i ($Mean_{Ri}$) is less than the mean of region j ($Mean_{Rj}$). The significant level is 5% hence if a p-value is less than 0.05, the null hypothesis of equal means is rejected and the alternative is accepted

TEXTURE FEATURE	**Comparing Region 1 And Region 2**		**Comparing Region 2 And Region 3**		**Comparing Region 3 And Region 1**	
	P value of $Mean_{R1} > Mean_{R2}$	**P value of $Mean_{R1} < Mean_{R2}$**	**P value of $Mean_{R2} > Mean_{R3}$**	**P value of $Mean_{R2} < Mean_{R3}$**	**P value of $Mean_{R3} > Mean_{R1}$**	**P value of $Mean_{R3} < Mean_{R1}$**
MEAN	0.0282			0.0023	0.0087	
VARIANCE	0.0153			*	*	*
SKWENESS		0.0187		0.0056	0.0102	
KURTOSIS		0.0350	*	*	*	*
UNIFORMITY	3.892E-17			0.0029	*	*
ENTROPY	0.0174		*	*	*	*

* P-values are greater than 0.05, hence the null hypothesis is accepted.

Table 5.5: Statistical analysis of Frist order texture features in tumour grading with the two sample t-test assuming unequal variance.

H0 (Null hypothesis): There is no statistical difference between the mean of the texture feature of grade 2 and grade 3 masses. The significant level is 5% hence if a p-value is less than 0.05, the null hypothesis of equal means is rejected

TEXTURE FEATURES	**mean**	**variance**	**skewness**	**kurtosis**	**uniformity**	**entropy**
P-VALUES	0.850697	**0.019144**	**0.04576**	0.084231	0.090016	**0.022137**

5.7.2 Variation in run length statistical texture features.

Variation in run length statistical texture features in regions 1, 2 and 3 .The sampling window sizes (winsize) were 7, 9, 11 and 13 while the bit-depth of each image was 8 bits

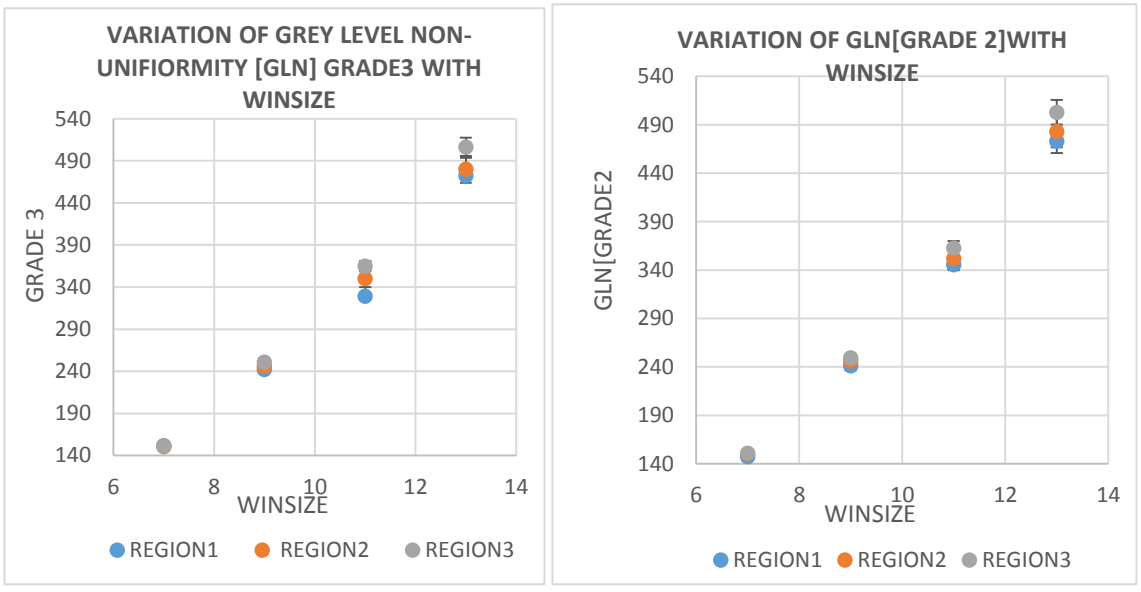

(a) (b)

Fig.5.9. Variation of grey level non-uniformity [GLN] in grade 3 (a) and grade 2 (b) masses

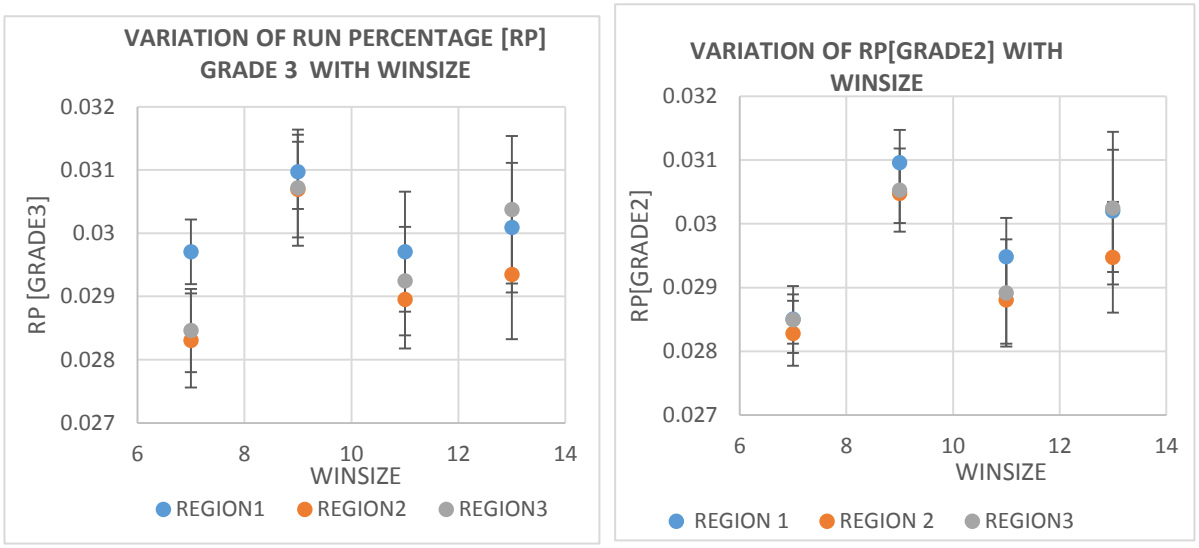

(a) (b)

Fig.5.10. Variation of Run percentage [RP] in grade 3(a) and grade 2(b) masses

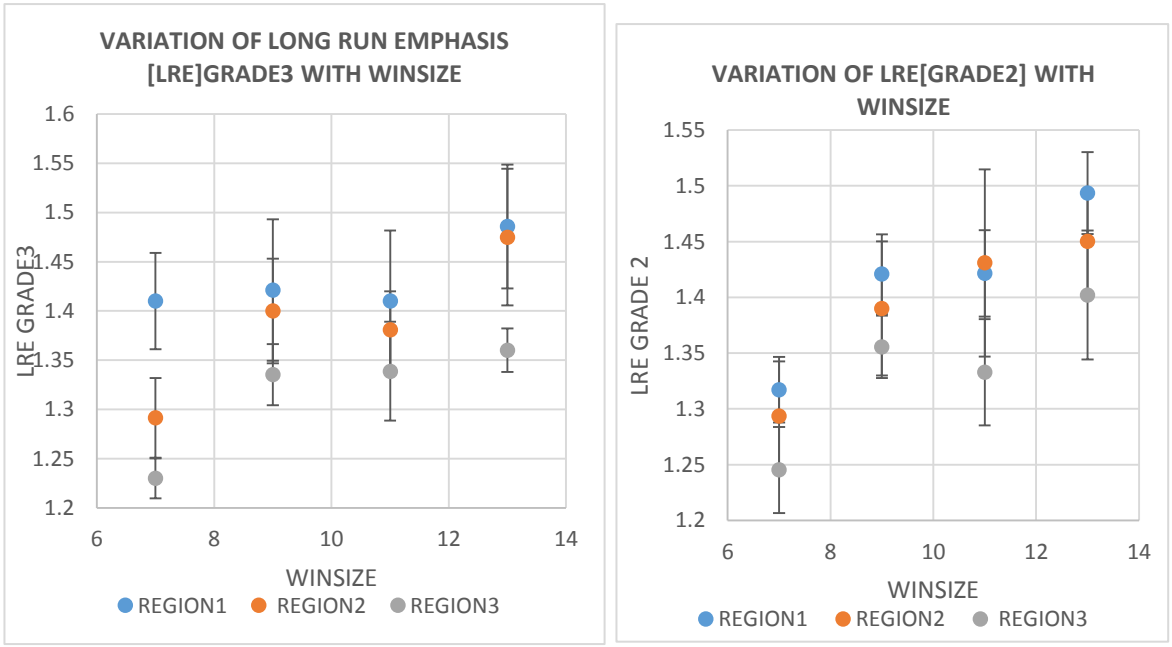

(a) (b)

Fig.5.11. Variation of Long run emphasis [LRE] in grade 3(a) and grade 2(b) masses

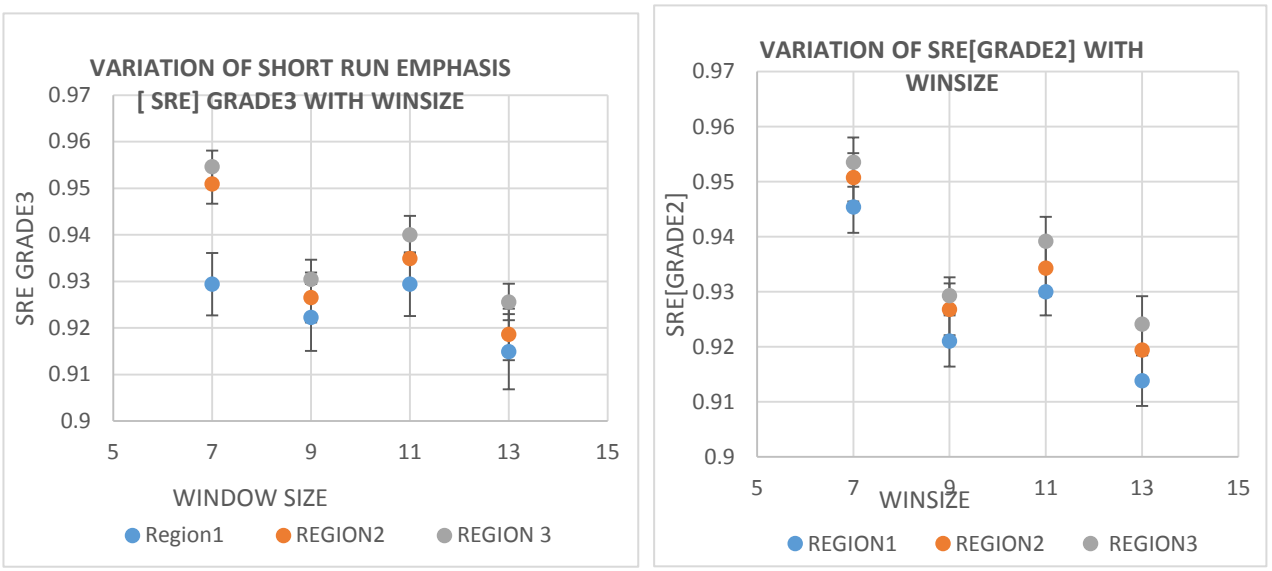

(a) (b)

Fig.5.12. Variation of short run emphasis [SRE] in grade 3(a) and grade 2(b) masses

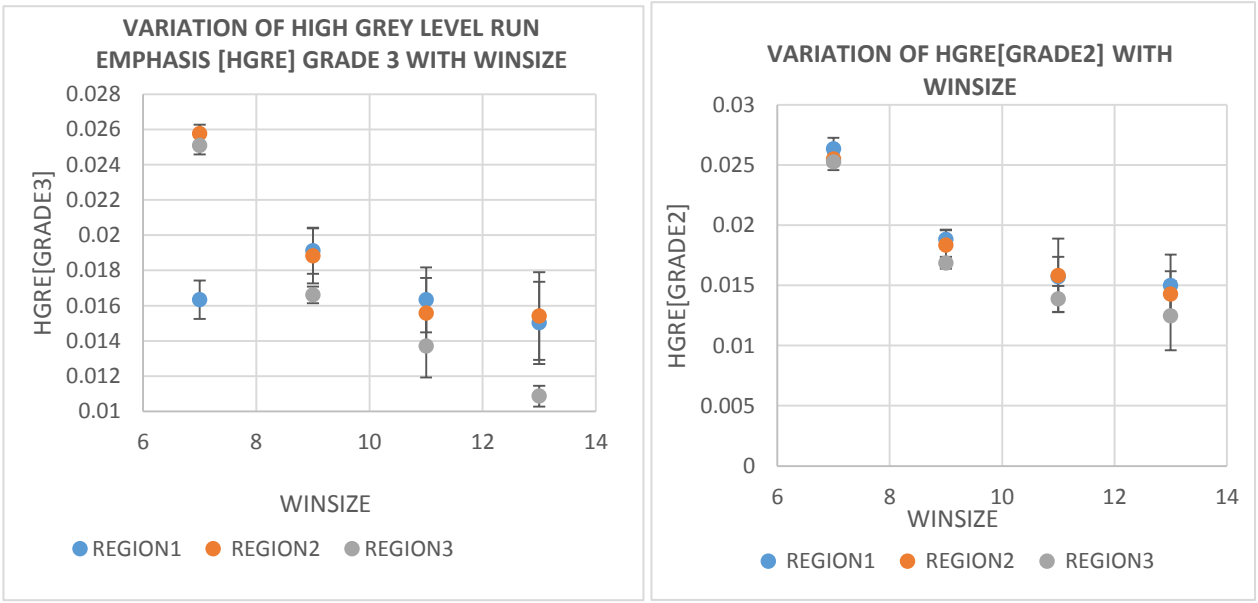

(a) (b)

Fig.5.13. Variation of high grey level run emphasis[HGRE] in grade 3(a) and grade 2(b) masses

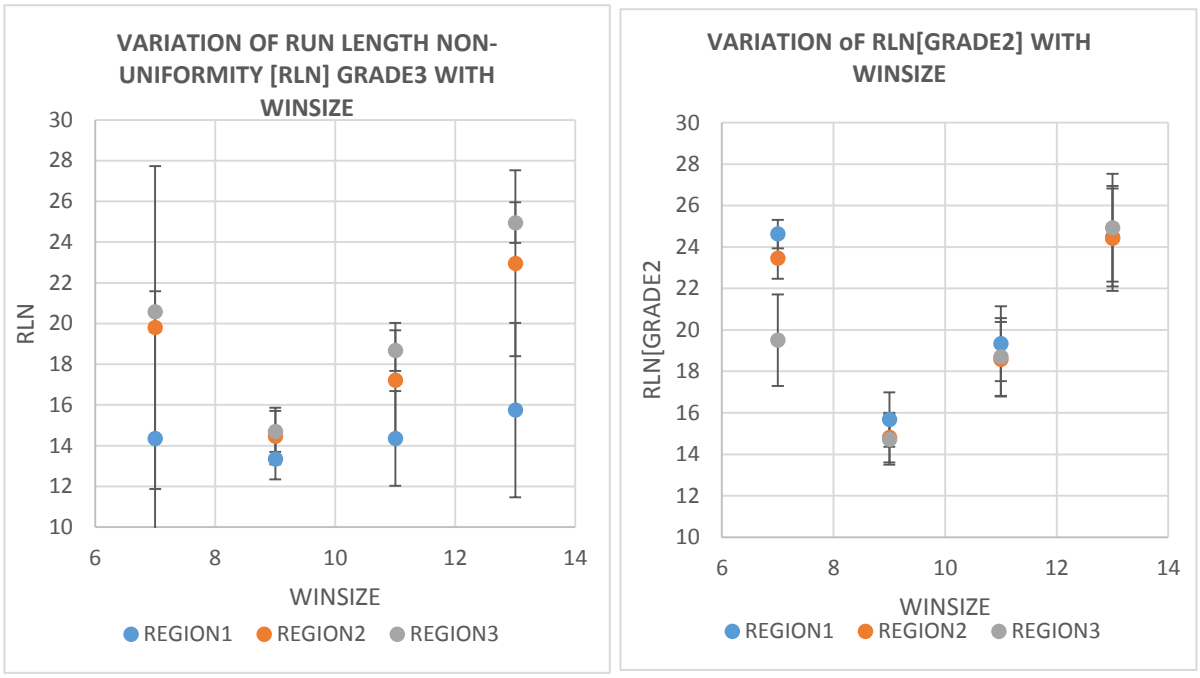

(a) (b)

Fig.5.14. Variation of run length non-uniformity [RLN] in grade 3(a) and grade 2(b) masses

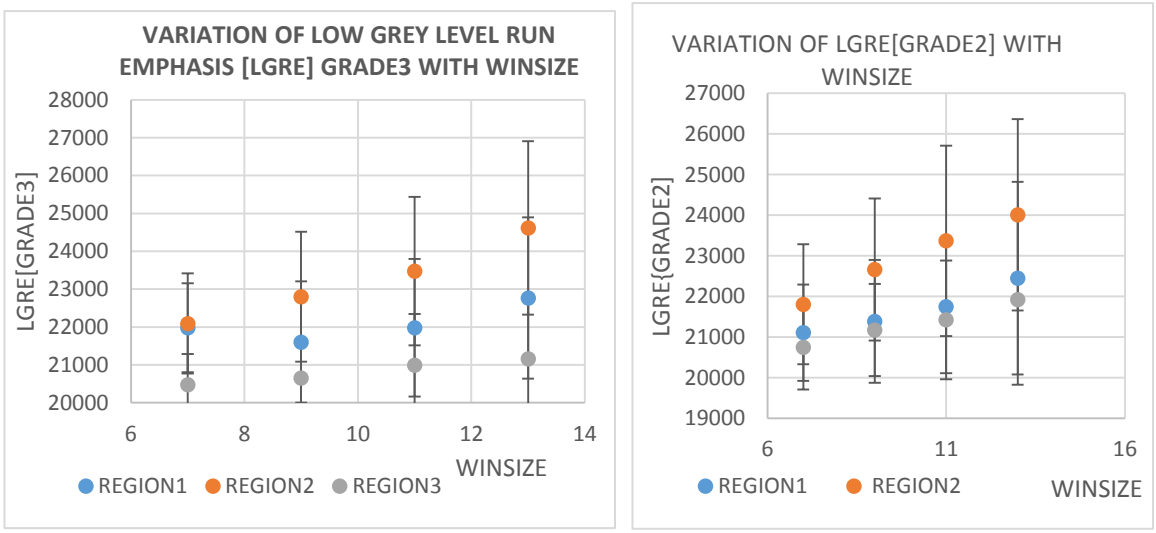

(a) (b)

Fig.5.15. Variation of low grey level run emphasis [LGRE] in grade 3(a) and grade 2(b) masses

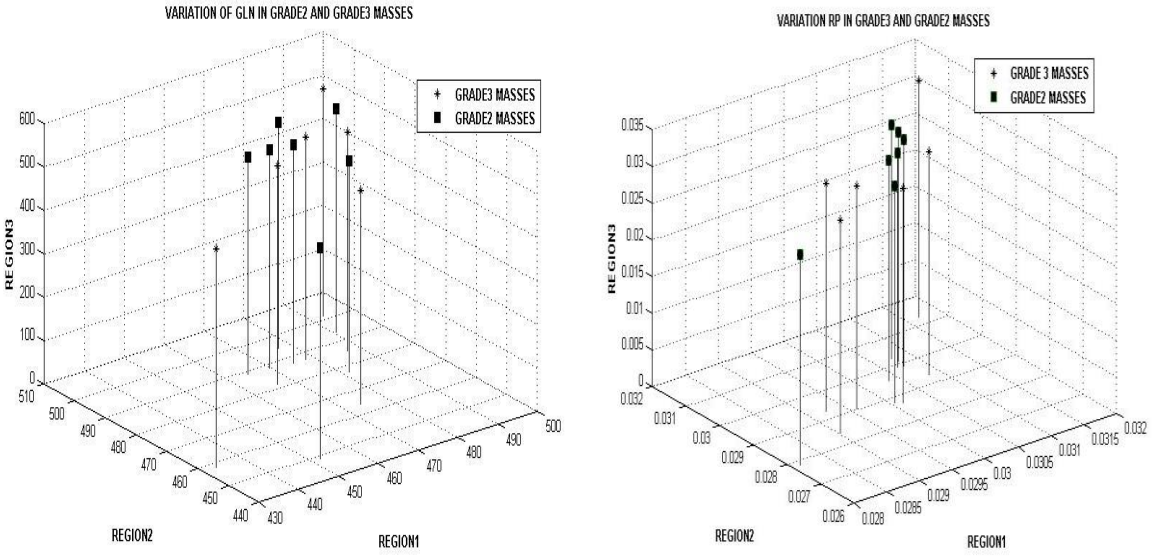

(a) (b)

Fig.5.16. Variation of grey level non-uniformity [GLN] (a) and run percentage [RP] (b) in grade 2 and grade 3 masses

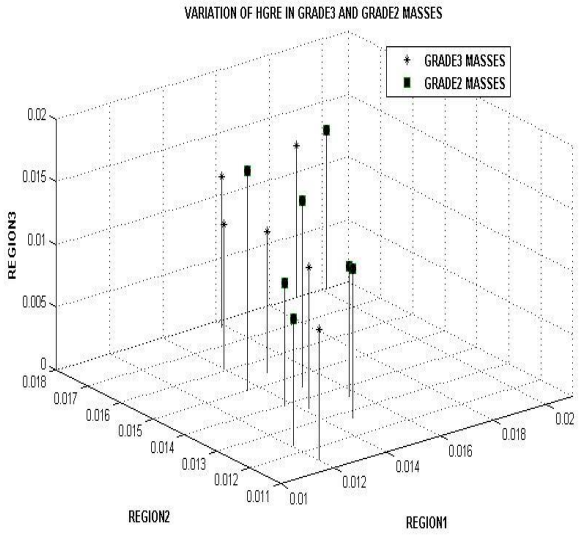

Fig.5.17. Variation high grey level run emphasis [HGRE] in grade 2 and grade 3 masses

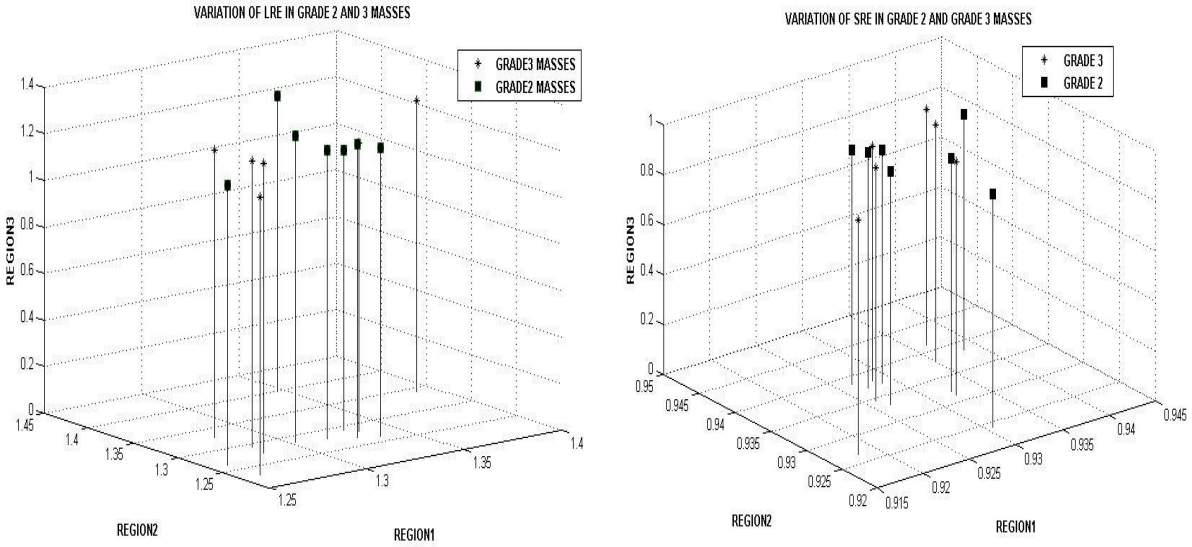

(a) (b)

Fig.5.18. Variation long run emphasis [LRE] (a) and short run emphasis [SRE] (b) in grade 2 and grade 3 masses

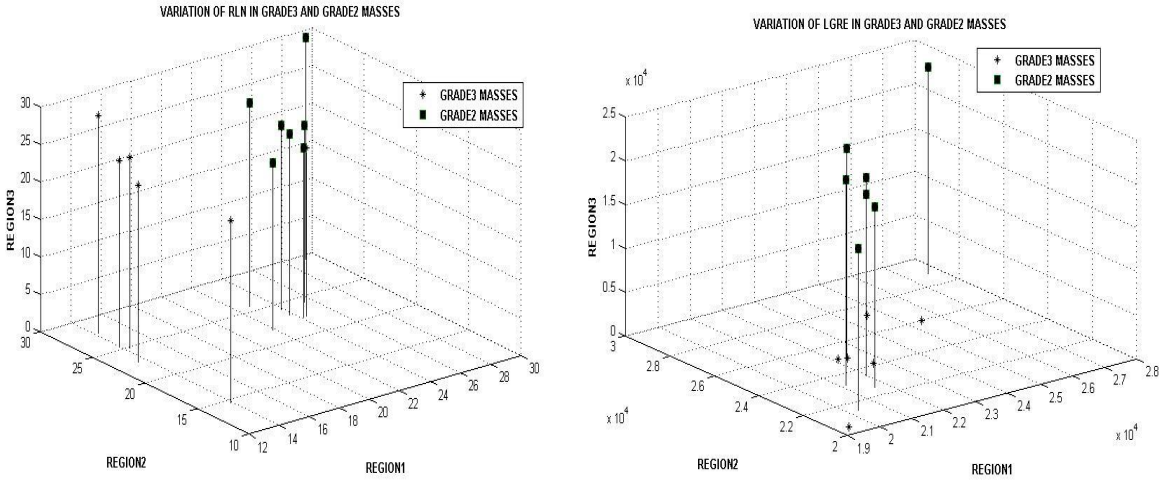

(a) (b)

Fig. 5.19. Variation run length non-uniformity [RLN] (a) and low grey level run emphasis [LGRE] (b) in grade 2 and grade 3 masses

Table 5.6**:** Statistical analysis of runlengths texture features in tumour modelling with the two sample t-test for difference of means

H0 (Null hypothesis): The mean of region i ($Mean_{Ri}$) is equal to the mean of region j ($Mean_{Rj}$) H1 (Alternative): The mean of region i ($Mean_{Ri}$) is greater than the mean of region j ($Mean_{Rj}$) Or that the mean of region i ($Mean_{Ri}$) is less than the mean of region j ($Mean_{Rj}$). The significant level is 5% hence if a p-value is less than 0.05, the null hypothesis of equal means is rejected, and the alternative is accepted

RUN LENGTHS	**Comparing Region 1 And Region 2**		**Comparing Region 2 And Region 3**		**Comparing Region 3 And Region 1**	
TEXTURE FEATURES	**P values of $Mean_{R1} > Mean_{R2}$**	**P values of $Mean_{R1} < Mean_{R2}$**	**P values of $Mean_{R2} > Mean_{R3}$**	**P values of $Mean_{R2} < Mean_{R3}$**	**P Value of $Mean_{R3} > Mean_{R1}$**	**P values of $Mean_{R3} < Mean_{R1}$**
SRE		0.0021		6.14E-07	6.21E-06	
LRE	0.0115		0.0001			9.121E-06
GLN		0.0076		7.303E-07	3.01E-06	
RP	2.282E-05			0.0001	*	*
RLN		0.0275		0.0651	0.0093	
LGRE		7.188E-07	3.08E-05			0.0455
HGRE	*	*	0.0006			0.0009

* P-values are greater than 0.05, hence the null hypothesis is accepted.

Table 5.7: Statistical analysis of runlength texture features in tumour grading with the two sample t-test assuming unequal variance.

H0 (Null hypothesis): There is no statistical difference between the mean of the texture feature of grade 2 and grade 3 masses. The significant level is 5% hence if a p-value is less than 0.05, the null hypothesis of equal means is rejected

TEXTURE FEATURES	**SRE**	**LRE**	**GLN**	**RP**	**RLN**	**LGRE**	**HGRE**
P-VALUES	0.1780	0.0914	0.0614	0.6857	**0.0001**	0.4298	0.1233

5.7.3 Variation in second order statistical texture features.

Variation in second order statistical texture features in regions 1, 2 and 3 .The sampling window sizes (winsize) were 7, 9, 11 and 13 while the bit-depth of each image was 8

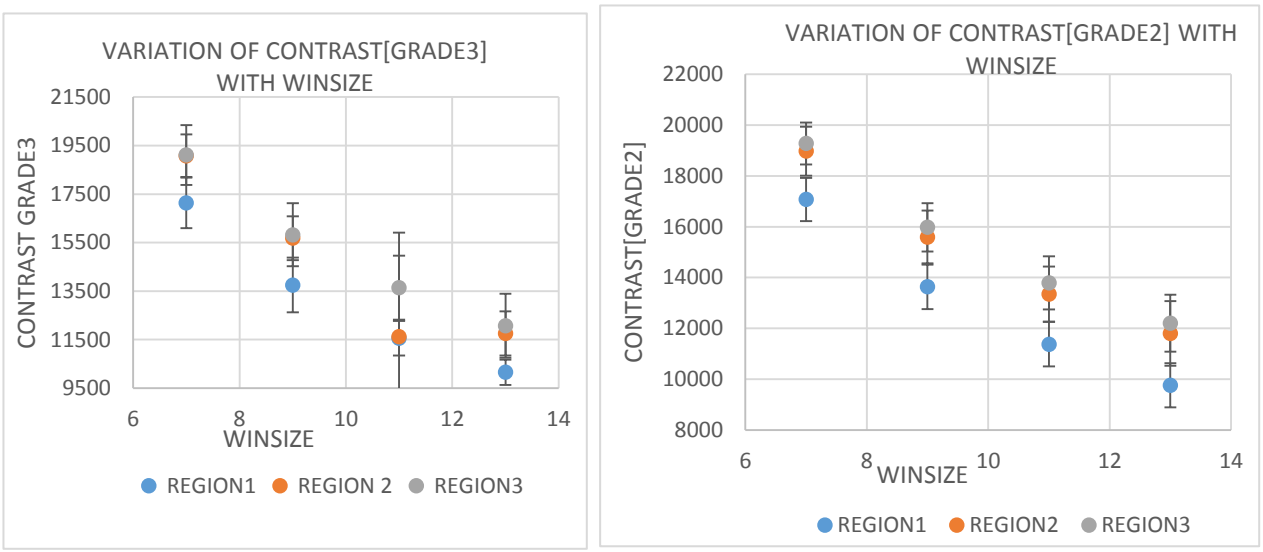

(a) (b)

Fig. 5.20 Variation of contrast grade 3(a) and grade 2 masses (b)

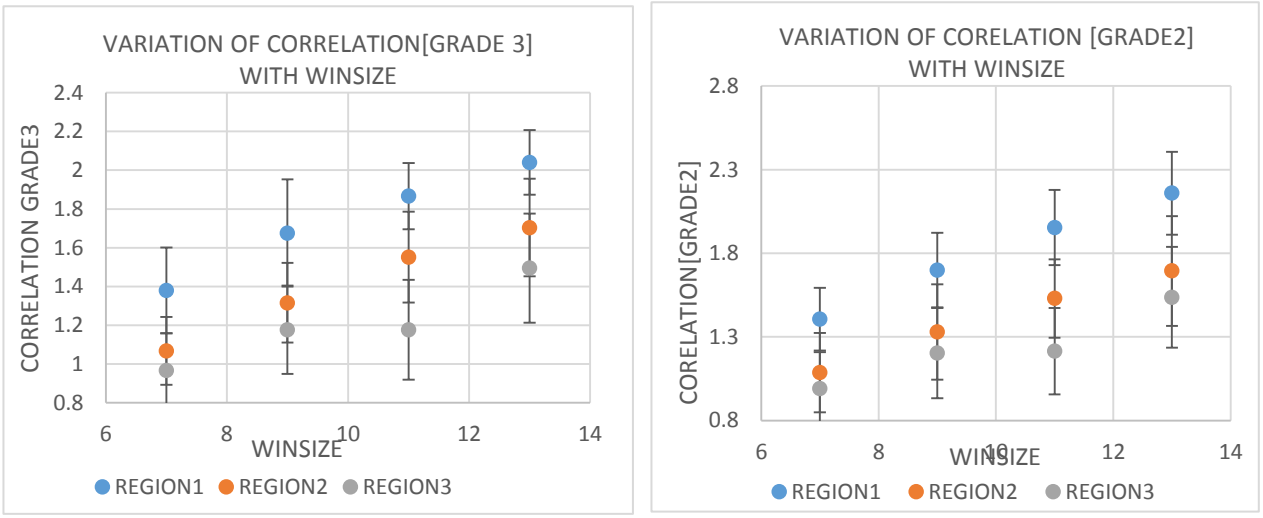

(a) (b)

Fig. 5.21.Variation of correlation grade 3(a) and grade 2 masses (b)

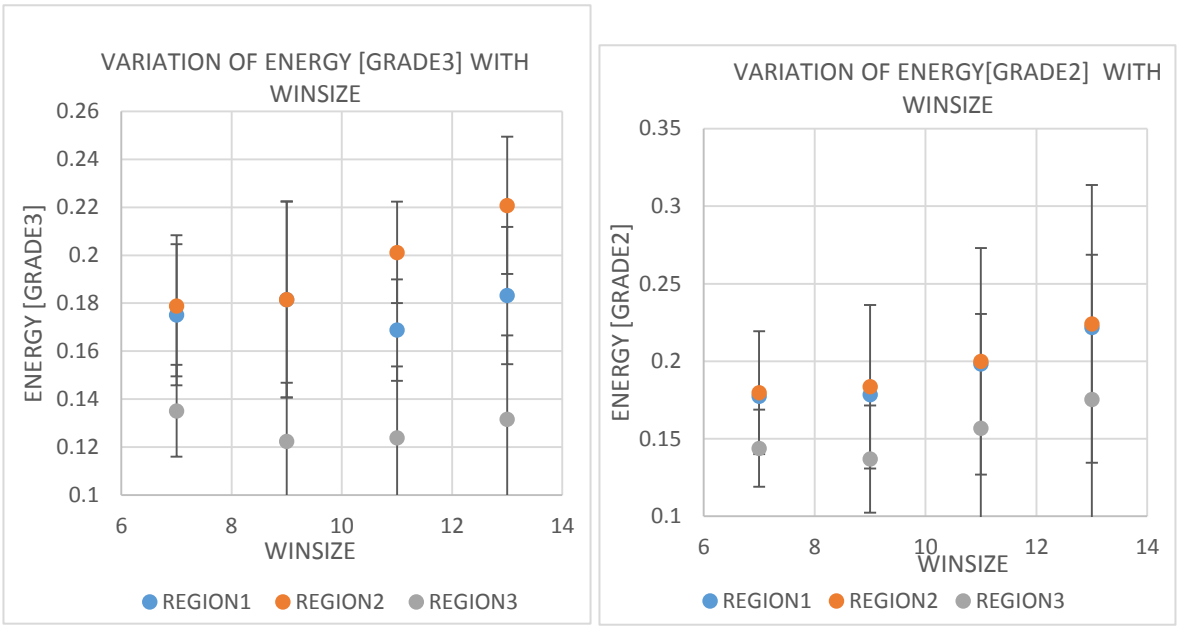

(a) (b)

Fig.5.22 Variation of energy grade 3(a) and grade 2 masses (b)

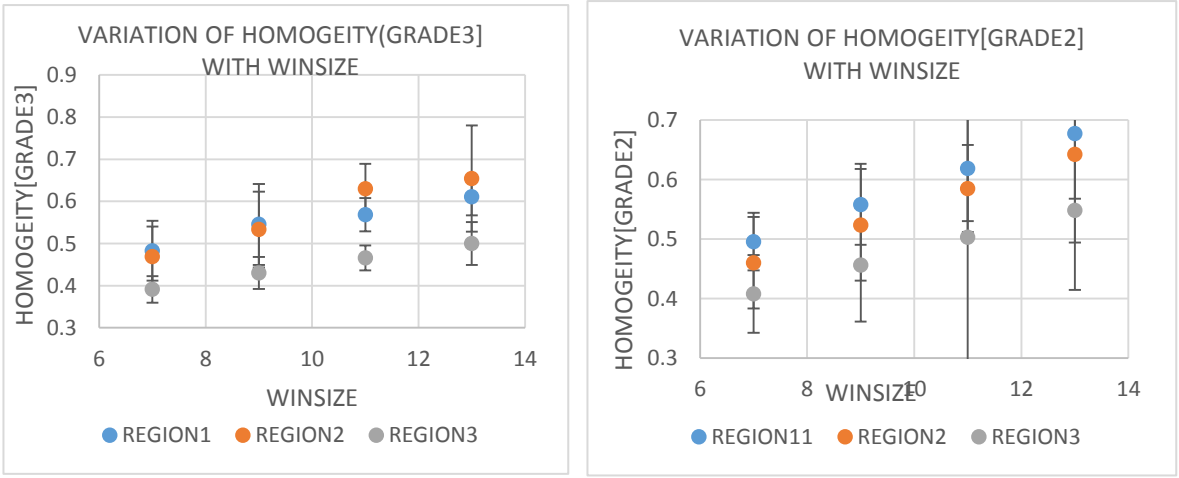

(a) (b)

Fig.5.23 Variation of homogeneity grade 3(a) and grade 2 masses (b)

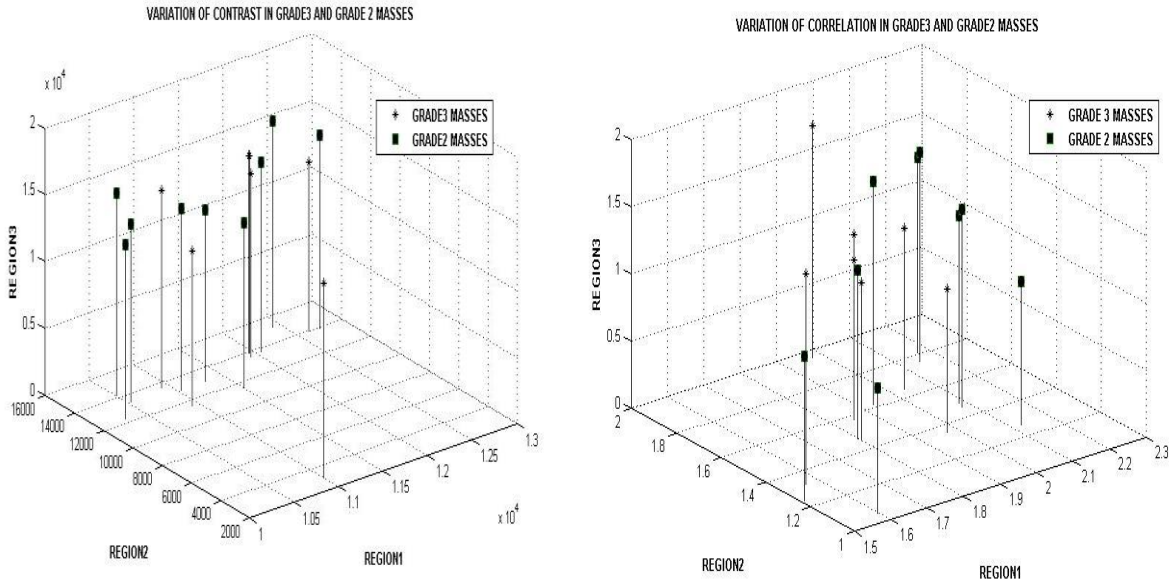

(a) (b)

Fig.5.24 Variation of contrast (a) and correlation (b) grade 3 and grade 2 masses

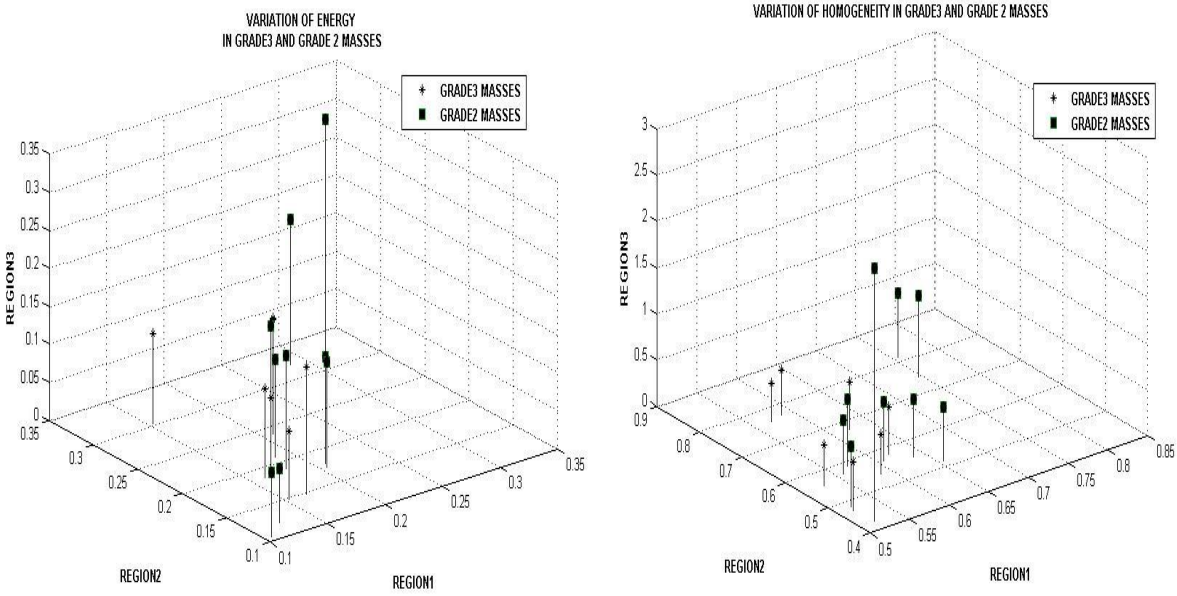

(a) (b)

Fig. 5.25. Variation of energy (a) and homogeneity (b) grade 3 and grade 2 masses

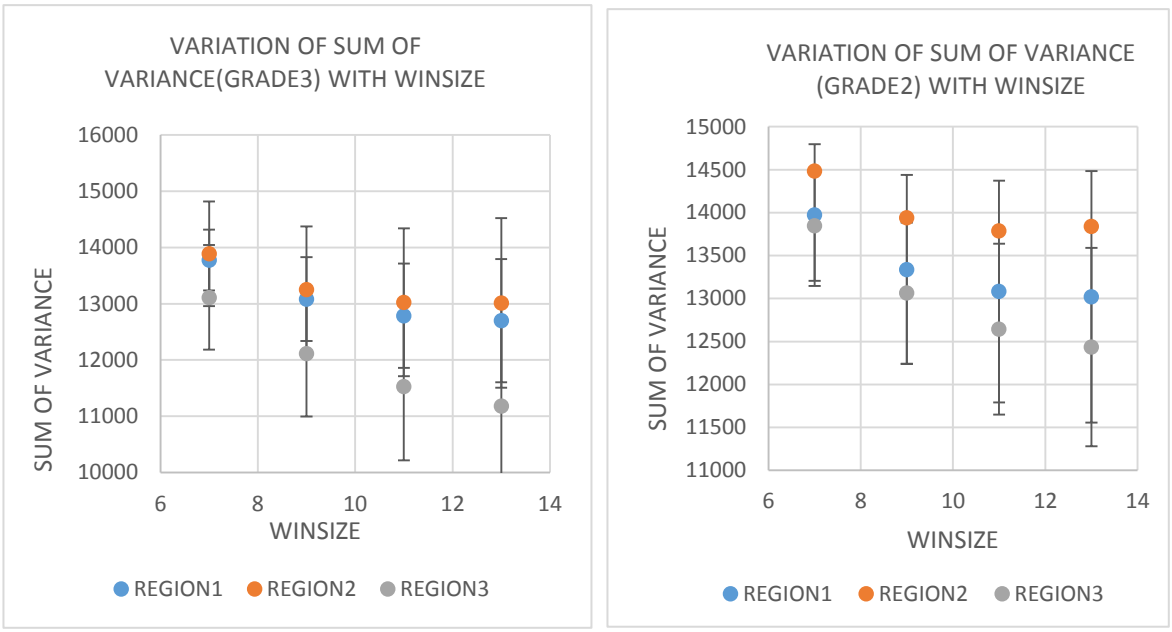

(a) (b)

Fig.5.26. Variation of sum of variance in grade 3 (a) and grade 2 (b) masses

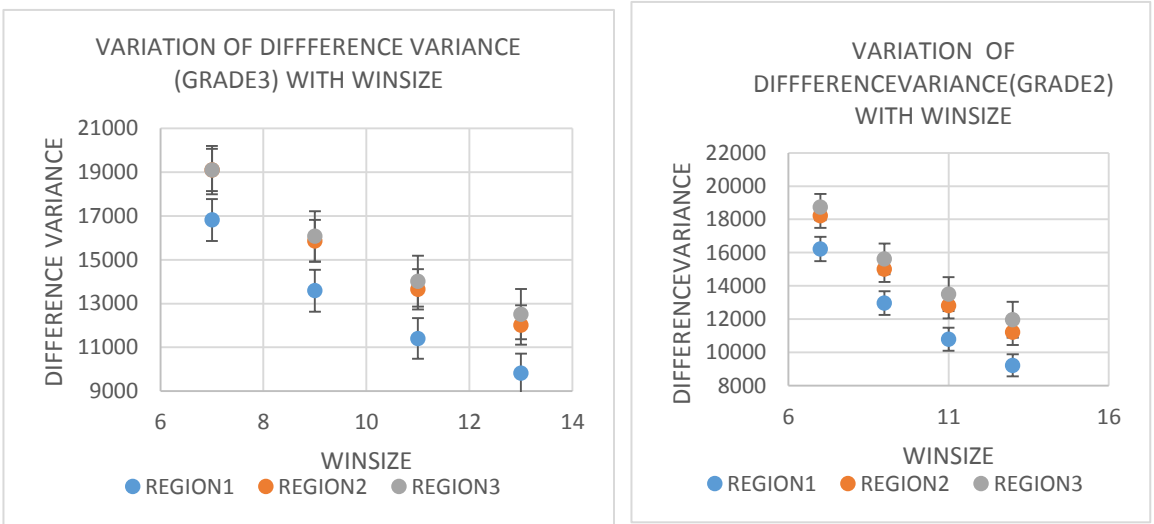

(a) (b)

Fig.5.27. Variation of difference variance in grade 3 (a) and grade 2(b) masses

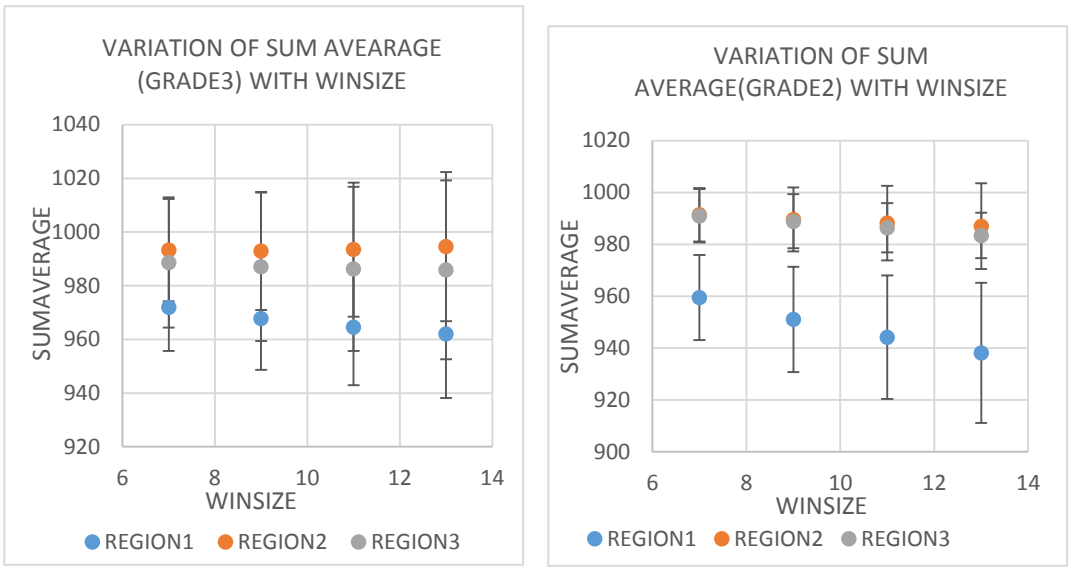

(a) (b)

Fig. 5.28. Variation of sum average in grade 3 (a) and grade 2 (b) masses

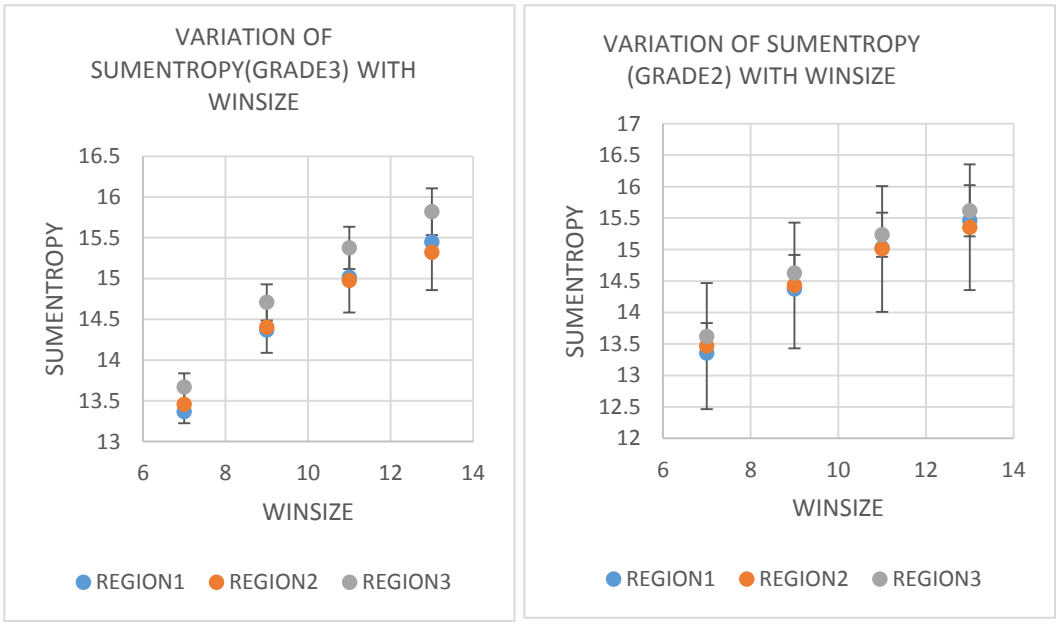

(a) (b)

Fig.5.29. Variation of sum entropy in grade 3 (a) and grade 2 (b) masses

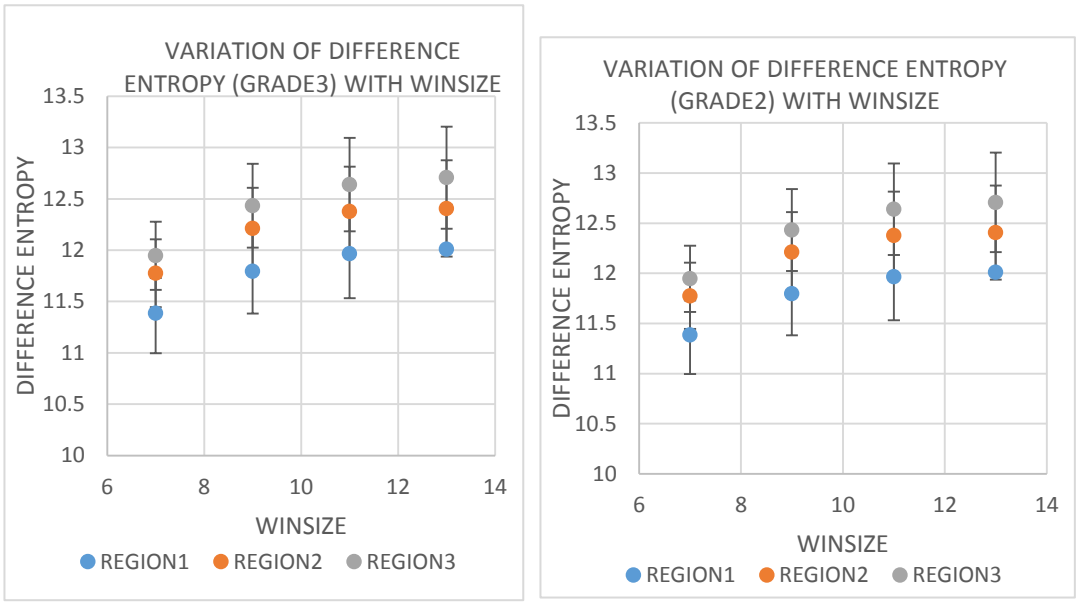

(a) (b)

Fig.5.30. Variation of difference entropy in grade 3 (a) and grade 2 (b) masses

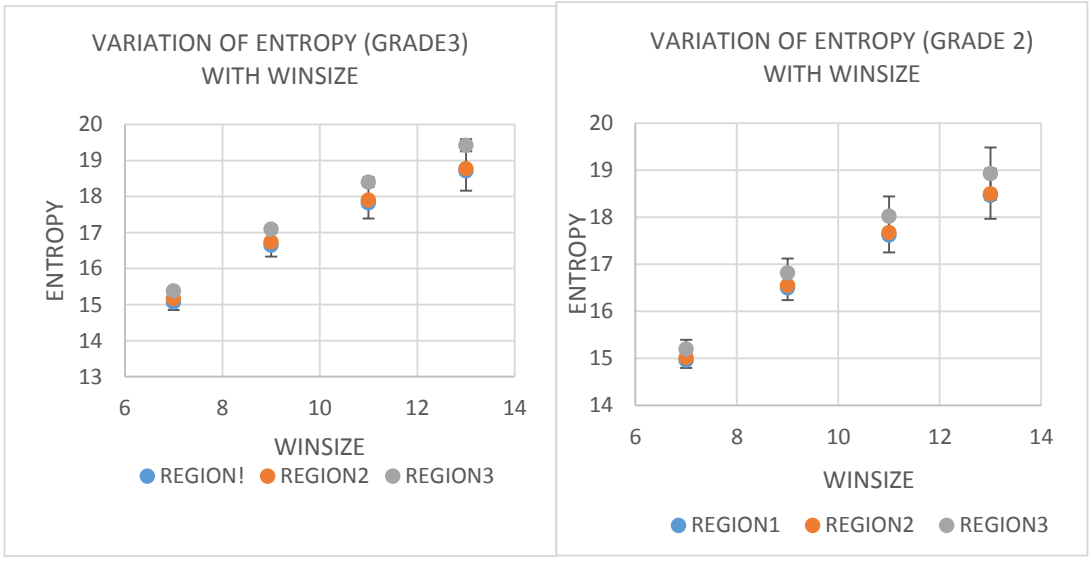

(a) (b)

Fig5.31. Variation of entropy in grade 3 (a) and grade 2 (b) masses.

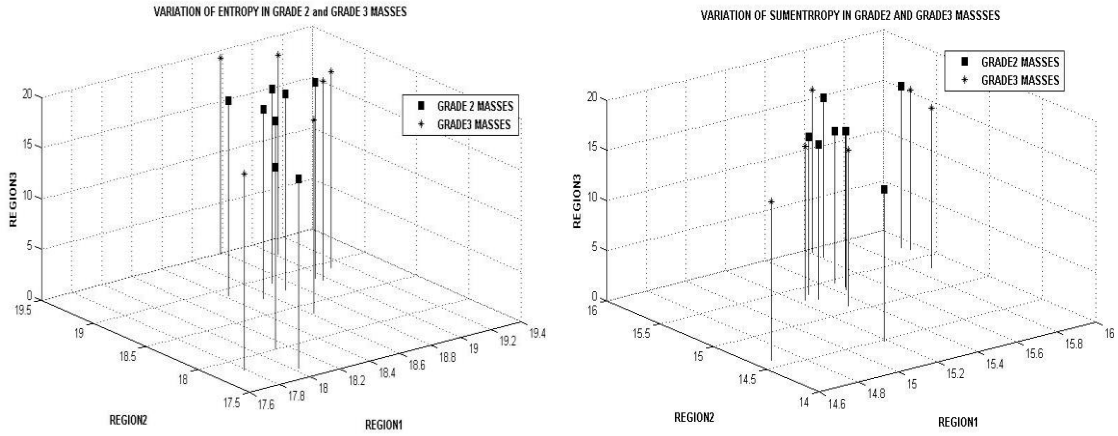

(a) (b)

Fig.5.32. Variation of entropy (a) and sumentropy (b) in grade 2 and grade 3 masses

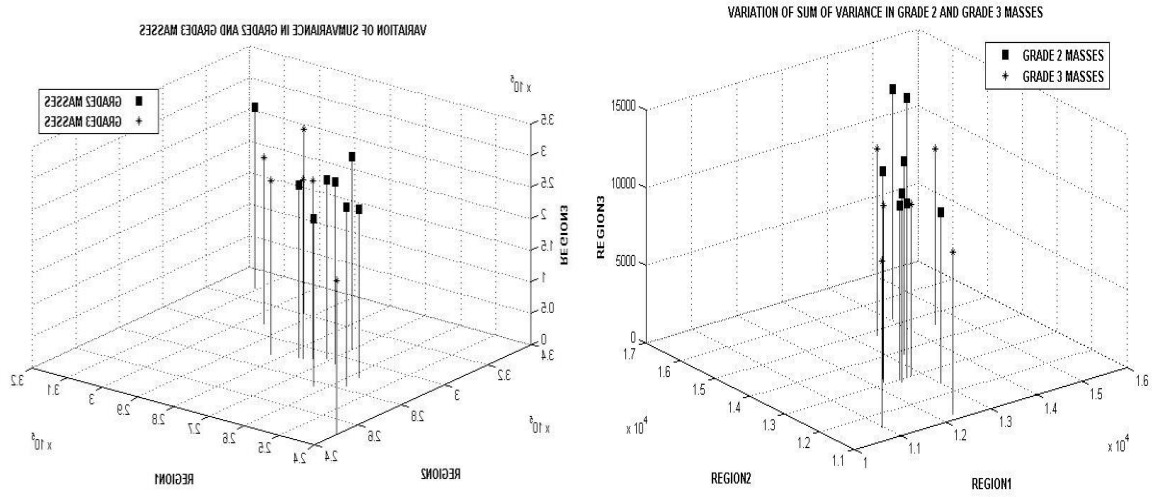

(a) (b)

Fig.5.33. Variation of sum variance (a) and sum of variance (b) with grade 2 and grade 3 masses

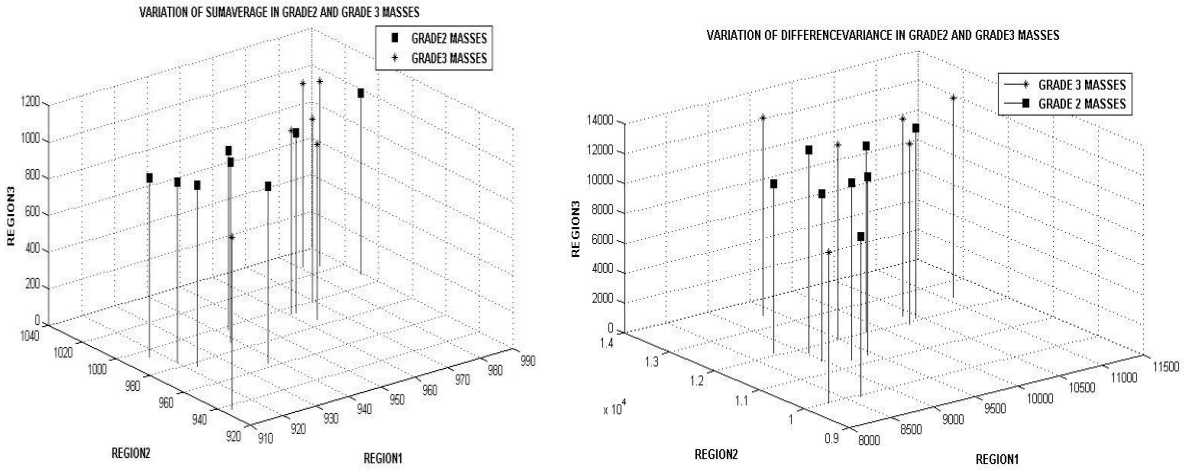

Fig.5.34. Variation of sum average (a) and difference variance (b) with grade 2 and grade 3 masses

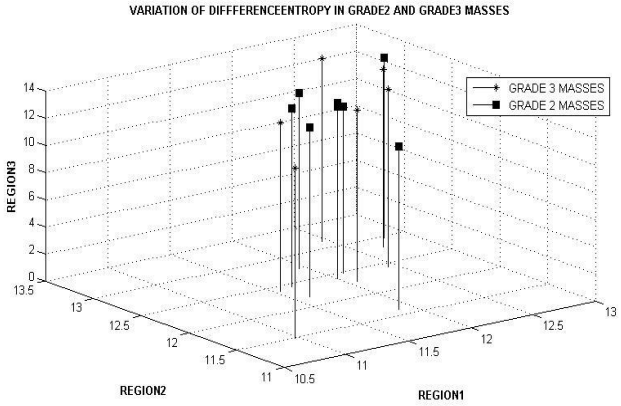

Fig.5.35. Variation of difference entropy with grade 2 and grade 3 masses

Table 5.8 : Statistical analysis of second order texture features in tumour modelling with the two sample t-test for difference of means. H0 (Null hypothesis): The mean of region i ($Mean_{Ri}$) is equal to the mean of region j ($Mean_{Rj}$) H1 (Alternative): The mean of region i ($Mean_{Ri}$) is greater than the mean of region j ($Mean_{Rj}$) Or that the mean of region i ($Mean_{Ri}$) is less than the mean of region j ($Mean_{Rj}$). The significant level is 5% hence if a p-value is less than 0.05, the null hypothesis of equal means is rejected, and the alternative is accepted

	Comparing Region 1 And Region 2		**Comparing Region 2 And Region 3**		**Comparing Region 3 And Region 1**	
SECOND ORDER TEXTURE FEATURES	**P value of $Mean_{R1} > Mean_{R2}$**	**P value of $Mean_{R1} < Mean_{R2}$**	**P value of $Mean_{R2} > Mean_{R3}$**	**P value of $Mean_{R2} < Mean_{R3}$**	**P value of $Mean_{R3} > Mean_{R1}$**	**P value of $Mean_{R3} < Mean_{R1}$**
Contrast		2.502E-05		0.0284		1.083E-05
Correlation	0.0002		0.00072		4.731E-06	
Energy	*	*	0.0009			0.0003
Homogeneity	*	*	0.0004		1.619E-05	
Entropy	*	*		0.0005		0.0001
Sum of variance		0.0215	0.0002			0.0021
Sum average		6.418E-07		*		7.703E-05
Sum variance		5.604E-07		0.0004	*	*
Sum entropy	0.0298			0.0011		0.0159
Difference variance		1.047E-07		0.0102		2.322E-08
Difference entropy		0.0007		0.0003		1.448E-05

Table 5.9: Statistical analysis of runlength texture features in tumour grading with the student t-test of two samples assuming unequal variance.

H0 (Null hypothesis): There is no statistical difference between the means of the texture feature of grade 2 and grade 3 masses. The significant level is 5% hence if a p-value is less than 0.05, the null hypothesis of equal means is rejected.

TEXTURE FEATURES	P-VALUES
Contrast	0.864
Correlation	0.722
Energy	0.202
Homogeneity	0.343
Entropy	0.072
Sum of variance	0.074
Sum average	0.297
Sum variance	0.693
Sum entropy	0.722
Difference variance	0.285
Difference entropy	0.718

5.8 Summary of Results and Discussion

Some clinical traits of mammographic masses are reflected in their shapes and textural composition. Fig5.4 and Fig. 5.5 shows the variation of first order texture features with winsize in regions 1, 2 and 3. The variance and uniformity for regions 1, 2 and 3 decrease as the size of the sampling window increases, as shown in Fig. 5.4a and 5.5b respectively. While Fig.5.5.a and Fig.5.6 shows that the kurtosis and the entropy of the region of interest increases with the size of the sampling window in regions 1, 2 and 3. The skewness behaves differently; in region 1 the skewness decreases with increase in winsize, in region 3 it increases with winsize and in region 2 it varies very slowly with winsize as shown in Fig.5.4b. The relationship between the kurtosis (Fig 5.5a) and the sampling size indicates that as the sampling size increases the histogram of the region is heavy-tailed relative to a normal distribution, hence the data set of the histogram tends to have many outliers. Skewness is a measure of the symmetry of a distribution. From Fig. 5.4 (b), it illustrates that the distribution of the pixel values in region 2 is close to that of a normal distribution as compared to that of region 1 and region 3. Region 1 has a mean negative skewness while region 3 has a mean positive skewness, hence a good candidate illustrating the difference in texture from the core of the mass to the periphery with the three layers concentric ring model, moreover, these signs are independent of winsize. The distance between the skewness of region 1 and region 2, region 2 and region 3 increases with winsize, hence winsize 13 provides the best separation for this texture measure. The first order statistical texture features were evaluated with the two tailed two sample t-test for difference of means, to find out if there were statistical differences between the means of the texture features of the different regions for winsize 13. The significant level was set at 0.05. Those regions with p values less than 0.05 were further investigated with the one tailed two sample t-test to find out which mean texture values were greater. Table 5.4 shows that there was no difference in the mean texture features of variance, kurtosis, uniformity and entropy between region 3 and region 1while there were statistical differences in the mean texture features of region 1 and region 2 However skewness is consistent in its performance because region 1 is less than region 2 and region 2 is less than region 3. Fig.5.7 and Fig. 5.8 shows a 3-dimensional graph of the first order texture measures for region 1, region 2 and region 3 for all the masses in this study (grade 2 and grade 3). From these graphs there is no distinct first order texture

feature that can be used to distinguish between grade 2 and grade 3 masses, because visually, there is no distinct margin separating these texture features into grade 2 and grade 3, however this may not be the case with the application of a clustering algorithm. Further evaluation of these features with the two sample t-test for difference of means, revealed that there were significant differences between the means of texture features of variance, skewness and entropy for grade 2 and grade 3 masses as shown in Table 5.5

Fig. 5.9 to Fig. 5.15 show the comparison between the run length texture features of grade 3 and grade 2 masses. They are similar in magnitude and show similar trend as the winsize increases. The GLN feature increase with increase in winsize with region 3 having the highest value with each winsize as illustrated in Fig.5.9a and Fig.5.9b. As the winsize increases the distances between the GLN feature of region 1 and 2, region 2 and 3 increase. Fig. 5.10 shows that the RP texture is maximum for all regions when the winsize is 9, however region 2 has the minimum value for all winsizes. The region 3 has the minimum value for the LRE texture feature for both grade 3 and grade 2 masses with winsize 13 having the highest values for all regions as shown in Fig.5.11. The SRE feature was maximum for region 3 and minimum for region 1 for all winsizes while SRE and HGRE had minimum values with winsize13 as shown in Fig. 5.12 and Fig. 5.13 respectively. Thus, SRE can be used to monitor the change in texture from the core to the periphery of a grade 2 or grade 3 mass. The LGRE feature was minimum for region 3 and maximum for region 2 in grade 2 and grade 3 masses for all winsizes. However, for winsize 13 the LGRE and the RLN were maximum as illustrated in Fig. 5.14 and Fig. 5.15 respectively. The two tailed two sample t-test for difference of means was used to determine if the difference between the means of any two regions was statistically significant. These results are shown in Table 5.6. There was no statistical difference between the means of texture feature HGRE for region 1 and region 2, and for texture feature RP for region 1 and region 3. Further analysis with the one tailed two sample t-test for difference of means on the same data, shows that the mean of texture feature LRE of region 1 was greater than that of region 2 and that of region 2 is greater than that of region 3. For texture features SRE, GLN and RLN, the mean of region 1 was less than that of region 2 and that of region 2 was less than that of region 3. Hence LRE, SRE, GLN and RLN showed consistency in their performance. Thus SRE, GLN, RLN and LRE can be used to monitor the change in texture from the core to

the periphery of grade 2 and grade 3 masses. Fig. 5.16 to Fig5.19 illustrate scatter plots for the run length statistical features for grade 2 and grade 3 masses. From visual inspection, the run length texture features RLN and LGRE can separate grade 2 and grade 3 masses because there exists a margin of separation between the two grades as shown in Fig.5.19. In Fig 5.19a, the margin of separation for the RLN texture feature is located in the region 1 plane while in Fig.5.19b, the margin of separation for the LGRE texture feature is situated in the region 3 plane. Fig.5.16 , Fig5.17and Fig.5.18 show that SRE,GLN, RP and HGRE do not exhibit a distinct margin separation between grade 2 and grade 3 masses , however with the application of a clustering algorithm the presence of such margin can be discovered. Further investigation with the two tailed two sample t-test assuming unequal variance, indicated that only texture feature RLN rejected the null hypothesis with p-value = 0.0001, as shown in table 5.7

Fig. 5.20 to Fig. 5.23 illustrate the variation of some second order statistical texture feature of region 1, region 2 and region 3 with winsize. The contrast decreases with an increase in winsize and region 1 had minimum values for all winsizes while region 3 had maximum values. Both correlation, energy and homogeneity increase with an increase in winsize with region 3 having minimum values while region 1 exhibited maximum values for correlation texture feature. Fig. 5.24 to 5.25 illustrates the scatter plots for the second order texture features for the grade 3 and grade 2 masses. From visual inspection there is no margin of separation between the two grades of masses, hence these features cannot be used for tumour grading in mammography. However, the presence of hidden margins of separation can be revealed with clustering algorithms.

Fig.5.26 shows the variation of the sum of variance with winsize for the different masses. As the winsize increases the sum of variance decreases but the overall distances between the sum of variance of the regions increases, hence winsize 13 represents measurable distances of separation between the sum of variance of region 1 and region 2 and also region 2 and region 3. The distances of separation of sum entropy and entropy between region 1 and region 2, region 2 and region 3 are very small as shown in Fig.5.29 and Fig.5.31 respectively while the texture feature, difference entropy gives measurable distance of separations for these regions. The two tailed two sample test was applied to the data to verify if there were statistical differences between the mean texture features of these regions. It revealed that there were no

statistical differences between the means of texture features, energy, homogeneity and entropy of region 1 and region 2. Further analysis with the one tailed two sample t-test for difference of means, showed that the mean contrast of region 1 is greater than that of region 2 and that of region 2 is greater than that of region 3. For, sum variance, difference variance and difference entropy, the means of region 1 were less than that of region 2 and that of region 2 were less than that of region 3 as shown in Table 5.8. Table 5.9 shows that there were no statistical differences between means of grade 2 and grade 3 second order texture features. Hence second order texture features cannot be used for tumour grading.

Statistical analysis had shown that means of skewness, SRE, GLN, RLN, contrast, sum variance, difference variance and difference entropy decrease in the following order region 1, region 2 and region 3 while for correlation and LRE the reverse is true. Statistically the result shows that there is a difference between the mean values of grade 2 and grade 3 masses for the following texture features, entropy, skewness, variance and RLN

5.9 Conclusion

This study shows that there exists a statistical measurable change in the magnitude of some texture features from the core to the periphery of grade 2 and grade 3 masses. Skewness, SRE, GLN, RLN, contrast, sum variance, difference variance, LRE and difference entropy texture features present measurable statistical changes between these regions (p-values <0.05) for winsize 13. The magnitudes of these changes might depend on the winsize. These features can be used for tumour modelling, where, tumour growth is related to the change in texture features for these masses.

This study also illustrates the existence of statistical difference in mean values between grade 2 and grade 3 for, entropy, skewness, variance and RLN as shown in Table 5.5 and Table 5.7. Thus, these texture features can be used for tumour grading.

However, the number of masses assessed in this study was limited and further study would be useful to better understand this phenomenon and to extend it to include tomographic and tomo-synthetic type breast imaging so that the problem of overlying tissue is overcome.

5.10 References

[1] R. M. Haralick and . S. Karthikeyan , "Textural features for image classification," *IEEE Transactions on systems, man, and cybernetics,* vol. 6, pp. 610-621, 1973.

[2] E. A. Sickles, C. J. D'Orsi, L. W. Bassett, C. M. Appleton, W. A. Berg and . E. S. Burnside, Acr bi-rads® mammography. ACR BI-RADS® atlas, breast imaging reporting and data system, vol. 5, American College of Radiology (ACR), 2013.

[3] S. Berkman, C. Heang-Ping, P. Nicholas, A. H. Mark and M. G. Mitchell, "Computerized characterization of masses on mammograms: The rubber band straightening transform and texture analysis," *Medical Physics,* vol. 26, no. 4, pp. 516-526, 1998.

[4] M. E Mavroforakis, H. V. Georgiou, N. Dimitropoulos, D. Cavouras and S. Theodoridis, "Mammographic masses characterization based on localized texture and dataset fractal analysis using linear, neural and support vector machine classifiers," *Artificial Intelligence in Medicine,* vol. 37, no. 2, pp. 145-162, 2006.

[5] S. V. da Rocha, G. B. Junior, C. A. Silva, A. C. de Paiva and M. Gattass, "Texture analysis of masses malignant in mammograms images using a combined approach of diversity index and local binary patterns distribution.","* Expert Systems with Applications,* vol. 66, pp. 7-19, 2016.

[6] A. Kamra, V. K. Jain, S. Singh and S. Mittal, "Characterization of Architectural Distortion in Mammograms Based on Texture Analysis Using Support Vector Machine Classifier with Clinical Evaluation," *Journal of digital imaging,* Vols. 104-114, no. 1, p. 29, 2016.

[7] J. Dheeba, A. Singh and S. T. Selvi, "Computer-aided detection of breast cancer on mammograms: A swarm intelligence optimized wavelet neural network approach," *Journal of biomedical informatics,* vol. 49, pp. 45-52, 2014.

[8] M. L. Giger, H. Chan and J. Boone, "Anniversary paper: History and status of CAD and quantitative image analysis: the role of Medical Physics and AAPM," *Medical physics,* vol. 35, no. 12, pp. 5799-5820, 2008.

[9] E. A. Rakha, J. S. Reis-Filho, F. Baehner, D. J. Dabbs, T. Decker, V. E. Eusebi, . S. B. Fox, S. Ichihara, J. Jacquemier, S. R. Lakhani and J. Palacios, " Breast cancer prognostic classification in the molecular era: the role of histological grade," *Breast Cancer Research,* vol. 12, no. 4, p. 207, 2010.

[10] C. Varela, S. Timp and N. Karssemeijer, "Use of border information in the classification of mammographic masses."," *Physics in Medicine and Biology,* vol. 51, no. 2, p. 425, 2006.

[11] W. Xie, Y. Li and Y. Ma, "Breast mass classification in digital mammography based on extreme learning machine.," *Neurocomputing,* vol. 173, pp. 930-941, 2016.

[12] I. Zyout, J. Czajkowska and M. Grzegorzek, "Multi-scale textural feature extraction and particle swarm optimization based model selection for false positive reduction in mammography," *Computerized Medical Imaging and Graphics,* vol. 46, pp. 95-107, 2015.

[13] R. M. Rangayyan, T. M. Nguyen, F. J. Ayres and A. K. Nandi, "Effect of Pixel Resolution on Texture Features of Breast Masses in Mammograms," *Journal of digital imaging,* vol. 23, no. 5, pp. 547-553, 2010.

[14] J. Y. Choi,, D. H. Kim, K. N. Plataniotis and Y. . M. Ro, ""Classifier ensemble generation and selection with multiple feature representations for classification

applications in computer-aided detection and diagnosis on mammography," *Expert Systems with Applications,* vol. 46, pp. 106-121, 2016.

[15] A. Fritz, "Statistical texture measures computed from gray level coocurrence matrices," *Image Processing Laboratory, Department of Informatics, University of Oslo,* vol. 20, pp. 1-14, 1995.

[16] A. K. Mohanty, R. M. Manas, S. Beberta and K. S. Lenka, "Texture-based features for classification of mammograms using decision tree," *Neural Computing and Applications,* vol. 23, no. 3-4, pp. 1011-1017, 2013.

[17] N. H. Eltonsy, G. D. Tourassi and A. S. Elmaghraby, "A concentric morphology model for the detection of masses in mammography," *IEEE transactions on medical imaging,* vol. 26, no. 6, pp. 880-889, 2007.

[18] Y. Wang, J. Li and X. Gao, "Latent feature mining of spatial and marginal characteristics for mammographic mass classification," *Neurocomputing,* pp. 107-118, 2014.

[19] N. R. Mudigonda, R. Rangayyan and J. L. Desautels, "Gradient and texture analysis for the classification of mammographic masses.," *IEEE transactions on medical imaging,* vol. 19, no. 10, pp. 1032-1043, 2000.

[20] American College of Radiology, Breast Imaging Reporting and Data System (BI-RADS), 2nd ed., Reston, VA: American College of Radiology, 2003.

CHAPTER 6: CONCLUSION AND FUTURE WORK

6.1 Conclusion

Segmentation algorithms and texture analysis are useful tools to analyze mammograms. Segmentation methods partition mammograms into a smaller number of meaningful regions while texture analysis derives texture features from these regions. When attempting to quantitatively compare and categorize these regions of clinical mammography images, for purposes of screening, diagnosis, prognostication or follow up, these texture features are fundamental in assessing the image derived traits of these regions.

The first section of the thesis focused on some of the segmentation algorithms currently used for the delineation of mammographic masses. A segmentation method partitions the mass region from the surrounding breast tissues so that the contour delineating the mammographic mass can be clearly identified. These contours provide shape-based descriptors which are an important part of the assessment of the clinical pathology of these masses. Active contour segmentation algorithms are commonly used for delineation of mammographic masses. However, in digital mammography, these segmentation algorithms are often presented with masses having variable signal intensity (often including relative low signal regions within the mass), and masses with weak and ill-defined boundaries. This makes contouring of the masses more challenging. Low signal regions within a mass can result in the entrapment of an evolving contour, while weak boundaries can provide a pathway for contour leakage, and these can give rise to segmentation outcomes that are not reproducible and may not be reliably representative of the shape of the masses. As a result, the placement of the initial contour (or starting point (seed point) for deriving a contour) for curve evolution can influence the outcome of the segmentation process and this is undesirable.

This study has quantified changes in shaped-based descriptors due to changes in the location of the initial contour for curve evolution in mammographic mass delineation. It has shown that

boundary moments are sensitive to the placement of initial level set contours while Fourier descriptors, shape convexity and shape rectangularity exhibit a certain degree of robustness to changes in the location of these contours. [1]

This study proposes an active contour segmentation method for digital mammographic masses whose final level set contours are independent of the positions of the initial contours. This approach utilizes the fast global minimization model, whose energy functional is convex, hence the curve evolution process does not require the implementation of the contour re-initialization procedures because deformable contours are not expressed as zero level sets of higher dimensional functions. However, a fast global minimization model requires a fixed threshold value of the global minimum for the convex energy functional. This presents a problem in segmenting a database of mammographic masses. A fixed threshold value for the global minima of a database of mass lesions is not feasible because the grey level intensity distributions of the background tissues surrounding most masses are heterogeneous. A fixed threshold value may underestimate or overestimated the optimum threshold values of these masses and consequently lead to unsuitable segmentation. Furthermore, hand tuning each threshold value for an optimum mass boundary delineation of each mass in the database is time consuming.

This study proposes an automatic parameter tuning process that embraces the morphological characteristics of each mass lesion, and provides a reliable threshold value. This novel approach makes use of reliable information from the random walk probability matrix of each digital mass to provide a reliable mass-dependent estimate of the threshold value for each global minimizer symbolising the intrinsic nature of the mass lesion [2]. It utilises the particle swarm optimization algorithm to provide a mass-specific threshold value of the global minimum for the convex energy functional of each mass in the database.

The second section of the thesis focuses on tumour modelling and tumour grading in mammography as proof of concepts. Generally mammographic masses have highlighted the focal core region surrounded with successively dimmer concentric layers radiating outwards

with diverse clinical indicators. This suggests a change in texture from the core of the mass to its periphery hence evidence of the concept of tumour modelling in mammography. We have implemented a concentric morphology model to investigate the above concept in biopsy-proven grade 2 and 3 masses.

This study shows that there exists a statistical measurable change in some texture features from the core to the periphery of grade 2 and grade 3 masses. Skewness, SRE, GLN, RLN, contrast, sum variance, difference variance, LRE and difference entropy texture features present measurable statistical changes between region 1 and region 2, region 2 and region 3 (p-values <0.05) for winsize 13. The magnitudes of these changes may depend on the size of the sampling window,

In mammography the grade of a mammographic mass is an indication of the degree of its abnormality. This study shows the existence of a visual margin of separation of the RLN and LGRE run length texture features between grade 2 and grade 3 masses, hence the feasibility of using texture analysis as a tool in tumour grading. However, the two tailed two sample t-test reveals that, there are statistical differences between the means of grade 2 and grade 3 for, entropy, skewness, variance and RLN texture features for winsize13. The margins of separations may also depend on the concentric region of interest, that is, region 1 (outer boundary region of the mass) or region 3 (core of the mass). Application of clustering algorithms on all these texture features might also reveal hidden margins of separations between these grades of masses.

Computer aided detection (CAD) systems are currently used as prompting systems in breast imaging centers. The core of these systems are segmentation and texture analysis algorithms. The above findings can be incorporated into these systems to improve the segmentation algorithms and also to explore the concept of texture analysis in tumour modelling and tumour grading and their relationship to the different tumour growth models presented in literature.

6.2 Limitation of the Study

Some limitations were experienced during the course of this study. The mammography unit used for acquisition of the original images was replaced during the study and the Picture Archiving and Communication System (PACS) was unavailable for a protracted period and the archives were not made readily available on the new PACS. Thus, the number of images available for analysis was limited to those originally available. As this study was done to develop the theory and methods for the analysis of mammographic masses it was felt that the 15 biopsy proven mammograms included would be sufficient, but that a larger study should be done in future to be able to establish the technique and apply it to a wider range of mammographic images.

6.3 Future work

Mammography, although debated and contentious in current literature, is widely accepted as being a very useful tool in the armamentarium available to the clinician in assessing and treating breast pathology. There is still a large amount of work to be done to fully understand the imaging of the breast and the effects of the many and varied modalities available for the acquisition and analysis of breast images. This work is a small contribution to progress in this field.

There is a need to do more detailed analysis of the transition zone which moves from the area which is predominantly over the tumour to the area which surrounds the tumour. This should also be done on images acquired using breast tomosynthesis or breast computed tomography so that the transition largely excludes overlying tissues. This should allow more accurate understanding of the image characteristics of tumours as represented by their texture and morphologic measures. This field of study is still in a developmental stage and much other work also can be proposed and needs to be done before automated diagnosis and detection

could be achieved with accuracies approaching (or even exceeding) those achieved by expert readers.

The extension of breast image analysis to images acquired and analysed by an increasingly diverse and complex set of tomographic algorithms is also needed. This should also include some standardisation of metrics so that understanding of the range of measures produced is possible.

Only when all this has been done can the application of many of these methods of breast image analysis and quantification be meaningfully used as a tool for the modelling and staging of breast tumours.

6.4 REFERENCES

[1] S. N. Acho and W. D. Rae, "Dependence of shape-based descriptors and mass segmentation areas on initial contour placement using the Chan-Vese method on digital mammgrams," *Computational and Mathematical Methods in Medicine,* vol. 2015, no. Article ID 349874, 2015.

[2] S. N. Acho and W. D. Rae, "Interactive breast mas segmentation using a convex active contour model with optimal threshold values," *Physica Medica*, vol. 32, pp. 1352-1359, 2016.

6.5 ACKNOWLEDEMENTS

I would like to express my special appreciation and thanks to my promoter, Prof. William Rae, you have been a tremendous mentor to me. I would like to thank you for your encouragement and for allowing me to grow and to think as a research scientist. Your advice on this topic of research as well as other topics have been invaluable.

I would especially like to thank the Department of Radiology, Universitas Academic Hospital, which allowed us access to their archived mammographic images, Dr. G. Van Der Westhuizen who provided ground truths for this study and Mrs. Ina Nel for her positive attitude and words of encouragement during the course of this study.

My sincere thanks to all my colleagues for their words of encouragement and support throughout this study.

A special thanks to my late parents. Words cannot express how grateful I am to my parents for all the sacrifices that they made on my behalf. Mama and Papa, your prayers have sustained me thus far and will continue to sustain me. Thank You.

I would also like to thank to my beloved husband, Prof. T. M. Acho. I can't thank you enough for your support and encouragement throughout this experience. To my beloved daughter Petra-Marie and my beloved son, Christian-Thomas, I would like to express my thanks for being such wonderful kids, always cheering me up.

My sincere thanks to the Blessed Virgin Mary for all your prayers and intercessions before the throne of your son Jesus Christ for His guidance, wisdom and knowledge needed for the completion of this degree.

Finally, I thank, the Most Holy Trinity, for all the difficulties I encountered during the course of this study. I have experienced Your guidance, protection and faithfulness to Your Word each day. You are the one who let me finish my degree. I will keep on trusting in You for my entire future. Thank You.

6.6 APPENDIXES

Appendix 1: S. N. Acho and W. D. Rae, "Dependence of shape-based descriptors and mass segmentation areas on initial contour placement using the Chan-Vese method on digital mammgrams," *Computational and Mathematical Methods in Medicine,* vol. 2015, no. Article ID 349874, 2015.

Appendix II: S. N. Acho and W. D. Rae, "Interactive breast mas segmentation using a convex active contour model with optimal threshold values," *Physica Medica,* vol. 32, pp. 1352-1359, 2016

Hindawi Publishing Corporation
Computational and Mathematical Methods in Medicine
Volume 2015, Article ID 349874, 16 pages
http://dx.doi.org/10.1155/2015/349874

Research Article

Dependence of Shape-Based Descriptors and Mass Segmentation Areas on Initial Contour Placement Using the Chan-Vese Method on Digital Mammograms

S. N. Acho and W. I. D. Rae

Department of Medical Physics, University of the Free State, P.O. Box 339, Bloemfontein 9300, South Africa

Correspondence should be addressed to S. N. Acho; gnbisa.md@ufs.ac.za

Received 16 February 2015; Revised 14 July 2015; Accepted 30 July 2015

Academic Editor: Chuangyin Dang

Variation in signal intensity within mass lesions and missing boundary information are intensity inhomogeneities inherent in digital mammograms. These inhomogeneities render the performance of a deformable contour susceptible to the location of its initial position and may lead to poor segmentation results for these images. We investigate the dependence of shape-based descriptors and mass segmentation areas on initial contour placement with the Chan-Vese segmentation method and compare these results to the active contours with selective local or global segmentation model. For each mass lesion, final contours were obtained by propagation of a proposed initial level set contour and by propagation of a manually drawn contour enclosing the region of interest. Differences in shape-based descriptors were quantified using absolute percentage differences, Euclidean distances, and Bland-Altman analysis. Segmented areas were evaluated with the area overlap measure. Differences were dependent upon the characteristics of the mass margins. Boundary moments presented large percentage differences. Pearson correlation analysis showed statistically significant correlations between shape-based descriptors from both initial locations. In conclusion, boundary moments of digital mass lesions are sensitive to the placement of initial level set contours while shape-based descriptors such as Fourier descriptors, shape convexity, and shape rectangularity exhibit a certain degree of robustness to changes in the location of the initial level set contours for both segmentation algorithms.

1. Introduction

Breast masses are one of the most common indications of breast cancer. They are frequently identified on mammograms, due to their saliency relative to the surrounding regions and also to comparable regions on the mammograms with the same projection of the opposite breast [1]. Computer Aided Detection algorithms for breast mass classification exploit suitable shape-based descriptors derived from the mass boundary which are powerful enough to differentiate between benign and malignant masses. Segmentation algorithms are necessary for mass contouring in direct digital mammography. However, in this imaging modality, mass margins are embedded in complex backgrounds of overlying and underlying tissues which creates missing boundary information and local minima where a deforming contour can be entrapped and as a consequence produces an undesirable segmentation outcome. Moreover, the wide dynamic range of flat panel detector systems of direct digital mammography units records small differences between the attenuation coefficients of structures or regions present in a mass lesion and they are clearly distinguishable over a wide range of densities, whereas in film screen mammography the exposure latitude of the film limits the dynamic range of information captured on the film. Hence, masses which may have appeared as dense structures without significant topographical relief features on film screen mammograms can emerge following digital imaging, as regions with varying densities on soft copy display. Enhancement of these variations, following postprocessing by the processing algorithms of the manufacturer, may also be present. Usually, small differences in densities may sometimes appear as low signal areas which can act as local

minima for contour entrapment each time an evolving curve determines its path within the mass lesion. Consequently, local minima and missing boundary information render deformable contours susceptible to their initial locations.

A geometric active contour is a deformable contour based approach for image segmentation. In breast mass segmentation, an initial contour is deformed and driven by a partial differential equation (PDE) towards the boundary of the candidate mass. It is categorized into two groups: edge based models [2–4] and region based models [5–13]. Both models make use of a stopping term which reduces the speed of the evolving contour as it approaches the boundary of the object and finally reaches a steady state at the boundary. In edge based models, the stopping term utilizes an edge indicator function modelled on the image gradient; consequently, objects with weak and noisy boundaries may present some difficulties to this segmentation model [14, 15].

The Chan-Vese region based algorithm models energy functionals as a competition of regional statistical information [16]. They defined the stopping term as a competition of the first moments of the local intensity distribution of the foreground and the background within a narrowband, which takes into consideration only pixels which will influence the propagation of the interface (zero level set function) between these two regions. The energy functionals drive the initial contour from its initial location toward a desirable local minimum, which in principle should correspond to the delineated boundary of an expert radiologist. However, these are determined by localized statistics; hence, the evolution of the curve becomes sensitive to the location of the initial level set contour and segmentation results will depend on the placement of this contour, especially when tuning parameters for an arbitrary collection of masses are fixed. This becomes evident during segmentation of direct digital masses with obscured or ill-defined margins and low signal areas within.

The active contours with selective local or global segmentation model [9] are a region based energy functional formulated as a signed pressure force function which propagates the initial contour by modulating the signs of the pressure forces inside and outside the region of interest. These pressure forces are derived from the means of the local intensity distributions of the foreground and the background. The algorithm penalizes the level set function to be binary and regularizes it with a Gaussian smoothing kernel. It can effectively handle images with weak edges and interior intensity inhomogeneity.

In most segmentation problems, the initial contour is either drawn by the operator or estimated from other segmentation algorithms [17, 22–25] and this may place the initial level set contour on different locations within the mass. Any variation in segmentation outcomes will cause changes in shape-based descriptors and the area occupied by the segmented mass. Variations in segmentation outcomes which are due to the placement of the initial level set contours in complicated images have been mentioned [11]. Mass lesions on mammograms are complicated image domains for curve evolution and variations in mass lesion segmented areas and their influences on shape-based feature vectors due to changes in the placement of the initial level set contours are not found in the literature.

Understanding these inconsistencies can improve the choice of tuneable parameters and initial contour locations for curve evolution either for a data set of mass lesions with labelled margin characteristics or unlabelled margin characteristics. Shape-based descriptors [26–28] are feature vectors in training sets for binary classification of mass lesions in mammography and changes in these descriptors can play a role in determining the interclass separability measures, the choice of margin hyperplanes, and hence the classification efficiencies of these algorithms.

In this study, we investigate changes in one-dimensional shape-based descriptors and the segmented areas of masses in direct digital mammograms due to changes in the location of the initial level set contours with the implementation of the Chan-Vese segmentation method and the active contours with selective local or global segmentation model. Two groups of masses are considered in this study, one with obscured or ill-defined margins and low signal areas within and the other with well-defined and distinct margins. We consider a contour which encloses the mass lesion and is propagated towards the margin of the lesion. We propose a semiautomatic method which derives the initial contour as a curve connecting points with maximum gradient in the radial direction, representing an optimum curve characterizing the intrinsic shape of the mass lesion, and then assess the differences in the segmentation results.

2. Background to Mathematical Methods

In mammography, smoothed images present topological surfaces that can be thresholded into multiple layers to obtain topographical relief maps of dominant structures found on the images. Mammograms are filtered with edge-preserving denoising methods such as weighted total variation (TV) scale-space smoothing technique [29, 30] to remove noise and fine details while preserving dominant edge characteristics through different degrees of smoothing.

2.1. Weighted Total Variation Scale-Space Smoothing Technique. Suppose $I : \Omega \rightarrow \mathbb{R}$ denotes an image and $\Omega \subset \mathbb{R}^2$ the image domain. The variational approach for image denoising for this model involves the minimization of the following energy functional:

$$E_{\mathrm{TV}}(I, \lambda) = \int_{\Omega} \left(|\nabla I| + \lambda \left(I - I_0 \right)^2 \right) dx\, dy, \tag{1}$$

where I_0 is the noisy input image and I its regularized approximation. λ is the Lagrange multiplier indicating the scale of detail desired in the smoothed image. Bresson et al. proposed a modified model [30] in which the L^2-norm square of Rudin et al.'s model is replaced with an L^1-norm to preserve image contrast [31] and in addition the TV norm of I is multiplied with a function, g, which is an edge indicator function. This represents the weighted TV model with

an L^1-norm as a data fidelity measure. The energy functional for minimization is given as

$$E_{g\mathrm{TV}}(I,\lambda)=\int_{\Omega}\left(g\left|\nabla I\right|+\lambda\left|I-I_0\right|\right)dx\,dy \tag{2}$$

with

$$g=\frac{1}{1+\Upsilon\left|\nabla G_\theta * I_0\right|^2}, \tag{3}$$

where Υ is a constant >0 and G_θ is a Gaussian kernel with standard deviation, θ. The minimization of $E_{g\mathrm{TV}}(I,\lambda)$ results in the following weighted TV flow equation:

$$I_t=\mathrm{div}\left(g\frac{\nabla I}{|\nabla I|}\right)+\lambda\left(\frac{I-I_0}{|I-I_0|}\right). \tag{4}$$

For small values of λ, the degree of image smoothing increases and edge is preserved; therefore, the global boundary information which is essential for segmentation algorithms can be modelled as the initial contour for the gradient descent flow equation of the level set. This contour will depend on the boundary properties of a given mass lesion.

2.2. Chan-Vese's Piecewise Constant Model for Binary Segmentation. Suppose C is an evolving curve that partitions the image domain into the foreground, Ω_1, and the background, Ω_2. The Chan-Vese model [16] seeks an optimal contour, representing the boundary of an object by minimizing the following energy functional:

$$F(C,c_1,c_2)=\mu\mathrm{length}(C)+\upsilon\mathrm{Area}(\mathrm{inside}(C))+F_{\mathrm{data}}, \tag{5}$$

where F_{data} represents the regional term guiding the contour in the image domain and is given by

$$F_{\mathrm{data}}=\lambda_1F_1(C)+\lambda_2F_2(C) \tag{6}$$

in which

$$\begin{aligned}F_1(C)&=\int_{\mathrm{inside}(C)}\left|I(x,y)-c_1\right|^2dx\,dy,\\ F_2(C)&=\int_{\mathrm{outside}(C)}\left|I(x,y)-c_2\right|^2dx\,dy.\end{aligned} \tag{7}$$

$\mu\geq 0$, $\nu\geq 0$, and λ_1 and λ_2 are positive constants while the average image intensities of regions inside and outside the contour are c_1 and c_2, respectively. In level set formulation, the interface of the foreground and background is embedded as the zero level set of a Lipschitz function, $\phi(x,y)$: $\Omega\rightarrow\mathbb{R}$ with $\phi(x,y)>0$ for pixel positions in Ω_1 and $\phi(x,y)<0$ for pixel positions in Ω_2 whilst $\phi(x,y)=0$ on the curve C. Using the Heaviside step function, $H_\varepsilon(\phi)$, $F(C,c_1,c_2)$ can be expressed as

$$\begin{aligned}&F(C,c_1,c_2)\\ &=\mu\int_{\Omega}\left|\nabla H_\varepsilon(\phi)\right|dx\,dy\\ &\quad+\lambda_1\int_{\Omega}\left(I(x,y)-c_1\right)^2H_\varepsilon(\phi)\,dx\,dy\\ &\quad+\lambda_2\int_{\Omega}\left(I(x,y)-c_2\right)^2\left(1-H_\varepsilon(\phi)\right)dx\,dy.\end{aligned} \tag{8}$$

Minimizing $F(C,c_1,c_2)$ with respect to ϕ yields the following gradient descent flow:

$$\begin{aligned}\frac{\partial\phi}{\partial t}&=\delta_\varepsilon(\phi)\left[\mu\nabla\left(\frac{\nabla\phi}{|\nabla\phi|}\right)-\upsilon-\lambda_1\left(I(x,y)-c_1\right)^2\right.\\ &\quad\left.+\lambda_2\left(I(x,y)-c_2\right)^2\right],\end{aligned} \tag{9}$$

where $\delta_\varepsilon(\phi)$ is the Dirac function.

2.3. Active Contours with Selective Local or Global Segmentation Model. The signed pressure force function [9] is derived from the means of regions inside and outside the contour and it is defined as

$$\mathrm{spf}(I(x,y))=\frac{I(x,y)-(c_1+c_2)/2}{\max\left(\left|I(x,y)-(c_1+c_2)/2\right|\right)},\quad x,y\in\Omega_p, \tag{10}$$

where c_1 and c_2 are defined in (8). The active contour with selective local or global segmentation model utilizes the geodesic active contour to formulate the level set equation as

$$\begin{aligned}\frac{\partial\phi}{\partial t}&=\mathrm{spf}(I(x,y))\cdot\left(\mathrm{div}\left(\frac{\nabla\phi}{|\nabla\phi|}\right)+\alpha\right)|\nabla\phi|\\ &\quad+\nabla\mathrm{spf}(I(x,y))\cdot\nabla\phi,\quad x,y\in\Omega_p.\end{aligned} \tag{11}$$

Using the Gaussian filtering process to regularize the level set function, the above equation can be written as follows:

$$\frac{\partial\phi}{\partial t}=\mathrm{spf}(I(x,y))\cdot\alpha\left|\nabla\phi\right|,\quad x,y\in\Omega_p, \tag{12}$$

where α is a tuneable parameter.

3. Method

3.1. Data Set Description. Direct digital mammograms were acquired from a Hologic Selenia Dimensions system with an image receptor consisting of a 70 μm pixel pitch selenium direct-capture detector. Ninety mammograms with mass lesions were selected for this study. Forty mammograms had masses with low signal areas within the mass and margins described as obscured, or ill-defined, while the others had masses with well-defined or distinct margins. On each mammogram, the region of interest containing the mass lesion was cropped and then resized to a 208 × 208 matrix to create a submammogram. Each submammogram was denoised and thresholded to localize the initial level set contour.

3.2. Search Space for Localizing the Initial Level Set Contour. The weighted total variation scale-space smoothed breast mass region is represented as a topological surface in which the grey level value of each pixel is the height of the surface. Let $IS:\Omega\rightarrow\mathbb{R}$ denote a smoothed image and $\Omega\subset\mathbb{R}^2$ the image domain. The image domain Ω is thresholded into

(a) (b) (c) (d) (e)

Figure 1: Search space for localizing the initial contour. (a) The original mass lesion, (b) the weighted TV flow denoised image with $\lambda = 0.05$, (c) dense nested patterns of iso-level contours representing the search space for localizing the initial contour on the gradient map, (d) radial distances from a reference point to the iso-level contours, and (e) initial level set contour, representing points with maximum gradient in the radial direction within a predefined radius.

multiple regions with an ordered set of equally spaced grey level threshold values within the intensity range of the image domain [32–34]. Suppose $I_{\max}$ = the maximum grey level intensity in the image domain; $I_{\min}$ = minimum grey level intensity; $W = \{w_1, w_2, w_3, \ldots, w_N\}$, a finite sequence of equally spaced partition weights in ascending order; N = number of threshold values; and $T = \{t_1, t_2, t_3, \ldots, t_N\}$, an ordered set of equally spaced grey level threshold values; then,

$$T = I_{\max} * W \tag{13}$$

with $t_N \leq I_{\max}$ and $t_1 \geq I_{\min}$.

The subregions in the image domain with grey level intensities less than or equal to the threshold value, t_i, are given as

$$R(t_i) = \{(x, y) \mid IS(x, y) \leq t_i\}, \quad \forall (x, y) \in \Omega, \tag{14}$$

and the iso-level contours $C(t_i)$'s of these regions are boundaries of $R(t_i)$. The iso-level contour map of the image domain represents the set of all $C(t_i)$ for $i = 1 : N$. A graph-based representation of the iso-level contour map evaluates the enclosure relationship between an iso-level contour and its nearest neighbour, to identify the path to the base contour that delineates the mass. Details of this method can be found in the literature [32, 33]. In our implementation, the boundary region of the breast mass is the region around the base contour with a dense nested pattern of iso-level contours, indicating the search space for the actual boundary of the mass and the placement of the initial level set contour. The dense nested pattern of iso-level contours is extracted and superimposed on the gradient map of the smoothed image.

3.3. Placement of the Initial Level Set Contour. A set of uniformly spaced radial lines, $L = \{l_1, l_2, \ldots, l_m\}$, are generated from a point close to the centre of mass of the innermost iso-level contour, defining the search space on the gradient map of the mass as shown in Figure 1(d). Let this point be the reference point. The gradient strength is noted at every point of intersection of the nested iso-level contours and radial lines. Along each radial line, l_i, for $i = 1, 2, \ldots, m$, the coordinates of the point of intersection with the greatest gradient strength are noted and the radial distance from this point to the reference point is calculated and noted as r_i.

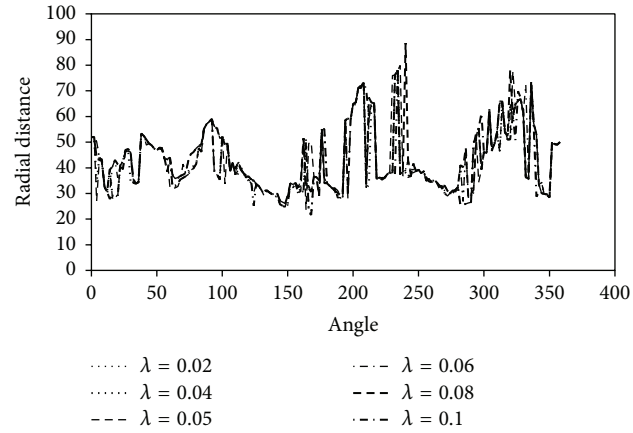

Figure 2: Variation of the radial distance function of the initial level set contours sampled at an angle of 1° with different λ's for the mass lesion in Figure 1.

Let $r_{\text{ave}} = (1/m)\sum_{i=1}^{m} r_i$ and $r_{\text{std}} = \sqrt{\sum_{i=1}^{m}(r_i - r_{\text{ave}})^2/(m-1)}$; then radial description of the initial level set contour is given by

$$r_i = \begin{cases} r_i, & r_i < r_{\text{ave}} + n r_{\text{std}} \\ r_{\text{ave}}, & r_i \geq r_{\text{ave}} + n r_{\text{std}}, \end{cases} \tag{15}$$

$$i = 1, 2, \ldots, m, \ n = 1 \text{ or } 2.$$

The spatial coordinates of the points of intersection of r_i's and the iso-level contours are the coordinates of the initial level set contour. Figure 1 illustrates the summary of the methodology in acquiring the initial level set contour and Figure 2 shows the variation of the radial distance function, r_i, for $i = 1 : m$, with the scale of observation, λ, in weighted total variation scale-space smoothing technique. The radial distance function of the initial level set contour corresponds to the radial distance from each point on the initial contour to the reference point with a sampling angle of 1°.

3.4. Evaluation Metrics of Segmentation Results. Manually drawn initial contours and those obtained from our proposed method were propagated with the Chan-Vese algorithm and

the active contours with selective local or global segmentation model. Feature vectors representing boundary-based shape signatures and the areas occupied by the segmented mass lesions were assessed to provide relative measures of the differences between the segmented mass lesions.

3.4.1. Area Metric of Relative Size of Segmented Mass Lesion. Let im$Y$ represent the binary image obtained by evolving the initial level set contour from our proposed method and im$X$ from the manually drawn initial level set contour; then, the area overlap measure, which is the Jaccard similarity coefficient between the binary images, im$X$ and im$Y$, is given as

$$\mathrm{JSC}\left(\mathrm{im}X, \mathrm{im}Y\right) = \frac{\mathrm{im}Y \cap \mathrm{im}X}{\mathrm{im}Y \cup \mathrm{im}X}. \tag{16}$$

JSC(im$X$, im$Y$) lies between 0 and 1. A perfect match between im$X$ and im$Y$ is achieved as JSC(im$X$, im$Y$) $\rightarrow$ 1, consequently, the same segmentation outcome for both initial level set contours.

3.4.2. Evaluation Metrics of Shape-Based Descriptors

Boundary Moments. A boundary-based shape signature of the segmented mass lesion from each initial contour model is represented as the centroid distance function, which is a one-dimensional function representing the Euclidean distance $r(n)$ between an ordered set of boundary coordinates $((x(n), y(n))$, for $n = 0, 2, 3, \ldots, N-1)$ and the centroid (xc, yc) signifying the centre of mass of the binary image generated from the contour:

$$r\left(n\right) = \sqrt{\left(\left(x\left(n\right) - xc\right)^2 + \left(y\left(n\right) - yc\right)^2\right)}, \tag{17}$$

where N is the total number of points on the contour.

The centroid distance function captures the local and global characteristics of the final shape of the segmented mass lesion. Its statistical characteristics are assessed as shape features derived from the contour sequence moments m_p and μ_p [35] where the pth contour sequence moment is estimated as

$$m_p = \frac{1}{N}\sum_{n=0}^{N-1}\left[r\left(n\right)\right]^p \tag{18}$$

and the pth central moment is estimated as

$$\mu_p = \frac{1}{N}\sum_{n=0}^{N-1}\left[r\left(n\right) - m_1\right]^p. \tag{19}$$

These shape features are normalized low-order boundary moments [36, 37] described as

$$\begin{aligned} F_1 &= \frac{\left(\mu_2\right)^{1/2}}{m_1}, \\ F_2 &= \frac{\left(\mu_4\right)^{1/4}}{m_1}, \\ F_3 &= F_1 - F_2, \end{aligned} \tag{20}$$

where F_1 is the normalized amplitude variation and F_2 and F_3 are indicators of shape roughness.

Spicules are fine extensions radiating from the margin of a mass lesion. The presence of these boundary features generates variations in the radial distances, which are indicative of contour roughness along the boundary of a mass lesion. The evaluation metric $\%\Delta F_i(\mathrm{im}X, \mathrm{im}Y)$ is the percentage change in the degree of spiculation between im$X$ and im$Y$ and is expressed as the percentage difference in the boundary moments, F_i's:

$$\%\Delta F_i\left(\mathrm{im}X, \mathrm{im}Y\right) = \left|\frac{F_i\left(\mathrm{im}Y\right) - F_i\left(\mathrm{im}X\right)}{\mathrm{average}\left(F_i\left(\mathrm{im}Y\right), F_i\left(\mathrm{im}X\right)\right)}\right| \times 100. \tag{21}$$

Fourier Descriptors. The centroid distance function can be analysed in the frequency domain to obtain spectral descriptors of its characteristics. Its spectral representation is expressed as the coefficients of its discrete Fourier transform, yielding

$$a_i = \frac{1}{N}\sum_{n=0}^{N-1} r\left(n\right)\exp\left(\frac{-j2\pi in}{N}\right), \quad i = 0, 1, 2, \ldots, N-1. \tag{22}$$

Feature vectors which are invariant to translation, scale, and rotation are extracted from these coefficients and are known as the Fourier descriptors (FD_i) for shape representation:

$$\mathrm{FD}_i = \left[\frac{\left|a_i\right|}{\left|a_0\right|}\right], \quad i = 1, 2, \ldots, \frac{N}{2}. \tag{23}$$

Zhang and Lu [38] have shown that FD_i derived from the centroid distance function outperforms FD_i's derived from using complex coordinates, cumulative angles, and curvature function as boundary signatures in shape-based image retrieval system, and furthermore, in Zhang and Lu [39], they mentioned that 60 FD_i's are sufficient for shape indexing.

We define the evaluation metric of the initial level set contours yielding im$X$ and im$Y$ based on the boundary signatures of the final contours delineating im$X$ and im$Y$ in the frequency domain as the Euclidean distance (DF(im$Y$, im$X$)) between the Fourier descriptors of the images:

$$\mathrm{DF}\left(\mathrm{im}Y, \mathrm{im}X\right) = \sqrt{\sum_{i=1}^{60}\left|\mathrm{FD}_i\left(\mathrm{im}Y\right) - \mathrm{FD}_i\left(\mathrm{im}X\right)\right|^2}, \tag{24}$$

where FD_i(im$X$) and FD_i(im$Y$) are the ith Fourier descriptors of the final contours delineating im$X$ and im$Y$.

Shape Convexity. Shape convexity measures the degree of spiculation in masses. The shape convexity of a binary image is defined as the ratio of the area of the binary image to the area of its convex hull [26]. Let Cim$X$ and Cim$Y$ be the convexity of binary images im$X$ and im$Y$, respectively;

the evaluation metric of the difference between the shape convexities of images im$X$ and im$Y$ is defined as

$$\%\Delta\mathrm{SC}\,(\mathrm{im}X, \mathrm{im}Y) = \left|\frac{C\mathrm{im}Y - C\mathrm{im}X}{\mathrm{average}\,(C\mathrm{im}Y, C\mathrm{im}X)}\right| \times 100. \quad (25)$$

Shape Rectangularity. Shape rectangularity [40] is defined as the ratio of the area of the binary image to the area of its minimal bounding rectangle. Let $R\mathrm{im}X$ and $R\mathrm{im}Y$ be the shape rectangularity of binary images im$X$ and im$Y$, respectively; the evaluation metric of the difference between the shape rectangularities of images im$X$ and im$Y$ is defined as

$$\%\Delta\mathrm{SR}\,(\mathrm{im}X, \mathrm{im}Y) = \left|\frac{R\mathrm{im}Y - R\mathrm{im}X}{\mathrm{average}\,(R\mathrm{im}Y, R\mathrm{im}X)}\right| \times 100. \quad (26)$$

Differences in shape-based descriptors of the final contours were further evaluated with Bland-Altman analysis to explore the agreement and trends between placements of the initial level set contours in digital mass lesions segmentation while Pearson correlation analysis assessed the correlation between these descriptors.

4. Experimental Results and Discussion

In our implementation of the Chan-Vese method, we set $\mu = 0.2$, $\lambda_1 = 2.5$, and $\lambda_2 = 1$. We chose $\lambda_1 > \lambda_2$ to give a greater weight to the variance of pixels in the foreground so as to achieve measurable segmentation differences between the proposed locations for the initial level set contours. Furthermore, we assigned $\lambda_1 = \lambda_2 = 1$ to investigate changes in the final segmentation results due to differences in tuneable parameters. In practice, for a given database of masses, the values assigned to λ_1 and λ_2 depend on the similarity indices between segmentation results of a proposed algorithm and the gold standard of a training set of masses, which in some cases is a subset of the database. For the active contour with selective local or global segmentation model, we set $\alpha = 5$ for this database so that masses with ill-defined boundaries should be accurately segmented. The segmentation performances of this algorithm were poor with values of $\alpha > 5$ for this group of masses. The average time for curve evolution for these images was 15 ± 10 s for the segmentation methods.

Boundary information represents sharp changes in image properties. Figure 2 shows that as the degree of smoothing increases the radial distance functions of the initial level set contours form a dense nested pattern of curves. The differences between these curves are very small because edge is preserved through different values of λ's in weighted TV scale-space smoothing technique; consequently, segmentation results with the initial level set contours generated from these curves are expected to be similar.

Segmentation results for some masses with low signal areas and having obscured, or ill-defined, margins are shown in Figure 3. The proposed method defines the initial level set contour as the curve connecting points with maximum gradients in the radial direction as shown in column 3. Each curve characterizes the intrinsic shape of its mass lesion and its evolution is guided by the statistics of pixels surrounding the region. For this group of masses, the mean area overlap measure between segmented areas generated from the final contours of our proposed method and that of the manually drawn initial level set contours were 0.81 ± 0.01 for the Chan-Vese model and 0.86 ± 0.09 with the selective local or global segmentation model. This is almost comparable to the mean area overlap measures between expert radiologists [17] and expert radiologists against segmentation methods [17–21] as shown in Table 1. Therefore, changes in shape-based descriptors as expressed in our setup will be suggestive of changes in shape-based descriptors encountered by the abovementioned publications.

Table 2 shows the variation in the area overlap measures with percentage differences in boundary moments F_1, F_2, and F_3 when masses in Figure 3 were evolved with tuneable parameters $\lambda_1 = 2.5$, $\lambda_2 = 1$. The area overlap measure of mass D is greater than 0.8; however, the percentage difference in boundary moments was above 50%, with $\%\Delta F_1$ being 87.0%. The mean values of $\%\Delta F_1$, $\%\Delta F_2$, and $\%\Delta F_3$ for this group were 23.9% (range 1.0–87.0%), 24.5% (range 1.7–86.8%), and 32% (range 1.4–86.0%), respectively, as shown in Table 6. The mean values are large with wide range. For $\lambda_1 = 1$, $\lambda_2 = 1$, the mean values of the percentage change of each boundary moment were less than 20.2%. These large ranges and mean values show that boundary moments are sensitive to the location of the initial level set contour for masses with obscured or ill-defined margins and the degree of sensitivity depends on the choice of tuneable parameters. As shown in Table 7, the mean values of boundary moments $\%\Delta F_1$, $\%\Delta F_2$, and $\%\Delta F_3$ were obtained as 15.1% (range 0–74%), 15.4% (range 0–67.5%), and 23.5% (range 0–52%), respectively, by using the selective local or global segmentation model. These values are comparable to values obtained by implementing the Chan-Vese model for $\lambda_1 = 1$, $\lambda_2 = 1$.

In Table 3, the variation in Euclidean distances of the Fourier descriptors and the percentage differences in shape convexity and rectangularity for the masses in Figure 3 are illustrated. In Table 6, for $\lambda_1 = 2.5$, $\lambda_2 = 1$, the mean Euclidean distance between the Fourier descriptors of the segmented areas was 0.09 ± 0.05 while the mean values of percentage changes in shape convexity and rectangularity were 8.3% (range 0.0–28.1%) and 11.7% (range 0.1–42.0%), respectively, with more than 50% reduction in the mean values with tuneable parameters $\lambda_1 = 1$, $\lambda_2 = 1$. The values for the mean percentage difference in shape convexity and rectangularity and their range were less than those from boundary moments for both Chan-Vese algorithms. The selective local or global segmentation model presented similar results for the percentage differences in shape convexity and shape rectangularity as shown in Table 7.

Figure 4 illustrates the segmentation results with different locations for the initial level set contours for some masses with distinct, or well-defined, margins. The initial level set contour from the proposed method is shown in column 3. Fewer points defining the maximum gradients in the radial direction are found within the mass lesion, as compared with the previous group. Most points defining the maximum gradients in the radial direction are found on the mass boundary;

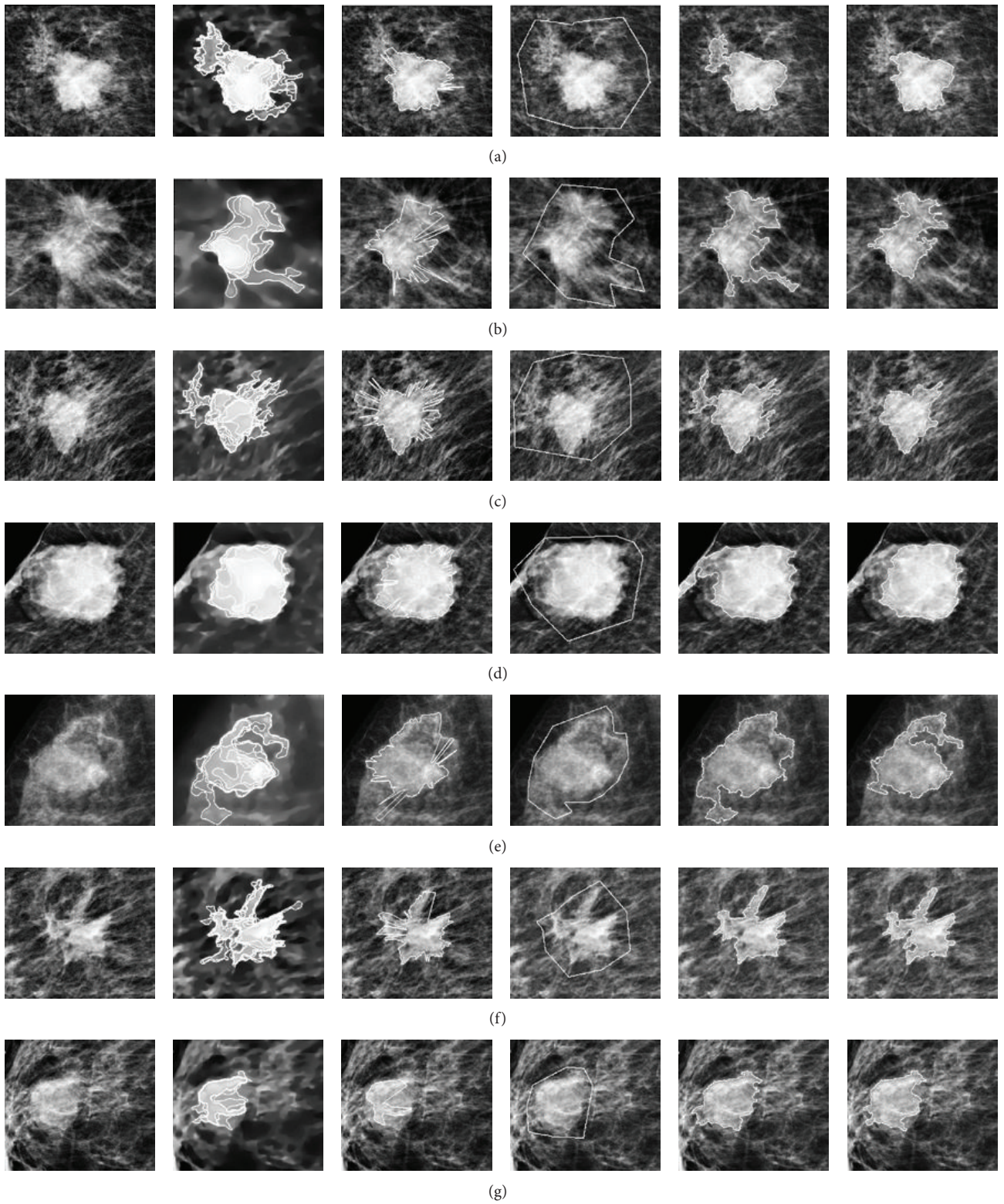

Figure 3: Comparisons of segmentation results with different locations for the initial level set contours for masses with low signal areas having obscured, or ill-defined, margins with the Chan-Vese model. The first column presents the original mass lesions; the second column shows the corresponding weighted TV flow images and the search space for locating the initial contour. The third column shows the initial contours as curves connecting points with maximum gradients in the radial direction. The fourth column shows the manually drawn initial level set contours. The fifth column presents the segmentation outcomes with manually drawn initial level set and the last column presents the final segmentation results of the proposed method evolved with the same tuning parameters.

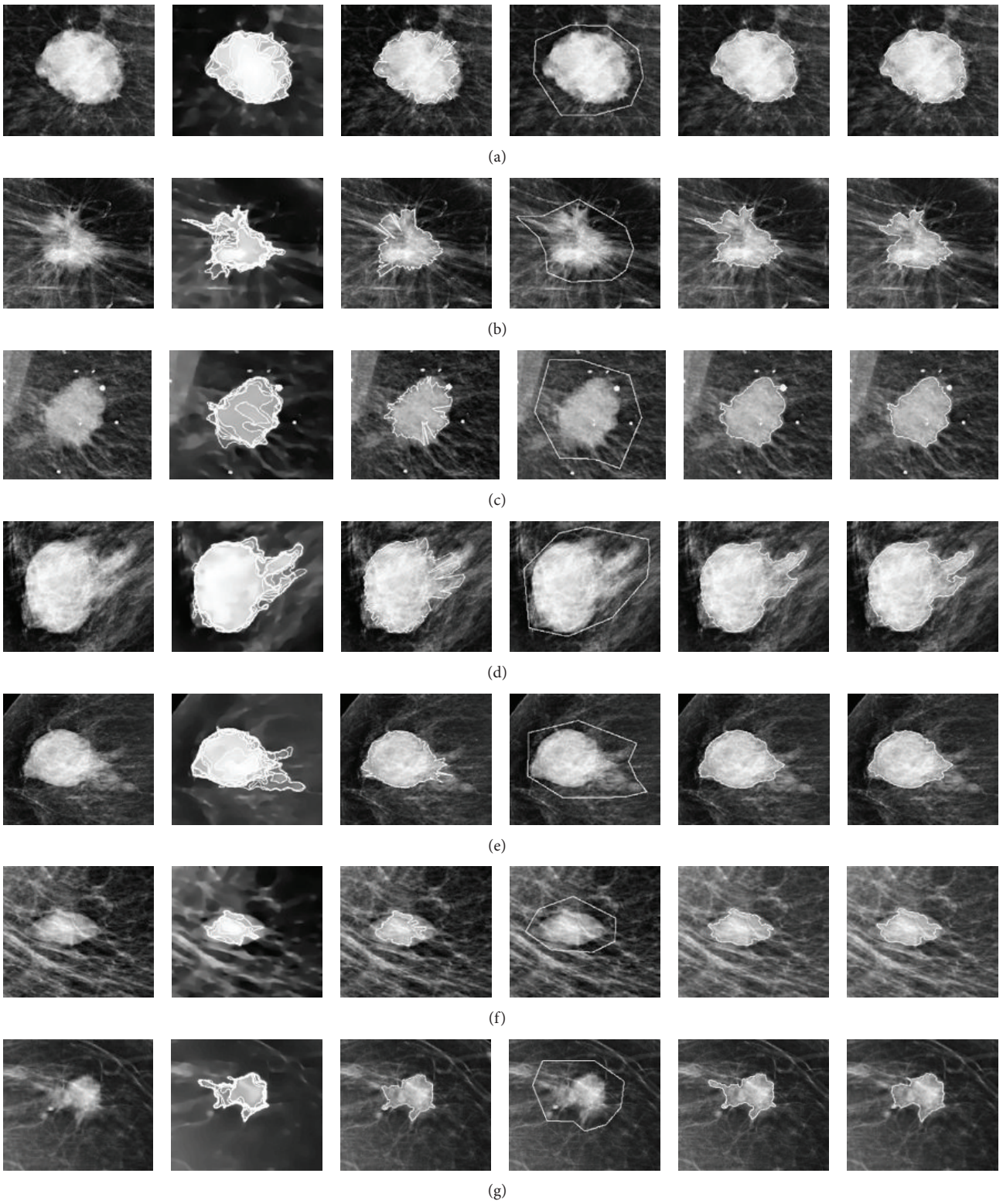

Figure 4: Comparisons of segmentation results with different locations for the initial level set contours for masses with distinct, or well-defined, margins by implementing the Chan-Vese model. The first column presents the original mass lesions; the second column shows the corresponding weighted TV flow images and the search space for locating the initial contour. The third column shows the initial contours as curves connecting points with maximum gradients in the radial direction. The fourth column shows the manually drawn initial level set contours. The fifth column presents the segmentation outcomes with manually drawn initial level set contours and the last column presents the final segmentation results of the proposed method evolved with the same tuning parameters.

Table 1: Comparison of mean area overlap measures of masses with characterized margins due to changes in the location of the initial level set contour with cited interobserver variability amongst radiologists and with mean area overlap measures between radiologists and other segmentation methods in boundary delineation.

	Characteristics of mass lesion margins	Mean area overlap measures due to interobserver variability amongst radiologists	Mean area overlap measures between radiologists and other segmentation methods	Mean area overlap measures due to the placement of the initial level set contours in this study
Sahiner et al. [17]	—	0.76 ± 0.13	0.74 ± 0.13	
Tao et al. [18]	Ill-defined and spiculated		0.69 ± 0.16	
Xu et al. [19]	—		0.72 ± 0.13	
Rahmati et al. [20]	—		0.87 ± 0.05	
Pereira et al. [21]	—		0.79 ± 0.08	
This study ($\lambda_1 = 2.5, \lambda_2 = 1$)	Obscured/ill-defined with low signal areas within			0.81 ± 0.01
This study ($\lambda_1 = 2.5, \lambda_2 = 1$)	Distinct/well-defined			0.96 ± 0.03
This study ($\lambda_1 = 1, \lambda_2 = 1$)	Obscured/ill-defined with low signal areas within			0.87 ± 0.13
This study ($\lambda_1 = 1, \lambda_2 = 1$)	Distinct/well-defined			0.95 ± 0.06
This study ($\alpha = 5$)	Obscured/ill-defined with low signal areas within			0.86 ± 0.09
This study ($\alpha = 5$)	Distinct/well-defined			0.91 ± 0.04

Table 2: Evaluation metrics for differences in segmented areas (JSC) and boundary moments ($\%\Delta F_1$, $\%\Delta F_2$, and $\%\Delta F_3$), due to changes in the location of the initial level set contours evolved with tuneable parameters $\lambda_1 = 2.5$, $\lambda_2 = 1$ for masses in Figure 3.

Masses	JSC	F_1	F_2	F_3	Method	$\%\Delta F_1$	$\%\Delta F_2$	$\%\Delta F_3$
A	0.83	0.3186	0.3715	0.0530	Manual	68.4	67.1	59.8
		0.1563	0.1848	0.0286	Proposed			
B	0.77	0.3417	0.4264	0.0846	Manual	8.1	7.2	3.5
		0.3152	0.3969	0.0817	Proposed			
C	0.78	0.2691	0.3269	0.0578	Manual	9.7	3.1	23.0
		0.2442	0.3170	0.0728	Proposed			
D	0.84	0.2505	0.3120	0.0615	Manual	87.0	86.8	86.0
		0.0986	0.1231	0.0245	Proposed			
E	0.71	0.2715	0.3300	0.0585	Manual	6.0	8.1	17.6
		0.2882	0.3580	0.0698	Proposed			
F	0.89	0.2969	0.3826	0.0857	Manual	8.2	7.4	4.8
		0.3224	0.4122	0.0899	Proposed			
G	0.87	0.1835	0.2168	0.0333	Manual	1.7	9.9	45.3
		0.1866	0.2394	0.0528	Proposed			

consequently, the statistics of the pixels surrounding the initial level set contour will be similar to those of the manually drawn contour when it arrives at the edge of the mass lesion.

Table 4 shows the variation in the area overlap measures and the percentage differences in boundary moments F_1, F_2, and F_3 while Table 5 illustrates the variation in Euclidean distances between the Fourier descriptors (DF), percentage differences in shape convexity (%ΔSC), and shape rectangularity (%ΔSR) when the masses in Figure 4 were evolved with tuneable parameters $\lambda_1 = 2.5$, $\lambda_2 = 1$. The area overlap measure of mass B was greater than 0.95; however, the percentage differences in boundary moments were above 18%. For masses with distinct or well-defined margins, similar segmentation results are expected and this is confirmed with a mean area overlap measure of 0.96 ± 0.03 as shown in Table 6. For this category of masses, the mean value of $\%\Delta F_1$ was 8.9% (range 0.3–25.0%); of $\%\Delta F_2$, 8.6% (range 2.1–33%); and of $\%\Delta F_3$, 14.1% (range 0.9–53.0%). The mean Euclidean distance between the Fourier descriptors of the segmented areas was 0.05 ± 0.02 and the mean values of

Table 3: Variation in Euclidean distances between Fourier descriptors (DF), percentage differences in shape convexity (%ΔSC), and shape rectangularity (%ΔSR) due to changes in the location of the initial level set contours evolved with tuneable parameters $\lambda_1 = 2.5$, $\lambda_2 = 1$ for masses in Figure 3.

Masses	DF	SC	SR	Method	%ΔSC	%ΔSR
A	0.16	0.7152	0.4861	Manual	16.5	31.5
		0.8439	0.6681	Proposed		
B	0.10	0.5373	0.3762	Manual	22.4	9.6
		0.6731	0.4143	Proposed		
C	0.08	0.5610	0.3845	Manual	28.2	21.6
		0.7450	0.4774	Proposed		
D	0.13	0.8071	0.6301	Manual	12.5	16.6
		0.9143	0.7440	Proposed		
E	0.06	0.7737	0.5017	Manual	16.7	3.8
		0.9143	0.4830	Proposed		
F	0.05	0.5955	0.4188	Manual	10.1	10.9
		0.5383	0.3755	Proposed		
G	0.03	0.7899	0.5297	Manual	1.7	8.8
		0.8036	0.5786	Proposed		

Table 4: Evaluation metrics for differences in segmented areas (JSC) and boundary moments ($\%\Delta F_1$, $\%\Delta F_2$, and $\%\Delta F_3$), due to changes in the location of the initial level set contours evolved with tuneable parameters $\lambda_1 = 2.5$, $\lambda_2 = 1$ for masses in Figure 4.

Masses	JSC	F_1	F_2	F_3	Method	$\%\Delta F_1$	$\%\Delta F_2$	$\%\Delta F_3$
A	0.98	0.0827	0.1051	0.0224	Manual	29.0	31.2	39.4
		0.1107	0.1440	0.0334	Proposed			
B	0.97	0.2084	0.2783	0.0699	Manual	21.9	21.1	18.7
		0.2597	0.3440	0.0843	Proposed			
C	0.99	0.1489	0.1785	0.0295	Manual	6.1	2.6	13.6
		0.1401	0.1739	0.0338	Proposed			
D	0.98	0.2130	0.2568	0.0437	Manual	12.0	9.0	6.6
		0.2402	0.2811	0.0409	Proposed			
E	0.98	0.1080	0.1376	0.0296	Manual	2.2	2.9	5.9
		0.1057	0.1336	0.0279	Proposed			
F	0.94	0.1888	0.2192	0.0304	Manual	2.0	1.3	19.3
		0.1851	0.2220	0.0369	Proposed			
G	0.94	0.2971	0.3676	0.0705	Manual	18.7	12.4	10.9
		0.2463	0.3248	0.0786	Proposed			

percentage changes of shape convexity and rectangularity were 4.5% (range 0.07–17.2%) and 5.7% (range 0.04–14.9%), respectively. The values for the mean percentage differences in shape convexity and rectangularity were almost 50% less than those from boundary moments. This group presented a small percentage change in shape convexity and shape rectangularity and also a small mean Euclidean distance of the Fourier descriptors as compared to the previous group due to segmentation results having relatively similar shapes. For these groups of masses, shape-based descriptors derived from final contours of tuneable parameters $\lambda_1 = 1$, $\lambda_2 = 1$ were less sensitive to changes in the location of the initial level set contours. Table 6 shows that the mean percentage differences of the shape convexity and shape rectangularity are less than the values for the boundary moments. Table 7 illustrates similar trends with the selective local or global segmentation model; however, the Jaccard similarity indices of the Chan-Vese segmentation model for this group of masses were greater than values obtained by using the selective local or global segmentation model.

The evaluation metrics of shape-based descriptors of both groups of masses were combined and assessed with Bland-Altman plots to investigate the intermethod agreement between placements of the initial level set contours. Each Bland-Altman plot was evaluated within a 95% confidence interval as the limits of agreement.

Figures 5 and 6 illustrate the linear regression plots of boundary moments, shape rectangularity, and shape convexity with their associated Bland-Altman plots with the Chan-Vese segmentation method. The Pearson correlation

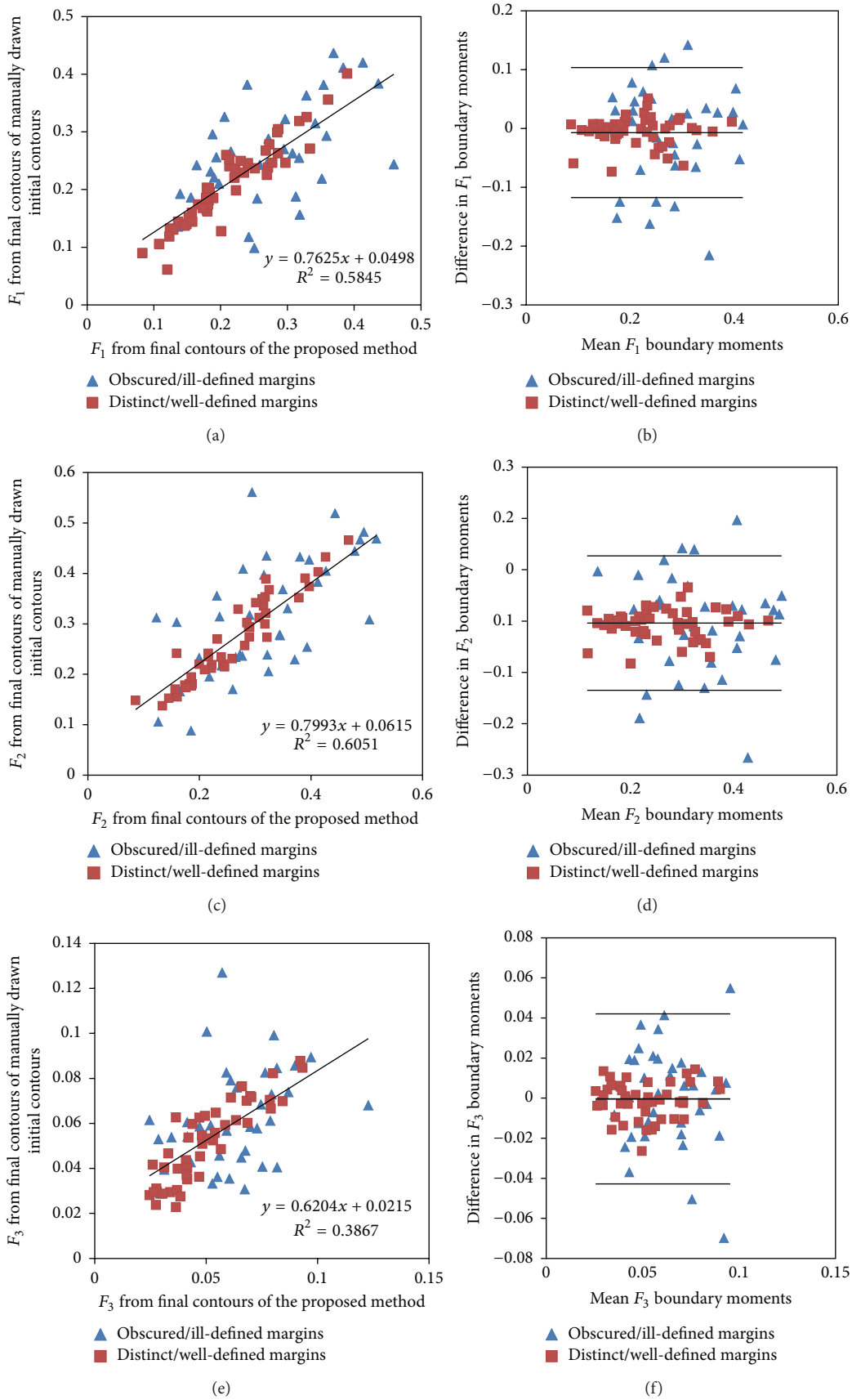

FIGURE 5: Linear regression plots ((a), (c), and (e)), along with Bland-Altman plots ((b), (d), and (f)), of boundary moments F_1, F_2, and F_3, respectively, for tuneable parameters $\lambda_1 = 2.5$, $\lambda_2 = 1$.

Table 5: Variation in Euclidean distances between the Fourier descriptors (DF), percentage differences in shape convexity (%ΔSC), and shape rectangularity (%ΔSR) due to changes in the location of the initial level set contours evolved with tuneable parameters $\lambda_1 = 2.5$, $\lambda_2 = 1$ for masses in Figure 4.

Masses	DF	SC	SR	Method	%ΔSC	%ΔSR
A	0.0368	0.6612	0.4619	Manual	17.1	14.5
		0.7852	0.5339	Proposed		
B	0.0624	0.6637	0.4596	Manual	7.0	14.4
		0.7116	0.5307	Proposed		
C	0.0377	0.8894	0.6148	Manual	1.1	1.2
		0.8995	0.6224	Proposed		
D	0.0762	0.8508	0.6093	Manual	0.0	0.0
		0.8508	0.6093	Proposed		
E	0.0216	0.9267	0.6544	Manual	0.3	1.1
		0.9295	0.6472	Proposed		
F	0.0298	0.8606	0.6024	Manual	2.9	5.2
		0.8360	0.5716	Proposed		
G	0.0717	0.6612	0.4619	Manual	17.1	14.5
		0.7852	0.5339	Proposed		

Table 6: Mean values for the Jaccard similarity coefficient (JSC) and the Euclidean distances of the masses. The mean values and ranges of percentage differences in boundary moments ($\%\Delta F_1$, $\%\Delta F_2$, and $\%\Delta F_3$), percentage differences in shape convexity (%ΔSC), and percentage differences in shape rectangularity (%ΔSC) for the masses, labelled as groups with predefined margin characteristics and also a group with arbitrary margin characteristics, due to changes in the location of the initial level set contours evolved with tuneable parameters $\lambda_1 = 2.5$, $\lambda_2 = 1$ and $\lambda_1 = 1$, $\lambda_2 = 1$.

Margin characteristics	Obscured/ill-defined margins		Distinct/well-defined margins		Unlabelled margins	
Tuneable parameters	$\lambda_1 = 2.5, \lambda_2 = 1$	$\lambda_1 = 1, \lambda_2 = 1$	$\lambda_1 = 2.5, \lambda_2 = 1$	$\lambda_1 = 1, \lambda_2 = 1$	$\lambda_1 = 2.5, \lambda_2 = 1$	$\lambda_1 = 1, \lambda_2 = 1$
Average JSC	0.81 ± 0.01	0.87 ± 0.13	0.96 ± 0.03	0.95 ± 0.06	0.89 ± 0.02	0.92 ± 0.09
Average DF	0.09 ± 0.05	0.05 ± 0.04	0.05 ± 0.02	0.04 ± 0.02	0.07 ± 0.05	0.05 ± 0.03
Mean of $\%\Delta F_1$	23.9%	17.5%	8.9%	11.4%	16.4%	14.5%
Range of $\%\Delta F_1$	1.0–87.0%	0–62.6%	0.3–25.0%	0–24.4%	1.0–87.0%	0–62.6%
Mean of $\%\Delta F_2$	24.5%	17.2%	8.6%	9.6%	16.6%	13.4%
Range of $\%\Delta F_2$	1.7–86.8%	0–59.1%	2.1–33%	0–46.0%	1.7–86.8%	0–59.1%
Mean of $\%\Delta F_3$	32%	20.1%	14.1%	13.4%	23.1%	16.8%
Range of $\%\Delta F_3$	1.4–86.0%	0–80.9%	0.9–53.0%	0–54.0%	0–86.0%	0–80.9%
Mean of %ΔSC	8.3%	2.4%	4.5%	2.9%	6.4%	2.7%
Range of %ΔSC	0.0–28.1%	0–21.0%	0.07–17.2%	0.2–13.9%	0.3–28.1%	0–21.0%
Mean of %ΔSR	11.7%	7.6%	5.7%	4.3%	8.7%	5.9%
Range of %ΔSR	0.1–42.0%	0–38.9%	0.04–14.9%	0–21.9%	0.1–42.0%	0–38.9%

analysis indicated good correlations between the shape-based descriptors: shape rectangularity ($r = 0.82$) and shape convexity ($r = 0.82$) resulting from the final contours of the proposed and manual methods as compared to boundary moments F_1 ($r = 0.76$), F_2 ($r = 0.77$), and F_3 ($r = 0.68$). The selective local or global segmentation method gave higher correlation coefficients for these shape descriptors. Table 8 shows the summary results of the linear regression analysis of shape-based descriptors for these masses and their variation with tuneable parameters. p values indicated that the correlations of shape-based descriptors derived from these methods were statistically significant ($p < 0.0001$). The strength of the linear relationship (r) between the descriptors derived from these methods depends on the values of tuneable parameters, λ_1 and λ_2, for the Chan-Vese model. For this database of masses, the correlation coefficients of descriptors obtained with tuneable parameters $\lambda_1 = 1$ and $\lambda_2 = 1$ were higher than those with parameters $\lambda_1 = 2.5$ and $\lambda_2 = 1$; however, this does not imply that tuneable parameters $\lambda_1 = 1$ and $\lambda_2 = 1$ will provide higher values of similarity measures when segmentation results are compared with segmentation outcomes of expert radiologists. Overall, the performance of

Table 7: Mean values for the Jaccard similarity coefficient (JSC) and the Euclidean distances of the masses. The mean values and ranges of percentage differences in boundary moments ($\%\Delta F_1$, $\%\Delta F_2$, and $\%\Delta F_3$), percentage differences in shape convexity (%ΔSC), and percentage differences in shape rectangularity (%ΔSC) for the masses, labelled as groups with predefined margin characteristics and also a group with arbitrary margin characteristics, due to changes in the location of the initial level set contours evolved with the selective local or global segmentation model with tuneable parameter $\alpha = 5$.

Margin characteristics	Obscured/ill-defined margins	Distinct/well-defined margins	Unlabelled margins
Average JSC	0.86 ± 0.09	0.91 ± 0.04	0.89 ± 0.07
Average DF	0.05 ± 0.04	0.04 ± 0.03	0.05 ± 0.04
Mean of $\%\Delta F_1$	15.1%	11.1%	13.1%
Range of $\%\Delta F_1$	0–74%	0–38%	0–74%
Mean of $\%\Delta F_2$	15.4%	13.4%	14.4%
Range of $\%\Delta F_2$	0–67.5%	0–44.2%	0–67.5%
Mean of $\%\Delta F_3$	23.5%	15.1%	19.3%
Range of $\%\Delta F_3$	0–52%	0–41.1%	0–52%
Mean of %ΔSC	10.2%	8.7%	9.5%
Range of %ΔSC	0–30%	0–25.1%	0–30%
Mean of %ΔSR	11.7%	9.2%	10.5%
Range of %ΔSR	0–30%	0–28%	0–30%

Table 8: Summary results of linear regression analysis for tuneable parameters $\lambda_1 = 2.5$, $\lambda_2 = 1$ and $\lambda_1 = 1$, $\lambda_2 = 1$ and the selective local or global segmentation method.

	Tuneable parameters						Selective local or global segmentation method		
	$\lambda_1 = 2.5, \lambda_2 = 1$			$\lambda_1 = 1, \lambda_2 = 1$			$\alpha = 5$		
	Slope	r	p value	Slope	r	p value	Slope	r	p value
F_1	0.76	0.76	<0.0001	0.83	0.81	<0.0001	0.69	0.81	<0.0001
F_2	0.79	0.77	<0.0001	0.72	0.80	<0.0001	0.75	0.86	<0.0001
F_3	0.62	0.68	<0.0001	0.75	0.74	<0.0001	0.7	0.74	<0.0001
SC	0.85	0.82	<0.0001	0.93	0.88	<0.0001	0.88	0.83	<0.0001
SR	0.92	0.82	<0.0001	0.82	0.88	<0.0001	0.85	0.94	<0.0001

the selective local or global segmentation model was similar to the performance of the Chan-Vese segmentation model for this database of direct digital mammographic masses.

The difference plots in Figures 5 and 6 show that differences in shape-based features for masses with distinct or well-defined margins are scattered very close to the central bias line as compared to masses with obscured, or ill-defined, margins, thus indicating that the magnitude of differences in shape-based descriptors due to changes in the placement of the initial level set contours depends on the mass margin characteristics. Other researches have reported the variation of segmentation accuracy with the characteristic of the mass margins for a given segmentation algorithm [41]. The correlations ($rs < 0.06$, $p > 0.05$) between differences in shape-based descriptors due to changes in the placement of the initial level set contours and the average magnitude of descriptors from both algorithms were very poor and they were not significantly different from zero.

In general, the mean area overlap measure of the combined categories was 0.89 ± 0.02, the mean Euclidean distance between the Fourier descriptors was 0.07 ± 0.05, and moreover, in the Bland-Altman plots, the differences in shape-based descriptors of 90% of these masses are within the limits of agreement; therefore the interplacement agreement of the initial level set contours based on these descriptors is acceptable. However, both segmentation methods illustrated large variation in boundary moments as compared to shape-based descriptors such as shape convexity, shape rectangularity, and Euclidean distance of the Fourier descriptors. Hence, boundary moments should be utilized with caution because they exhibit large percentage differences.

Interobserver variability amongst radiologists and intermethod variability in delineating masses in mammography translate to differences in shape-based feature vectors. The magnitude of these differences should however not be so large as to compromise the interclass separability measures and hence the classification accuracies of shape-based binary classifiers. This can be achieved if these feature vectors show a certain degree of robustness to interobserver and intermethod variability in segmented masses.

5. Conclusion

We have investigated and quantified the variations in shape-based features in segmentation outcomes due to differences

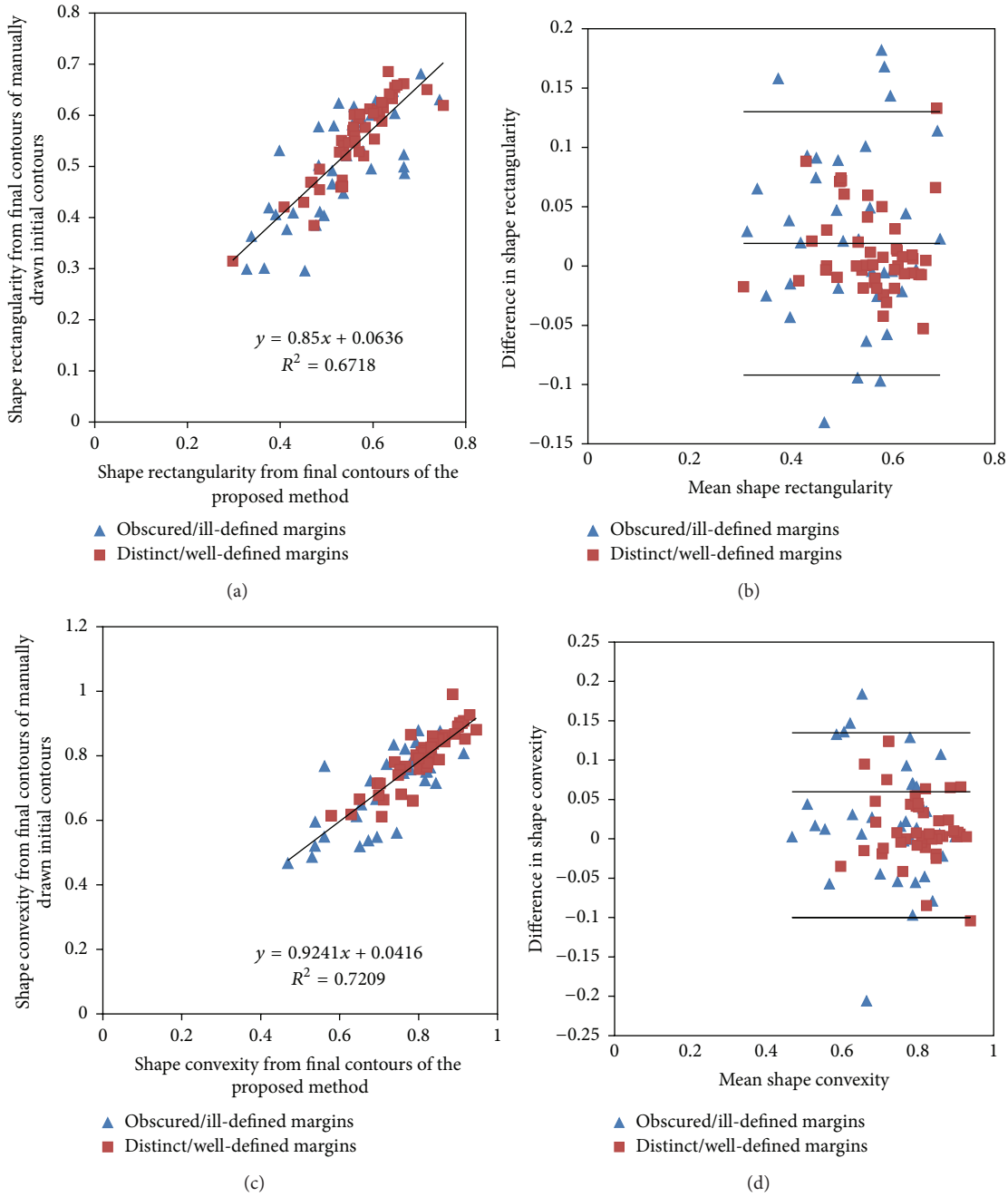

FIGURE 6: Linear regression plots ((a) and (c)) along with associated Bland-Altman plots ((b) and (d)) of shape rectangularity (SR) and shape convexity (SC), respectively, for tuneable parameters $\lambda_1 = 2.5$, $\lambda_2 = 1$.

in the location of the initial level set contour for mass lesion segmentation in direct digital mammography. The Chan-Vese segmentation method and the active contours with selective local or global segmentation model presented similar results. The results show that the magnitude of these variations expressed as area overlap measures and percentage differences in shape-based features depend on the characteristics of the mass margins and the choice of tuneable parameters. For masses with distinct or well-defined margins, percentage differences are reduced as compared to those with ill-defined or obscured margins for both segmentation algorithms. The mean percentage differences in boundary moments and their ranges were large as compared to those of shape convexity and shape rectangularity, even though the area overlaps measures were within acceptable values. The influences of these variations on the classification accuracy of shape-based binary classifiers will depend on the magnitude of the interclass separability measures; however, large fluctuations in these values for the same mass are undesirable. Finally, we concluded that boundary moments are sensitive

to the placement of initial level set contours while Fourier descriptors, shape convexity, and shape rectangularity exhibit a certain degree of robustness to changes in the location of the initial level set contours.

Conflict of Interests

Both authors declare that there is no conflict of interests regarding the publication of this paper.

References

[1] J. Padayachee, M. J. Alport, and W. I. Rae, "Mammographic CAD: correlation of regions in ipsilateral views—a pilot study," *South African Journal of Radiology*, vol. 13, no. 3, 2009.

[2] R. Malladi, J. A. Sethian, and B. C. Vemuri, "Shape modeling with front propagation: a level set approach," *IEEE Transactions on Pattern Analysis and Machine Intelligence*, vol. 17, no. 2, pp. 158–175, 1995.

[3] G. Zhu, S. Zhang, Q. Zeng, and C. Wang, "Boundary-based image segmentation using binary level set method," *Optical Engineering*, vol. 46, no. 5, Article ID 050501, 2007.

[4] N. Paragios and R. Deriche, "Geodesic active contours and level sets for the detection and tracking of moving objects," *IEEE Transactions on Pattern Analysis and Machine Intelligence*, vol. 22, no. 3, pp. 266–280, 2000.

[5] A. Yezzi, A. Tsai, and A. Willsky, "A statistical approach to snakes for bimodal and trimodal imagery," in *Proceedings of the International Conference on Computer Vision*, vol. 2, pp. 898–903, 1999.

[6] D. Cremers, M. Rousson, and R. Deriche, "A review of statistical approaches to level set segmentation: integrating color, texture, motion and shape," *International Journal of Computer Vision*, vol. 72, no. 2, pp. 195–215, 2007.

[7] O. Michailovich, Y. Rathi, and A. Tannenbaum, "Image segmentation using active contours driven by the Bhattacharyya gradient flow," *IEEE Transactions on Image Processing*, vol. 16, no. 11, pp. 2787–2801, 2007.

[8] S. Lankton and A. Tannenbaum, "Localizing region-based active contours," *IEEE Transactions on Image Processing*, vol. 17, no. 11, pp. 2029–2039, 2008.

[9] K. Zhang, L. Zhang, H. Song, and W. Zhou, "Active contours with selective local or global segmentation: a new formulation and level set method," *Image and Vision Computing*, vol. 28, no. 4, pp. 668–676, 2010.

[10] K. Zhang, H. Song, and L. Zhang, "Active contours driven by local image fitting energy," *Pattern Recognition*, vol. 43, no. 4, pp. 1199–1206, 2010.

[11] X.-F. Wang, D.-S. Huang, and H. Xu, "An efficient local Chan-Vese model for image segmentation," *Pattern Recognition*, vol. 43, no. 3, pp. 603–618, 2010.

[12] F. Akram, J. H. Kim, C.-G. Lee, and K. N. Choi, "Segmentation of regions of interest using active contours with SPF function," *Computational and Mathematical Methods in Medicine*, vol. 2015, Article ID 710326, 14 pages, 2015.

[13] A. Sezer, H. B. Sezer, and S. Albayrak, "Segmentation of bone with region based active contour model in PD weighted MR images of shoulder," *Computational and Mathematical Methods in Medicine*, vol. 2015, Article ID 754894, 13 pages, 2015.

[14] C. Li, C.-Y. Kao, J. C. Gore, and Z. Ding, "Implicit active contours driven by local binary fitting energy," in *Proceedings of the IEEE Computer Society Conference on Computer Vision and Pattern Recognition (CVPR '07)*, pp. 1–7, June 2007.

[15] C. Li, C.-Y. Kao, J. C. Gore, and Z. Ding, "Minimization of region-scalable fitting energy for image segmentation," *IEEE Transactions on Image Processing*, vol. 17, no. 10, pp. 1940–1949, 2008.

[16] T. F. Chan and L. A. Vese, "Active contours without edges," *IEEE Transactions on Image Processing*, vol. 10, no. 2, pp. 266–277, 2001.

[17] B. Sahiner, N. Petrick, H.-P. Chan et al., "Computer-aided characterization of mammographic masses: accuracy of mass segmentation and its effects on characterization," *IEEE Transactions on Medical Imaging*, vol. 20, no. 12, pp. 1275–1284, 2001.

[18] Y. Tao, S.-C. B. Lo, M. T. Freedman, E. Makariou, and J. Xuan, "Multilevel learning-based segmentation of ill-defined and spiculated masses in mammograms," *Medical Physics*, vol. 37, no. 11, pp. 5993–6002, 2010.

[19] S. Xu, H. Liu, and E. Song, "Marker-controlled watershed for lesion segmentation in mammograms," *Journal of Digital Imaging*, vol. 24, no. 5, pp. 754–763, 2011.

[20] P. Rahmati, A. Adler, and G. Hamarneh, "Mammography segmentation with maximum likelihood active contours," *Medical Image Analysis*, vol. 16, no. 6, pp. 1167–1186, 2012.

[21] D. C. Pereira, R. P. Ramos, and M. Z. do Nascimento, "Segmentation and detection of breast cancer in mammograms combining wavelet analysis and genetic algorithm," *Computer Methods and Programs in Biomedicine*, vol. 114, no. 1, pp. 88–101, 2014.

[22] Y. Yuan, M. L. Giger, H. Li, K. Suzuki, and C. Sennett, "A dual-stage method for lesion segmentation on digital mammograms," *Medical Physics*, vol. 34, no. 11, pp. 4180–4193, 2007.

[23] J. Shi, B. Sahiner, H.-P. Chan et al., "Characterization of mammographic masses based on level set segmentation with new image features and patient information," *Medical Physics*, vol. 35, no. 1, pp. 280–290, 2008.

[24] J. Liu, J. Chen, X. Liu, L. Chun, J. Tang, and Y. Deng, "Mass segmentation using a combined method for cancer detection," *BMC Systems Biology*, vol. 5, supplement 3, article S6, 2011.

[25] X. Hao, Y. Shen, and S.-R. Xia, "Automatic mass segmentation on mammograms combining random walks and active contour," *Journal of Zhejiang University: Science C*, vol. 13, no. 9, pp. 635–648, 2012.

[26] B. Sahiner, H.-P. Chan, N. Petrick, M. A. Helvie, and L. M. Hadjiiski, "Improvement of mammographic mass characterization using spiculation measures and morphological features," *Medical Physics*, vol. 28, no. 7, pp. 1455–1465, 2001.

[27] R. M. Rangayyan, N. M. El-Faramawy, J. E. L. Desautels, and O. A. Alim, "Measures of acutance and shape for classification of breast tumors," *IEEE Transactions on Medical Imaging*, vol. 16, no. 6, pp. 799–810, 1997.

[28] T. Mu, A. K. Nandi, and R. M. Rangayyan, "Classification of breast masses using selected shape, edge-sharpness, and texture features with linear and kernel-based classifiers," *Journal of Digital Imaging*, vol. 21, no. 2, pp. 153–169, 2008.

[29] D. Strong and T. Chan, "Spatially and adaptive total variational based regularization and anisotropic diffusion in image processing," UCLA CAM Report 96-46, 2004.

[30] X. Bresson, S. Esedoglu, P. Vandergheynst, J. P. Thiran, and S. Osher, "Global minimizers of the active contour/snake model," UCLA CAM Report 05-04, 2005.

[31] L. I. Rudin, S. Osher, and E. Fatemi, "Nonlinear total variation based noise removal algorithms," *Physica D: Nonlinear Phenomena*, vol. 60, no. 1–4, pp. 259–268, 1992.

[32] B.-W. Hong and M. Brady, "A topographic representation for mammogram segmentation," in *Proceedings of the 6th International Conference Medical Image Computing and Computer-Assisted Intervention, (MICCAI '03)*, pp. 730–737, November 2003.

[33] F. Ma, M. Bajger, and M. J. Bottema, "Automatic mass segmentation based on adaptive pyramid and sublevel set analysis," in *Proceedings of the Digital Image Computing: Techniques and Applications (DICTA '09)*, pp. 236–241, IEEE, Melbourne, Australia, December 2009.

[34] J. Padayachee, M. J. Alport, and W. I. D. Rae, "Identification of the breast edge using areas enclosed by iso-intensity contours," *Computerized Medical Imaging and Graphics*, vol. 31, no. 6, pp. 390–400, 2007.

[35] L. Gupta and M. D. Srinath, "Contour sequence moments for the classification of closed planar shapes," *Pattern Recognition*, vol. 20, no. 3, pp. 267–272, 1987.

[36] L. Shen, R. M. Rangayyan, and J. L. Desautels, "Detection and classification of mammographic calcifications," *International Journal of Pattern Recognition and Artificial Intelligence*, vol. 07, no. 06, pp. 1403–1416, 1993.

[37] L. Shen, R. M. Rangayyan, and J. E. L. Desautels, "Application of shape analysis to mammographic calcifications," *IEEE Transactions on Medical Imaging*, vol. 13, no. 2, pp. 263–274, 1994.

[38] D. Zhang and G. Lu, "A comparative study of Fourier descriptors for shape representation and retrieval," in *Proceedings of the 5th Asian Conference on Computer Vision (ACCV '02)*, pp. 646–651, Melbourne, Australia, 2002.

[39] D. Zhang and G. Lu, "Shape retrieval using fourier descriptors," in *Proceedings of the International Conference on Multimedia and distance Education*, pp. 1–9, Fargo, ND, USA, 2001.

[40] M. Yang, K. Kpalma, and J. Ronsin, "A survey of shape feature extraction techniques," in *Pattern Recognition Techniques, Technology and Applications*, P.-Y. Yin, Ed., chapter 3, pp. 43–90, InTech, Rijeka, Croatia, 2008.

[41] J. Lou, X. Yang, and A. Cao, "A spatial shape constrained clustering method for mammographic mass segmentation," *Computational and Mathematical Methods in Medicine*, vol. 2015, Article ID 891692, 16 pages, 2015.

Physica Medica 32 (2016) 1352–1359

Contents lists available at ScienceDirect

Physica Medica

journal homepage: http://www.physicamedica.com

Original paper

Interactive breast mass segmentation using a convex active contour model with optimal threshold values

Sussan Nkwenti Acho, William Ian Duncombe Rae *

Department of Medical Physics, University of the Free State, Bloemfontein 9300, South Africa

ARTICLE INFO

Article history:
Received 31 December 2015
Received in Revised form 17 May 2016
Accepted 18 May 2016
Available online 2 June 2016

Keywords:
Segmentation
Chan–Vese
Mass
Convex active contour

ABSTRACT

Introduction: A convex active contour model requires a predefined threshold value to determine the global solution for the best contour to use when doing mass segmentation. Fixed thresholds or manual tuning of threshold values for optimum mass boundary delineation are impracticable.

Introduction: A proposed method is presented to determine an optimized mass-specific threshold value for the convex active contour derived from the probability matrix of the mass with the particle swarm optimization method. We compared our results with the Chan–Vese segmentation and a published global segmentation model on masses detected on direct digital mammograms.

Methods and materials: The regional term of the convex active contour model maximizes the posterior partitioning probability for binary segmentation. Suppose the probability matrix is binary thresholded using the particle swarm optimization to obtain a value T_1, we define the optimal threshold value for the global minimizer of the convex active contour as the mean intensity of all pixels whose probabilities are greater than T_1.

Results: The mean Jaccard similarity indices were 0.89 ± 0.07 for the proposed/Chan–Vese method and 0.88 ± 0.06 for the proposed/published segmentation model. The mean Euclidean distance between Fourier descriptors of the segmented areas was 0.05 ± 0.03 for the proposed/Chan–Vese method and 0.06 ± 0.04 for the proposed/published segmentation model.

Conclusions: This efficient method avoids problems of initial level set contour placement and contour re-initialization. Moreover, optimum segmentation results are realized for all masses improving on the fixed threshold value of 0.5 proposed elsewhere.

1. Introduction

Projection X-ray images of the breast are routinely used to diagnose breast diseases, including those presenting with masses. These mammographic masses are often superimposed on anatomical structures which create local minima within the mass regions, and can result in mass margins having incomplete or missing boundary information. This has led to reported significant inter-observer variability in manual delineation of mass boundaries amongst experts [1,2], and in choosing lexicon for describing mass margin, density and shape of mammographic masses amongst resident radiologists [3]. Consequently, the task of mass boundary delineation is still challenging and in some cases can produce unsuitable segmentation solutions.

In recent years, interactive segmentation algorithms have been proposed to assist radiologists in delineating mass boundaries, hopefully, to achieve realistic segmentation solutions which accurately represent the physical attributes of these masses and thus, decrease the statistical significance of the variability associated with manual delineation. The initialization of these algorithms requires some user-specified seeds to indicate the search area for the mass boundary. Some of these methods seek to partition an image into meaningful regions with information both from the entire image and from the anatomical information provided by the user, while adhering to certain pre-defined criteria.

The geometric active contour model [4] is one such interactive segmentation algorithm widely employed in boundary delineation of anatomical structures in medical image analysis. It minimizes energy functionals, derived from the statistical distribution of the gray level intensities or image gradients, of the image to produce closed and smoothed contours depicting the boundaries of these structures.

* Corresponding author at: Medical Physics (G68), Faculty of Health Sciences, University of the Free State, PO Box 339, Bloemfontein 9330, South Africa.
E-mail addresses: Gnbisa@ufs.ac.za (S.N. Acho), RaeWID@ufs.ac.za (W.I.D. Rae).

http://dx.doi.org/10.1016/j.ejmp.2016.05.054
1120-1797/

Region-based models utilize statistical information obtained from regions inside and outside an initial contour to evolve the contour towards the desired boundary. The Chan–Vese region-based active contour model [5] is one of the methods widely used for image segmentation. To deal with topological changes, the initial contour is embedded in the level set of a function in higher dimensions. Its energy functional is non-convex, and it is derived from the local statistical distribution of the gray level intensities within a narrow band of pixels. Hence, the energy functional is minimized with the gradient descent method which is susceptible to local minima within the search path. Zhang et al. [6] proposed a region-based active contour model to delineate objects with weak or blurred edges. Their model is known as the 'active contours with selective local or global segmentation model'. Zhang et al. formulated the statistical information, inside and outside the initial contour, as a signed pressure force function for curve propagation while regularizing the level set function with a Gaussian smoothing kernel. Direct digital mammograms exhibit intensity inhomogeneity, consequently, masses with ill-defined margins and local minima within the mass region. Delineation of direct digital mass lesions with these algorithms, produces segmentation results which are dependent on the placement of the initial level set contours [7].

Bresson et al. [8] proposed a region-based active contour model whose energy functional is convex. It is derived from the global statistical distribution of the gray level intensities of the image. This model allows for the implementation of a global minimization algorithm, based on the dual formulation of the total variation (TV), to search for a global minimum of the active contour rather than using the gradient descent method. The segmentation results are independent of the placements of the initial level set contours, and do not require the implementation of the contour re-initialization process as level sets are not involved in their method of curve evolution.

Medical image analysis methods have exploited spatial prior probabilistic atlases as guides or confidence maps, to segment magnetic resonance images of the brain [9] and prostate [10] with the active contour segmentation model. In mammography, such a map is difficult to establish because breast tissues vary greatly in texture, shape and size. Nonetheless, algorithms such as the random walker method can provide mass-specific confidence maps which can be incorporated into other segmentation algorithms to improve their competence in delineating ill-defined mass boundaries [11].

Nguyen et al. [12] combined the probabilistic matrix from the random walker segmentation method with a convex energy functional to derive a robust interactive segmentation model. They modeled the convex energy functional as a linear mixture of Gaussian distributions, and expressed the probability matrix as a binary classifier to propagate the contour whenever the statistical models of the foreground and the background are similar. However, in their implementation, the user fixes the threshold value of the global minimum for the convex energy functional. In mass lesion segmentation, a fixed threshold value for the global minima of a database of direct digital mass lesions is not feasible because the gray level intensity distributions of the background tissues surrounding most masses are heterogeneous. This approach may underestimate or overestimate the optimum threshold values of these masses and, consequently, lead to unsuitable segmentation outcomes. Furthermore, hand tuning each threshold value for optimum mass boundary delineation is impractically time consuming. The concentric morphology model of a mass describes a mass lesion as possessing a highlighted focal region surrounded with successively less intense concentric layers.

This study proposes an interactive segmentation model to derive a reliable estimate of the mass-specific threshold value from the morphological characteristics of the mass lesion for the global minimizer of its convex energy functional. Our method assumes that the statistical properties of the highlighted focal region represent the statistical model of the ground truth label. Subsequently, the mass-specific threshold value for the global minimizer can be derived from the threshold value that maximizes the between-class variance of the highlighted focal region and the non-mass region of the probability matrix of the mass lesion. Our approach defines the mass-specific value as the mean pixel gray level of all pixels whose probability of belonging to the highlighted focal region is greater than the threshold value. The main contribution of this paper lies in extracting reliable information from the probability matrix to provide a mass-dependent reliable estimate of the threshold value for each global minimizer.

2. Mathematical background

2.1. Maximum likelihood active contour model for binary segmentation

The binary partition of the image domain Ω into Ω_1 and Ω_2 by an evolving curve, C, can be achieved by maximizing the posterior partitioning probability for binary segmentation. Assuming that all pixel intensities are independently distributed and all prior probabilities are equally likely, the binary partition can be formulated as the minimization of the following energy functional:

$$E(\Omega_1,\Omega_2,p_1,p_2) = -\sum_{i=1}^{2}\int_{\Omega_i} log(p_i((I(x,y)|\Omega_i)))dxdy + \mu length(C) \quad (1)$$

where $I(x,y)$ is the value of the gray intensity value at pixel position (x,y) in region $\Omega_i, p_i((I(x,y)|\Omega_i))$ the likelihood of a pixel (x,y) in Ω_i having the value $I(x,y)$, and $\mu > 0$ is a constant.

Assuming that the gray level pixel values, $I(x,y)$, are drawn from a Gaussian distribution, then:

$$p_i((I(x,y)|\Omega_i)) = \frac{1}{\sqrt{2\pi}\sigma_i}\exp -\frac{(I(x,y)-\mu_i)^2}{2\sigma_i} \quad (2)$$

where σ_i^2 and μ_i are the variance and mean of Ω_i, respectively.

Suppose the curve, C, is embedded in the level set function, $\phi(x,y)$, such that the regularized Heaviside function, H_ϵ, is the characteristic function separating the foreground and background. Then, optimum partition is obtained by solving the following gradient descent flow:

$$\frac{\partial\phi}{\partial t} = H'_\epsilon(\phi)\left[div\left(\frac{\nabla\phi}{|\nabla\phi|}\right) + log(\sigma_2) - log(\sigma_1) + \left(\frac{(I(x,y)-\mu_2)^2}{2\sigma_2^2}\right) - \left(\frac{(I(x,y)-\mu_1)^2}{2\sigma_1^2}\right)\right] \quad (3)$$

2.2. Convex energy functional modeled with the posterior partitioning probability for binary segmentation

The steady state solution of Eq. (3) is given as:

$$\frac{\partial\phi}{\partial t} = div\left(\frac{\nabla\phi}{|\nabla\phi|}\right) + \lambda\left(log(\sigma_2) - log(\sigma_1) + \left(\frac{(I(x,y)-\mu_2)^2}{2\sigma_2^2}\right) - \left(\frac{(I(x,y)-\mu_1)^2}{2\sigma_1^2}\right)\right) \quad (4)$$

This is the gradient descent flow of the energy functional:

$$E(\phi,\sigma_1,\sigma_2,\mu_1,\mu_2) = \int_\Omega |\nabla\phi|dxdy + \lambda\int_\Omega r(x,y,\sigma_1,\sigma_2,\mu_1,\mu_2)\phi dxdy \quad (5)$$

in which $r(x,y,\sigma_1,\sigma_2,\mu_1,\mu_2) = log(\sigma_2) - log(\sigma_1) + \left(\frac{(I(x,y)-\mu_2)^2}{2\sigma_2^2}\right) - \left(\frac{(I(x,y)-\mu_1)^2}{2\sigma_1^2}\right)$

$E(\phi,\sigma_1,\sigma_2,\mu_1,\mu_2)$ has a global minimizer [8] when the minimization of ϕ is restricted to the interval [0,1]. Using the same approach as Bresson et al. [8], we propose an expression for the energy functional in Eq. (5) as:

$$E(u,\sigma_1,\sigma_2,\mu_1,\mu_2) = TV_g(u) + \lambda \int_\Omega r(x,y,\sigma_1,\sigma_2,\mu_1,\mu_2)u\,dxdy \quad (6)$$

where $TV_g(u)$ is the weighted TV energy, and it is given as:

$$TV_g(u) = \int_\Omega g(x,y)|\nabla u|dxdy \quad (7)$$

with $g(x,y)$ as an edge indication function.

The constrained convex minimization problem for the binary segmentation with the energy functional, $E(u,\sigma_1,\sigma_2,\mu_1,\mu_2)$, is expressed as:

$$\min_{0\leqslant u\leqslant 1}\left\{TV_g(u) + \int_\Omega \lambda r(x,y,\sigma_1,\sigma_2,\mu_1,\mu_2)u\,dxdy\right\} \quad (8)$$

The unconstrained minimization expression of Eq. (8) is expressed as follows:

$$\min_{u,\varphi}\left\{TV_g(u) + \frac{1}{2\theta}\|u-\varphi\|_{L^2}^2 + \int_\Omega (\lambda r(x,y,\sigma_1,\sigma_2,\mu_1,\mu_2)\varphi + \alpha\upsilon(\varphi))dxdy\right\} \quad (9)$$

where $\alpha > \frac{\lambda}{2}\|r\|_{L\infty(\Omega)}$, $\upsilon(\varphi) = max\{0, 2|-0.5|-1\}$, λ and θ are constants, $TV_g(u)$ is the boundary term, and $r(x,y,\sigma_1,\sigma_2,\mu_1,\mu_2)$ is the global term representing the statistical competition between the regions inside and outside the contour.

The Chambolle's dual formulation [13] of the TV regularization function is implemented to solve the relaxed minimization problem by iterating u and φ, separately. This approach splits the relaxed minimization problem into two problems:

1. Fix φ and solve for u in the following minimization problem:

$$\min_u\left\{TV_g(u) + \frac{1}{2\theta}\|u-\varphi\|_{L^2}^2\right\} \quad (10)$$

where the gradient descent flow is given by:

$$u_t = div\left(\frac{\nabla u}{|\nabla u|}\right) - \frac{u-\varphi}{\theta} \quad (11)$$

and it is solved [8] as:

$$u = \varphi - \theta.div(p) \quad (12)$$

with a fixed point method and with the update scheme for p as:

$$p^{n+1} = \frac{p^n + \Delta t\nabla(div(p^n) - \varphi/\theta)}{1 + \Delta t/g(x,y)|\nabla(div(p^n) - \varphi/\theta)|} \quad (13)$$

while setting $p^0 = (0,0)$ and $\Delta t \leqslant 1/8$ for convergence.

2. Fix u and solve for ϕ in the following minimization problem:

$$\min_\varphi\left\{\frac{1}{2\theta}\|u-\varphi\|_{L^2}^2 + \int_\Omega (r(x,y,\sigma_1,\sigma_2,\mu_1,\mu_2)\varphi + \alpha\upsilon(\varphi))dxdy\right\} \quad (14)$$

The minimization solution can be written as:

$$\varphi_t = min\{max(u - \theta\lambda(r(x,y,\sigma_1,\sigma_2,\mu_1,\mu_2),0),1)\} \quad (15)$$

Generally, $r(x,y,\sigma_1,\sigma_2,\mu_1,\mu_2)$ is updated after a few iterations, and upon convergence the final segmentation solution is obtained by thresholding $u(x,y)$. The threshold value is an arbitrary constant restricted to the interval [0,1] and is typically 0.5, as cited by some researchers [12,14].

2.3. Random walk probability matrices

The probability matrices are derived from the random walk algorithm by minimizing a combinatorial Dirichlet problem [15]. This algorithm models an image as a weighted graph consisting of nodes and edges. Image pixels are denoted as nodes, and two neighboring nodes are connected with an edge. The weight assigned to an edge is determined by the distance between the pixel values of the nodes, and is generally expressed as the likelihood of a random walker crossing the edge.

The algorithm requires pre-defined labeled pixels. Sets of pixels are labeled as belonging to the highlighted focal region of the mass and non-mass regions. The probability matrix generated by the random walker, starting from each unlabeled pixel and first reaching the labeled pixel of the highlighted focal region, is the mass-specific probabilistic map for the segmentation tasks. In our implementation, the mass-specific probabilistic map was derived from the weighted TV scale-space smoothed model of the original mass. This approach preserves edges in the image through different degrees of smoothing.

3. Methods

3.1. Proposed convex energy functional modeled with global probability distributions and mass-specific probabilistic maps

The global term representing the statistical competition between the regions inside and outside the contour is modeled as:

$$r(x,y,\sigma_1,\sigma_2,\mu_1,\mu_2,P,\beta) = \beta * r(x,y,\sigma_1,\sigma_2,\mu_1,\mu_2) + (1-\beta) * (1 - 2 * P(x,y)) \quad (16)$$

where $P(x,y)$ is the mass-specific probabilistic map of the mass with values within the interval [0,1]. The term $(1 - 2 * P(x,y))$ acts as a classifier [12] which influences the direction of propagation of every pixel position (x,y). In regions where $P(x,y) = 0.5$, $u(x,y)$ is propagated with the global probability distribution and the contribution of the classifier to the global term is zero. While for regions with $P(x,y) > 0.5$, $u(x,y)$ expands and favors classification of these regions as the highlighted focal regions and vice versa. The classifier propagates $u(x,y)$, whenever $r(x,y,\sigma_1,\sigma_2,\mu_1,\mu_2) = 0$. β is a positive constant, $(0 \leqslant \beta \leqslant 1)$, which controls the influence of the classifier on the global term.

The proposed unconstrained minimization problem for binary segmentation of the TV regularization function is expressed as:

$$\min_{u,\varphi}\left\{TV_g(u) + \frac{1}{2\theta}\|u-\varphi\|_{L^2}^2 + \int_\Omega \lambda r(x,y,\sigma_1,\sigma_2,\mu_1,\mu_2,P,\beta)\varphi + \alpha\upsilon(\varphi)dxdy\right\} \quad (17)$$

3.2. Mass-specific threshold value for the global minimizer of the proposed relaxed minimization problem

We define a confidence threshold level, T_1, as the value of $P(x,y)$ that partitions the mass-specific probabilistic map, $P(x,y)$, into the highlighted focal region of the mass and the non-mass region by maximizing an objective function with a heuristic optimization procedure. The optimal threshold value for the global minimizer, T_2, of each mass is expressed as the mean gray level of pixels whose probability of belonging to the highlighted focal region is greater than T_1.

Suppose the confidence map, $P(x,y)$, is rescaled to an interval [0,255] and its histogram can be partitioned into two categories (C_1 and C_2) with an objective function, $(f(t))$, where the pixel values of C_1 range from 0 to $t-1$ and those of C_2 from t to 255. Based

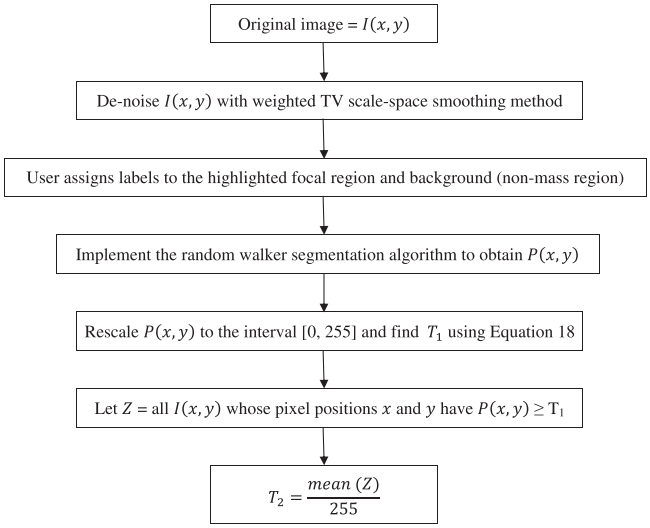

Figure 1. The proposed framework for a mass-specific threshold value (TV) of a global minimum for a convex energy functional in digital mammography.

on the Otsu's nonparametric method [16] for bi-level thresholding, the optimal threshold value (T_1) is obtained by maximizing ($f(t)$), that is:

$$T_1 = argmax(f(t)) \tag{18}$$

Table 1
Qualitative evaluation of the performance of proposed method with the ground truths (expert) for masses in Figs. 2, 4 and 5, where: Jaccard Index (JI), Euclidian Distance between Fourier Descriptors (EDFD) are the parameters compared.

Masses	JI	EDFD
Fig. 2 (I)	0.80	0.02
Fig. 2 (II)	0.83	0.06
Fig. 2 (III)	0.90	0.01
Fig. 2 (IV)	0.86	0.03
Fig. 4	0.79	0.11
Fig. 5 (I)	0.80	0.01
Fig. 5 (II)	0.72	0.12
Fig. 5 (III)	0.87	0.02
Fig. 5 (IV)	0.81	0.09

where $f(t)$ is the between-class variance and it is expressed as:

$$f(t) = w_1(\mu_1 - \mu_T)^2 + w_2(\mu_2 - \mu_T)^2 \tag{19}$$

μ_1 is the mean intensity of C_1, μ_2 the mean intensity of C_2, μ_T the mean intensity of the original whole image, w_1 is the cumulative probability of C_1, and w_2 is the cumulative probability of C_2.

We implemented the particle swarm optimization method to solve for T_1. This method uses equations, representing the velocities and positions of a group of birds to simulate their social behavior as a means to search for a global minimum of an objective function [17]. Each particle position describes a potential solution for minimizing the objective function ($f(t)$). The particle keeps a

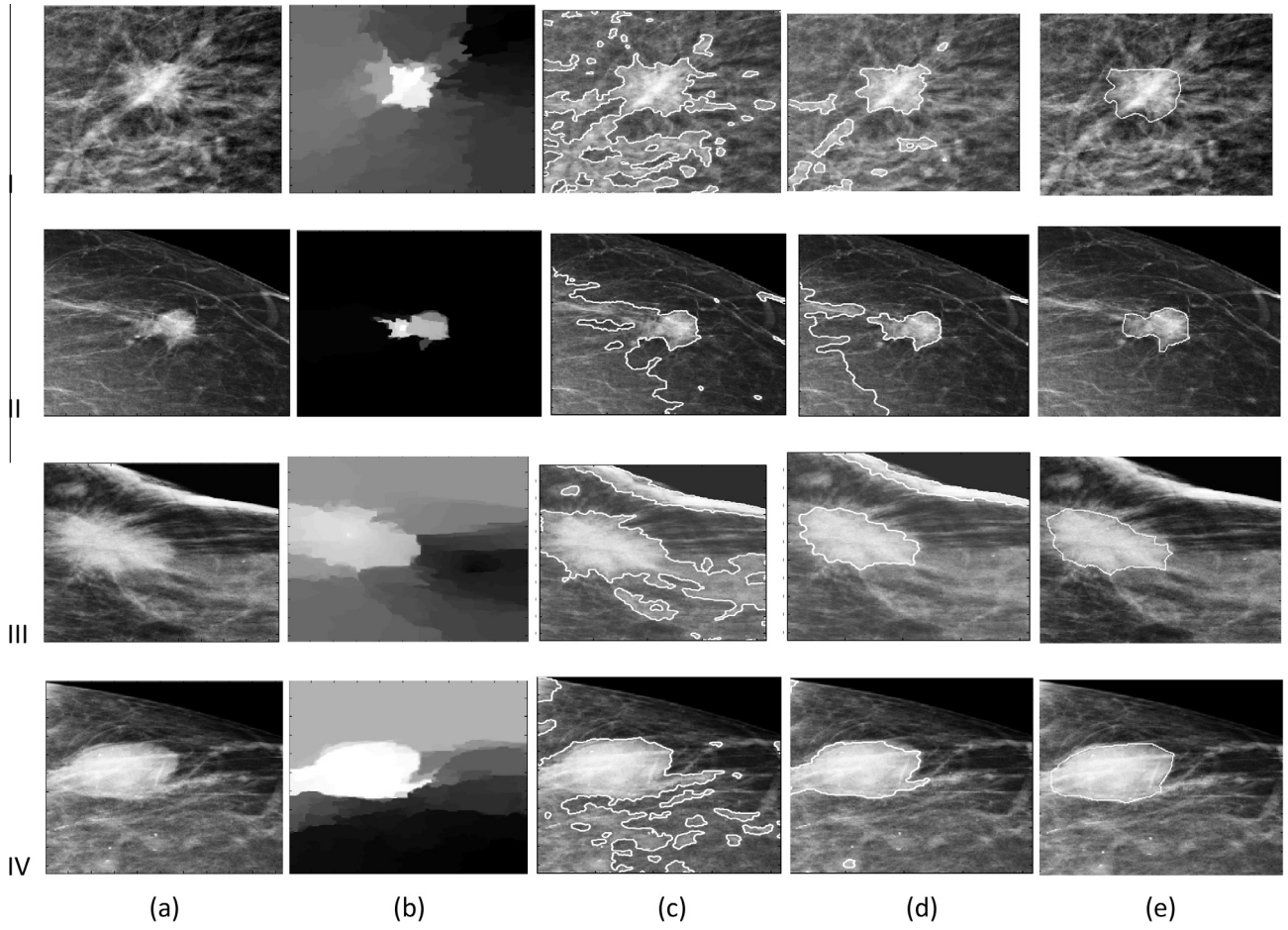

Figure 2. Differences in global minimizers with the typical threshold value of 0.5 and mass-specific threshold values from the proposed iterative method and the ground truths. (a) Original mass lesions. (b) Confidence maps from the random walk method. (c) The global minimizer with threshold values of 0.5. (d) Global minimizer with threshold values from proposed iterative method, and (e) the ground truths.

record of its coordinates in the problem space, and iteratively updates its solution with its historical personal best solution (*pbest*) and the best solution of the group (*gbest*) until particles in the group surround the one with the most optimal solution. This solution represents the best value for the objective function, hence, the global minimum. The updating equations for each particle, *i*, are mathematically modeled as follows:

$$\upsilon_i^{t+1} = w\upsilon_i^t + r_1 \times rand \times (pbest_i - x_i^t) + r_2 \times rand \times (gbest - x_i^t) \quad (20)$$

and

$$x_i^{t+1} = x_i^t + \upsilon_i^{t+1} \quad (21)$$

where w is the inertia weight, υ_i^t is the velocity of the particle at iteration t, r_1 and r_2 are the personal and social learning rates, respectively, *rand* is a random variable generated from a uniform distribution in the range [0, 1], $pbest_i$ is the personal best solution of the particle, and x_i^t is the current position of the particle.

The proposed framework for a mass-specific threshold value of a global minimum for a convex energy functional in digital mammography is illustrated in Fig. 1.

3.3. Segmentation procedure

The proposed iterative procedure can be summarized as follows:

Step 1: Compute $P(x,y)$ and T_2.
Step 2: Minimize Eq. (17) using the dual formulation as shown in Eqs. (13) and (15).
Step 3: Update $r(x,y,\sigma_1,\sigma_2,\mu_1,\mu_2,P,\beta)$ after a few iterations until convergence.
Step 4: Segmentation outcome $= u(x,y) > T_2$.

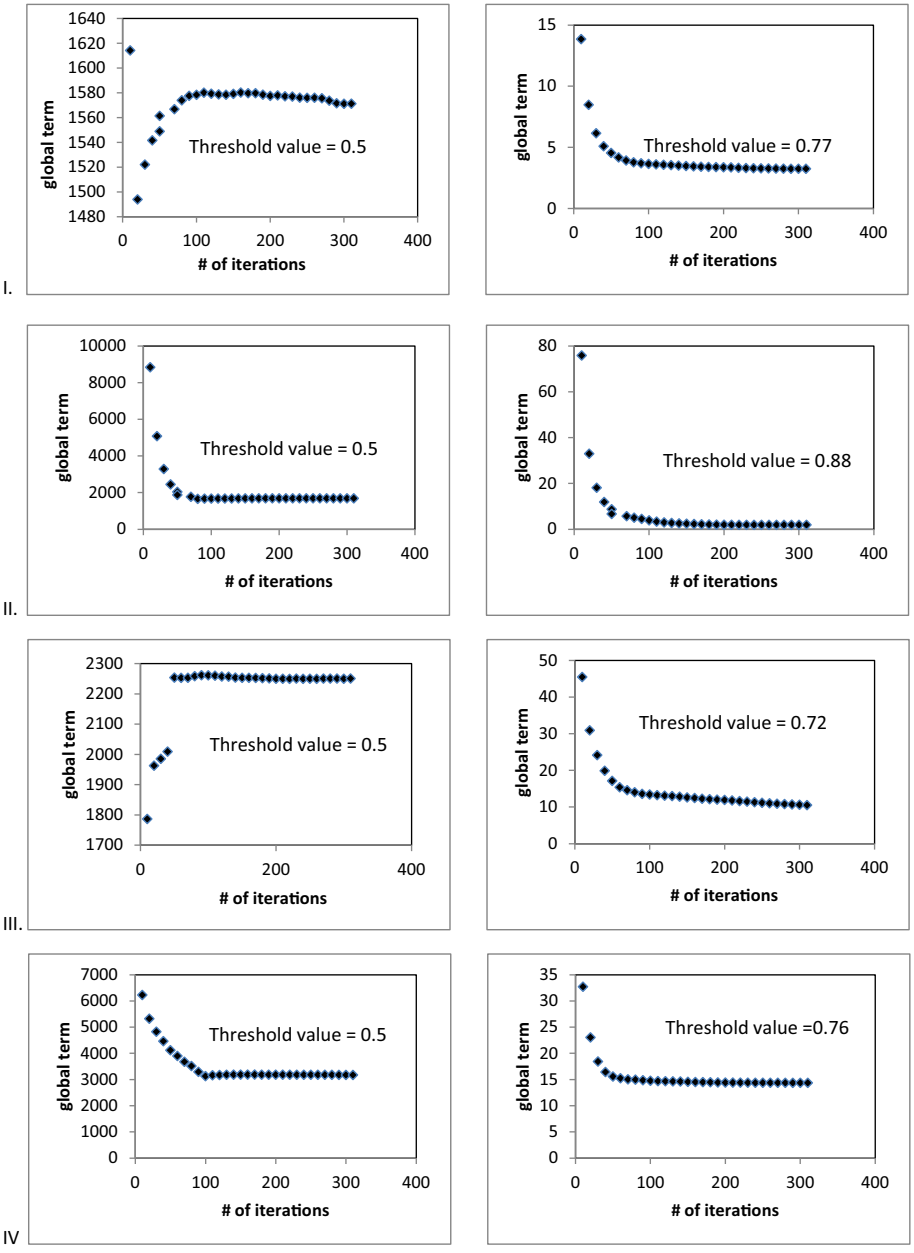

Figure 3. Variation of the global term, $r(x,y,\sigma_1,\sigma_2,\mu_1,\mu_2,P,\beta)$, with the number of iterations for mass lesions in Fig. 2 for a typical threshold value of 0.5 and for threshold values derived from the proposed method (PM).

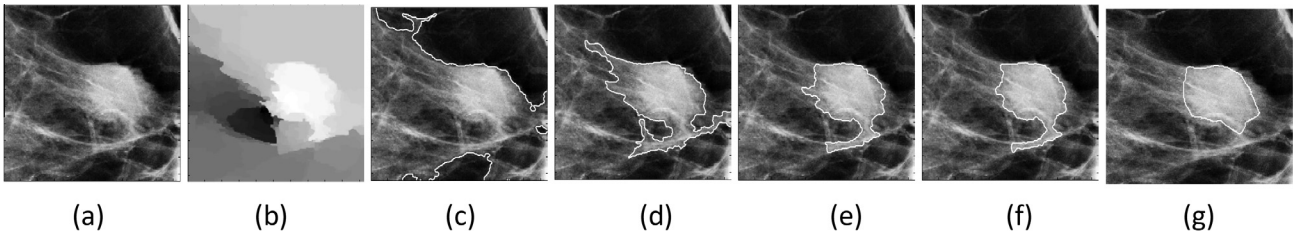

Figure 4. Sensitivity of segmentation results to the threshold value, T_2: (a) original mass, (b) probability map of the mass, (c) segmentation result with $T_2 = 0.5$, (d) segmentation result with $T_2 = 0.6$, (e) segmentation result with our PM ($T_2 = 0.67$), (f) segmentation result with $T_2 = 0.8$, and (g) the ground truth.

4. Results

The performance of the proposed iterative procedure was evaluated on 50 mammograms with mass lesions acquired from a Hologic Selenia™ Dimensions™ system with an image receptor consisting of a 70 μm pixel pitch, selenium direct-capture detector. It was implemented in Matlab 7.0 on an Intel Core 2 Duo 3.0 GHz processor with default parameters set to $\phi = 1/1.5, \lambda = 1, \beta = 0.5$.

Fig. 2 shows the differences in the performance of a global minimizer with a typical threshold value of 0.5 and the mass-specific threshold values from the proposed iterative method, with ground truths from the experienced expert. The highlighted focal region of the mass lesion is represented with higher probability values of being classified as a mass region than other regions in the image domain. Therefore, the threshold value for binary segmentation of the probability matrix of a mass lesion can be considered as a

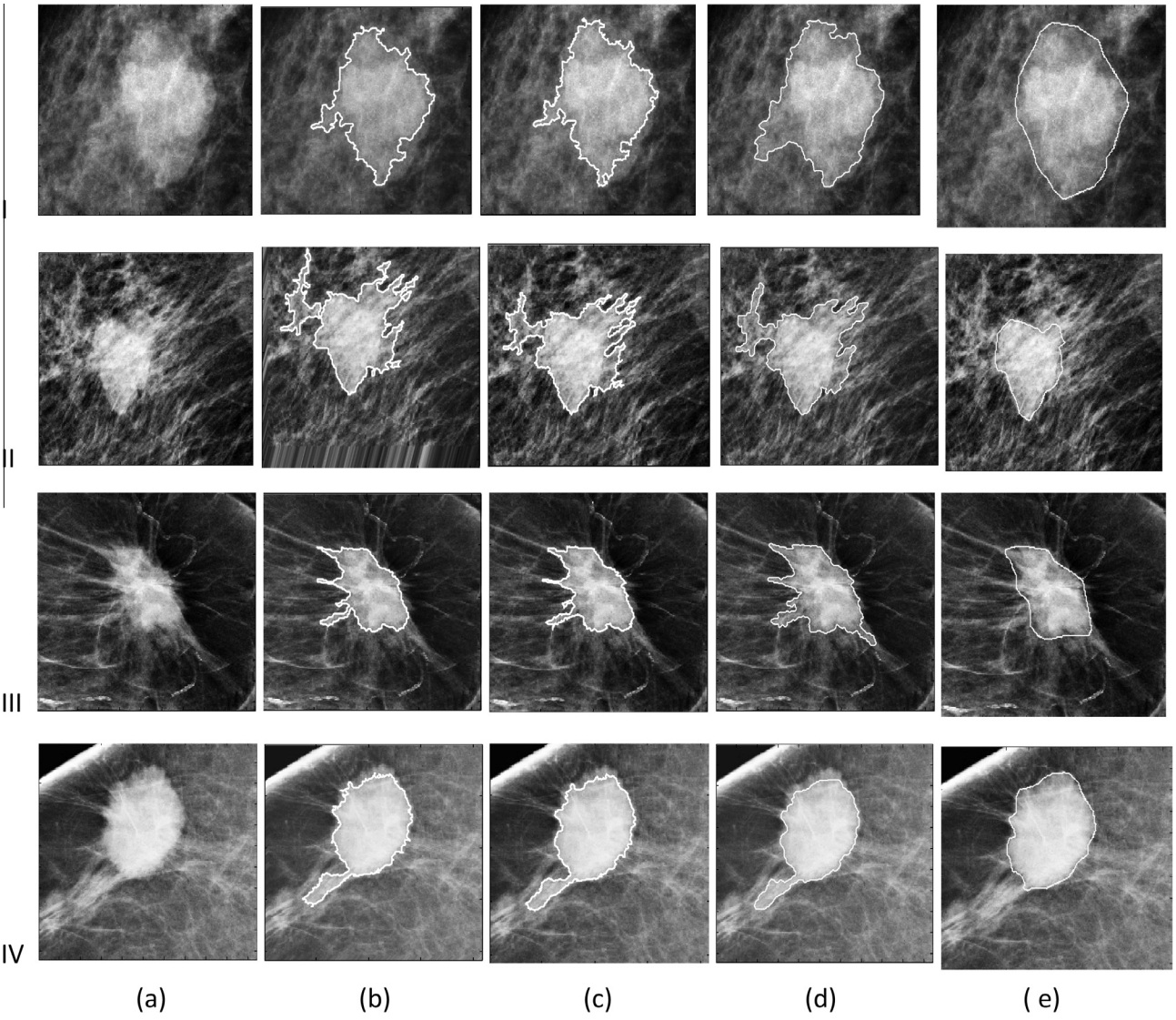

Figure 5. Comparison of the proposed method (PM) with other segmentation schemes and the ground truth: (a) original images, (b) segmentation results with the select local or global segmentation model, (c) segmentation results with the Chan–Vese model, (d) segmentation result with the PM, and (e) the ground truths.

Table 2
Qualitative evaluation of the performance of proposed method (PM) with different segmentation models, where: proposed method, Chan–Vese model (CV), global segmentation model (GS), Jaccard Index (JI), Euclidian Distance between Fourier Descriptors (EDFD) are the parameters compared.

Paired segmentation models	Mean values of JIs	Mean values of EDFDs
PM/CV	0.89 ± 0.07	0.05 ± 0.03
PM/GS	0.88 ± 0.06	0.06 ± 0.04
CV/GS	0.95 ± 0.04	0.04 ± 0.03

realistic estimate of the mass-specific threshold value for the global minimizer of its convex energy functional. Fig. 2(e) shows that these threshold values give rise to segmentation results that are similar to manually delineated masses by an experienced expert (ground truths). Quantitative results are shown in Table 1.

When T_2 is a good estimate for the global minimum, the global term, $r(x, y, \sigma_1, \sigma_2, \mu_1, \mu_2, P, \beta)$ converges to a low value as illustrated in Fig. 3. Moreover, $r(x, y, \sigma_1, \sigma_2, \mu_1, \mu_2, P, \beta)$ decreases rapidly as the number of iterations increases and finally remains stable on this value. Fig. 4 shows that T_2 may not be the only threshold value for a reliable segmentation outcome for a given mass, but in most instances, our PM provides the required minimum threshold value for the global minimizer. For this database, the mean value for T_2 was 0.67 ± 0.09 with a minimum value of 0.4 and a maximum value of 0.8.

Fig. 5 compares the segmentation performance of the PM, the classical Chan–Vese (CV) model, the active contour with selective local or global segmentation (GS) model and the manually delineated boundaries of masses on direct digital mammograms. Fig. 5 (I) and (III) show that the PM achieved similar segmentation performance as the CV and GS models, except in regions with slowly varying pixel intensity values wherein the PM slightly undersegments. We quantified the differences between segmented areas with the Jaccard similarity index (JI) also expressed as the relative overlap [18].

Fourier descriptors are the best performing shape-based descriptor for binary classification of mammographic masses, and some researchers have estimated that 60 Fourier descriptors are sufficient for shape indexing [19]. Consequentially, the shape of each segmented mass lesion was indexed with 60 Fourier descriptors and we estimated the agreement between the shape-based descriptors of the segmented areas with the Euclidean Distance between Fourier descriptors (EDFD) [20].

Table 1 shows the evaluation of the differences between the segmentation results of some of the masses with the proposed method and the ground truths from the expert. From the JIs, both methods give similar results, but lower JIs for masses with spiculations such as masses in Figs. 4 and 5 (II). This is expected because mass margins are usually obscured and embedded in surrounding tissue, and hence delineation of the mass boundary becomes subjective. Zheng et al. [21] have cited the variation in the classification of spiculation levels in mass margins between their computer scheme and observer's rating as 49.2% (kappa = 0.218) and between paired observers from 41.3% to 58.8% (kappa = 0.136–0.309). Furthermore, other researchers have reported that manual delineation of mass boundaries amongst experts is subjective [1,2].

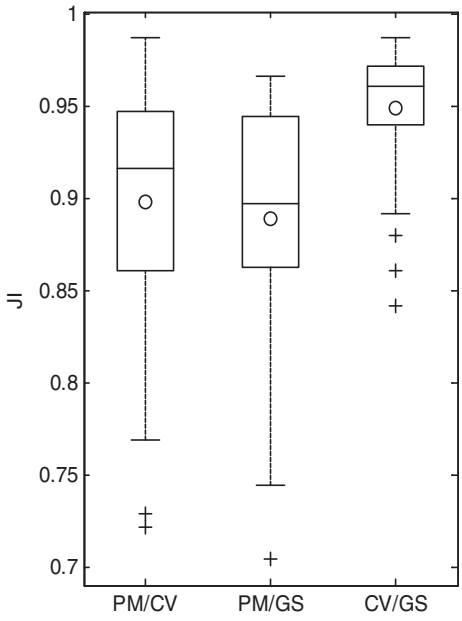

Figure 6. Box plots illustrating the distribution of JIs with paired segmentation schemes. The central lines and the circles are the median and mean values of the JIs, respectively. The edges of the box represents the 25th and 75th percentile, the end of the whiskers extreme values and the crosses are the values that are more than 1.5 times the interquartile range away from the top or bottom of the box, also known as outliers.

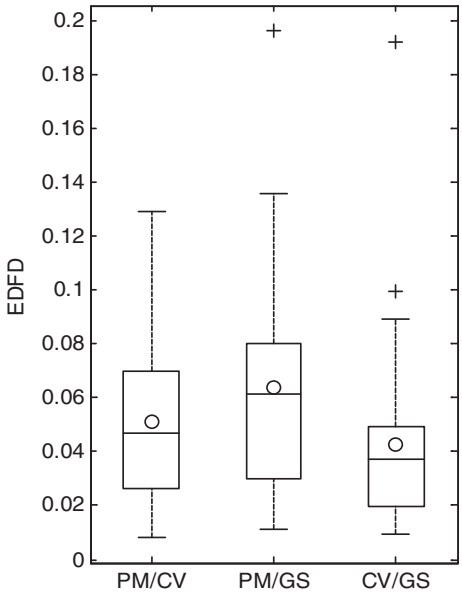

Figure 7. Box plots illustrating the distribution of EDFDs with paired segmentation schemes. The central lines and the circles are the median and mean values of the EDFDs, respectively. The edges of the box represent the 25th and 75th percentile, the end of the whiskers extreme values and the crosses are the values that are more than 1.5 times the interquartile range away from the top or bottom of the box, also known as outliers.

5. Discussion

The mean value of the JIs and the mean value of the EDFDs for the database of masses in this study are listed in Table 2. The PM achieved similar segmentation results as the CV and GS models on the size and shape of the segmented areas. Rahmati et al. [22], reported a value of 0.87 for JIs between their segmentation algorithm and expert radiologists, while Hao et al. [11] reported JIs less than 0.85 for their PM and other segmentation methods. The mean values for the PM are higher than the values reported by these researchers, and moreover their masses were not from direct digital mammograms.

The distributions of the JIs and EDFDs for each paired segmentation models were investigated with box plots, as shown in Figs. 6

and 7, respectively. Less than 7% of the JIs and EDFDs were classified as outliers for each paired segmentation scheme. The EDFDs show that the shapes of the segmented areas from the PM are similar to those of the CV and GS models, although the GS model presented more outliers than the others. The average processing time for the PM was 14 ± 2.5 s as compared to the CV and GS models, which were 10 ± 1.5 s and 8 ± 2.1 s, respectively.

The PM combines the random walker algorithm and particle swarm optimization to search for a reliable estimate of a mass-specific threshold value for the global minimum, therefore, factors influencing any of the above-mentioned algorithms may compromise the segmentation accuracy of the PM. The particle swarm optimization method is prone to premature convergence to a local minimum. Consequently, this step can be avoided if T_1 is set to a value representing the mean pixels in the focal region of the probability map. We set $T_1 = 0.7$ for our database, and more than 80% of the masses produced reasonable segmentation results with the derived T_2 values, but could not successfully segment masses whose gray intensity distributions were similar to surrounding background tissues.

6. Conclusions

The proposed approach successfully searches for a mass-specific threshold value for the global minimization of the convex energy functional that is representative of the mean pixel values of the highlighted focal region of the mass to derive segmentation results which are independent of the placement of the initial contours. The segmentation results of this method are comparable to other classical segmentation methods and manually delineated boundaries from the expert.

In the future, we hope to evaluate the PM on a larger database of direct digital mammograms and also investigate the effects of the position of the foreground/background seed on the segmentation accuracy. And, furthermore, evaluate the differences between the proposed method and the ground truths for the entire database.

Acknowledgements

The Department of Radiology, Universitas Academic Hospital, University of the Free State, who allowed us access to their archived mammographic images, and Dr. G. Van Der Westhuizen who provided ground truths for the study.

Ms. Theanette Mulder, Medical Editor, School of Medicine, University of the Free State, for technical and editorial preparation of the manuscript.

References

[1] Sahiner B, Petrick N, Chan HP, Hadjiiski LM, Paramagul C, Helvie MA, et al. Computer-aided characterization of mammographic masses: accuracy of mass segmentation and its effects on characterization. IEEE Trans Med Imaging 2001;20(12):1275–84. http://dx.doi.org/10.1109/42.974922.

[2] Kinnard L, Lo SC, Makariou E, Osicka T, Wang P, Chouikha MF, Freedman MT. Steepest changes of a probability-based cost function for delineation of mammographic masses: a validation study. Med Phys 2004;31(10):2796–810. http://dx.doi.org/10.1118/1.1781551.

[3] Singh S, Maxwell J, Baker JA, Nicholas JL, Lo JY. Computer-aided classification of breast masses: performance and interobserver variability of expert radiologists versus residents. Radiology 2011;258(1):73–80. http://dx.doi.org/10.1148/radiol.10081308.

[4] Caselles V, Catté F, Coll T, Dibos F. A geometric model for active contours in image processing. Numer Math 1993;66(1):1–31. http://dx.doi.org/10.1007/BF01385685.

[5] Chan TF, Vese LA. Active contour without edges. IEEE Trans Image Process 2001;10(2):266–77. http://dx.doi.org/10.1109/83.902291.

[6] Zhang K, Zhang L, Song H, Zhou W. Active contours with selective local or global segmentation: a new formulation and level set method. Image Vis Comput 2010;28:668–76. http://dx.doi.org/10.1016/j.imavis.2009.10.009.

[7] Acho SN, Rae WID. Dependence of shape-based descriptors and mass segmentation areas on initial contour placement using the Chan–Vese method on digital mammograms. Comput Math Methods Med 2015;2015:349874. http://dx.doi.org/10.1155/2015/349874.

[8] Bresson X, Esedoglu S, Vandergheynst P, Thiran JP, Osher S. Fast global minimization of the active contour/snake model. J Math Imaging Vis 2007;28:151–67. http://dx.doi.org/10.1007/s10851-007-0002-0.

[9] Wang L, Shi F, Lin W, Gilmore JH, Shen D. Automatic segmentation of neonatal images using convex optimization and coupled level sets. Neuroimage 2011;58(3):805–17. http://dx.doi.org/10.1016/j.neuroimage.2011.06.064.

[10] Gao Y, Tannenbaum A. Combining atlas and active contour for automatic 3D medical image segmentation. Proc IEEE Int Symp Biomed Imaging 2011:1401–4.

[11] Hao X, Shen Y, Xia S. Automatic mass segmentation on mammograms combining random walks and active contour. J Zhejiang Univ Sci C 2012;13(9):635–48. http://dx.doi.org/10.1631/jzus.C1200052.

[12] Nguyen TN, Cai J, Zhang J, Zheng J. Robust interactive image segmentation using convex active contours. IEEE Trans Image Process 2012;21(8):3734–43. http://dx.doi.org/10.1109/TIP.2012.2191566.

[13] Chambolle A. An algorithm for total variation minimization and applications. J Math Imaging Vis 2004;20:89–97. http://dx.doi.org/10.1023/B:JMIV.0000011320.81911.38.

[14] Moreno JC, Prasath VBS, Proença H, Palaniappan K. Fast and globally convex multiphase active contours for brain MRI segmentation. Comput Vis Image Underst 2014;125:237–50. http://dx.doi.org/10.1016/j.cviu.2014.04.010.

[15] Grady L. Random walks for image segmentation. IEEE Trans Pattern Anal Mach Intell 2006;28(11):1768–83. http://dx.doi.org/10.1109/TPAMI.2006.233.

[16] Otsu N. A threshold selection method from gray-level histograms. IEEE Trans Syst Man Cybern 1979;9(1):62–6.

[17] Kennedy J, Eberhart R. Particle swarm optimization. Proc IEEE Int Conf Neural Networks 1995;4:1942–8.

[18] Tangaro S, Amoroso N, Boccardi M, Bruno S, Chincarini A, Ferraro G6, et al. Automated voxel-by-voxel tissue classification for hippocampal segmentation: methods and validation. Phys Med 2014;30(8):878–87. http://dx.doi.org/10.1016/j.ejmp.2014.06.044.

[19] Zhang D, Lu G. Shape retrieval using Fourier descriptors, Proceedings of the international conference on multimedia and distance education (ICMADE'01), Fargo, ND, USA.

[20] Zhang D, Lu G. A comparative study on shape retrieval using Fourier descriptors with different shape signatures. In: International conference on intelligent multimedia and distance education (ICIMADE01); 2001.

[21] Zheng B, Abrams G, Hardesty LA, Park SC, Drescher J, Maitz GS, et al. Mass margins spiculations: agreement between ratings by observers and a computer scheme. In: Progress in biomedical optics and imaging – proceedings of SPIE, Part 1 ed., vol. 6514; 2007. p. 65141. Available from: doi: http://dx.doi.org/10.1117/12.705754 [accessed 09.04.16].

[22] Rahmati P, Adler A, Hamarneh G. Mammography segmentation with maximum likelihood active contours. Med Image Anal 2012;16(6):1167–86. http://dx.doi.org/10.1016/j.media.2012.05.005.